Epr Crystallography; Studies of Defect Centres in Single Crystals

by

Nicholas Sean Lees

A thesis submitted in partial
fulfillment of the requirements
for the degree of
Doctor of Philosophy in Chemistry.

Department of Chemistry,
The University of Canterbury.

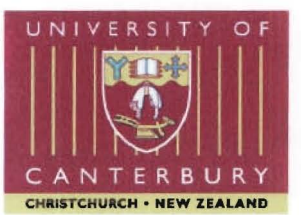

September 2001

Acknowledgements

I would like to thank both my supervisor Dr. R. F. C. Claridge for his support and guidance throughout the course of my Ph.D. studies, and my associate supervisor Dr. W. C. Tennant for his considerable assistance, including many discussions on the theoretical work contained in this thesis. I would also like to thank Dr. C. J. Walsby for help with the collection and fitting of experimental data. I thank Professor J. A. Weil for supplying the crystal used in the α-quartz work described in this thesis, and also for providing his advice and expertise in this area. Thanks also to Dr. R. G. A R. Maclagan for producing molecular-orbital calculations for the quartz work. Finally, I am grateful for the financial assistance provided by a teaching assistantship in the University of Canterbury Department of Chemistry.

Contents

List of Figures

List of Tables

Abstract

This thesis presents the results of precise X-band electron paramagnetic resonance studies of zircon ($ZrSiO_4$) and α-quartz (SiO_2) single crystals at temperatures between 15 and 100 K, and the synthesis of the zircon crystals studied.

Zircon crystals have been grown using the flux-growth technique, producing well-shaped crystals up to 4 mm in length. The technique was used to grow both doped and nominally undoped crystals. Dopants successfully incorporated into the zircon crystals were titanium, chromium, yttrium, aluminium and boron.

Analysis of Ti^{4+}/Y^{3+}-doped zircon crystals revealed four defect centres new to the Canterbury research group. Two oxygenic hole centres have been analysed, one compensated by yttrium ($[SiO_4/Y]^0$), and the other by an unknown ion ($[SiO_4/M]^n$). A crystal-field spin-orbit coupling analysis of hole centres with a range of g values has shown that their anisotropy may be directly related to crystal-field splittings of orbital energy levels. A Ti^{3+} electron centre, $Si(Ti^{3+})$, has been shown to be located in a silicon lattice position in contrast to an earlier-discovered Ti^{3+} centre in a zirconium lattice position, $Zr(Ti^{3+})$. Another electron centre labelled H ($g_{\|} = 1.9875$, $g_{\perp} = 1.9550$) has been measured, but is not yet understood.

A previously observed electron centre (Z) with effective g values of 1.9991 and 3.9118 has been shown to be a chromium ion in a silicon lattice position. A +3 oxidation state, and a large zero-field splitting has been inferred from an analysis of the effective g values. Two closely related boron centres have been observed in zircon crystals with relatively high boron doping, and have been interpreted as impurity electron centres in a zirconium lattice site. Both have almost identical g values $g_x = 1.969$, $g_y = 1.981$, $g_z = 1.969$. One of the centres has the unusual point-group symmetry for defects in zircon of $mm2$ (C_{2v}), which is explained by two adjacent ions along one of the zircon fourfold rotation-inversion axes.

Two centres in α-quartz have been measured and analysed. One has been interpreted as a silicon-vacancy oxygenic-hole centre, $[HLi_2O_4]^0$, compensated by one hydrogen and two

lithium ions. The hyperfine matrices have been analysed with some success using three different methods to ascertain the locations of the compensating nuclei. The second centre is a previously reported hydrogen-compensated iron centre in a silicon lattice site, $[FeO_4/H]^0_\alpha$. A pseudocube analysis has been carried out in order to confirm the location of the iron ion, but the results have been found inconclusive.

Chapter 1

Introduction

The properties of single crystals in applications such as oscillators, semiconductors, solid-state lasers and high-temperature superconductors are fundamentally dependent on the concentration and nature of impurities which they contain. Because of this, a great deal of research has been carried out analysing crystalline defects, using a number of spectroscopic techniques, including electron paramagnetic resonance (epr).

Crystal defects may be macroscopic, such as in the case of dislocations, inclusions and twinning, which can all be visible to the naked eye, or localised 'point' defects, such as in the case of isolated impurity centres, vacancies and electron holes and traps. Macroscopic crystals are never 'perfect', and even submicron crystallites are likely to contain defects unless synthesised under extremely controlled conditions using materials of utmost impurity. It is thus inevitable that crystals to be used in devices will contain defects, which may in some cases be undesirable, and in other cases crucial to the purpose for which they are intended. The macroscopic defects are virtually universally undesirable, as they affect not only the electronic and optical properties of the crystal in an uncontrolled fashion, but also the mechanical properties of the crystal and its behaviour under stress. The localised defects may fit into either category. For example, without the presence of Cr^{3+}, Al_2O_3 would not be capable of lasing.

Epr has been a powerful tool for the structural analysis of point defects in crystals since the early 1950s, shortly after its inception in the 1940s with Zavoiski's experiments [1]. This came about following the advances in radio and microwave technology during the Second World War. The main advantage of the technique is its selectivity for paramagnetic species within a

diamagnetic host. Point defects in crystals are often paramagnetic, or can be made paramagnetic by the action of high-energy radiation such as UV, x- or gamma rays. Electron centres or holes thus formed can be trapped on, or near impurities or vacancies, as the site can often be a potential well with respect to such radiation damage within the pure crystal structure. Other spectroscopies related to epr, such as electron-nuclear double resonance (ENDOR), can also be used in conjunction with epr to provide more detailed information about a defect site.

The key to the structural analysis of a defect centre from epr data is the interpretation of the spin-Hamiltonian parameters, a task which can often be non trivial. However single-crystal epr measurements have the potential to provide a great deal of structural information about the paramagnetic site. On these grounds, the work carried out during the course of this thesis has been described as 'epr crystallography'. The goal of the research has been to use this epr crystallography to reveal and characterise a range of paramagnetic defect centres in single zircon ($ZrSiO_4$) and α-quartz (SiO_2) crystals.

1.1 The epr technique

1.1.1 Fundamental principles

Epr spectroscopy is analogous to other, older forms of absorption spectroscopy, in that electromagnetic radiation is passed through a sample and absorption of the radiation at specific wavelengths due to transitions between energy levels is detected and plotted. In epr spectroscopy, the electromagnetic radiation is in the microwave region, with lower photon energies than IR, visible or UV radiation. The energy-level transitions are induced by the interaction of a magnetic moment in the sample with the oscillating magnetic-field component of the electromagnetic radiation. This is in contrast to most non magnetic-resonance techniques, which involve the interaction of the electric-field component of the radiation with an electric-dipole moment. The other obvious difference of magnetic resonance spectroscopy is the application of a magnetic field, which perturbs the energy levels, and broadens the scope of the technique vastly over what could be achieved with zero applied field.

The magnetic-resonance techniques nmr and epr share many aspects, but differ in the nature of the magnetic moment which interacts with the applied radiation. Nmr deals with nuclear

magnetic moments, while epr deals with electron magnetic moments. Epr spectra may however involve simultaneous transitions arising from interaction of the radiation with both nuclear and magnetic moments, as will be seen later. The origin of the electron magnetic moment is the spin angular momentum associated with the electron[1]. Discussions of the concept of electron spin may be found in many quantum mechanics texts (see for example, [2]).

The two quantities of angular momentum and magnetic moment are proportional in both classical and quantum mechanics. An expression for the electron spin magnetic moment in terms of the spin angular momentum may be derived by considering the classical description of a magnetic dipole. A particle of mass m and charge q travelling in a circle of radius r in the xy plane generates a magnetic field equivalent to that produced by a point magnetic dipole. The dipole moment is along the z axis, and is given by (Weil, Bolton and Wertz (1994), [3]):

$$\mu_z = iA = \pm\frac{qv}{2\pi r} \times \pi r^2 = \pm\frac{q}{2m}mvr = \frac{q}{2m}l_z = \gamma l_z \tag{1.1}$$

where i is the effective current due to the moving charge, and A is the area enclosed. l_z is the orbital angular momentum of the particle about the axis z. The magnetogyric ratio γ is the derived conversion factor between the angular momentum and magnetic moment. γ is more generally defined as:

$$\gamma = \frac{gq}{2m} \tag{1.2}$$

where g is the Zeeman factor.

This relation between the angular momentum and magnetic moment may also be applied to the spin angular momentum. In this case l_z is replaced by the component of the electron spin moment along the z axis (along which a magnetic field is applied), or the eigenvalues of the $\hat{S}_z{}^2$ operator, M_s. Thus for a free electron the spin magnetic moment component parallel to an applied magnetic field μ_z is given by:

$$\mu_z = \gamma_e \hbar M_s = -g_e \beta_e M_s \tag{1.3}$$

[1]Hence epr is also known as electron spin resonance, esr. Orbital angular momentum also plays a part by influencing the spin states through spin-orbit coupling.

[2]Throughout this thesis, operators will be represented with a circumflex,$\hat{}$. Vectors, matrices and tensors are written in bold type, and individual components of these, vector magnitudes, and scalar operators, in italic.

where γ_e is the gyromagnetic ratio for an electron and g_e is the free electron g factor, which has the well-determined value 2.002319304386 [3]. β_e is the Bohr magneton[3], given by:

$$\beta_e = \frac{|e|\hbar}{2m_e} \tag{1.4}$$

The negative sign in equation 1.3 arises because of the above definition of β_e (and also g_e) as a positive number, and the negative charge of the electron.

The energy of a magnetic moment in a magnetic field defined as the z direction is given by:

$$E = -\mu_z B = g_e \beta_e B M_s \tag{1.5}$$

Thus for the single electron which has the $\hat{S}_z$ eigenvalues $M_s = \pm\frac{1}{2}$, often referred to as up (α) or down (β) spin, the energy levels are $\pm\frac{1}{2} g_e \beta_e B$. This expression predicts that for a single electron the α and β spins are degenerate for zero magnetic field, and diverge linearly as the field magnitude B increases, as shown in figure 1-1.

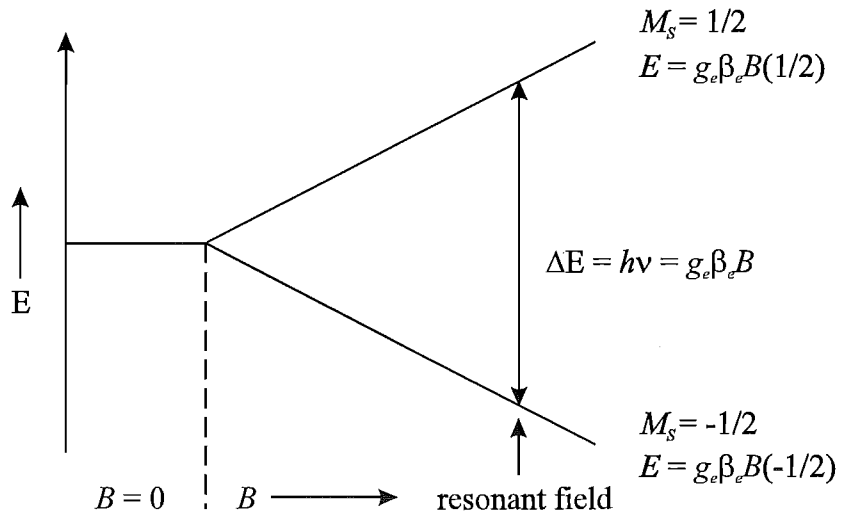

Figure 1-1: Energy level diagram for single electron in a magnetic field.

A transition between these two spin states may be induced by interaction with the magnetic-

[3]The SI symbol for the Bohr magneton is μ_B, but β_e is normally used in epr to avoid confusion with magnetic moments.

field component of the microwave radiation ($\mathbf{B}_1$), for which the photon energy $h\nu$ matches the energy difference between the states. Thus, in order for resonance to occur,

$$\Delta E = h\nu = g_e \beta_e B \tag{1.6}$$

Conservation of angular momentum imposes the selection rule $|\Delta M_s| = 1$ in the general case for epr transitions, as the photon has one unit of angular momentum. Another requirement is that the excitation field $\mathbf{B}_1$ has some component perpendicular to the applied magnetic field.

In an epr experiment, one of the two variables in equation 1.6 is held constant while the other is varied over a range, so that absorbance may potentially occur and be detected wherever the resonance condition is satisfied. Conventionally it is the magnetic-field strength which is swept, as it is easy to do so over a wide range using an electromagnet. For a free electron, the epr spectrum would consist of a single resonance at a field or frequency corresponding to $g = g_e$.

In practice, the unpaired electron(s) in an epr sample will be subject to many interactions which affect the position and number of epr lines. A g factor calculated using equation 1.6 for such resonances is an 'effective' g factor, and reflects the deviation of the magnetic-field magnitude at the site of the unpaired electron from the applied field B due to local effects:

$$\mathbf{B}_{eff} = \frac{g}{g_e}\mathbf{B} \tag{1.7}$$

Effective g values can vary considerably from the free-electron value, and can sometimes be indicative of the paramagnetic ion present, particularly in the case of transition metal ions.

1.1.2 The spin Hamiltonian

The complete Hamiltonian operator for a paramagnetic system in a magnetic field contains the free-ion terms, as well as terms due to the crystal field, spin-orbit coupling, electron spin-spin interactions, the electronic Zeeman interaction, electron-nuclear (hyperfine) interactions and nuclear terms (principally nuclear Zeeman and quadrupole interactions):

$$\widehat{\mathcal{H}} = \widehat{\mathcal{H}}_0 + \widehat{\mathcal{H}}_{CF} + \widehat{\mathcal{H}}_{SO} + \widehat{\mathcal{H}}_{SS} + \widehat{\mathcal{H}}_Z + \widehat{\mathcal{H}}_{SI} + \widehat{\mathcal{H}}_N \tag{1.8}$$

The eigenvalues of the Hamiltonian for the system are the discrete energy levels of the possible states of the system.

$$\widehat{\mathcal{H}}\Psi_i = E_i\Psi_i \tag{1.9}$$

The free-ion term in equation 1.8 describes the energy levels of different electronic configurations of the ion. The excited-state energies are well separated from the ground state from the point of view of epr, and play no part in the analysis. Within each electronic configuration are orbital levels which are split by crystal-field interaction, and spin-orbit coupling. The energy levels which are of concern to the epr spectroscopist consist of a set of spin states within the ground-state orbital level. In theory, it is possible to develop a full Hamiltonian expression for the purposes of epr from the appropriate terms in equation 1.8, which would completely describe the observed epr spectra. In practice, finding the eigenvalues of such a Hamiltonian for a given system would be a difficult or impossible task. However, it is possible to derive a Hamiltonian expression, the spin Hamiltonian, consisting of spin operators only, and parameter matrices. The spin Hamiltonian effectively results from an integration over all of the spatial variables in the Hamiltonian to produce numerical parameter matrices which are fully derivable from the experimental data, and contain all the information about the state of the system. Knowledge of the interactions responsible for each parameter matrix then allows theoretical interpretation of these numbers.

The reduction of the Hamiltonian to an expression containing only spin operators necessarily implies that the number of eigenvalues, or spin-state energies, is dependent only on the number and magnitude of spins present, both electronic and nuclear. The order of the spin-Hamiltonian matrix for a single electronic spin is given by:

$$(2S+1)\prod^{i}(2I_i+1) \tag{1.10}$$

where S and I are the electronic and nuclear spin quantum numbers. The spin quantum number S is often a fictitious or effective spin S', such that $\left(2S'+1\right)$ gives the correct multiplicity of the lower-lying spin states which are involved in the epr experiment. Cases in which it is common to have $S \neq S'$ include the f-block ions, where the only spin states of interest are frequently a single Kramers doublet, hence $S' = \frac{1}{2}$, even though S may be $> \frac{1}{2}$.

The first spin-Hamiltonian expressions were formulated by Pryce (1950) [4] and Abragam and Pryce (1950) [5] using a perturbation treatment of the various interactions according to their relative magnitudes. Abragam and Pryce gave a general spin Hamiltonian as a summation of terms:

$$W = D_{ij}\hat{S}_i\hat{S}_j + \beta g_{ij}H_i\hat{S}_j + A_{ij}\hat{S}_i\hat{I}_j + Q_{ij}\hat{I}_i\hat{I}_j - \gamma\beta_N\mathbf{H}.\hat{\mathbf{I}} \tag{1.11}$$

This bears a strong resemblance to the spin Hamiltonian commonly used to analyse epr spectra today:

$$\widehat{\mathcal{H}} = \beta_e\mathbf{B}^T.\mathbf{g}.\hat{\mathbf{S}} + \hat{\mathbf{S}}^T.\mathbf{D}.\hat{\mathbf{S}} + \hat{\mathbf{S}}^T.\mathbf{A}.\hat{\mathbf{I}} - \beta_n\mathbf{B}^T.\mathbf{g}_n.\hat{\mathbf{I}} + \hat{\mathbf{I}}^T.\mathbf{P}.\hat{\mathbf{I}} \tag{1.12}$$

where $\mathbf{g}$, $\mathbf{g}_n$[4], $\mathbf{D}$, $\mathbf{A}$, $\mathbf{P}$ are symmetric parameter matrices containing five ($\mathbf{D}$, $\mathbf{P}$) or six independent parameters describing the spectrum in a non-principal axis coordinate system. The T subscripts refer to the transpose of the vector (or matrix) where row i becomes column i. The general expression $\mathbf{A}^T.\mathbf{B}.\mathbf{C}$, where $\mathbf{A}$ and $\mathbf{C}$ are column vectors of n dimension, and $\mathbf{B}$ is a square matrix of n dimension, is a scalar. Equation 1.12 contains all of the possible terms to second degree in spin, though higher terms are also allowed depending on the magnitude of the spins present. A short discussion of the fitting of these parameter matrices to orientationally dependent data is given in section 1.1.3.

As the theoretical analysis of the epr parameters requires knowledge of the fuller expressions of the Hamiltonian interactions, it is worthwhile to discuss these term by term.

Crystal-field interaction

The crystalline electric field raises the degeneracy of the free-ion spectroscopic terms, giving a number of orbital states. Some orbital degeneracy usually remains, unless the site is of low symmetry. Crystal-field calculations are commonly carried out using a point-charge model (see Hutchings (1964) [6] and section 5.2.3). The interaction may be treated as a perturbation with the perturbing Hamiltonian:

$$\widehat{\mathcal{H}}_{CF} = \sum_i \sum_j \frac{q_i q_j}{|\mathbf{R}_j - \mathbf{r}_i|} \tag{1.13}$$

[4] $\mathbf{g}_n$ is often assumed to be isotropic in epr experiments, being given by $g_n \times \mathbf{U}$, where $\mathbf{U}$ is the identity matrix, and g_n is a tabulated value for the nucleus concerned . For all of the centres reported in this thesis, attempts at fitting a matrix $\mathbf{g}_n$ resulted in either unchanged, or nonsensical values for the elements.

where q_i is the charge of the magnetic electron(s) at distance r_i from the origin (nucleus), surrounded by point charges q_j at distance R_j from the origin. This expression represents the potential energy of the charge q_i in the potential field given by equation 5.2.

The magnitude of the crystal-field energy perturbations may be greater or less than the spin-orbit coupling, depending on the nature of the bonding, and the atom and orbital which contains the unpaired electrons. For the 3d ions and 2p hole centres studied in this thesis, the crystal-field effect is larger than the spin-orbit-coupling interaction.

Spin-orbit coupling

The spin-orbit coupling between spin and orbital angular momenta perturbs the orbital energy levels by mixing excited orbital states of appropriate symmetry into the ground-state wavefunction. When the ground-state term is orbitally degenerate, the spin-orbit coupling will usually remove the degeneracy, leaving a ground state in which the remaining degeneracy can be treated as being effectively due only to spin, the states which are of interest in an epr experiment. The spin-orbit coupling for a single spectroscopic term is given by:

$$\widehat{\mathcal{H}}_{SO} = \lambda \left(\hat{\mathbf{L}}.\hat{\mathbf{S}} \right) \tag{1.14}$$

where λ is the spin-orbit-coupling parameter for that spectroscopic term. Calculations which will be carried out later in this thesis use the spin-orbit-coupling constant, ζ, as they deal with a single electron (or hole[5]). The spin-orbit interaction is then given by:

$$\widehat{\mathcal{H}}_{SO} = \zeta \left(\hat{\mathbf{l}}.\hat{\mathbf{s}} \right) \tag{1.15}$$

λ and ζ are related by:

$$\lambda = \pm \frac{\zeta}{2S} \tag{1.16}$$

[5] λ should strictly be used here, as ζ is always defined as a positive number for a single electron and in the case of a shell more than half full, the value should be negative. For the single hole $\lambda = -\zeta$, i.e. - the parameters are equal in magnitude but of opposite sign. The ζ nomenclature is used in this thesis, but the value was taken as negative for the hole-centre calculations.

where the sign is positive for a shell less than half full and negative for a shell more than half full.

Spin-spin interactions

Coupling between electron spin angular momenta can produce a splitting in the spin state energies at zero field (zero-field splitting, zfs) when $S \geq 1$ (as does the spin-orbit coupling). The interaction is given by (Pilbrow (1990), [7]):

$$\widehat{\mathcal{H}}_{SS} = -\rho \sum_{p,q} \left[\frac{1}{2} \left(\hat{L}_p \hat{L}_q + \hat{L}_q \hat{L}_p \right) - \frac{1}{3} L \left(L+1 \right) \delta_{pq} \right] \hat{S}_p \hat{S}_q \tag{1.17}$$

for a singlet orbital ground state. The summation is over $p, q = x, y, z$, δ_{pq} is the Kronecker delta function, and ρ is a spin-spin parameter (see Abragam and Bleaney (1970), [8], p678).

Electron Zeeman interaction

Interaction of the unpaired electron(s) with an applied magnetic field removes all degeneracy of the spin states, and is thus crucial to epr. The interaction is given by:

$$\widehat{\mathcal{H}}_Z = \beta_e \left(\hat{\mathbf{L}} + g_e \hat{\mathbf{S}} \right) . \mathbf{B} \tag{1.18}$$

Hyperfine interaction

Coupling between the electron spin angular momentum and the nuclear spin angular momentum of any nearby spin-bearing nuclei gives a number of non-degenerate nuclear spin states within each electronic spin state. The perturbation Hamiltonian expression is [7]:

$$\widehat{\mathcal{H}}_{HF} = \wp \left[\left(\xi L \left(L+1 \right) - \kappa \right) \hat{\mathbf{S}} . \hat{\mathbf{I}} - \frac{3}{2} \xi \left(\hat{\mathbf{L}} . \hat{\mathbf{S}} \right) \left(\hat{\mathbf{L}} . \hat{\mathbf{I}} \right) - \frac{3}{2} \xi \left(\hat{\mathbf{L}} . \hat{\mathbf{I}} \right) \left(\hat{\mathbf{L}} . \hat{\mathbf{S}} \right) + \hat{\mathbf{L}} . \hat{\mathbf{I}} \right] \tag{1.19}$$

where:

$$\wp = g_e g_n \beta_e \beta_n \left\langle r^{-3} \right\rangle_{nl} \tag{1.20}$$

and:

$$\xi = \frac{2l + 1 - 4S}{S \left(2l - 1 \right) \left(2l + 3 \right) \left(2L - 1 \right)} \tag{1.21}$$

κ is a parameter which relates to the spin density at the nucleus due to core polarisation. The hyperfine interaction is investigated in more detail in section 5.2.3, and derived in terms of one-electron operators for a single d electron from a more general expression. Discussion of κ and $\wp$ may also be found in this section.

Nuclear Zeeman interaction

The nuclear Zeeman interaction is an analogue of the electron Zeeman interaction for the nuclear spin, given similarly to equation 1.18 by:

$$\widehat{\mathcal{H}}_{NZ} = -\beta g_n \hat{\mathbf{I}}.\mathbf{B} \tag{1.22}$$

where there is no orbital angular momentum term expressed for a nucleus. The interaction is usually assumed to be isotropic, although attempts have sometimes been made to fit an anisotropic g_n matrix [9].

Nuclear electric quadrupole interaction

The nuclear electric quadrupole interaction is an interaction between the nuclear spin and the electric-field gradients (efg) acting upon it due to the surrounding electron distribution and the lattice for $I \geq 1$. The efg can orient the charge ellipsoid of the nucleus, with an energy of alignment given by the Hamiltonian:

$$\widehat{\mathcal{H}}_{\mathrm{NEQ}} = \sum_{p,q} q' \left[\frac{1}{2}(\hat{L}_p\hat{L}_q + \hat{L}_q\hat{L}_p) - \frac{1}{3}\delta_{pq}L(L+1)\right]\left[\frac{1}{2}(\hat{I}_p\hat{I}_q + \hat{I}_q\hat{I}_p) - \frac{1}{3}\delta_{pq}I\,(I+1)\right] \tag{1.23}$$

where:

$$q' = \frac{3e^2Q}{2I(I-1)}\left\langle r^{-3}\right\rangle \langle L|\,|\alpha|\,|L\rangle \tag{1.24}$$

$\langle L|\,|\alpha|\,|L\rangle$ is a reduced matrix element, which represents that portion of the total interaction which is independent of quantum number m_l, and is given by [8]:

$$\langle L|\,|\alpha|\,|L\rangle = \mp\frac{2(2l+1-4S)}{(2l-1)(2l+3)(2L-1)} \tag{1.25}$$

for a ground state obeying Hund's rules. The sign choice is negative for a shell less than half full, positive if more than half full. $\langle L|\,|\alpha|\,|L\rangle$ is closely related to the parameter ξ (equation 1.21) which appears in the hyperfine interaction term.

1.1.3 Construction of the parameter matrices

The parameter matrices in equation 1.12 are fitted to experimental data collected with different orientations of the sample within the applied magnetic field. As noted previously, deviations of g from g_e may occur due to deviation of the effective magnetic field at the unpaired electron from the applied field, due to local effects. The term $\mathbf{B}^T.\mathbf{g}$ in equation 1.12 may be regarded as a transformation of the applied field $\mathbf{B}$ to an effective field:

$$\mathbf{B}^T_{eff} = \frac{\mathbf{B}^T.\mathbf{g}}{g_e} \tag{1.26a}$$

$$\mathbf{B}_{eff} = \frac{\mathbf{g}^T.\mathbf{B}}{g_e} \tag{1.26b}$$

The magnitude of the effective field is then given by:

$$B_{eff} = \frac{\sqrt{\mathbf{B}^T.\mathbf{g}.\mathbf{g}^T.\mathbf{B}}}{g_e} \tag{1.27a}$$

$$= \frac{\sqrt{\mathbf{n}^T.\left(\mathbf{g}.\mathbf{g}^T\right).\mathbf{n}}}{g_e}B \tag{1.27b}$$

where:

$$\mathbf{n} = \frac{\mathbf{B}}{B} \tag{1.28}$$

is a unit vector in the direction of $\mathbf{B}$. Comparison of equation 1.27b with 1.7 gives:

$$g = \sqrt{\mathbf{n}^T.\left(\mathbf{g}.\mathbf{g}^T\right).\mathbf{n}} \tag{1.29}$$

a scalar whose value is dependent on the orientation of the magnetic field vector in the coordinate frame in which the matrix is expressed. It is the matrix $\mathbf{g}.\mathbf{g}^T$ ($\mathbf{gg}$) which is obtained directly from the experimental data. The matrix $\mathbf{g}$ may by obtained by diagonalising the matrix $\mathbf{gg}$, taking the positive square root of the diagonal elements, and then transforming the diagonal matrix $\mathbf{g}$ back into the original coordinate frame by the reverse of the similarity transformation

used to diagonalise gg (see section 1.2.1 and equation 1.33). The matrix g obtained in this way is always symmetric. In a similar fashion all of the other parameter matrices are derived as symmetric matrices. A detailed discussion of the hyperfine anisotropy may be found in chapter five of [3].

1.2 Epr of single crystals

1.2.1 Symmetry and site splitting

Single crystals are perhaps the most complicated system to study by epr, in comparison to powders, glasses, liquids or gases, but by the same token may offer the most information. As noted earlier, the epr technique is particularly useful for the study of localised units within the bulk crystal. Epr has been instrumental in the studies of crystal point defects, as they are often paramagnetic, or can be made paramagnetic by irradiation. The ability of epr to probe oriented systems within the crystal, producing orientation dependent data, leads to the observation of distinct symmetry-related sites (Weil, Buch and Clapp (1973), [10]).

The point-group symmetry of a given crystal implies certain symmetry elements that relate identical constructions of atoms, which can have different physical orientations within the crystal. When a paramagnetic defect site is placed within one of these constructions, the defect will also be repeated in these differently oriented, but otherwise identical sites[6]. Because the observed spectrum is dependent on the orientation of the applied magnetic field with respect to the defect site, these differently oriented sites produce separate spectra.

The relations between crystal symmetry and the properties of crystals are extensively covered in a textbook by Nye (1957) [11]. A central principle is that of Neumann, which states that "the symmetry elements of any physical property of a crystal must include the symmetry elements of the point group of the crystal". This principle may be applied to epr in that the experimentally-determined parameter matrices may be regarded as a physical property of the crystal. In this case it is the symmetry elements of the point group of the paramagnetic site which are important. Thus the spin-Hamiltonian parameters must reflect the point-group

[6]Populations of defects in the different sites are not necessarily equal. The direction of growth of the crystal may influence which sites become occupied, leading to an imbalance in the populations. Experimentally, the use of polarised radiation may also selectively render a given site paramagnetic or diamagnetic.

symmetry of the defect site.

Neumann's principal does not preclude the physical property from containing symmetry elements which are not part of the point group. In epr, time reversal invariance imposes an apparent centre of symmetry on the spin-Hamiltonian parameter matrices. Thus, from the point of view of epr, defect sites are always centrosymmetric. This restriction can also be shown by considering the relation between the parameter matrices describing the symmetry-related sites, as will be demonstrated in equation 1.32 below.

The parameter matrices which describe each of the symmetry-related sites may be generated from the site-one matrices by a similarity transformation [10][7]:

$$\mathbf{Y}_i = \mathbf{R}_i.\mathbf{Y}.\mathbf{R}_i^{-1} \tag{1.30}$$

where $\mathbf{Y} \equiv \mathbf{Y}_i$ is any one of the parameter matrices, and the 3×3 matrices $\mathbf{R}_i$ represent the symmetry operations of the crystal point group which are proper rotations. The index i runs over all of these operations, and $\mathbf{R}_1$ is the identity matrix. The matrices $\mathbf{R}_i$ are always real orthogonal matrices, and thus equation 1.30 may also be written:

$$\mathbf{Y}_i = \mathbf{R}_i.\mathbf{Y}.\mathbf{R}_i^{T} \tag{1.31}$$

The matrices $\mathbf{R}_i$ are a property of the crystal point group, and do not depend on the point group of the site under consideration.

Because of the relation [10]:

$$(\mathbf{R}.\mathbf{i})\,.\mathbf{Y}.\,(\mathbf{R}.\mathbf{i})^{-1} = \mathbf{R}.\mathbf{Y}.\mathbf{R}^{-1} \tag{1.32}$$

where $\mathbf{R}$ is any proper rotation matrix and $\mathbf{i}$ is the inversion matrix, any rotatory inversion $\mathbf{R}.\mathbf{i}$ (or $\mathbf{i}.\mathbf{R}$) is indistinguishable from the corresponding proper rotation $\mathbf{R}$. Thus it is again shown that a centre of symmetry is imposed on the spin-Hamiltonian parameter matrices. This

[7] Similarity transformations are often written as the reverse of this equation, where the inverse matrix comes first. Written this way, a diagonalisation is carried out using a matrix of column eigenvectors. When written as shown here, it is a matrix of row eigenvectors. Transformation of the transformed matrix back to the original matrix may be performed by multiplying the transformed matrix on the left and right-hand side as before, but with the order reversed.

Table 1.1: Division of the 32 crystallographic point groups into 11 Laue classes. Schönflies notation is given in brackets. The first point group in each column contains only proper rotations, and the final point group contains the inversion element (the Laue class).

Triclinic	Monoclinic	Orthorhombic	Tetragonal		Trigonal		Hexagonal		Cubic	
1 (C_1)	2 (C_2)	222 (D_2, V)	4 (C_4)	422 (D_4)	3 (C_3)	32 (D_3)	6 (C_6)	622 (D_6)	23 (T)	432 (O)
$\bar{1}$ (C_i, S_2)	$\bar{2}, m$ (C_s, C_{1h})	$mm2$ (C_{2v})	$\bar{4}$ (S_4)	$4mm$ (C_{4v})	$\bar{3}$ (C_{3i}, S_6)	$3m$ (C_{3v})	$\bar{6}, 3/m$ (C_{3h})	$6mm$ (C_{6v})	$m3$ (T_h)	$\bar{4}3m$ (T_d)
	$2/m$ (C_{2h})	mmm (D_{2h}, V_h)	$4/m$ (C_{4h})	$\bar{4}2m$ (D_{2d}, V_d)		$\bar{3}m$ (D_{3d})	$6/m$ (C_{6h})	$\bar{6}m2$ (D_{3h})		$m3m$ (O_h)
				$4/mmm$ (D_{4h})				$6/mmm$ (D_{6h})		

result means that the 32 crystallographic point groups may be reduced to 11 classes, known as Laue classes, which may be distinguished by epr. Within each Laue class is a group which contains only proper rotations, and the corresponding groups, some of which contain rotatory inversions, and one of which contains the inversion element. This is shown in table 1.1. The proper rotation matrices for the 11 crystal Laue symmetries are given in [10].

The point-group symmetry of a paramagnetic defect is usually immediately apparent upon inspection of the site splitting in the epr spectrum in one or more planes. The site splitting can be seen in a plot of the epr line position against the rotation angle in a given plane, which is sometimes referred to as a roadmap. Examples may be found in this thesis in figures 4-4, 5-2 and 6-16. A stacked plot of the collected spectra also reveals the site splitting, as in figures 4-3, 5-5, 5-7, 5-11, 5-12, 5-15, 5-16, and 6-1. The number of sites in any given orientation depends on both the crystal symmetry and the site symmetry. In general, the lower the symmetry of the site, the greater the number of sites in an arbitrary orientation. For a site of Laue symmetry $\bar{1}$[8], the number of sites in an arbitrary orientation is equal to i, as in equation 1.30. The highest symmetry that a site in a crystal can have is the same as the symmetry of the

[8]Point-group symmetry labels throughout this thesis are given in the (short) International (Hermann-Mauguin) system. The Schönflies notation may be determined with reference to table 1.1.

Table 1.2: Number of sites observed in selected directions for all point-group symmetries in a crystal of Laue class $4/mmm$. The superscripts 1, 2, 3 refer to the primary (c), secondary (a, b) and tertiary (bisectors of a, b) axes.

Laue symmetry of species	Number of species observed in different directions (100)	(lm0)	(110)	(010)	(lmn)	(001)	(lln)	(l0n)
$\bar{1}$	2	4	2	2	8	1	4	4
$2/m^1$	2	4	2	2	4	1	2	2
$2/m^2$	2	2	1	2	4	1	2	3
$2/m^3$	1	2	2	1	4	1	3	2
mmm^2	2	2	1	2	2	1	1	2
mmm^3	1	2	2	1	2	1	2	1
$4/m$	1	1	1	1	1	1	1	1
$4/mmm$	1	1	1	1	1	1	1	1

crystal. In this case there is always one site in all orientations. Rae [12], has tabulated the number of sites observed for every combination of crystal and site symmetry in various special or arbitrary orientations. Roadmaps are also included for $\bar{1}$ sites in each crystal Laue class in various rotation planes. Thus from the observed site splitting, the epr experiment immediately allows determination of the site symmetry of a point defect. This in turn offers clues as to the location and nature of the defect, as will be detailed later in reference to zircon and α-quartz. The appropriate table for a crystal of Laue class $4/mmm$ is shown in table 1.2, reproduced from Rae (1969) [12].

Another useful aspect of the site splitting lies in the increase in site degeneracy of low-symmetry sites in certain special orientations. In all of the α-quartz experiments carried out in this thesis, the crystal was first aligned with the rotation axis precisely in the x (a_1) axis direction by adjusting the mount and observing the collapse of the six sites of a $\bar{1}$ centre into three sites in this special orientation. Once the correct rotation plane was located, the z (c) axis within this plane could be found by rotating until the three sites collapsed to one. More details of this process are given in the experimental equipment section 1.3.

The site splitting may also allow complete determination of the spin-Hamiltonian parameter matrices from measurement in a reduced number of planes. Without the phenomenon of site

splitting, three independent planes of measurement would be required generally to determine the parameter matrices. However, the different sites represent different planes of measurement in a suitably chosen rotation plane, so that complete determination is often possible using only one plane. Even when only one site is observed, the very fact that the sites are degenerate reveals the high symmetry of the centre, and the much simplified spin-Hamiltonian parameter matrices may still be determined from the single plane of data. A paper by Weil *et al.* [10] describes the determination of crystal tensor properties from experimental data for various crystal symmetries in detail. Of all the centres fitted in this thesis, only the Z-centre (section 5.3) parameter matrices were fitted using data in more than one plane.

Analysis of the epr parameter matrices requires diagonalisation to produce the eigenvalues and eigenvectors. The eigenvalues are the values on the diagonal of the diagonalised matrix (principal values), and the eigenvectors are the unit-vector columns (or rows) of the transformation matrices which carry out the diagonalisation (a similarity transformation):

$$\begin{bmatrix} g & h & i \\ j & k & l \\ m & n & o \end{bmatrix} \begin{bmatrix} a & b & c \\ b & d & e \\ c & e & f \end{bmatrix} \begin{bmatrix} g & j & m \\ h & k & n \\ i & l & o \end{bmatrix} = \begin{bmatrix} p & 0 & 0 \\ 0 & q & 0 \\ 0 & 0 & r \end{bmatrix} \tag{1.33}$$

where $\begin{bmatrix} g & h & i \end{bmatrix}$, $\begin{bmatrix} j & k & l \end{bmatrix}$, and $\begin{bmatrix} m & n & o \end{bmatrix}$ (or their transposes) are the eigenvectors. The directions given by these orthogonal eigenvectors are the principal directions of the matrix, and they form the axis system under which the parameter matrix is diagonal.

The symmetry-related matrices which are generated using the similarity transformation of equation 1.30 all have the same principal values, but different principal directions. When analysing the matrices and principal directions, and making relations to directions and positions in the crystal, it is crucial in some cases that the correspondence is known between the sites as measured and fitted and the actual sites in the crystal relative to the axis system defined. Further comments will be made in chapter two.

1.2.2 Crystal point defects

Paramagnetic defects in single crystals can be divided generally into two main categories: electron centres and hole centres. These two terms refer only to the nature of the paramagnetic

electrons, and either category may be associated with other features such as vacancies or impurities. The labels imply that the centre has been formed by loss or gain of an electron, which is often, but not always, the case. However, even in the case of a transition ion impurity, for example, which may enter the crystal in an oxidation state which already carries unpaired electrons, it is useful to describe the defect in these terms.

Electron-hole centres occur when an electron is removed from an electron-rich centre, often by irradiation, leaving behind an unpaired electron which is usually detectable by epr. The excess electrons may become associated with a more electron-deficient centre, thus creating an electron centre. These centres are often referred to as trapped-hole or trapped-electron centres, as the hole or electron will generally occur at a site which is more energetically favourable than the bulk unperturbed crystal. It is for this reason that the epr technique becomes so useful in the analysis of point defects in crystals, as they are more likely to trap an electron or hole and become paramagnetic.

The irradiation to which a crystal is exposed can be natural, or imposed by the experimentalist. Natural sources include radioactive minerals in proximity to where a natural crystal grew (see for example [13], [14]), or radioactive ions incorporated into the crystal itself ([13], [15], [16]). Paramagnetic centres have also been produced by deliberate radiation over a range of photon energies at the shorter wavelength end of the spectrum, from UV through to X-rays and gamma rays.

The epr parameters of hole centres and electron centres are usually quite distinctive. Hole centres are normally single holes (i.e., $S = \frac{1}{2}$) which occur on anionic sites, and require few terms in the spin Hamiltonian, usually only g, g_n and nuclear terms if appropriate. Exceptions to this generalisation exist, such as the aluminium double-hole centre [17] and the biradical centre [18] in α-quartz, which involve interacting single-hole centres on two oxygen atoms (2.6 Å apart in the former, 8.0 Å apart in the latter). The g values of hole centres are normally greater than the free-electron value, with one value close to it, and are not very anisotropic (see especially figure 4-1). This is discussed in the crystal-field analysis of the hole centres contained in chapter four.

The electron centres display a range of electronic spins, and often require a number of terms in the spin Hamiltonian. They are normally associated with metal ions, although F-type

centres also fit into the electron-centre category and are quite different to the former type. The metal-ion type centres have g values which are often less than the free-electron value and may show considerable anisotropy. In systems with $S > \frac{1}{2}$, when the zfs is large, it is often possible to fit transitions within a single Kramers doublet as an effective spin $\frac{1}{2}$ system, to produce anisotropic g values which are indicative of the true spin (see for example section 5.3.3). The "natural" centres, which do not require irradiation to be observed as they are already paramagnetic, usually fit into this category of electron centres. Ferric (Fe^{3+}) ions in α-quartz are an example of this kind of centre, although some of these ferric centres can be destroyed by thermal treatment implying that the oxidation state may be changed from 3+ [19]. In other cases the most stable form of the defect may be paramagnetic, in which case it could persist regardless of any irradiation or annealing treatment. The F-type centres are single electrons trapped in anionic vacancy sites, and thus have $S = \frac{1}{2}$, and usually quite isotropic. In some ways they resemble hole centres more than electron centres, but they are formed by the trapping of an electron.

The stability of defect centres varies considerably. Many are only observable following irradiation at low temperature, such as under liquid nitrogen, and measurement under cryogenic conditions. If the crystal is then annealed and recooled, the spectrum may no longer be visible. The well known Zr(α) centre in zircon is an example of this type [20] - [22]. Other centres survive annealing to room temperature, or even extended heating to temperatures of several hundred °C. In the zircon and α-quartz crystals studied during the course of this thesis, annealing of the crystals at high temperatures (900 °C for zircons, 400 °C for α-quartz[9]) was sufficient to remove most paramagnetic centres except for the Zr(Ti^{3+}) [23], [24], [9] and so-called 'Z' (Cr^{3+}) [25], [26] centres in zircon (sections 5.2 and 5.3).

1.3 Experimental details

A simplified block diagram of an epr experimental setup is shown in figure 1-2. All of the epr spectra measured during the course of this thesis were collected using a modified Varian E12 spectrometer, with a magnetic-field-strength range of 0-1200 mT. The microwave source

[9] α-quartz undergoes a transition to β-quartz at *ca* 573 °C, so temperatures were kept well below this value.

was an X-band klystron within a Varian E-101 microwave bridge producing continuous-wave X-band radiation within the range 8.9-9.6 GHz. Frequencies were measured using a Systron-Donner frequency counter model 6054A with a frequency reference provided by a Hewlett-Packard 5081A caesium-beam frequency standard with an accuracy of 1 part in 10^{10}. For most experiments, the magnetic flux density was measured using a Brüker nmr probe connected to a Brüker ER 035M nmr gaussmeter, with an operational range of 130-1900 mT (well beyond the magnet capability). Field measurement as low as 45 mT was possible using a low-field Brüker probe. The microwave cavity was a modified Varian E235 wide-access cavity with external modulation coils operating at 100 kHz. The cavity has a specified minimum unloaded Q of 20000, and is estimated to be *ca* 6000 when loaded.

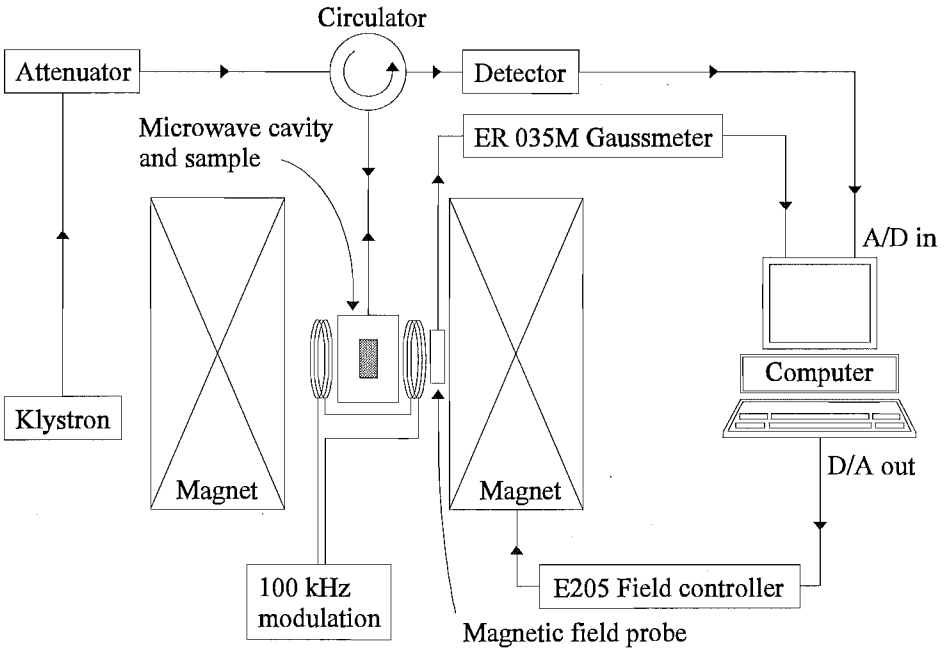

Figure 1-2: Simplified block diagram of a typical epr spectrometer setup.

The majority of experiments were carried out at *ca* 15 K, the lowest operating temperature which could be generated using a Displex A5A 202 (Air Products) closed-cycle helium refrigerator unit. Sample crystals were fixed to copper mounts as shown in figure 1-3 using Supa Glue, and screwed into the Displex head, which was then lowered into the resonant cavity, forming an airtight seal. The pressure inside the cavity was maintained at *ca* 10^{-6} Torr at the lowest

temperature by a Pfieffer TPH 330 turbo-molecular pump and a Welch 1397 Duo Seal® rotary backing pump. The low pressures prevented rapid heat transfer between the sample and mount and the surroundings, so that a steady low temperature could be maintained, and minimised the occurrence of ionisation of gas molecules within the cavity resulting in high-intensity spurious signals. Experiments at temperatures between 15 K and room temperature were carried out using a model 4107 temperature controller with heating coils at the end of the Displex head. Complete rotation of the Displex head and sample mount through 360° about an axis perpendicular to the applied magnetic field and parallel to the excitation field $\mathbf{B}_1$ was possible. The rotation angle was measured using a permanent goniometer system with a Vernier scale marked on the fixed stage and rotating Displex head.

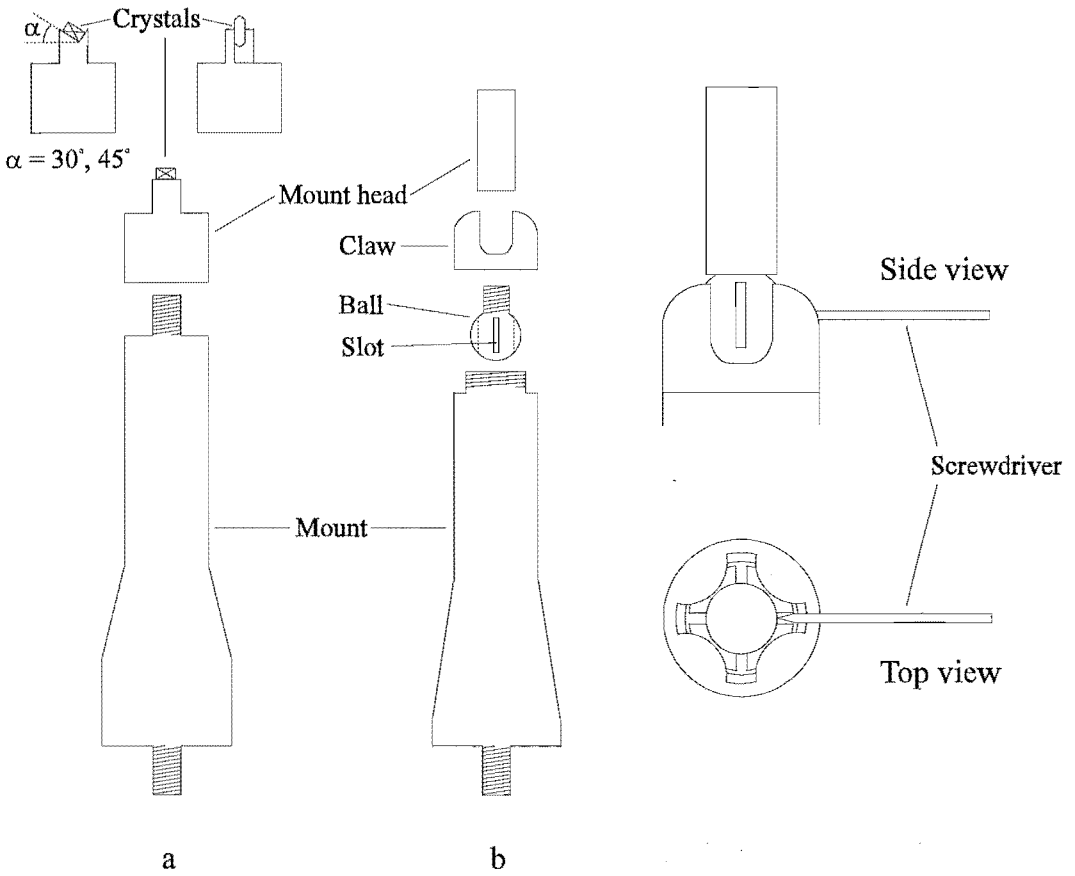

Figure 1-3: Fixed (a) and adjustable (b) copper crystal mounts.

Two types of sample mount were used, as shown in figure 1-3. One mount (a) was fixed, so

that the mount head was always precisely perpendicular to the rotation axis, which was along the long axis of the mount. This mount was used for the measurements of zircon crystals, which always had faces parallel to the *bc* plane in which most measurements were made. Measurements in other planes such as *ab*, or a *bc* plane rotated about the *c* axis were made using the fixed mount and one of the alternative mount heads shown in figure 1-3. The *bc* faces of the synthetic crystals grown during the course of this thesis were natural faces, and thus very precisely oriented. A larger synthetic zircon crystal which was grown by Aerospace Corporation in a similar fashion was cut with faces perpendicular to all three orthogonal crystal axes.

The second mount (b) was adjustable, and was used for the measurements of α-quartz. This was necessary because the quartz crystals did not have faces precisely perpendicular to the crystal axes. As shown in figure 1-3, the adjustable mount consisted of ball with slots cut into it which fitted into a rounded socket at the top of the mount and was held in place by a claw which screwed onto the mount. The mount head then screwed onto the ball. A special cavity which was used in conjunction with the adjustable mount allowed a screwdriver to pass into the sample cavity and into the any of the four slots in the ball which were located 90° apart. Turning the screwdriver in any two adjacent slots allowed the mount head to be tilted in two dimensions, so that any plane could be obtained which was not too far from that perpendicular to the rotation axis. Thus the mount was adjusted until the α-quartz crystal was precisely oriented with the x (a_1) axis parallel to the rotation axis. This was achieved by viewing the signals from the high-intensity $[AlO_4]^0$ centre on an oscilloscope, for instant feedback, and adjusting the tilt until pairs of lines due to symmetry-related sites became degenerate. This was repeated at adjacent screwdriver slots until the degeneracy remained as the crystal was rotated.

A summary of uncertainties in the various experimental parameters is summarised in table 1.3. The uncertainty of the mount plane was variable, and depended on the size of the crystal mounting faces for zircon measurements, and the sensitivity of the reference signals used to adjust the mount for quartz. Most zircon and quartz measurements in this thesis made in the *bc* plane have an estimated uncertainty of *ca* $\pm 0.1°$. The exception is the H centre in zircon, which was measured in a gamma-irradiated crystal with small *bc* faces. The uncertainty in the mount plane for this crystal is estimated to be *ca* 1°. The *ab*-plane measurements carried out

on the Z centre (section 5.3) also have a larger uncertainty, estimated at *ca* 1°.

Table 1.3: Experimental uncertainties in measured parameters.

Quantity	Typical value	Uncertainty
Magnetic flux density	130 - 1100 mT	±0.001 mT
Microwave frequency	9.2-9.4 GHz	±10 kHz
Rotation angle	0 - 360°	±1′ (±0.017°)
Crystal mount plane	*ab*, *bc* planes	±0.05-1.0°[a]
Temperature	15 K	±5 K

[a] Dependent on nature of plane, size of crystal faces

Spectra were collected on a PC with the aid of a modified software package [27]. Signal averaging was used to increase the signal-to-noise ratio, where the number of samples could be set by the user for each spectrum. A single scan could last anywhere between 30 seconds and 24+ hours, depending on the resolution and number of samples selected.

The collection of data by computer interfacing results in an uncertainty in frequency measurements in table 1.3 greater than that quoted in earlier publications by the Canterbury epr group (±1 kHz). This is due to the recording of a single frequency to apply to the whole scan, despite small variations during the scan. Previously measurements were taken on a chart recorder, and the frequency noted at each line position of interest. Thus measurements were only limited by the precision of the frequency counter. However, frequency measurements are still very precise, and the computer interfacing allows great improvements in signal-to-noise ratios.

Most of the zircon spectra were recorded after the crystals had been x-irradiated using a Phillips model PW2264-20 X-ray generator with a tungsten target source, operating at 45 kV and 40 mA. Many irradiations were carried out under liquid nitrogen in a polystyrene container in order to generate the non room-temperature stable centres. Following irradiation, the mount was transferred quickly to the cooled Displex head using a metal dewar 'screwdriver' so that minimal heating occurred. The α-quartz crystal used for the work described in chapter six was gamma-irradiated overseas. It was irradiated at room temperature for *ca* 18 hours at 2687 rads per minute.

The growth of the synthetic zircon crystals carried out during the course of this thesis is described in chapter 3. Hydrothermal growth of α-quartz is also described.

1.4 Data fitting

Fitting of experimental data to spin-Hamiltonian parameters was carried out using the computer programme EPR-NMR, developed at the University of Saskatchewan, Canada [28]. The programme sets up a spin-Hamiltonian matrix using the parameter matrices entered by the user, and then uses "exact" numerical diagonalisation to produce the energy eigenvalues. There are then four categories of operations which can be carried out. In increasing order of complexity, these are energy-level calculation, spectrum simulation, comparison with observed data and parameter optimisation.

The final category is used to optimise the spin-Hamiltonian parameter matrices so that the root-mean-squared deviation (rmsd) between the calculated transition fields (if field-swept epr) and experimental data is minimised. All of the spin-Hamiltonian parameter matrices reported in this thesis were fitted in this way. The information required to carry out a fitting for field-swept epr data are the transition labels, microwave frequencies and line positions in magnetic-field units for each crystal orientation. The transitions are labelled by specifying the energy levels involved in the transition, which are numbered from highest to lowest. As the number of energy levels is dependent on the spins present, a guess must be made as to the nature of the spins present based on the roadmaps and appearance of the spectrum. After a fitting has been carried out, simulation of the spectrum can be a very useful indication of the validity of the model used. A good example of this is the fitting of the $[HLi_2O_4]^0$ centre described in section 6.2.2.

Chapter 2

Crystal structure of zircon and α-quartz

2.1 Zircon

Zircon crystal structures were first published in the 1920s [29] - [31]. More recent refinements of the structure were carried out by Robinson *et al.* [32] and Hazen and Finger [33]. The reported structural parameters are very similar, and those of the more recent paper [33] for 300 K and 1 atmosphere have been used in this thesis. Hazen and Finger's results show that the parameters are not likely to differ significantly at the low pressures used in the epr experiments, and it is assumed that the same will be true of the low temperatures.

Zircon ($ZrSiO_4$) is a mixed ionic-covalent crystal consisting of covalently bound SiO_4^{4-} units linked by ionically bound Zr^{4+} ions. The space group is tetragonal, $I4_1/amd$. The silicon and zirconium atoms lie on fourfold rotation-inversion axes ($\bar{4}$) running parallel to the crystal c-axis direction, and the oxygen atoms lie in perpendicular mirror planes intersecting at the $\bar{4}$ axes, whose normals are parallel to the crystal a and b axes. Thus when viewed along the c axis all atoms line up in a grid pattern, as shown in figure 2-1. The 4_1 fourfold screw axes of the zircon space group lie in the centre of the channels inside the grid pattern, running parallel to the c axis. There are also twofold rotation axes bisecting the a and b axes.

Robinson *et al.* describe the structure as consisting of chains of alternating edge-sharing SiO_4 tetrahedra and ZrO_8 triangular dodecahedra running parallel to the c axis, linked laterally

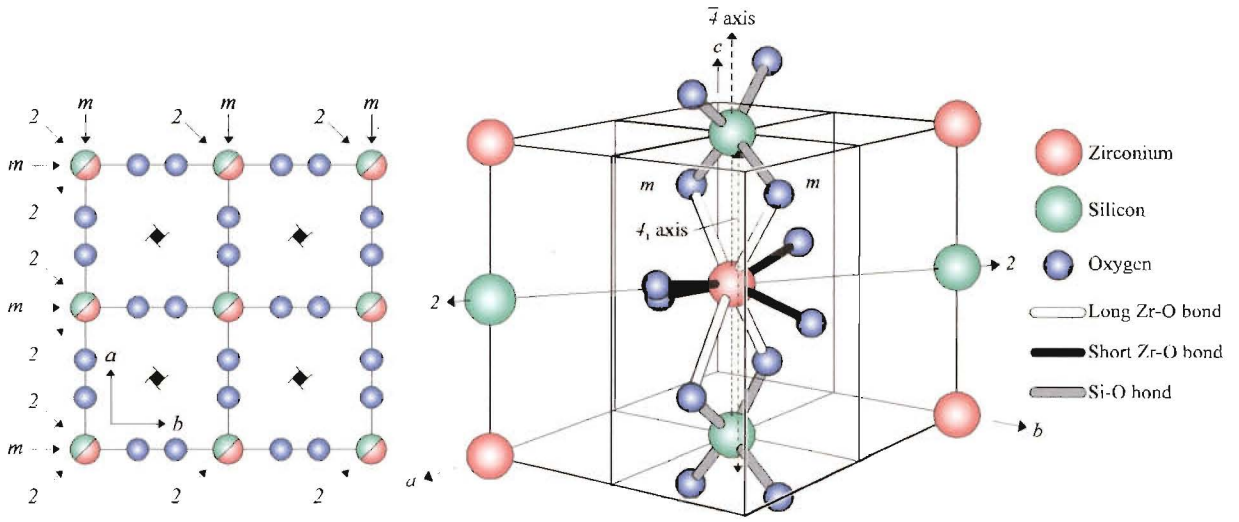

Figure 2-1: Projection of zircon crystal structure onto *ab* plane (left) and portion of unit cell showing ZrO_8 dodecahedron and two SiO_4 tetrahedra in a *c*-axis chain.

by edge-sharing ZrO_8 dodecahedra. The ZrO_8 dodecahedra consist of two interleaving distorted tetrahedra, with Si-O bond lengths of 2.128(2) and 2.267(3) Å respectively. The SiO_4 tetrahedra are also distorted, with an Si-O bond length of 1.623(2) Å and O-Si-O bond angles of 97.0(2)° and 116.1(1)° [33]. Figure 2-1 also shows a portion of the zircon unit cell viewed in three dimensions, showing the ZrO_8 dodecahedron and two SiO_4 tetrahedra in a chain running parallel to the *c* axis. A fourfold screw and fourfold rotation-inversion axis, twofold axis and two mirror planes are also indicated. Most of the atoms outside the central chain have been omitted for clarity. An alternate view of a section of the unit cell may also be found in figure 4-5.

Wyckoff [34] gives the independent coordinates of 16 atoms which allow any atomic position to be calculated, in terms of unit-cell fractional coordinates and the parameters u and v. They are given relative to an origin taken as a centre of symmetry with respect to the oxygen atoms, so that only four oxygen positions with a $\pm$ tag need be specified. It has been found useful to translate these positions to a new origin centred on a zirconium atom at $(0, \frac{1}{4}, \frac{7}{8})$ in Wyckoff's system. Thus the 16 coordinates translated by $(0, -\frac{1}{4}, +\frac{1}{8})$ are as follow in table 2.1. Hazen and Finger give the unit-cell dimensions a and c as 6.6042(4) and 5.9796(3) Å, and the parameters u and v as 0.0660(4) and 0.1951(4).

Table 2.1: Atomic coordinates of zircon given as fractions of the unit-cell dimensions. All coordinates have been chosen between 0 and 1.

Zr	$(0,\ 0,\ 0)$	$(\frac{1}{2},\ 0,\ \frac{3}{4})$	$(\frac{1}{2},\ \frac{1}{2},\ \frac{1}{2})$	$(0,\ \frac{1}{2},\ \frac{1}{4})$
Si	$(0,\ 0,\ \frac{1}{2})$	$(0,\ \frac{1}{2},\ \frac{3}{4})$	$(\frac{1}{2},\ \frac{1}{2},\ 0)$	$(\frac{1}{2},\ 0,\ \frac{1}{4})$
O	$(0,\ u+\frac{3}{4},\ v+\frac{1}{8})$ $(0,\ \frac{3}{4}-u,\ \frac{9}{8}-v)$	$(0,\ \frac{1}{4}-u,\ v+\frac{1}{8})$ $(0,\ u+\frac{1}{4},\ \frac{9}{8}-v)$	$(u+\frac{1}{4},\ 0,\ v-\frac{1}{8})$ $(\frac{3}{4}-u,\ \frac{1}{2},\ \frac{3}{8}-v)$	$(\frac{3}{4}-u,\ 0,\ v-\frac{1}{8})$ $(u+\frac{1}{4},\ \frac{1}{2},\ \frac{3}{8}-v)$

Crucial to the interpretation of epr spectra is a knowledge of the site symmetry of various positions in the crystal structure. As noted earlier, the maximum site symmetry possible is the same as the crystal point-group symmetry. Lower site symmetries will of course also exist, but must contain only symmetry elements which are found within the crystal point group. The zircon Laue symmetry is $4/mmm$, thus in an epr experiment, the apparent maximum possible site symmetry is also $4/mmm$. In zircon, the silicon and zirconium atoms lie on the highest symmetry sites, with a point-group symmetry of $\bar{4}2m$. This point group is indeed a subgroup of the Laue class $4/mmm$, as seen in table 1.1. The oxygen atoms occupy sites of point-group symmetry m, Laue class $2/m$. From the viewpoint of point defects in zircon, one could envisage any point-group symmetry made up of symmetry elements in the crystal point group: $\bar{4}2m$, 222, $mm2$, m, 2 or 1. Thus the Laue symmetries one might expect to observe for defects in zircon are $4/mmm$, mmm, $2/m$ and $\bar{1}$.

The first and third of these Laue symmetries are by far the most commonly reported. Site symmetry $\bar{4}2m$, Laue class $4/mmm$, occurs whenever a defect resides solely on a silicon or zirconium site. It is assumed that any relaxation which occurs amongst the surrounding atoms in the presence of the defect does not change the point-group symmetry of the unperturbed site. As many centres have been observed which show no site splitting within the limits of the epr linewidths in any orientation, this seems a reasonable assumption. There are two ways in which a paramagnetic defect could occupy a silicon or zirconium site alone. One is the loss or gain of electron(s) by the normal silicon or zirconium atom to form a paramagnetic centre, and the other is the occupation of the site by a paramagnetic impurity, which could be an electron or foreign atom. No examples of the former category appear to have been reported.

Zr^{3+} electron centres are known, but are always associated with nearby impurities. The best known example is probably the Zr(α) centre [20] - [22], which is associated with a phosphorus atom. Examples of the second category are numerous. Ti^{3+}, Cr^{3+}, V^{4+}, Mn^{4+}, Fe^{3+}, Nb^{4+}, Mo^{5+}, and a number of lanthanide centres with uniaxial symmetry have been reported (see forthcoming review article [35]).

Laue symmetry $2/m$ covers sites of point-group symmetry m or 2. Most hole centres in zircon have point-group symmetry m. This is because the oxygen atoms which are located in sites of point-group symmetry m are the only electron-rich species in the pure zircon lattice, and thus are the only atoms upon which electron holes are likely to occur. An oxygenic hole centre may be associated with nearby impurities without the site symmetry being lowered, provided the impurities are located within the mirror plane which passes through the oxygen atom. A number of such centres have been studied by the Canterbury epr group, where the oxygenic hole has been associated with B^{3+} [36], Al^{3+} [37] or Y^{3+} [38]. There are also a number of hole centres with no observable hyperfine which have m symmetry.

The Canterbury epr group has also reported a defect centre with point-group symmetry 2, named the P centre [39]. Such a centre must be located on one of the twofold axes bisecting the a and b axes. In this case, the centre was reported as an electron trap centre on a titanium atom substituting for zirconium, with a phosphorus atom located in the nearest lattice position along the twofold axis.

Reports of centres with Laue symmetry $\bar{1}$ in zircon are less common. As there is no centre of symmetry in the zircon crystal structure, only point-group symmetry 1 is possible in this Laue class. Thus such centres must have no symmetry elements at all, apart from the identity element. This can be most reasonably envisaged as a centre involving an interstitial ion, or two atomic sites in different mirror planes. Interstitially located ions are common in α-quartz, but reports of interstitial ions in zircon are rare. An example of the second type of centre with point-group symmetry 1 may be found in a paper by Barker and Hutton which reports an oxygen hole centre compensated by a Y^{3+} ion in a "next-nearest-neighbour" zirconium position [40].

There appear to be no reports of centres of Laue symmetry mmm. References are sometimes made to "orthorhombic" symmetry of the g matrix, but this almost invariably refers simply to

matrices which have symmetry lower than uniaxial, i.e. - three different principal values. A true centre of orthorhombic symmetry in the zircon crystal structure may have a point-group symmetry 222 or $mm2$. The former symmetry could be envisaged, for example, as two foreign atoms located in silicon or zirconium positions along the twofold axis, separated by one normal silicon or zirconium position. In this situation there would be three mutually perpendicular twofold axes intersecting at the normal silicon/zirconium position between the two foreign atoms. There have been no reports of such a centre. The second symmetry has been proposed for a new boron centre discussed in this thesis (section 5.5), where the centre lies along one of the usual fourfold rotation-inversion axes, but the $\bar{4}$ element has been removed.

The selection of sites in epr studies of zircon is not as crucial as in the study of α-quartz, to be discussed later. For defects with point-group symmetry $\bar{4}2m$, all sites are equivalent (table 1.2, Laue symmetry $4/mmm$), and the matrix principal directions are constrained to lie along the crystallographic axes. The sense of direction is completely arbitrary. For point-group symmetry $mm2$, the matrix principal directions are again constrained to lie along the crystallographic axes. The maximum of two sites (table 1.2, Laue symmetry mmm^2) which may be observed will correspond to an operation of the usual fourfold rotation-inversion on the centre, which is no longer a symmetry element. The operation leaves the normal zircon atoms unchanged, but changes at least some of the atoms comprising the defect. The two sets of principal directions will merely be the inverse of each other. As any set of principal directions is equivalent to the negative (opposite pointing) set of directions, there is no reason to choose either set, though one might arbitrarily state that the direction along the c axis centred on a given atom points towards the centre of gravity of the centre, rather than away from it. The situation for point-group symmetry 222 is similar, but in this case the principal directions will lie along the twofold axes, two of which bisect the crystallographic axes, rather than lying parallel to them. Once again, the alternative site is equivalent to operation of the fourfold rotation inversion on the first (or one of the mirror planes in this case), and the spin-Hamiltonian parameter-matrix principal directions will be equivalent for the two sites.

For a defect with m point-group symmetry, complete determination of the spin-Hamiltonian parameter matrices may be carried out by measurement only in the bc plane. One site is observed in the c-axis orientation (as for all site symmetries), three sites in any arbitrary orien-

tation in the bc plane ($l0n$), and two sites in the b-axis orientation (table 1.2, Laue symmetry $2/m^2$). Four sites may be observed in a completely arbitrary orientation. Taking the simplest case of an oxygenic hole with no associated impurities, one may identify the three distinct oxygen sites for measurement in the bc plane. All of the oxygen atom sites in the mirror plane parallel to the experimental rotation axis are equivalent, while there are two distinct sites in the mirror plane perpendicular to the rotation axis. The principal directions of the spin-Hamiltonian parameter matrices are constrained to have one direction perpendicular to the mirror plane, and thus two directions within the mirror plane. The parameter matrices of the four arbitrary sites have principal directions (θ, 0), (θ, 90), (θ, 180) and (θ, 270), i.e. - making an identical angle with the c axis in each direction within the two mirror planes. The two groupings for each plane ((θ, 0), (θ, 180) and (θ, 90), (θ, 270)) are completely equivalent, and the only confusion which may arise is the choice between θ, 0 and θ, 180 for a given oxygen site. For all of the hole centres studied by the Canterbury group, it has been found that an assignment may be chosen such that the principal directions of the parameter matrices point approximately in the direction of the nearby bonded silicon and zirconium atoms. The opposite choice yields directions with no readily apparent significance (see also figure 4-5).

A defect with point-group symmetry 2 also has four sites in an arbitrary orientation (table 1.2, Laue symmetry $2/m^3$), which correspond to the two perpendicular twofold axes and two senses of direction in a similar fashion to the mirror planes of the m centres. One of the principal directions of the spin-Hamiltonian parameter matrices is here constrained to lie along the twofold axis, so that the other two must lie in the perpendicular plane. In choosing a physical site for each set of principal directions, one might select the site which orients the constrained principal direction towards the centre of gravity of the centre when placed on the site of maximum spin density. The principal directions are not likely to carry much useful information for this point-group symmetry. For the P centre [39], the matrix principal directions were found to lie along special directions relative to the crystallographic axes rather than any particular lattice directions.

A defect with point-group symmetry 1 could potentially make the assignment of spectra and derived matrices to sites in the crystal very difficult. There are no constraints on the principal directions, and there are eight sites in an arbitrary orientation (table 1.2, Laue symmetry $\bar{1}$).

Such a situation is best approached on a case-by-case basis, where examination of the principal directions coupled with knowledge of the nature of the centre and the available configurations in the crystal may allow an assignment to be made. Most centres in zircon are fortunately of higher symmetry, and even those of point-group symmetry 1 are likely to involve only lattice positions, as there has been little evidence of interstitial ions in zircon. In all of the zircon centres studied in this thesis, and by other members of the Canterbury group, site assignment has been a reasonably straightforward matter.

2.2 α-Quartz

α-Quartz is a low-temperature crystalline form of silica, SiO_2. As it contains no centres of symmetry or mirror planes, it exists in two enantiomeric forms, left and right α-quartz. The existence of two enantiomeric forms, coupled with the numerous conventions which have been used to define a coordinate system have led to much confusion in the literature where studies of α-quartz[1] have been carried out. Donnay and Le Page [41] describe the various conventions which have been used in considerable detail. The epr work carried out in this thesis is consistent with the right-hand coordinate system (RHCS) described by Nuttall and Weil [42], the details of which will be described below.

Under the RHCS, left quartz has the trigonal space group $P3_121$, and right quartz $P3_221$ (this is reversed under a left-hand coordinate system). The threefold screw axis referred to in the space group is a right screw axis in left quartz, and a left screw axis in right quartz. Wyckoff [43] gives the hexagonal coordinates in table 2.2 for nine independent atomic positions, in terms of fractional unit-cell coordinates and parameters, from which all positions may be derived by translations, for right quartz under a RHCS system[2]:

The unit-cell dimensions and values of the parameters may be found in various sources at different temperatures and pressures. Nuttall and Weil [42], and subsequent papers by Weil's group use the parameters of Le Page *et al.* [44] from x-ray diffraction measurements at 94 K, and cell dimensions interpolated for 94 K from the results of Danielsson *et al.* [45] over the range 86-298 K. After extrapolation of the results in these papers, it was concluded that the

[1] Hereafter in this chapter, the α will be dropped except where it is deemed necessary for clarity.
[2] See details of Wyckoff's system in [41].

Table 2.2: Atomic coordinates of α-quartz given as fractions of the unit-cell dimensions.

Si	$(u,\ 0,\ 0)$	$(-u,\ -u,\ 1/3)$	$(0,\ u,\ 2/3)$
O	$(x,\ y,\ z)$	$(y-x,\ -x,\ z+1/3)$	$(-y,\ x-y,\ z+2/3)$
	$(x-y,\ -y,\ -z)$	$(y,\ x,\ 2/3-z)$	$(-x,\ y-x,\ 1/3-z)$

variation of the parameters between 94 K and the temperature of measurement (35 K in [42]) would not hamper the interpretation of the epr results. The extrapolation was based on the equations given by Le Page *et al.* and Danielsson *et al.* describing the parameter values as functions of T for the temperature range used in their experiments. Though it may not be entirely valid to extrapolate these to much lower temperatures, this has also been done for a temperature of 15 K, and these values given in table 2.3, along with the 94-K values. They are compared with the results of Lager *et al.* [46], which were carried out at 13 K using neutron diffraction techniques.

Table 2.3: Comparison of unit-cell dimensions at different temperatures using different techniques.

	15 K[a]	94 K[b]	13 K[c]
u	0.46733(4)	0.46808(6)	0.4680(2)
x	0.41278(3)	0.41303(14)	0.4124(2)
y	0.27186(3)	0.27068(13)	0.2712(2)
z[d]	0.11556(5)	0.11651(9)	0.1163(1)
a (Å)	4.9008(7)	4.9079(11)	4.9021(1)
c (Å)	5.3973(7)	5.3991(11)	5.3997(1)

[a] 15-K data calculated by extrapolation from 94-K x-ray diffraction data [44][45].
[b] 94-K x-ray diffraction data [44].
[c] 13-K neutron diffraction data [46].
[d] The z parameter has been converted from the $r(+)$ convention used in [44] and [46] to the $z(+)$ [41] convention used in this thesis by a sign change.

The extrapolated parameters do not agree with the Lager *et al.* values within the experimental error. This is not surprising, since the temperature dependences calculated by Le Page

et al. and Danielsson *et al.* are likely to break down at very low temperatures. The different technique used may also result in some variation, even had the results been carried out at the same temperature. The unit-cell dimension c, for example, is actually greater in the 13-K results than the 94-K results.

All of the diagrams and calculations in this thesis utilise the 94-K data. This is certainly valid for the work carried out on the $[HLi_2O_4]^0$ centre, which makes up the bulk of the quartz studies, as this centre was measured at *ca* 100 K. The only analysis of the $[FeO_4/H]^0$ centre matrices, which were derived from *ca* 15-K data, is a pseudocube analysis. The results of this analysis would not be noticeably changed by the use of any of the parameter sets in table 2.3.

Figure 2-2 shows the quartz crystal structure derived from the 94 K data, viewed along the c-axis direction. Quartz comprises distorted SiO_4 tetrahedra linked at every vertex, arranged in such a way as to form helical Si-O-Si-O structures which surround channels running parallel to the c axis. Figure 2-2 shows one of the larger c-axis channels at the centre, and six of the smaller channels surrounding it. There are threefold screw axes running down the centre of each of the channels. Three twofold axes 120° apart lie perpendicular to the screw axes and c axis, and pass through the centre of the larger c-axis channel, labelled $a_{1,2,3}$ in figure 2-2. They repeat every half unit cell in the c-axis direction, so that there is a set which passes through the centre of silicon atoms on either side of the channels, and a set which passes through a vacant area between adjacent silicon atoms along the c axis. This latter set run along smaller channels perpendicular to the c-axis channels, which are not large enough for small positive ions to diffuse through in electrodiffusion experiments, in contrast to the c-axis channels (see for example [47], [48] and references therein).

The distortion of the SiO_4 tetrahedra in α-quartz is such that the point-group symmetry at each of the silicon sites is only 2. There are two Si-O bond lengths, 1.6145 Å and 1.6101 Å, with four different O-Si-O bond angles (of six), ranging from 108.65° to 110.54°.

The Wyckoff hexagonal coordinates place the origin at the centre of the large c-axis channel, lying on one of the three twofold axes, which is defined as the x axis (a_1 in figure 2-2). The y and z axes are defined by a_2 and $\mathbf{a}_1 \times \mathbf{a}_2$, respectively. The system used in this thesis is described as the z(+) system [41], as used by Nuttall and Weil [42]. Even though a cartesian, rather than hexagonal system is used, the z(+) description may be retained. Here right quartz

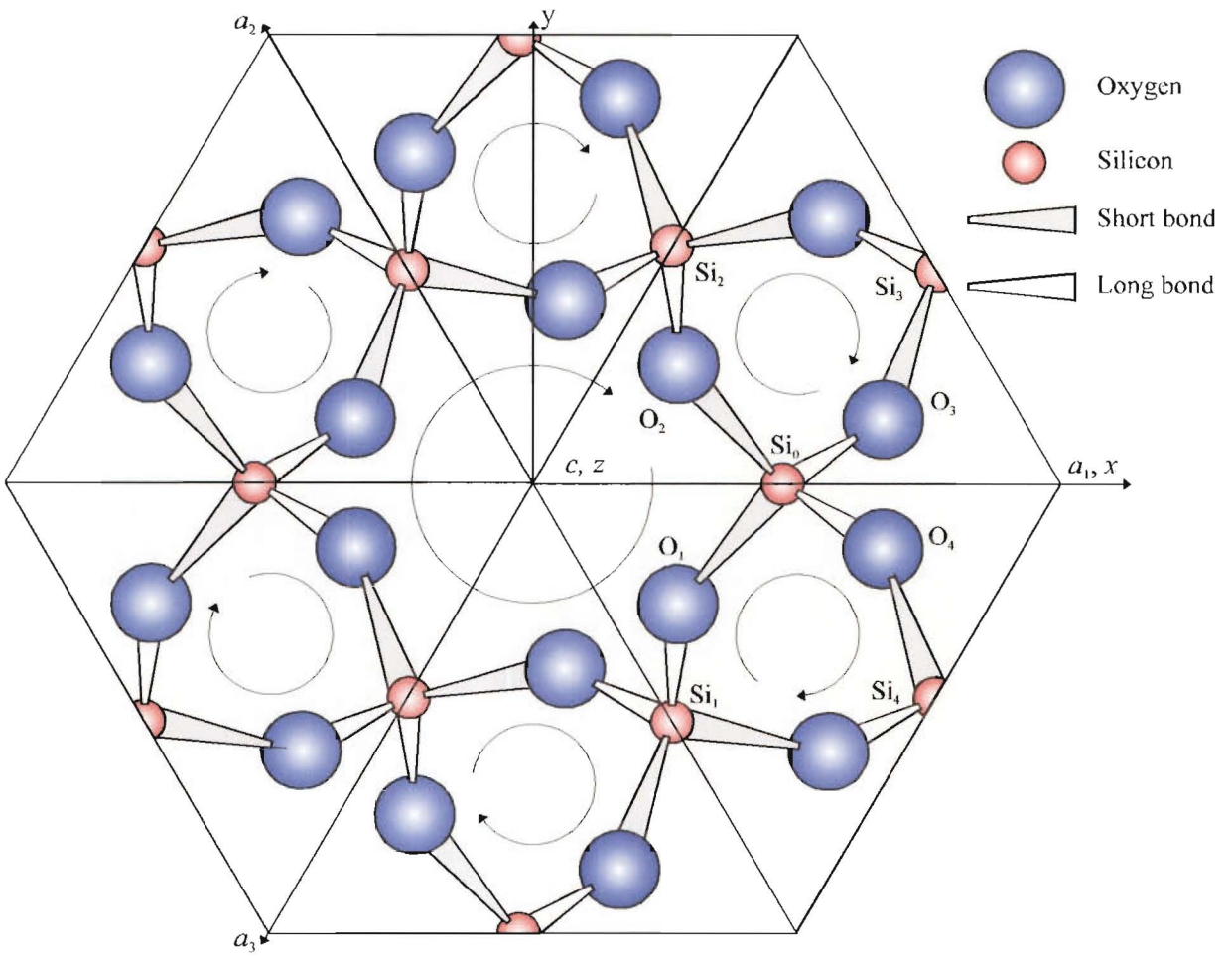

Figure 2-2: Crystal structure of right α-quartz viewed along the c axis. Circular arrows denote handedness of threefold screw axes.

is described in a RHCS, where the positive direction of the a_1 (and thus x) axis is taken as the end which develops a positive charge on extension, or a negative charge on compression[3]. The z axis is taken to be parallel to the c axis, with arbitrary sense, and the y axis is then defined by the RHCS.

The lack of symmetry elements in the quartz structure leaves only two possibilities for the site symmetry of point defects: 2 or 1. Unlike zircon, defects with point-group symmetry 1 are very common, and there are no constraints on parameter-matrix principal directions for these

[3]This phenomenon is known as the piezoelectric effect, and is observed for crystals which contain no centres of symmetry. The quartz a axes are polar, and known as the piezoelectric axes.

defects. This makes the site assignment of the parameter matrices more difficult, but crucial to a successful analysis.

Defects with point-group symmetry 2 retain the twofold symmetry element in the quartz structure, and thus any changes to the normal structure either occur on the axis, or are off the axis, but have a 'partner' related by the twofold rotation. The latter case can also occur when a single entity off the axis flips rapidly between the symmetry-related sites so that the epr experiment sees an averaged twofold symmetry. This is thought to be the case for a number of the compensated iron centres in quartz which exhibit point-group symmetry 2, or change from 1 to 2 when the temperature is sufficiently high to allow this motion (see quartz iron centre review article [19], table 4 and discussion).

Any defect centre in quartz which does not contain a real or apparent averaged twofold axis must have point-group symmetry 1. In the absence of averaging effects, this includes all the oxygenic hole centres, and electron centres which are located in silicon sites, but are associated with other ions off the twofold axis. There are a great number of centres which fit into these categories, making 1 the most common point-group symmetry of point defects in quartz.

In an epr experiment, defects with point-group symmetry 2 display three distinct sites in an arbitrary orientation, two when the applied magnetic field is oriented in the yz plane, and one when the applied field is directed along the z *(c)* axis [12]. Measurements are usually made in the yz plane, which is sufficient to fully determine the parameter matrices. The physical identity of the two sites in this plane is clear - one must correspond to the defect site associated with the twofold axis perpendicular to the plane of measurement, while the other must be doubly degenerate, corresponding to the defect site associated with the other two twofold axes, 30° outside the rotation plane. The site which corresponds to the twofold axis defined as the x axis is always assigned as site one. When fitting the data collected to spin-Hamiltonian parameters, an initial assignment of site one to the correct part of the observed roadmap needs to be made, but it can easily be checked once the parameters have been fitted. Point-group symmetry 2 constrains one of the principal directions of each parameter matrix to lie along the twofold axis for each distinct site, and thus the site-one matrices should have a principal direction $\theta = 90°$, $\phi = 0°$ or equivalent. If an incorrect initial assignment has been made, directions $\theta = 90°$, $\phi = 120°$, $240°$ or equivalent should be obtained, and can be easily refitted with the correct

assignment.

Defects with point-group symmetry 1 have six distinct sites in an arbitrary orientation, three when the applied magnetic field is oriented in the yz plane, and one when the applied field is directed along the z *(c)* axis [12]. As for defects with point-group symmetry 2, measurements made with $\mathbf{B}$ in the yz plane are sufficient to fully determine the parameter matrices. The six sites in an arbitrary orientation correspond to the three twofold axes, with two distinct sites for each related by operation of the twofold axis, which is not a local symmetry element. The papers of Weil frequently refer to the sites as 1, $1^{'}$, 2, $2^{'}$, 3, and $3^{'}$, where the number refers to each twofold axis and 1 corresponds to the rotation (x) axis, and the no-dash and dashed sites are related by a rotation about that twofold axis. Thus the sites within each set 1, 2, 3 and $1^{'}$, $2^{'}$, $3^{'}$ are related by 120° rotations about z. In the yz plane, the two sites associated with the rotation axis become degenerate (1 and $1^{'}$), as do two pairings between the other two axes, i.e. - 2 and $3^{'}$, and 3 and $2^{'}$. The latter pairings are degenerate because they are related by twofold rotation about the x axis, and therefore must give rise to identical spectra in this rotation plane.

When initially assigning the observed spectra to the different sites before carrying out a fitting, it is often possible to observe a "unique" site, which should be chosen as site one. As site 1 is associated with the twofold axis about which the crystal is being rotated, while the other sites are associated with twofold axes 30° outside the rotation plane, it might be expected that the spectra of the latter two sites, and particularly the roadmaps, will bear more resemblance to each other than to that of site one. While this is not a particularly precise or scientific statement, it can be a very useful tool in making an initial site assignment, and usually turns out to be correct where one site was seen to be quite different from the other two. Of course, it is quite possible that no site spectra or roadmap will bear much resemblance to that of either of the others. The strategy is often useful when the location of the spin density in the defect is on the twofold axis, and the interactions responsible for the observed line positions are mostly controlled by relatively unperturbed quartz atoms in the immediate vicinity which are related by the usual twofold symmetry. For example, the $[FeO_4/H]^0$ centre measured in this thesis comprises a silicon-substituting iron species, with a compensating hydrogen cation located off the axis, and associated with one of the oxygen atoms. The line positions for this centre

are highly anisotropic, and largely influenced by the spin-Hamiltonian parameter matrix **D**, which in turn is influenced by interactions with the surrounding tetrahedron of oxygen atoms. The proton clearly has a significant effect on the observed line positions, as the $[FeO_4/H]^0$ centre roadmap does not look like any of the other $[FeO_4/M]^0$ ($M = H^+$, Li^+, Na^+)[4] centre roadmaps (there are multiple centres of each type [19]), but one can see similarities between the roadmaps of sites two and three. Examination of the roadmap of figure 6-16, reveals that many of the turning points associated with these two sites for the same transition are very similar in field magnitude, while the plot associated with site one behaves quite differently. This is seen especially for the 3-4, 4-5 and 5-6 transitions.

The unique-site method is still readily applicable in many cases where the spin density is principally located away from the twofold axes, such as in oxygenic hole centres. The other quartz centre analysed in this thesis ($[HLi_2O_4]^0$) is an oxygenic hole, and was initially assigned by the unique-site method. This assignment was retained in the analysis of the fitted matrices, which indicated that the assignment had been correct. The stacked plot for this centre in figure 6-1 clearly shows a unique site.

There are sometimes other ways of making site assignments before any fitting has been carried out. As noted earlier, some defect centres display a different point-group symmetry at different temperatures, due to an averaging effect of rapidly flipping off-axis positions. If one observes which site spectra coalesce when the temperature is raised and the effective point-group symmetry changes from 1 to 2, a site assignment can be made. The 1 and $1'$ site spectra will retain the same degeneracy under both point-group symmetries, while the 2 and $3'$, and 3 and $2'$ site spectra which are distinct in under point-group symmetry 1 will become degenerate when the point-group symmetry changes to 2.

Another possible way of making site assignments before fitting is the observation of a defect centre in a crystal which has differently populated symmetry-related sites. This phenomenon may occur during growth, or can sometimes be created by irradiation with polarised light. An example of this may be found in the paper by Mombourquette *et al.* [49], where the site assignment for the $[FeO_4/H]^0$ centre was corroborated by measurement in a natural crystal

[4]The + sign of the M^+ ion is normally omitted when written in the form $[XO_4/M]^n$, where X is some cation, such as Al^{3+}, Ge^{3+} or Fe^{3+}.

which was known to have a lower population of iron on one of the three twofold axes. If the axis with the lower concentration of Fe^{3+} happened to be the one about which the crystal was being rotated, then site one would have lower intensity than the other two sites. If the lower-concentration axis was not the rotation axis, then it would contribute to both sites two and three (2 and 3′, and 3 and 2′), thus both of these sites would have a lower intensity than site one. In either case, site one would be identified as the one with a different intensity to the other two. Care would need to be taken that the observed differences in intensity were due to the differences in site population, and not transition probabilities, as determined by effective g values. This was avoided in the case described above by checking the intensities in the closest orientation to the c axis where the three sites were resolved.

After making the initial assignment of sites and fitting spin-Hamiltonian parameter matrices, the principal directions are also likely to offer some clues as to the correct site assignment. It is usually possible to correlate the parameter-matrix principal directions of a new centre with those of similar centres previously studied. For example, there is a trend in the g-matrix principal directions of various oxygenic hole centres which is discussed in section 6.2.3, even though the structure of the centre may be quite different apart from the oxygenic hole. Principal directions can often be correlated with atomic directions in the quartz structure, which will be different for the various symmetry-related sites. Site assignment by principal directions also allows discrimination between the degenerate spectra of sites which are measured in the yz plane. Sites 1 and 1′ give the same spectrum in the yz plane, but they have different parameter matrices and principal directions. Which matrix is obtained in the fitting will depend on the initial values which were given for the parameter matrices. The fit will fall into one or the other possibility for site one, probably whichever has the closest match in terms of the signs and magnitudes of the elements. Following the fitting of the oxygenic-hole-centre $[HLi_2O_4]^0$ (section 6.2), the initial assignment of sites 1 and 1′ was shown to be correct, but comparison with the other oxygenic hole centre principal directions showed that the fitted matrix was for 1′, rather than 1. The aluminium oxygenic-hole centres which were used to make the comparison were all given with site 1 corresponding to atom O_2 rather than O_1 (see figure 2-2) for short-bonded centres (with respect to Si_0), and O_3 rather than O_4 for long-bonded centres. The original $[HLi_2O_4]^0$ assignment placed site 1 at O_4, so was changed to be consistent with the

convention chosen for the aluminium oxygen hole centres.

Chapter 3

Crystal growth

3.1 Techniques

3.1.1 Zircon

There are many different techniques for the growth of single crystals of various materials (see for example, [50]). The most common techniques for the growth of zircon crystals are flux growth and hydrothermal growth. The technique of flux growth was used to produce all of the synthetic zircons which were analysed during the course of this thesis. Flux growth does not require very sophisticated equipment, and can generally produce crystals of acceptable size and quality for research purposes. Hydrothermal growth [51], [52], described in the quartz section of this chapter, requires some specialised equipment. This was previously available at Canterbury, but is no longer considered structurally sound enough to operate safely at the high pressures required, so hydrothermal growth was not an option.

Flux growth has been commonly used to grow refractory crystals for around 40-50 years, and first appears in the literature as early as the late 1800s [53]. The technique makes use of the high solvent power of molten inorganic salts and oxides (the flux) for these refractory materials. The raw components of the crystalline material to be grown are dissolved in hot molten flux, and then induced to crystallise out, usually through slow cooling or evaporation. In practice, there is a mixture of both, particularly where a volatile flux is used. The process is essentially the same as the crystallisation of simple ionic salts by cooling of a saturated solution in hot

water, but carried out at a much higher temperature using solvents which are solids at room temperature.

The ideal flux for a crystal growth would have all of a number of desirable properties. It would need to have a fairly high solubility for the solute at high temperature, but have a steep solubility versus temperature curve to ensure appreciable crystallisation upon cooling; have low viscosity to allow easy diffusion of solute through the molten flux; have low volatility to prevent significant flux loss; be unreactive with the crucible material; have a low solubility in the grown crystals, to prevent contamination; should not form stable compounds with the crystal components; be easy to dissolve away from the crystals after solidification; be readily obtainable, inexpensive, and non-toxic. It would be unusual to find a single flux which had all of these properties, but multi-component fluxes are commonly used, where the addition of a minor component can often considerably improve some of the more undesirable properties of the major component.

The very simplest flux-growth procedure, which was employed for the growth of zircon, relies on a linear, non-cycled cooling programme, and spontaneous nucleation, and also allows the flux to solidify around the grown crystals. The apparatus required for such an experiment is a furnace, usually a resistance or induction furnace, a thermocouple for temperature measurement connected to a variable temperature control, a crucible made of a suitable material with a tightly fitting lid, and a stand to place the crucible on within the furnace. Some possible crucible materials include alumina, silica, glass, carbon and platinum. The large number of crucible materials have various advantages and disadvantages in terms of their workability, maximum temperature of usage, resistance to attack by various fluxes and cost. A listing of properties and uses of various crucible materials may be found in tables 9.10 and 12.1 of [54] and 5.7 of [55]. Similar heat-resistant materials may be used for the stand such as silica, alumina and ceramics.

When larger crystals are desired, a seed crystal may be used to initiate growth. When a seed crystal is present, crystallisation essentially takes place only on the seed, so that all of the recovered material forms into a single crystal. However, seeded growth requires more sophisticated equipment than growth by spontaneous nucleation (see for example discussion in [50]). An alternative way of reducing the number of nucleation points and thus generate

fewer, larger crystals is to allow the temperature to oscillate in the region where nucleation occurs. The smaller crystal nuclei which form during the cooling period are redissolved during the heating period, while larger nuclei survive, and act as seeds during the next cooling period. After a given number of oscillations, the temperature is then slowly lowered as for a normal cooling programme.

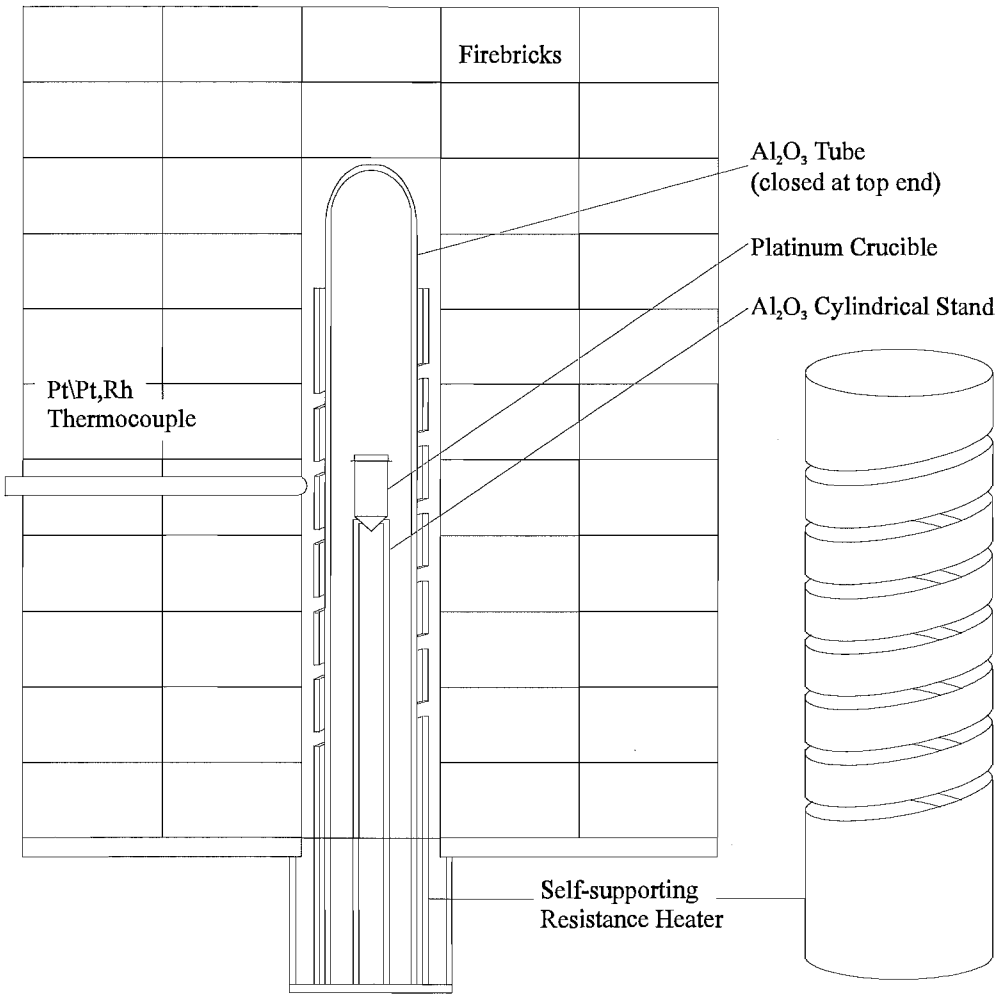

Figure 3-1: Simplified diagram of flux-growth apparatus.

Figure 3-1 shows the apparatus used. A 23 cm^3, and later, a 50 cm^3 platinum crucible was used which, while expensive, is easily workable, resistant to attack by halides and oxides, and can be heated in air to 1500 °C - well above the temperature required for the growth. The

crucible was supported by an alumina tube. A wider alumina tube, closed at one end, enclosed the crucible and support. This served to trap gaseous flux, and prevent it from attacking the furnace element. The element was a self-supporting silicon carbide resistance heater which was run at 240 V and 10 A at full power. Temperature was kept at the set level by a rapid switching mechanism, keeping temperature fluctuations to a minimum. Temperature measurement was achieved via a platinum against platinum/13 % rhodium thermocouple, the tip of which was located within the space between the outside of the furnace element and the firebrick insulation. The thermocouple device was housed inside a narrow alumina tube, closed at the inner end. The temperature setting was gradually lowered by an electric motor running at $\frac{1}{6}$ of a revolution per hour, equating to a cooling rate of 4 °C per hour. This process could be started after a selected length of time at the maximum temperature by setting an oven timer device, allowing the solute sufficient time to completely dissolve before cooling began.

Many flux growth "recipes" have been reported for any number of different crystals, and the same was found true of zircon [56] - [58]. The zircons were grown following Chase and Osmer (1966) [57], using a molybdenum trioxide (MoO_3) - lithium molybdate (Li_2MoO_4) flux. The minor component, Li_2MoO_4, lowers the volatility of the flux, without greatly reducing its solvent power for zircon. The most successful growth runs contained 84.5 molar % MoO_3, 9.5 molar % Li_2MoO_4, and 3 molar % of both ZrO_2 and Li_2SiO_3. When dopant was added to the crystals, amounts were usually no more than 0.1 molar % of the appropriate oxide. The powdered components were thoroughly mixed by stirring and manually pressed into the crucible. The mixture was heated to 1250 °C for 4-6 hours, before cooling began at the rate of 4 °C per hour until a temperature of 1000 °C was reached. After this point, the heating automatically shut off, allowing the furnace to cool to room temperature over several hours. The solidified flux was then dissolved away from the crystals by boiling in ammonia solution. The whole process could be completed, and the crucible cleaned and ready for another growth run in four to five days.

3.1.2 α-Quartz

Although the α-quartz crystals used in the work described in this thesis were not grown at Canterbury, it is worth noting the growth technique which was used. Crystals of α-quartz

have been grown previously at Canterbury, but the equipment is no longer considered safe, as noted at the beginning of this chapter. Hydrothermal growth is used almost exclusively to grow quartz crystals, particularly in large-scale industrial processes. The main piece of equipment required is an autoclave, a cylindrical metal vessel which is closed off at one end and sealable at the other, and capable of withstanding temperatures of 400 °C and pressures up to 2000 atmospheres. A discussion of some autoclave designs may be found in Ballman and Laudise [59].

Chips of unfaced quartz known as lascas are placed in the lower part of the autoclave, often using a wire-mesh basket. A metal plate with holes cut through it (the baffle) is set above this. The baffle controls the convection flow which will occur during the growth, and sets up two nearly isothermal regions in the top and bottom part of the autoclave. This promotes uniform growth of the crystals throughout the growth zone. Seed crystals, slices of natural or cultured quartz, are mounted on a solid support and lowered into the top part of the autoclave. The autoclave is then partially filled with an aqueous solution of sodium carbonate or hydroxide. This mineraliser makes the quartz more soluble than it would be in pure water, but the concentration must not be high enough to cause the growth of sodium silicates along with the α-quartz. The amount of solution added is known as the fill, and it is limited by the pressure which can be handled by the apparatus. A typical value may be around 80 %, that is 80 % of the available space inside the autoclave when all the parts of the growth run are in place. The autoclave is then sealed and heated, with a temperature differential between the top and bottom parts, the bottom part being hotter (dissolving zone). A typical ΔT is around 50 °C, with a dissolving-zone temperature of around 400 °C. The lascas dissolves in the hotter zone, is transported to the upper cooler growth zone by convection, and forms a supersaturated solution which recrystallises on the seed crystals. Cooled, spent solution cycles back into the hotter zone, continuing the process. A single growth in an industrial instrument may last from a few weeks to upwards of a year, depending on the desired size of the grown crystals.

The crystal in which the $[HLi_2O_4]^0$ and $[FeO_4/H^+]^0$ centres described in this thesis were observed was cut from a much larger grown crystal. The growth was carried out on a $\bar{Y}$ seed, a plate with faces perpendicular to the one of the crystallographic a axes. The solution used was 0.81 M sodium carbonate and 0.02 M lithium carbonate. The growth run lasted 64 days,

producing crystals with approximately 34 inclusions per cubic inch. The quality factor Q (see [60] for a discussion) was measured as 0.155×10^6, implying a relatively high concentration of defects. Many of these defects may be associated with iron and aluminium, both of which were observed in the cut crystals by epr. The iron most likely came from the inside of the autoclave which was not silver lined. Autoclaves with silver (or gold) lining are used for the preparation of highly pure crystals necessary in most technological applications. The aluminium may have been an impurity present in the mineraliser solution, and is quite ubiquitous.

3.2 Results

Table 3.1 summarises the results of all the zircon crystal growths carried out, some as part of an honours project [61]. The first attempted growth of zircons resulted in a large amount of flux loss (66.1 % of the initial total mass), and poorly shaped crystals. The irregularly shaped crystals were probably the result of rapid growth after a substantial loss of flux by evaporation. Crystals with the regular growth habit of zircon were desirable because they have natural faces corresponding to the *ac* and *bc* planes, making them convenient for mounting precisely and accurately for epr experiments. Well-formed zircon crystals grow as rectangular prisms with faces perpendicular to the *a* and *b* axes and pyramidal caps (figure 3-2, type a,b). The addition of certain dopants was found to increase the size of the capping faces until these were all that remained (type c of figure 3-2). The loss of flux was attributed to a poorly fitting lid and the high volatility of the MoO_3, so a new 50-cm^3 crucible with a better-fitting lid was used for subsequent growths. A V_2O_5-Li_2O flux and the MoO_3-Li_2MoO_4 flux with a higher percentage of Li_2MoO_4 was also tried to alleviate the volatility problem, but there were either no crystals or only very small crystals produced. Eventually, good crystals were produced from a MoO_3-Li_2MoO_4 system with the component percentages given above, with a loss of around 40 % of the flux by mass every time. Crystals ranged in size up to about 4 mm, which was ideal for epr experiments, so no attempts were made to improve the crystal size by adjusting the technique as described earlier.

The dopants used were chosen for various reasons; on the basis of their likelihood to be incorporated into the zircon structure; because centres had been observed in undoped or natural

Table 3.1: Composition of starting materials and results of all zircon crystal growths.

Growth	Component	Mol %	Mass %	Mass (g)	Used (g)	Loss %	Result
E	MoO_3	85.1	84.05	50.43			~40 crystals (1.99 g)
	Li_2MoO_4	7.4	8.83	5.30			irregular shapes
	ZrO_2	3.0	2.54	1.52	30.46	66.1	flux inclusions
	Li_2SiO_3	3.0	1.85	1.11			up to 3 mm
	TiO_2	1.0	1.62	0.97			
	La_2O_3	0.5	1.12	0.67			
F	V_2O_5	67.9	87.23	43.62			very small crystals
	Li_2O	22.6	4.77	2.38			dark blue colour
	ZrO_2	4.0	3.48	1.74	45.44	4.8	
	SiO_2	4.0	1.70	0.85			
	TiO_2	1.0	1.67	0.83			
	La_2O_3	0.5	1.15	0.58			
G	MoO_3	46.75	42.62	21.31			no crystals
	Li_2MoO_4	46.75	51.47	25.74			
	ZrO_2	2.5	1.42	0.71	49.95	15.1	
	Li_2SiO_3	2.5	1.95	0.98			
	TiO_2	1.0	1.50	0.75			
	La_2O_3	0.5	1.03	0.52			
H	MoO_3	66.96	63.49	31.75			~90 crystals (0.16 g)
	Li_2MoO_4	26.5	30.34	15.17			mostly small (~80 % < 1 mm)
	ZrO_2	2.52	2.04	1.02	49.94	4.8	largest 3 mm
	Li_2SiO_3	2.52	1.49	0.75			colourless
	TiO_2	1.0	1.55	0.78			well shaped (type a)
	La_2O_3	0.5	1.07	0.54			
I	Same composition as E				54.71	28.1	no crystals
J	MoO_3	86.5	86.5	47.57			no crystals
	Li_2MoO_4	7.5	9.1	4.98	54.92	25.9	
	ZrO_2	3.0	2.6	1.41			
	Li_2SiO_3	3.0	1.9	1.03			
K	Same composition as J, different Li_2SiO_3				54.92	44.5	~130 crystals (0.82 g) distribution of sizes up to 4 mm well shaped (type a) some colourless, some pale yellow pale yellow crystals better quality (no flux inclusions)
L	MoO_3	85.0	84.67	46.57			~30 crystals (0.83 g)
	Li_2MoO_4	8.8	10.59	5.82			mostly large (up to 4 mm)
	ZrO_2	3.0	2.56	1.41	54.74	42.8	most pale yellow colour
	Li_2SiO_3	3.0	1.87	1.03			some large misshapen crystals
	TiO_2	0.1	0.16	0.090			from sides of crucible
	Y_2O_3	0.1	0.16	0.086			mostly type-b/c shapes

Growth	Component	Mol %	Mass %	Mass (g)	Used (g)	Loss %	Result
M	MoO_3	84.5	84.16	45.45			~20 crystals (0.85 g)
	Li_2MoO_4	9.4	11.31	6.10			mostly large (up to 3 mm)
	ZrO_2	3.0	2.56	1.38	53.25	44.2	some colourless, some pale yellow
	Li_2SiO_3	3.0	1.87	1.01			pale yellow crystals better quality
	Fe_2O_3	0.1	0.11	0.06			(few or no flux inclusions)
							type-a crystal habit
N	MoO_3	84.5	84.19	45.46			~30 crystals (0.71 g)
	Li_2MoO_4	9.4	11.31	6.11			range of sizes (up to 4 mm)
	ZrO_2	3.0	2.56	1.38	53.98	39.5	range of colours
	Li_2SiO_3	3.0	1.87	1.01			(colourless - brown/yellow)
	Al_2O_3	0.1	0.071	0.038			type-a crystal habit
O	MoO_3	84.5	84.19	45.46			~90 crystals (0.33 g)
	Li_2MoO_4	9.0	10.83	5.85			almost entirely flakes
	ZrO_2	3.0	2.56	1.38	53.99	32.9	few recognisable crystals
	Li_2SiO_3	3.0	1.87	1.01			unusual appearance of solidified
	Fe_2O_3	0.5	0.55	0.30			flux (see text)
P	Same composition as O, different MoO_3				53.91	35.6	~80 crystals (0.46 g)
							flakes as for growth O
							some 5 mm across
Q	MoO_3	84.0	83.58	45.14			several hundred crystals
	Li_2MoO_4	9.9	11.90	6.42			very poor quality small rods
	ZrO_2	3.0	2.56	1.38	53.56	42.4	0.38 g
	Li_2SiO_3	3.0	1.87	1.01			
	P_2O_5	0.1	0.098	0.053			
R	Same composition as L				53.87	45.3	similar result to L
							~40 crystals (0.83 g)
							most pale yellow
							mostly type-b/c crystal habit
S	MoO_3	84.5	84.19	45.46			~100 crystals (1.08 g)
	Li_2MoO_4	9.4	11.31	6.11			mostly small, up to 3 mm
	ZrO_2	3.0	2.56	1.38	53.64	46.4	colourless, type-a crystal habit
	Li_2SiO_3	3.0	1.87	1.01			many with large flux inclusions
	GeO_2	0.1	0.072	0.039			
T	MoO_3	84.5	84.17	45.45			similar result to Q
	Li_2MoO_4	9.4	11.31	6.11			several hundred crystals
	ZrO_2	3.0	2.56	1.38	53.95	46.3	very poor quality small rods
	Li_2SiO_3	3.0	1.87	1.01			1.08 g
	P_2O_5	0.1	0.098	0.053			
99A	MoO_3	84.5	84.15	46.28			~120 crystals (0.91 g)
	Li_2MoO_4	9.5	11.42	6.28	54.96	39.0	range of sizes up to 3 mm
	ZrO_2	3.0	2.56	1.41			both colourless and pale yellow
	Li_2SiO_3	3.0	1.87	1.03			flux inclusions in colourless crystals
							type a crystal habit

Growth	Component	Mol %	Mass %	Mass (g)	Used (g)	Loss %	Result
99B	MoO_3	84.5	84.21	46.32			~120 crystals (0.70 g)
	Li_2MoO_4	9.4	11.31	6.22			mostly medium sizes (1-2 mm)
	ZrO_2	3.0	2.56	1.41	54.88	38.7	all pale yellow, most opaque
	Li_2SiO_3	3.0	1.87	1.03			(unlike previous yellow crystals)
	B_2O_3	0.1	0.048	0.026			type-a crystal habit
99C	MoO_3	84.42	84.04	46.22			similar result to Q, T
	Li_2MoO_4	9.4	11.30	6.22			several hundred crystals
	ZrO_2	3.0	2.56	1.41	54.95	38.8	very small poor quality rods
	Li_2SiO_3	3.0	1.87	1.03			0.08 g
	TiO_2	0.1	0.16	0.09			
	P_2O_5	0.08	0.079	0.043			
99D	MoO_3	84.5	84.16	46.29			similar result to Q, T, 99C
	Li_2MoO_4	9.3	11.18	6.15			only a few representative crystals
	ZrO_2	3.0	2.56	1.41	55.0	37.6	collected
	Li_2SiO_3	3.0	1.87	1.03			
	TiO_2	0.1	0.16	0.088			
	$NaPO_3$	0.1	0.071	0.039			
99E	MoO_3	84.5	84.16	46.29			~130 crystals (0.73 g)
	Li_2MoO_4	9.48	11.40	6.27			range of sizes (up to 2 mm)
	ZrO_2	3.0	2.56	1.41	54.96	36.0	range of colours
	Li_2SiO_3	3.0	1.87	1.03			(colourless - brown/yellow)
	B_2O_3	0.02	0.0096	0.0053			mostly type-a crystal habit
99F	MoO_3	84.5	84.12	46.27			several hundred crystals (0.79 g)
	Li_2MoO_4	9.39	11.29	6.21			rod shaped crystals again
	ZrO_2	3.0	2.56	1.41	54.97	37.1	larger than other P-doped growths
	Li_2SiO_3	3.0	1.87	1.03			longest 5 mm (but very narrow)
	TiO_2	0.1	0.16	0.09			colourless and pale yellow crystals
	$NaPO_3$	0.01	0.007	0.0039			
99G	MoO_3	84.5	84.15	63.11			~130 crystals (0.38 g)
	Li_2MoO_4	9.48	11.40	8.55			range of sizes (up to 2 mm)
	ZrO_2	3.0	2.56	1.92	74.97	29.9	range of colours
	Li_2SiO_3	3.0	1.87	1.40			(colourless - brown/yellow)
	Cr_2O_3	0.02	0.021	0.016			most type-a, few type-b/c habits
99H	MoO_3	84.5	84.15	63.11			~160 crystals (0.66 g)
	Li_2MoO_4	9.48	11.40	8.55			range of sizes (up to 2 mm)
	ZrO_2	3.0	2.56	1.92	74.93	31.6	range of colours, colourless - brown
	Li_2SiO_3	3.0	1.87	1.40			(many quite distinctly brown)
	Na_2CrO_4	0.02	0.022	0.017			all crystal-habit types
99I	as for 99A, different MoO_3				54.93	41.8	~90 crystals (1.02 g) some quite large (4 mm) larger crystals have flux inclusions many crystals not well shaped suprisingly all crystal-habit types mostly colourless or pale brown

Growth	Component	Mol %	Mass %	Mass (g)	Used (g)	Loss %	Result
99J	MoO_3	84.4	84.34	67.47			~40 small, poor crystals (0.06 g)
	Li_2MoO_4	9.1	10.98	8.78			
	ZrO_2	3.0	2.57	2.06	79.89	36.0	
	Li_2SiO_3	3.0	1.87	1.50			
	B_2O_3	0.5	0.24	0.19			
99K	MoO_3	84.45	84.21	67.37			~200 small crystals (0.58 g)
	Li_2MoO_4	9.35	11.26	9.01			up to 2 mm, mostly < 1 mm
	ZrO_2	3.0	2.56	2.05	79.65	33.3	almost all opaque pale yellow
	Li_2SiO_3	3.0	1.87	1.50			most not very well shaped
	B_2O_3	0.2	0.096	0.077			
99L	Same composition as 99B				79.97	34.9	~150 small crystals (0.41 g) opaque pale yellow up to 2 mm not well shaped, generally type a

crystals which were suspected to contain those species; or simply because they were deemed interesting for analysis, if they could be incorporated into a zircon crystal. The first growth which produced good crystals, K, was an undoped run. Two distinctive types of crystal were produced, which turned out to be a regular phenomenon. The first type (not to be confused with type-abc crystal habits) was colourless, sometimes translucent and sometimes opaque, and often had significant flux inclusions. The second type was usually pale yellow, but occasionally a darker yellow/brown, and rarely contained flux inclusions visible to the naked eye. The size of the first type crystals was on average much greater than the other type. The origin of the colouration of the yellow crystals or the reason for its absence in the other crystals is unknown. There was no readily apparent difference between crystals of the two types when epr measurements were carried out, although type-two crystals were often used in preference to type-one because of their better quality on visual inspection. Type-two crystals were used where there were no type-one crystals of a reasonable size. Epr spectra of these crystals were very similar to spectra of the synthetic, undoped zircon grown by Aerospace Corporation which was the source of most of the previous work on zircon at Canterbury.

The first doped crystals contained titanium, added as TiO_2, and yttrium, added as Y_2O_3. These dopants were chosen because of a centre which had been observed in an undoped crystal which was suspected to consist of a Ti^{4+} impurity with an associated Y^{3+} ion. The centre is

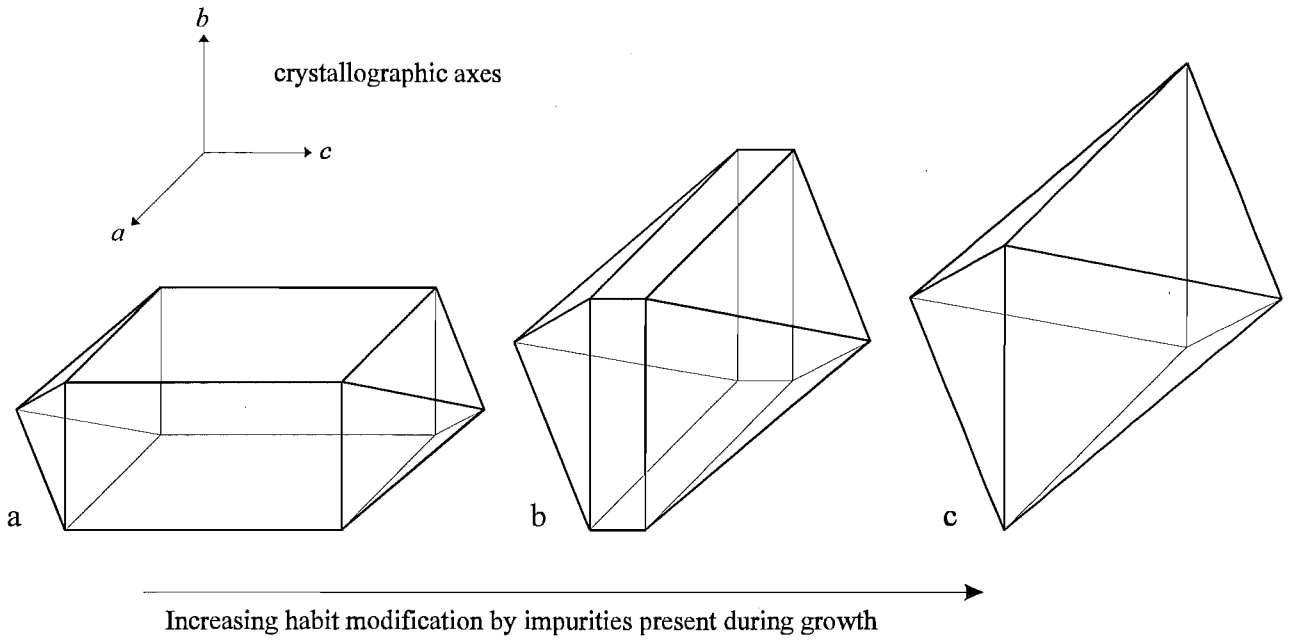

Figure 3-2: Morphology of synthetic zircon crystals.

now known to be a titanium-phosphorus centre [39], but epr spectra of one of these crystals revealed a number of intense, unknown signals, and resulted in the characterisation of four new centres (see chapters four and five and [38], [39]). The crystal habit was mainly type-b, characteristic of a growth in the presence of certain impurities, though it is not easy to predict which elements may have this effect. The yttrium is suspected to be the cause of the habit modification in this case. It is common practice in some crystal growths to deliberately add a growth agent which is known to change the crystal habit. The final crystal habit will be dominated by the slowest growing faces, hence the retardation of the rate of growth of some of the faces by adsorbed impurities will result in a modified habit. The effect is an undesirable one with regard to the epr experiments, as the *ac*/*bc* faces which are used for mounting are either very small or lost altogether.

Figures 3-3 - 3-5 show two crystals from the Ti^{4+}/Y^{3+}-doped growths (L and R). Figures 3-3 and 3-4 show the same crystal in two slightly different orientations. 3-3 shows the square-pyramidal capping face, while 3-4 is slightly tilted to show also one of the 'strips' on the left-hand side which are all that remains of the *bc* faces. The same chipped section along one of the edges

of the pyramidal face may be seen in both figures. Figure 3-5 shows a different crystal from the same growth which has been mounted in the *bc* plane on a fixed flat copper mount, as in figure 1-3. With such a small *bc* face, it is difficult to mount the crystal with the downward face exactly flush against the mount surface.

Figure 3-3: Ti^{4+}/Y^{3+}-doped synthetic zircon crystal viewed down pyramidal capping face. The crystal is *ca* 2 mm across.

Figure 3-4: Same crystal as above in slightly tilted orientation. One of the *bc* faces is now visible on the left-hand side.

The doping of crystals with selected impurities generally seemed successful with two major exceptions, iron and phosphorus. Iron as Fe^{3+} was considered an interesting species because of

Figure 3-5: Ti^{4+}/Y^{3+}-doped crystal mounted in *bc* plane. The mount head is 5 mm across.

its high electronic spin of $\frac{5}{2}$. Fe^{3+} centres in α-quartz are well known and studied [19], but there are few reports of Fe^{3+} in zircon [35]. Growth M was the first attempt at doping with Fe^{3+}, using Fe_2O_3. There was nothing unusual about the crystals produced, but epr experiments revealed no iron centres. In a subsequent growth, O, the amount of Fe_2O_3 was increased from 0.1 to 0.5 molar %. A new bottle of MoO_3 was also used, which had a slightly different appearance to the old MoO_3. When the crucible was removed from the furnace, there was a thin layer of flux suspended above the main body in the lower half of the crucible. The crystalline material was all contained in the upper layer, and was in the form of thin flakes, which were of little use. The next growth was carried out with an identical mixture, but some new MoO_3, to see if the problem was related to the MoO_3 used in the previous experiment. However, the result was the same, suggesting perhaps that there was a reaction going on between the Fe_2O_3 and the flux. Repetition of the experiment with an iron salt, such as $Fe_2(SO_4)_3$ might have produced better results, but was never attempted. A recent paper by Ball and Van Wyk [62] has reported the observation of iron centres in iron-doped synthetic zircon crystals. Some crystals have been obtained from these authors for future experiments at Canterbury.

The phosphorus-doped runs were first carried out using P_2O_5 as the dopant, in growths Q, T and 99C. Phosphorus was chosen because of several centres which had been thought to involve yttrium, including the titanium centre referenced above, but were then discovered more likely to be phosphorus-containing centres. In all three cases the crystals which were produced were very poor quality, small rods. Growth 99D was then carried out using sodium metaphosphate ($NaPO_3$) as the source of phosphorus in case the effect was peculiar to P_2O_5, a fairly reactive chemical. However, the result of this run was the same as all the previous ones, leading to the conclusion that it was the phosphorus itself which was causing the unusual results. One more growth was carried out (99F), with only 0.01 molar % of sodium metaphosphate, $\frac{1}{10}$ of the amount used in the previous growths. The result was once again rod-shaped crystals, but they were a little larger than those produced previously, up to 5 mm long, but very narrow. The c-axis epr spectrum of one of these crystals was very similar to an undoped crystal, with no evidence that significant amounts of phosphorus had been incorporated, above that which is almost invariably present.

Doping with germanium by the addition of GeO_2 was also attempted on one occasion (growth S). The crystals produced were well formed, but did not show any evidence of germanium-related defects (with a distinctive $I = \frac{9}{2}$ hyperfine set) when x-irradiation and epr measurements were carried out.

Chapter 4

Hole centres in zircon

4.1 Introduction

The number of different hole centres with m symmetry which have been reported is surprisingly large, considering that there is only one type of oxygen atom in the pure zircon structure. As described earlier, hole centres in zircon can usually be identified by the combination of point-group symmetry, which is m or lower, and the g anisotropy, which is usually small, with principal values which are greater than, or close to, the free-electron g value. The ground-state g value is always close to g_e, as will be discussed in section 4.3. Figure 4-1 shows the principal g values of the various reported hole centres in zircon, including all of those reported by the Canterbury epr group. This figure has been reproduced from [63][1], with a number of additions. While some of the centres shown on this diagram are likely to be the same centre, there are nevertheless many clearly distinguished hole centres. It can only be assumed that most of these hole centres are associated with different stabilising ions, or the same stabiliser in a different location.

Identification of the stabiliser is sometimes easy when the stabilising nucleus has a nuclear spin, resulting in the observation of characteristic hyperfine splitting in the spectrum. In such cases, the nuclear spin, and the natural abundance of the isotope with this spin may be determined from the spectrum, and compared with all the elements. There are usually only

[1]It should be noted that this book by Krasnobaev *et al.* 1988, written in Russian, is a very complete catalogue of epr centres in zircon. It has become apparent that many of the centres studied at Canterbury have been reported in this reference.

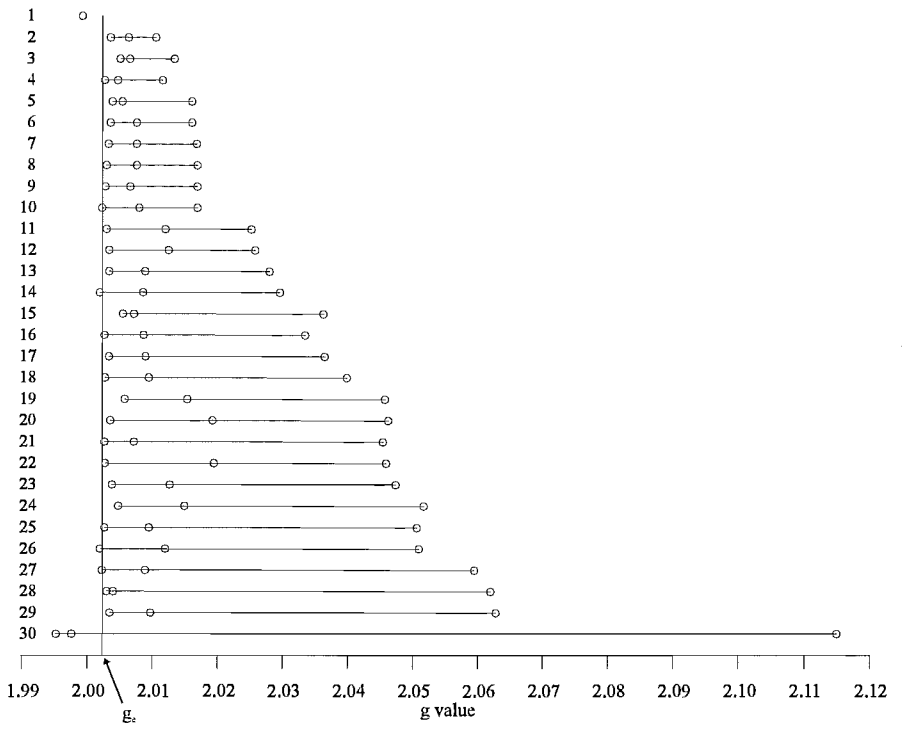

Figure 4-1: Principal g values of various oxygenic hole centres in zircon. **1** - SiO_4^{3-}/V(Zr) (C centre) [25], [26] **2** - SiO_4^{3-}(D centre) [21], **3** - SiO_4^{3-} (RT centre) [21], **4** - SiO_2^{3-} [63], **5** - SiO_2^{3-}/OH^- [63], **6** - SiO_4^{3-}/Y^{3+} [40], **7** - SiO_4^{3-}/Y^{3+} [64], **8** - $SiO_2^{3-}/2Y^{3+}$ [63], **9** - SiO_2^{3-}/Y^{3+} [63], **10** - $[SiO_3 - SiO_4]^{5-}$-$2Y^{3+}$ [20], **11** - SiO_4^{3-}/Y^{3+} [65], **12** - SiO_3^-/Y^{3+} [63], **13** - AlO_3^{2-} [63], **14** - SiO_4^{3-}/Y^{3+} [65], **15** - SiO_3^-/H^+ [63], **16** - $SiO_3^-/2H^+$ [63], **17** - SiO_3^-/V(Zr) [63], **18** - SiO_4^{3-}/OH^- [63], **19** - AsO_4^{2-} [63] **20** - $SiO_4^{3-}/2H^+$ [63], **21** - $SiO_4^{3-}/(H_2O + V(Zr))$ [63], **22** - $SiO_4^{3-}/(H_2O + V(Zr) + V(O))$ [63], **23** - $[BO_4]^0$ [36], **24** - $[AlO_4]^0$ [37], **25** - AlO_4^{4-} [63], **26** - AlO_4^{4-} [20], **27** - SiO_4^{3-}/Y^{3+} [63], **28** - SiO_4^{3-} [20], **29** - $[\mathbf{SiO_4/Y}]^0$ [38], **30** - $[\mathbf{SiO_4/M}]^n$ [38].

one or two possibilities, and the correct one can often be identified by fitting of the data. A number of hole centres with a +3 stabiliser have been identified in this way, such as Y^{3+} ($I = \frac{1}{2}$ 100 %), Al^{3+} ($I = \frac{5}{2}$ 100 %), and B^{3+} ($I = \frac{3}{2}$ 80 %, $I = 3$ 20 %)[2].

The prevalence of hole centres with +3 stabilisers can be explained by considering the charge balancing. When an electron is lost from an oxygen atom there is a net charge imbalance of +1, but if a nearby Zr^{4+} or Si^{4+} species has been substituted by a +3 charged species, there is

[2]The positions of these ions on the periodic table suggest that Sc^{3+} (100% $\frac{7}{2}$ nuclear spin) -compensated hole centres should also be formed easily. They may not have been observed because of a low abundance in nature. A scandium-doped synthetic crystal might produce such a centre.

a countering -1 charge imbalance making the overall centre neutral. It should be noted at this point that there are two conventions used in the naming of the hole centres in figure 4-1. All of the recent hole centres studied by the Canterbury group have been named with the charge given relative to the unperturbed SiO_4^{4-} or $ZrSiO_4$ unit, thus the +3-compensated centres which have overall charge neutrality are labelled with a zero charge, such as $[BO_4]^0$ [36] and $[SiO_4/Y]^0$ [38]. For a single hole centre $[MO_4]^n$ indicates Si^{4+} substitution by $M^{(3+n)+}$, and $[SiO_4/M]^n$ indicates Zr^{4+} substitution by $M^{(3+n)+3}$. Most of the centres reported by other authors have been labelled with the true formal oxidation number of each subunit, thus the $[BO_4]^0$ centre would be given BO_4^{4-} and $[SiO_4/Y]^0$ given as SiO_4^{3-}/Y^{3+}.

Figure 4-1 contains information for only one SiO_4^{4-}-based hole centre with a single stabilising impurity other than Y^{3+}, Al^{3+} or B^{3+}. It is labelled AsO_4^{2-} [63]. However, this centre may in fact be the $[BO_4]^0$ centre, as it has very similar g values, and boron and arsenic have the same major nuclear spin, so might easily have been misidentified. The compensator of the $[BO_4]^0$ centre was confidently identified as boron [36] by the observation of lines due to the lower abundance isotope, ^{10}B, and the observation of the centre in boron-doped crystals (99B and 99E of table 3.1). The ^{10}B lines are not visible in most orientations, so could easily be overlooked.

There are also a number of centres where no hyperfine splitting is observed, and it must be assumed that there is either a remote stabiliser, or one with either no nuclear spin, or only isotopes with a natural abundance too low to be observed. The number of candidates which fall into the latter category is fairly small, with carbon, sulphur, calcium, iron, nickel and zinc being the only nuclei other than some of the noble gases, oxygen and silicon consisting of isotopes with nuclear spin having a natural abundance of under 5%. The detectability limit of the hyperfine structure of the centre naturally depends on what signal-to-noise ratio may be obtained in the experiment. The 2.2 % abundant ^{57}Fe hyperfine was clearly visible in the $[FeO_4/H]^0$ spectrum in α-quartz shown in figure 6-14, but the main lines were relatively intense in comparison to many of the hole centres measured in zircon.

A stabiliser is assumed to be necessary for hole trapping, or any type of crystal defect which

[3]The $[SiO_4/M]^n$ label given to the centre described herein is not meant to imply zirconium substitution. In this case, the nature of any charge compensation is completely unknown.

makes the centre different from the unperturbed sites in the zircon structure. The hole would be expected to move around if identical sites were available to it in adjacent positions. If the hole were 'jumping' between adjacent oxygen sites at a rate of the order of the 'epr timescale' (the microwave frequency), it would be invisible to our epr experiments as the linewidth would be broadened beyond detection. At a much slower rate, different sites would be visible as separate spectra, and at a much faster rate, an averaged spectrum would be observable. Even if the rate were such that an epr signal could be observed, the hole might be expected to find its way quickly to a distorted site, and be trapped there. In a very pure crystal it might be possible, at very low temperatures, to observe a hole centre on a normal oxygen position with no associated impurities.

An alternative explanation for the number of hole centres observed which does not require many different compensators and compensator locations is the possible existence of atom vacancies associated with the centre. Many of the hole centres in figure 4-1, mostly from [63], are claimed to involve one or two oxygen vacancies. The authors' reasons for this assignment are not known, but it is implied that the centres may be roughly grouped according to their g anisotropy, and the most isotropic attributed to an SiO_2 unit (two oxygen vacancies), the next group to an SiO_3 unit (one oxygen vacancy), and the rest to an SiO_4 unit (no vacancies). The reasoning behind this may be that the anisotropy in the g values is related to the crystal-field splitting of the p-orbital energy levels for a single hole (see section 4.3). The presence of oxygen vacancies may have a significant effect on the crystalline electric field, and hence the anisotropy in the g values.

4.2 The $[SiO_4/Y]^0$ and $[SiO_4/M]^n$ centres

4.2.1 Experimental details

The $[SiO_4/Y]^0$ and $[SiO_4/M]^n$ centres have only been observed in the Ti^{4+}/Y^{3+}-doped crystals (growth L and R of table 3.1). In all experiments, the centres were generated by x-irradiation of the crystal at 77 K under liquid nitrogen, followed by cold transfer to the previously cooled Displex head. Epr measurements were carried out at *ca* 15 K.

Spectra were measured in the *bc* plane in 5° - 10° intervals over a 200° range, which was

sufficient to fully determine the parameter matrices by fitting the symmetry-related sites, as discussed in section 1.2.1. The *c*-axis orientation was confirmed by observation of the collapse of three symmetry-related sites of the Zr(α) centre [20] - [22] in an arbitrary orientation within the *bc* plane to one site with **B**$\|$**c**. Alignment of the synthetic crystal in which much previous work had been carried out in the Canterbury laboratory was achieved by observing the $[AlO_4]^0$ centre [37] in a similar fashion. The $[AlO_4]^0$ centre was preferred over the Zr(α) centre as it was more sensitive to alignment, but there was no $[AlO_4]^0$ spectrum in the new crystal. The *c*-axis orientation could still be located to within *ca* $\pm 4'$ using the Zr(α) centre.

The epr signals from the new centres were highly intense, which was unusual in comparison with other hole centres in zircon which had been measured in the Canterbury laboratory. However, they were completely removed after annealing to room temperature and remeasuring at 15 K, as are most of the hole centres which have been observed in zircon. The room-temperature (RT) centre [21] is one of the few hole centres which have been observed which is stable at room temperature, and can in fact be observed at room temperature.

4.2.2 Results

The *c*-axis spectrum of one of the identical growth-L/R (table 3.1) Ti^{4+}/Y^{3+}-doped crystals after x-irradiation at 77 K and cold transfer is shown in figure 4-2. There were a number of unidentified centres observed in these crystals, including the two hole centres, a titanium centre, and a centre simply labelled H, all of which are discussed in this thesis. The known centres RT [21], Z [25], [26], Zr(α) [20] - [22] and Zr(Ti^{3+}) [23], [24], [9] were also observed. In the *c*-axis orientation, the spectra from the two hole centres overlapped, but rotation away from *c* clearly showed that there were two centres. Figure 4-3 shows the stacked plot of spectra taken every 10° from **B**$\|$**c** to **B**$\|$**b**, and includes the spectra of all of the centres listed above.

The spectrum of one of the hole centres consisted of a pair of equal-intensity lines due to a nearby 100% abundance nucleus with nuclear spin $\frac{1}{2}$. The linewidth in the *b*-axis orientation was *ca* 0.05 mT. The other centre was a single intense line with a much larger linewidth of *ca* 0.2 mT in the *b*-axis orientation. The roadmap for the two centres in the *bc* plane is shown in figure 4-4, where the points correspond to experimental data, and the plotted lines are the line positions simulated from the fitted spin-Hamiltonian parameter matrices using EPR-NMR [28].

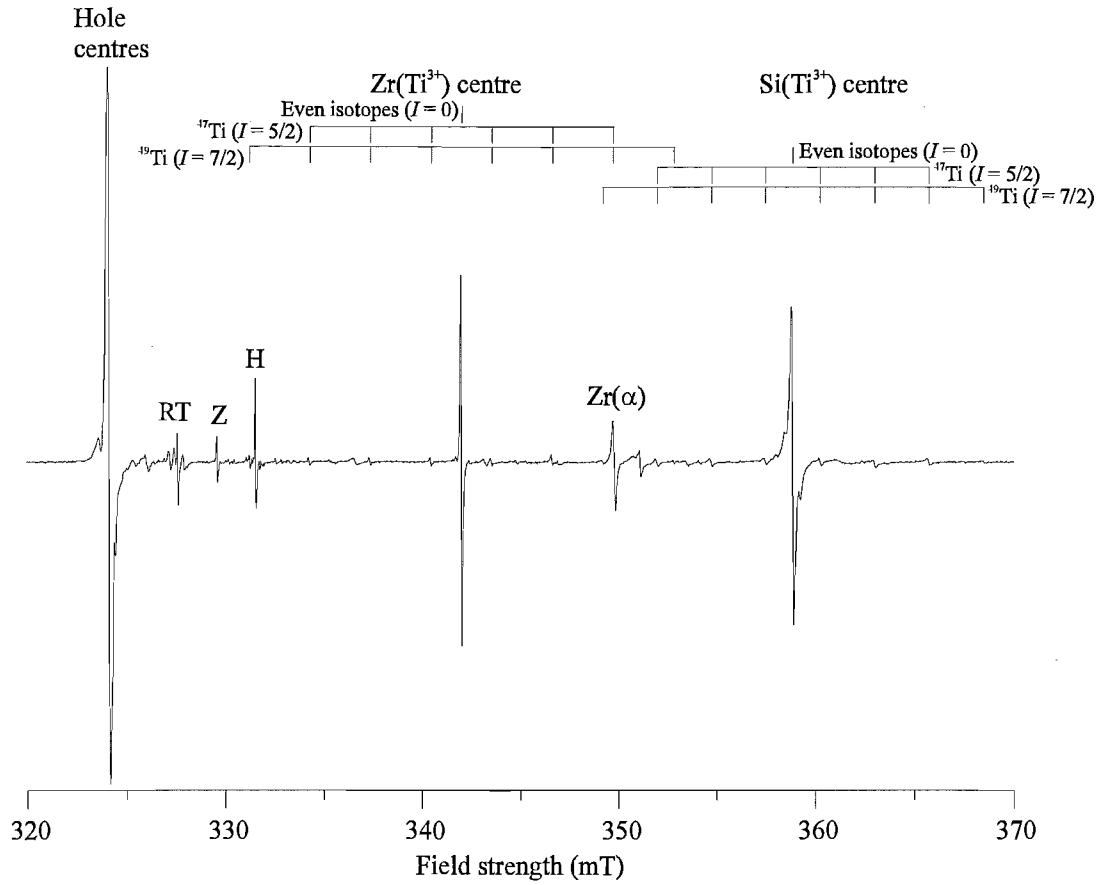

Figure 4-2: c-axis epr spectrum of titanium/yttrium-doped synthetic zircon crystal at *ca* 15 K after irradiation and cold transfer. Frequency = 9.22080 GHz.

For both of the centres, a single site was observed with the c axis parallel to the magnetic field, as must always be the case, while two sites were observed with the magnetic field parallel to the b axis. At all other orientations in the plane, three sites were observed. As described earlier, these site splittings are consistent with point-group symmetry m ([12] and table 1.2). Careful examination of figure 4-4 shows that the simulated line positions in the c-axis orientation are not entirely coincident, but they are too close to be experimentally resolved. The fitted positions differ by 0.05 mT, much less than the linewidth of the single-line centre.

Fitting of the experimental data for the two centres to spin-Hamiltonian parameter matrices

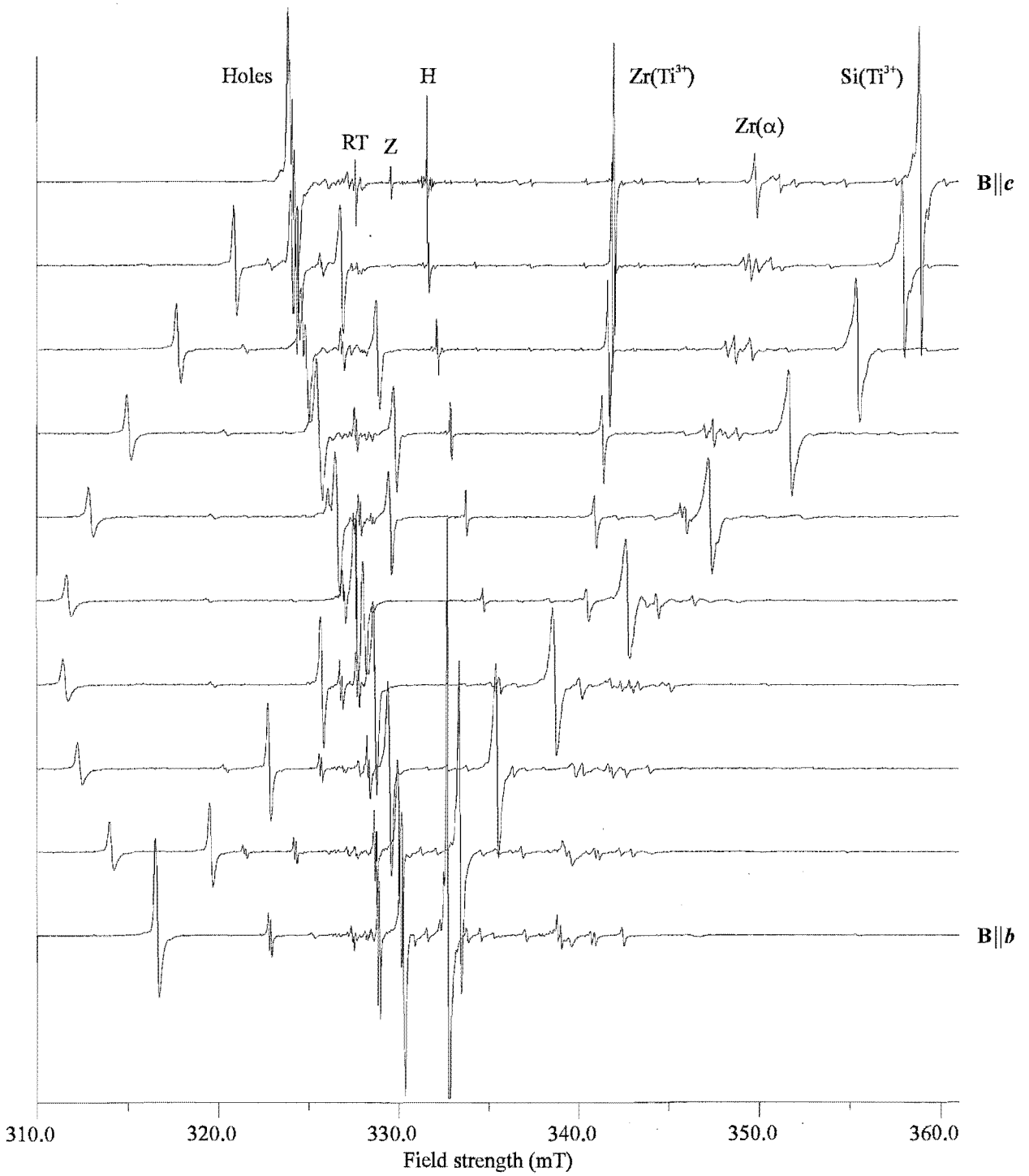

Figure 4-3: Stacked plot of Ti^{4+}/Y^{3+}-doped zircon crystal (growth L) epr spectra in the *bc* plane. Average frequency $\approx$ 9.2225 GHz.

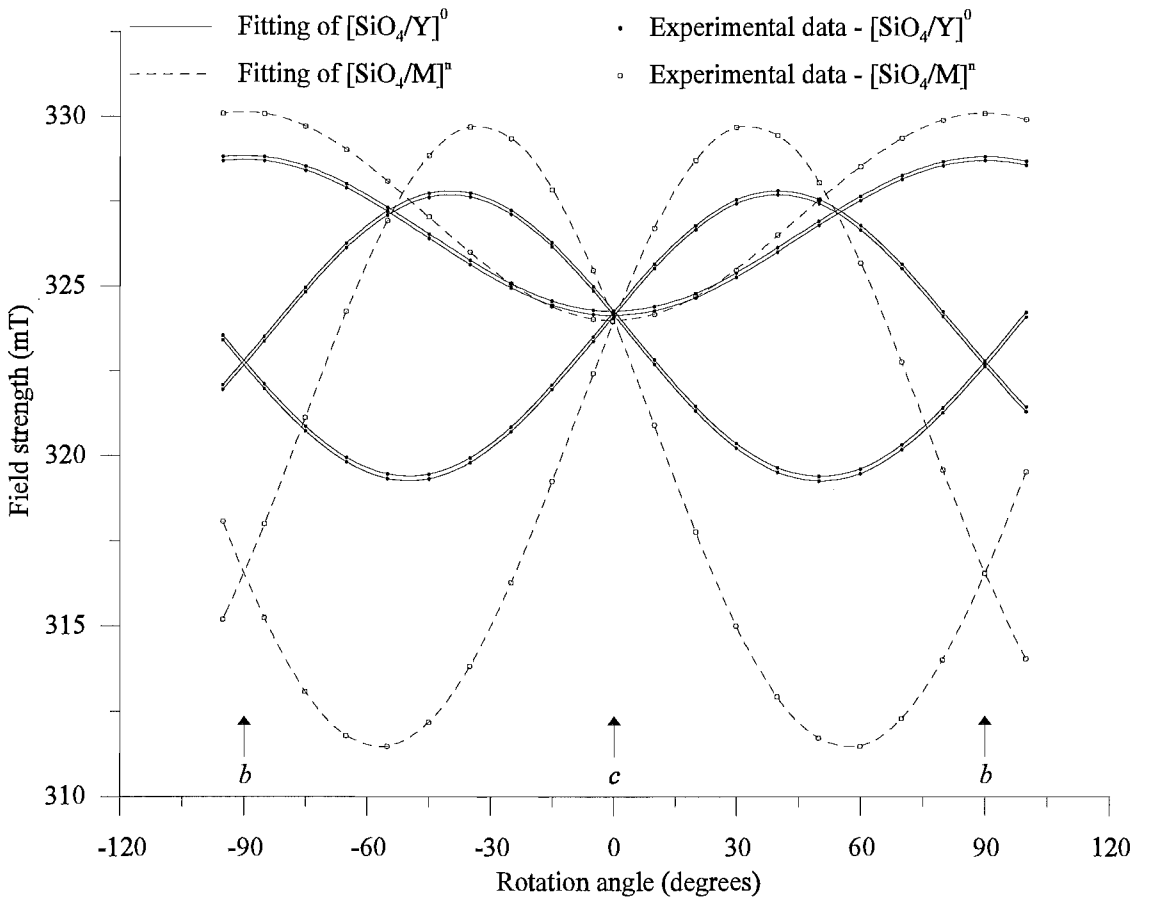

Figure 4-4: Angular dependence of $[SiO_4/M]^n$ and $[SiO_4/Y]^0$ hole-centre epr spectra in zircon in the *bc* plane; experimental data and simulation using fitted spin-Hamiltonian parameter matrices. Average frequency $\approx$ 9.2195 GHz.

was carried out using EPR-NMR with a spin Hamiltonian of the form:

$$\widehat{\mathcal{H}} = \beta_e \mathbf{B}.\mathbf{g}.\hat{\mathbf{S}} + \hat{\mathbf{S}}.\mathbf{A}.\hat{\mathbf{I}} - \beta_n \mathbf{B}.\mathbf{g}_n.\hat{\mathbf{I}} \tag{4.1}$$

Only the first term was required to fit the single-line centre due to the lack of visible hyperfine structure. For the two-line spectrum, $\mathbf{g}_n$ was set as the scalar matrix $-0.2748361\mathbf{U}$, where $\mathbf{U}$ is the 3×3 unit matrix, and -0.2748361 is the g_n value of ^{89}Y set internally by EPR-NMR. The hyperfine interaction resulting in the two-line spectrum for $[SiO_4/Y]^0$ was attributed to an yttrium nucleus on the basis that the crystal was doped with Y^{3+}, which has a 100%

abundant nuclear spin $\frac{1}{2}$ isotope. There are other such nuclei, such as phosphorus, which has been established as the compensator for the Zr(α) centre [21],[22], but as the $[SiO_4/Y]^0$ centre has only been observed in the Y^{3+} doped crystals, Y^{3+} is the most likely candidate. Y^{3+} also has the oxidation state discussed in the introduction to this chapter, which is required to give a charge-balanced hole centre. The principal g values of this centre (table 4.1 and figure 4-1) are also close enough to the SiO_4/Y^{3+} centre reported by Krasnobaev *et al.* [63], number 27 in figure 4-1, for them to be the same centre.

The data were first fitted with all parameter matrix elements allowed to vary. The results clearly showed that the xy and yz elements were equal to zero within error, as is expected for a centre with site symmetry m. The data were then refitted with these two elements set to zero, giving the results of table 4.1.

Table 4.1: Spin-Hamiltonian parameters for the $[SiO_4/M]^n$ and $[SiO_4/Y]^0$ centres in zircon at 15 K.

		Matrix **Y**		k	Principal value Y_k	Principal direction θ_k (deg)	Principal direction ϕ_k (deg)
$[SiO_4/M]^n$							
g	2.08026(1)	0	0.05356(1)	1	2.11497(2)	57.05(0)	0
		1.99527(1)	0	2	1.99762(2)	147.05(0)	0
			2.03233(1)	3	1.99527(1)	90	90
Data points: 84		Unit weighted: 72		$\sum$ weightings: 74.02		rmsd (mT): 0.0091	
$[SiO_4/Y]^0$							
g	2.040952(6)	0	0.026129(6)	1	2.062809(7)	50.09(0)	0
		2.003487(6)	0	2	2.009716(7)	140.09(0)	0
			2.031574(6)	3	2.003487(6)	90	90
$\mathbf{A}/g_e\beta_e$	0.139(2)	0	0.010(2)	1	0.144(2)	61.3(8)	0
(^{89}Y)(mT)		0.117(2)	0	2	0.120(2)	151.3(8)	0
			0.126(2)	3	0.117(2)	90	90
Data points: 168		Unit weighted: 124		$\sum$ weightings: 130.03		rmsd (mT): 0.0062	

4.2.3 Discussion

The g matrices for the two centres of table 4.1 have quite distinct principal values, but the principal directions are very similar. Indeed, this is the case for most of the recorded hole centres of site symmetry m as can be seen in figure 4-5 and table 4.2. The symmetry-related site chosen as site one has been selected as described in section 2.1, so that the g-matrix principal directions agree approximately with the crystal O-Zr and O-Si directions when the hole is placed on O_1 in figure 4-5.

As noted in section 2.1, the only symmetry requirement for the principal directions of an m-symmetry defect centre is that one of them is orthogonal to the mirror plane containing the oxygen hole, and hence the other two must have perpendicular orientations within the mirror plane. Figure 4-5 and table 4.2 show that, for the site selection made, most hole centres have one of the g-matrix principal directions in the mirror plane directed approximately towards Zr_1, and the other directed approximately towards Si_1. The correspondence of at least one of these directions to an atomic position cannot be considered significant as it is a consequence of the restriction of the directions to orthogonality within the mirror plane. The Zr_1-O_1-Si_1 angle of 99.1° means that the directions will either be close to both atoms or to neither. However, it can be seen from table 4.2 that one of the directions is always significantly closer to a bond direction. Four of the six centres listed have one g-matrix principal direction which lies within 2° of a bond direction, while the other two have one direction which differs by 4.0° and 5.2°, respectively. The agreement of the second direction in the mirror plane with a bond direction ranges from 7.5° to 21.6°.

It is strikingly obvious from figure 4-5 that the D-centre g-matrix principal directions do not fit into the pattern followed by the other five centres. The best agreement between a principal direction and bond direction for this centre is found for the O_1 - Zr_0 direction (0.6°), the zirconium atom which is short-bonded to the oxygen hole. This clear distinction suggests that the D centre is the only one of these hole centres which has a compensator (or vacancy) located in the short-bonded zirconium position, while the others are all associated with impurities in the silicon or long-bonded zirconium positions.

Table 4.2 also shows that the A-matrix principal directions can be correlated with bond directions. The directions for the A matrices have been taken from Zr_1 and Si_1 of figure 4-5.

Table 4.2: Comparison of g- and A-matrix principal directions with directions in zircon for six hole centres.

Centre	Matrix	principal value	principal direction θ	ϕ	direction to:	θ	ϕ	deviation
$[SiO_4/M]^n$	g	2.11497(2)	57.05(0)	0	Si($\frac{1}{2}$, 0, $\frac{1}{4}$)[a]	48.5	0	8.6
		1.99762(2)	147.05(0)	0	Zr($\frac{1}{2}$, 0, -$\frac{1}{4}$)	147.6	0	0.5
		1.99527(1)	90	90				
$[SiO_4/Y]^0$	g	2.062809(7)	50.09(0)	0	Si($\frac{1}{2}$, 0, $\frac{1}{4}$)	48.5	0	1.6
		2.009716(7)	140.09(0)	0	Zr($\frac{1}{2}$, 0, -$\frac{1}{4}$)	147.6	0	7.5
		2.003487(6)	90	90				
	A	0.144(2)	118.7(8)	180	O(0.32, 0, 0.07)[b]	131.5	180	12.8
		0.120(2)	28.7(8)	180	O(0.32, 0, 0.07)[c]	32.4	180	3.7
		0.117(2)	90	90				
$[BO_4]^0$	g	2.047430(2)	58.04(0)	0	Si($\frac{1}{2}$, 0, $\frac{1}{4}$)	48.5	0	9.5
		2.012714(2)	148.04(0)	0	Zr($\frac{1}{2}$, 0, -$\frac{1}{4}$)	147.6	0	0.4
		2.003859(2)	90	90				
	A	0.5193(2)	38.9(1)	180	O(0.32, 0, 0.07)[c]	32.4	180	6.5
		0.4884(3)	90	90				
		0.1904(3)	128.9(1)	180	O(0.32, 0, 0.07)[b]	131.5	180	2.6
$[AlO_4]^0$	g	2.05173(2)	62.78(2)	0	Si($\frac{1}{2}$, 0, $\frac{1}{4}$)	48.5	0	14.3
		2.01498(2)	152.75(2)	0	Zr($\frac{1}{2}$, 0, -$\frac{1}{4}$)	147.6	0	5.2
		2.00481(2)	90	90				
	A	-0.6735(19)	137.0(6)	180	O(0.32, 0, 0.07)[b]	131.5	180	5.5
		-0.8001(20)	47.0(6)	180	O(0.32, 0, 0.07)[c]	32.4	180	14.6
		-0.8198(17)	90	90				
D	g	2.01056(1)	169.2(2)	0	Zr($\frac{1}{2}$, 0, -$\frac{1}{4}$)	147.6	0	21.6
		2.00634(1)	79.2(2)	0	Si($\frac{1}{2}$, 0, $\frac{1}{4}$)	48.5	0	30.7
			(100.8)	(180)	Zr(0, 0, 0)	101.4	180	0.6
		2.00360(1)	90	90				
RT	g	2.01340(2)	151.6(1)	0	Zr($\frac{1}{2}$, 0, -$\frac{1}{4}$)	147.6	0	4.0
		2.00656(2)	61.6(1)	0	Si($\frac{1}{2}$, 0, $\frac{1}{4}$)	48.5	0	13.1
		2.00509(1)	90	90				

[a] All g-matrix directions taken from O(0.32, 0, 0.07) (O_1)
[b] Direction taken from Si($\frac{1}{2}$, 0, $\frac{1}{4}$) (Si_1)
[c] Direction taken from Zr($\frac{1}{2}$, 0, -$\frac{1}{4}$) (Zr_1)

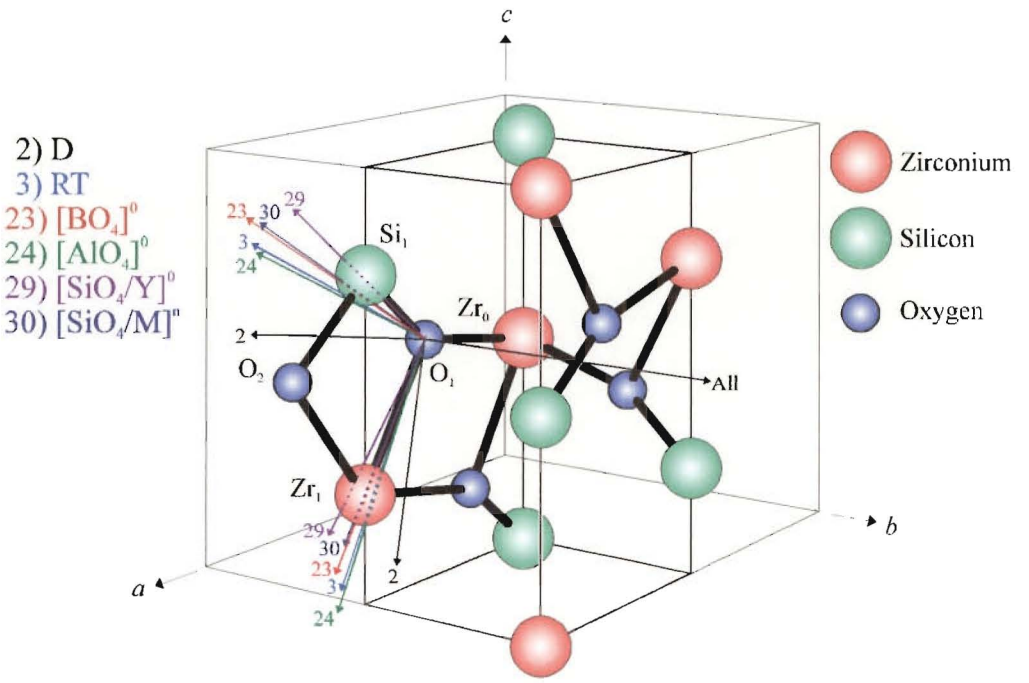

Figure 4-5: Portion of the zircon unit cell showing the g-matrix principal directions of six selected hole centres including the $[SiO_4/Y]^0$ and $[SiO_4/M]^n$ centres discussed in this thesis.

The origin which gives the closest agreement of one of the principal directions to the oxygen atom O_1 is found to be significant, as described below. This is completely equivalent to placing the origin on the oxygen atom and searching for the best agreement with the O-Zr and O-Si directions.

It is generally found that the atomic position which corresponds best to a principal direction is the one which is considered the most likely position of the stabiliser. In the case of the proposed $[SiO_4/Y]^0$ centre, the Y^{3+} stabiliser would seem more likely to occupy a Zr^{4+} site than an Si^{4+} site when the ionic radii are considered. While the bonding in zircon is part covalent, the ionic radii still give an indication of the size factors involved. The ionic radii of Zr^{4+}, Si^{4+} and Y^{3+} are 0.79 Å, 0.42 Å and 0.89 Å respectively [66]. Yttrium is also next to zirconium on the periodic table, and is thus chemically more similar to zirconium than silicon. As shown by table 4.2, the deviation between the two A-matrix principal directions in the mirror plane and the Zr-O and Si-O directions are 3.7° and 12.8° respectively, considerably closer for the zirconium position. This would appear to confirm the identity of the centre as an

oxygen hole with a nearby Y^{3+} ion substituting for a long-bonded zirconium atom. Similarly, the hyperfine matrices for the $[BO_4]^0$ and $[AlO_4]^0$ centres indicate that the stabiliser is located in a silicon substitutional site, as would be expected for Al^{3+} and B^{3+} by similar arguments.

It is interesting to note that the three hole centres for which both g and A matrices are determined share the property that the best agreement of one of the g-matrix principal directions to an atomic position is towards the atom which is thought not to be occupied by the compensator. This may be merely a coincidence, as there is no obvious reason why this should be true. It would be useful to see if this trend was followed by more hole centres. This pattern would place the unknown compensator of the $[SiO_4/M]^n$ centre in the neighbouring silicon site.

The problem with this model is that most species which might substitute for a nearby silicon (or zirconium) atom would have a visible hyperfine structure. The most obvious possible explanations for the observed lack of hyperfine are that the ion responsible has only very low abundance nuclear-spin isotopes or it is well removed from the site of spin density, so that any hyperfine interaction is small and possibly unresolved. The ions which fit into the first category were listed earlier in the chapter, but none are promising candidates, due to chemical dissimilarity with the ions they must replace, and the requirement that they have no electronic spin. The second possibility is more reasonable in the case of the $[SiO_4/M]^n$ centre, as the considerable linewidth could easily hide a small hyperfine interaction. It is possible that it is in fact another Y^{3+}-compensated centre, as the magnitude of the hyperfine splitting of the $[SiO_4/Y]^0$ centre is only *ca* 0.14 mT at its maximum, and could quite conceivably be smaller in the case of the $[SiO_4/M]^n$ centre. If the hyperfine splitting were considerably less than the linewidth, no splitting would be visible.

4.3 Crystal-field spin-orbit-coupling analysis

Given the wide range of g values observed for the many hole centres in figure 4-6, it was considered a useful exercise to carry out a crystal-field spin-orbit-coupling analysis of the g values. The observed g values were fitted to splittings in the crystal-field orbital energy levels as perturbed by the spin-orbit coupling. All but one of the centres chosen had been fitted in

the Canterbury laboratory and covered the complete range of g anisotropies[4].

Similar calculations were used to those outlined in Vannotti and Morton (for isoelectronic S^-) [67], and by Golding (1969) [68] for a single d electron. Stapelbroek *et al.* [69] carry out a related calculation for O^- based on a point-charge model. The electron hole is considered to be localised on an oxygen atom, in one of the outer-shell p orbitals. The oxygen atom before hole formation is treated as an O^{2-} ion with electronic configuration $1s^2 2s^2 2p^6$ and so the oxygen hole is an O^- ion with electronic configuration $1s^2 2s^2 2p^5$. The single hole may be treated like a single electron with a change in sign of the spin-orbit-coupling constant. The energy levels which are generated then represent placement of the hole in the various orbitals, or equivalently, a particular configuration of the five electrons.

Under m point-group symmetry the p_x and p_y orbitals independently transform as bases for the A' irreducible representation, and the p_z orbital transforms as a basis for the A'' representation. The spin-orbit-coupling interaction, given by equation 1.15, mixes the states. The matrix elements of the spin-orbit-coupling interaction yield a 6×6 crystal-field spin-orbit-coupling matrix which block diagonalises into two 3×3 matrices. The ground-state wavefunctions were generated by both direct diagonalisation of the matrix, and by a perturbation treatment as outlined by Golding [68] for a calculation of a single-d-electron system. Either treatment gives a Kramers doublet, two spin-degenerate wavefunctions, whose degeneracy is lifted by application of a magnetic field.

The magnetic-field interaction may be treated independently in the x, y, z directions, and is given by equation 1.18 with one electron scalar (x, y, z) operators replacing $\hat{\mathbf{L}}$ and $\hat{\mathbf{S}}$. The treatment of each interaction with the ground-state Kramers doublet, assuming the magnetic mixing of excited states into the ground state is negligible [68], gives three 2×2 matrices. The splittings between the energy-level eigenvalues of these matrices corresponds to the epr transition at the resonance frequency, given by equation 1.6. By equating the two expressions, g_x, g_y and g_z may be calculated for any given set of crystal-field splittings. A computer programme Pdorbit has been written [70], one function of which is to carry out these calculations and vary the crystal-field splittings until the calculated g's matched the experimental.

[4]Not including the completely isotropic C centre, which would require no mixing of the ground orbital state with excited-state wavefunctions, so no crystal-field splittings could be calculated.

The setup of the crystal-field spin-orbit-coupling matrix and calculation of the perturbation equations are carried out as follows. The p-orbital wavefunctions are first written in terms of the eigenvalues of the l_z operator [68]:

$$p_z \sim |0\rangle \tag{4.2a}$$

$$p_x \sim \frac{1}{\sqrt{2}}(-|+1\rangle + |-1\rangle) \tag{4.2b}$$

$$p_y \sim \frac{i}{\sqrt{2}}(|+1\rangle + |-1\rangle) \tag{4.2c}$$

The spin-orbit-coupling interaction is rewritten in terms of step-up and step-down operators to allow calculation of the spin-orbit-coupling matrix elements between the states given by equations 4.2:

$$\widehat{\mathcal{H}}_{SO} = \zeta[s_z l_z + \tfrac{1}{2}(l_- s_+ + l_+ s_-)] \tag{4.3}$$

where the step-up and step-down operators are defined generally as:

$$j_\pm = j_x \pm i j_y \tag{4.4a}$$

The calculated 6×6 crystal-field spin-orbit-coupling matrix is given below.

$$\begin{array}{c|cccccc}
 & \left|A''^{+}\right\rangle & \left|A'^{-}_{x}\right\rangle & \left|A'^{-}_{y}\right\rangle & \left|A'^{+}_{y}\right\rangle & \left|A'^{+}_{x}\right\rangle & \left|A''^{-}\right\rangle \\
\left\langle A''^{+}\right| & \mathrm{E}_{A''} & \frac{-\zeta}{2} & \frac{i\zeta}{2} & & & \\
\left\langle A'^{-}_{x}\right| & \frac{-\zeta}{2} & \mathrm{E}_{A'_x} & \frac{i\zeta}{2} & & & \\
\left\langle A'^{-}_{y}\right| & \frac{-i\zeta}{2} & \frac{-i\zeta}{2} & \mathrm{E}_{A'_y} & & & \\
\left\langle A'^{+}_{y}\right| & & & & \mathrm{E}_{A'_y} & \frac{i\zeta}{2} & \frac{-i\zeta}{2} \\
\left\langle A'^{+}_{x}\right| & & & & \frac{-i\zeta}{2} & \mathrm{E}_{A'_x} & \frac{\zeta}{2} \\
\left\langle A''^{-}\right| & & & & \frac{i\zeta}{2} & \frac{\zeta}{2} & \mathrm{E}_{A''}
\end{array} \tag{4.5}$$

The perturbation eigenfunctions to second order are calculated from equation 4.6 [68]:

$$\phi_i = \left[1 - \tfrac{1}{2}\sum_j{}' \frac{H'_{ji}H'_{ij}}{(E_i^0 - E_j^0)^2}\right]\phi_i^0 + \sum_j{}' \left[\frac{H'_{ji}}{E_i^0 - E_j^0} + \sum_k{}' \frac{H'_{ki}H'_{jk}}{(E_i^0 - E_j^0)(E_i^0 - E_k^0)} - \frac{H'_{ii}H'_{ji}}{(E_i^0 - E_j^0)^2}\right]\phi_j^0 \tag{4.6}$$

where the dashed summations refer to a sum over $j \neq i$, and $k \neq j \neq i$, and the H' refers to the matrix element of the perturbation operator, here the spin-orbit-coupling operator. ϕ_i is the perturbed wavefunction to be calculated, ϕ_i^0 is the unperturbed wavefunction, and the ϕ_j^0's are the other unperturbed wavefunctions (here the other p orbitals) mixed in by the perturbation. Taking p_z (A'') as the ground state gives the second-order wavefunctions (Kramers doublet):

$$|+\rangle = N\left|A''^{+}\right\rangle + \left(\frac{\zeta}{2\Delta_1} + \frac{\zeta^2}{4\Delta_1\Delta_2}\right)\left|A_x'^{-}\right\rangle + i\left(\frac{\zeta}{2\Delta_2} + \frac{\zeta^2}{4\Delta_1\Delta_2}\right)\left|A_y'^{-}\right\rangle \quad (4.7a)$$

$$|-\rangle = N\left|A''^{-}\right\rangle - \left(\frac{\zeta}{2\Delta_1} + \frac{\zeta^2}{4\Delta_1\Delta_2}\right)\left|A_x'^{+}\right\rangle + i\left(\frac{\zeta}{2\Delta_2} + \frac{\zeta^2}{4\Delta_1\Delta_2}\right)\left|A_y'^{+}\right\rangle \quad (4.7b)$$

$$N = \left(1 - \frac{\zeta^2}{4\Delta_1^2} - \frac{\zeta^2}{4\Delta_2^2}\right)^{\frac{1}{2}} \quad (4.7c)$$

where $\Delta_1 = E_{A_x'} - E_{A''}$ and $\Delta_2 = E_{A_y'} - E_{A''}$. Calculation of the magnetic-field interaction in the z direction between these states then gives the following results:

$$\langle +|\,\beta(l_z + g_e s_z)B\,|+\rangle = \beta B\left[\frac{g_e}{2}N^2 - \frac{g_e}{8}\left(\frac{\zeta^2}{\Delta_1^2}+\frac{\zeta^2}{\Delta_2^2}\right) + \frac{\zeta^2}{2\Delta_1\Delta_2} + \frac{(2-g_e)}{8}\left(\frac{\zeta^3}{\Delta_1^2\Delta_2}+\frac{\zeta^3}{\Delta_1\Delta_2^2}\right) + \frac{(2-g_e)}{16}\frac{\zeta^4}{\Delta_1^2\Delta_2^2}\right] \quad (4.8a)$$

$$\langle -|\,\beta(l_z + g_e s_z)B\,|-\rangle = -\langle +|\,\beta(l_z + g_e s_z)B\,|+\rangle \quad (4.8b)$$

$$\langle +|\,\beta(l_z + g_e s_z)B\,|-\rangle = 0 \quad (4.8c)$$

$$\langle -|\,\beta(l_z + g_e s_z)B\,|+\rangle = 0 \quad (4.8d)$$

therefore the energy eigenvalues of the Kramers doublet under a magnetic field are given by $\pm\langle +|\,\beta(l_z + g_e s_z)B\,|+\rangle$, and ΔE is given by $2\langle +|\,\beta(l_z + g_e s_z)B\,|+\rangle$. Comparison of this with equation 1.6 gives an expression for the experimental g value in the z direction, g_z:

$$g_z = g_e\left[N^2 - \frac{1}{4}\left(\frac{\zeta^2}{\Delta_1^2}+\frac{\zeta^2}{\Delta_2^2}\right) + \frac{\zeta^2}{g_e\Delta_1\Delta_2} + \frac{(2-g_e)}{4g_e}\left(\frac{\zeta^3}{\Delta_1^2\Delta_2}+\frac{\zeta^3}{\Delta_1\Delta_2^2}\right) + \frac{(2-g_e)}{8g_e}\frac{\zeta^4}{\Delta_1^2\Delta_2^2}\right] \quad (4.9)$$

where the terms are grouped in order of their significance, by the sum of the powers of the Δ values in the denominator. The first four terms in equation 4.9 may be found in Claridge *et al.* [38], while the cubic and quartic terms are given here only. It should be noted that the cubic and quartic terms which could arise from consideration of higher order terms in the ground

state wavefunctions 4.7a and b have not been considered. However, the terms given above, and those for the other g values calculated below, have been added to the programme Pdorbit [70]. They produce perturbation g values in better agreement with the direct diagonalisation values, for the same set of deltas.

Calculation of the magnetic-field interaction in the x and y directions yields 2×2 matrices with the diagonal elements equal to zero and equal values on the off-diagonals. The off-diagonals of the magnetic-field interaction in the y direction are of opposite sign as they are multiplied by i and must be complex conjugates for a Hermitian matrix. The eigenvalues of these matrices are then $\pm\langle+||-\rangle$, and the splitting in the Kramers doublet $|2\langle+||-\rangle|$. The perturbation expressions for g_x and g_y are then given by equations 4.10:

$$g_x = g_e\left[N^2 - \tfrac{2N}{g_e}\left(\tfrac{\zeta}{\Delta_2} + \tfrac{\zeta^2}{2\Delta_1\Delta_2}\right) + \tfrac{1}{4}\left(\tfrac{\zeta^2}{\Delta_2^2} - \tfrac{\zeta^2}{\Delta_1^2}\right) + \tfrac{1}{4}\left(\tfrac{\zeta^3}{\Delta_1\Delta_2^2} - \tfrac{\zeta^3}{\Delta_1^2\Delta_2}\right)\right] \quad (4.10a)$$

$$g_y = g_e\left[N^2 - \tfrac{2N}{g_e}\left(\tfrac{\zeta}{\Delta_1} + \tfrac{\zeta^2}{2\Delta_1\Delta_2}\right) + \tfrac{1}{4}\left(\tfrac{\zeta^2}{\Delta_1^2} - \tfrac{\zeta^2}{\Delta_2^2}\right) + \tfrac{1}{4}\left(\tfrac{\zeta^3}{\Delta_1^2\Delta_2} - \tfrac{\zeta^3}{\Delta_1\Delta_2^2}\right)\right] \quad (4.10b)$$

Equations 4.10a and 4.10b are completely equivalent expressions which are interchanged by swapping all of the deltas: $\Delta_1 \longleftrightarrow \Delta_2$. Thus if one carries out a fitting of the experimental g values choosing $g_x > g_y$, then $\Delta_1 > \Delta_2$, and the configuration which places the hole in the p_x orbital is higher in energy than the configuration with the hole in the p_y orbital. If g_x and g_y are chosen the other way around, then the exact opposite result will be obtained. There is no reason to prefer one selection over the other from the epr experiment.

Equivalent expressions are also obtained when p_x or p_y is taken as the ground state. The only change is that the equation for the g value corresponding to the new ground state (i.e., g_x or g_y for a p_x or p_y ground state, respectively) is equivalent to the expression for the old ground-state g value. Thus the terms up to second order for a p_x ground state are:

$$g_x = g_e\left[N^2 + \frac{\zeta^2}{g_e\delta_1\delta_2} - \frac{\zeta^2}{4\delta_1^2} - \frac{\zeta^2}{4\delta_2^2}\right] \quad (4.11a)$$

$$g_y = g_e\left[N^2 - \frac{2N\zeta}{g_e\delta_1} - \frac{N\zeta^2}{g_e\delta_1\delta_2} + \frac{\zeta^2}{4\delta_1^2} - \frac{\zeta^2}{4\delta_2^2}\right] \quad (4.11b)$$

$$g_z = g_e\left[N^2 - \frac{2N\zeta}{g_e\delta_2} - \frac{N\zeta^2}{g_e\delta_1\delta_2} - \frac{\zeta^2}{4\delta_1^2} + \frac{\zeta^2}{4\delta_2^2}\right] \quad (4.11c)$$

The new delta values are now defined as $\delta_1 = E_{A''} - E_{A'_x}$ and $\delta_2 = E_{A'_y} - E_{A'_x}$, with N given

by equation 4.7c with the new deltas.

While the selection of g_x and g_y is arbitrary, the ground-state g value must be chosen as the smallest-magnitude g value, when all g values are greater than g_e. This can be seen by examination of the most important terms in the perturbation expressions 4.9 and 4.10a. The g_z expression (or whichever is the ground state) contains positive and negative contributions to N^2 which are second order with respect to the powers of the deltas in the denominator. The g_z value is thus always close to g_e, but may be higher or lower. The g_x expression contains a larger, positive first-order term, and thus is always greater than g_e according to this analysis[5], and may be significantly greater. This also demonstrates the property of the hole centres noted earlier in the thesis that the g values are always close to, or above g_e, with one value very close to it. The analysis of a single p electron, rather than a single hole, would be identical other than a change in the sign of ζ, thus the g values would be less than g_e. The $[SiO_4/M]^n$ centre is most unusual, in that it has two g values significantly lower than g_e, which cannot be accounted for in the above model. This will be further discussed below.

The perturbation equations were not used in the minimisation of the deviation between experimental and calculated g values, but rather a direct diagonalisation of the crystal-field spin-orbit-coupling matrix (4.5) to give 'exact' wavefunctions for the Kramers doublets. The discussion which was given above based on the perturbation equations is still completely valid, however. The agreement between the perturbation-calculated g values and the direct-diagonalisation calculated g values improves as the crystal-field splitting of the orbital energy levels gets larger, and the magnitude of the spin-orbit-coupling perturbation comparitively less, as seen later in tables 4.3 and 4.4.

ζ was given a value of -1 so that the crystal-field spin-orbit-coupling matrix was effectively divided by ζ, with the sign taken into account, giving positive energy eigenvalues in terms of the unitless $-\frac{\Delta}{\zeta}$, rather than absolute values requiring an explicit value of ζ. The ground-state energy $E_{A''}$ was set to zero, and the other values on the diagonal were given initial values in an appropriate order of magnitude. The matrix was diagonalised, to obtain new crystal-field spin-orbit-coupling eigenvalues and the coefficients of the new wavefunctions. The new

[5]It is mathematically possible for this g value to be less than g_e when the negative second-order terms are larger than the positive first- and second-order terms. However, this requires one of the crystal-field splittings to be extremely large.

wavefunctions were dominated by the appropriate unperturbed wavefunction, but there was a slight mixing with the two upper unperturbed states (see equations 4.13). The g values were calculated using the exact wavefunctions for the ground-state doublet, and the process repeated automatically with adjusted delta values until the rmsd between observed and calculated g values was minimised.

It was found that the variation of the ground-state g values from g_e in the centres fitted was too large to get an exact fit using this approximate theory. An exact fit, where the calculated values agreed precisely with the experimental numbers entered, was obtainable only when a factor α was introduced into the magnetic-field-interaction expression (equation 1.18):

$$\widehat{\mathcal{H}}_Z = \beta B_i(\hat{l}_i + \alpha g_e \hat{s}_i) \tag{4.12}$$

The factor effectively changes the value of g_e slightly, taking into account effects in the real system which allow the ground-state g value to vary more from g_e than the above theory allows. It has not been attempted to rationalise the factor in terms of any particular way in which the above theory is inadequate to fit the results perfectly, but the effect of covalency is one obvious possibility. The answers which are obtained using Pdorbit when α is set to unity are not very different from the exact fits, and the variation of α from unity in these exact fits is very small.

The $[SiO_4/M]^n$ centre could also be fitted using the factor described above, but one is left with the problem of which g value to choose as the ground-state g value. The other centres all have the same g value smallest and closest to g_e. However, the $[SiO_4/M]^n$ centre has one g value which is closest to g_e, and another which is smaller. In all other cases, the ground-state g value is associated with the principal direction perpendicular to the mirror plane of the hole centre, implying that the ground-state orbital is a non-bonding orbital. If one makes the same assumption for the $[SiO_4/M]^n$ centre, then the smallest g value should be chosen as the ground-state g value. This was also the only way in which the g values could be successfully fitted by Pdorbit. As an example of the general form of the wavefunctions of the various hole centres fitted, the results for the $[SiO_4/Y]^0$ and $[SiO_4/M]^n$ centres are given below:

$$\Psi_{\pm}([SiO_4/Y]^0) = 0.99989\left|A''\right\rangle \mp 0.00158\left|A'_x\right\rangle - i0.01464\left|A'_y\right\rangle \quad \alpha = 1.000571 \tag{4.13a}$$

Table 4.3: Table of fitted crystal-field splittings for 7 selected hole centres in zircon.

Centre	Principal g values	$\frac{-\Delta_1}{\zeta}$	$\Delta_1(\mathrm{cm}^{-1})$*	$\frac{-\Delta_2}{\zeta}$	$\Delta_2(\mathrm{cm}^{-1})$*
D [21]	2.01056, 2.00634, 2.00360	727.9	98260	287.5	38810
RT [21]	2.01340, 2.00656, 2.00509	1355	183000	241.0	32530
SiO_4/Y [65]	2.0296, 2.0086, 2.0020	299.4	40410	72.71	9816
$[BO_4]^0$ [36]	2.047430, 2.012714, 2.003859	221.5	29900	46.18	6234
$[AlO_4]^0$ [37]	2.05174, 2.01498, 2.00481	192.6	26000	42.88	5789
$[SiO_4/Y]^0$ [38]	2.062809, 2.009716, 2.003487	312.2	42140	34.09	4602
$[SiO_4/M]^n$ [38]	2.11497, 1.99762, 1.99527	802.0	108300	17.14	2315

* calculated using $\zeta = -135$ cm^{-1}, the free ion value for O^- derived from an isoelectronic sequence of ions [71]

$$\Psi_{\pm}([SiO_4/M]^n) = 0.99958\left|A''\right\rangle \mp 0.00061\left|A'_x\right\rangle - i0.02911\left|A'_y\right\rangle \quad \alpha = 0.998136 \quad (4.13b)$$

While the mixing between the states due to the spin-orbit coupling is small, it is enough to fit the observed g anisotropy exactly in each case, as the result of a pure A'' wavefunction would be $g_x = g_y = g_z = \alpha g_e$. The α factor is also not required to deviate significantly from 1, although the deviation is relatively large for the $[SiO_4/M]^n$ centre. With α fixed at 1.0, the $[SiO_4/M]^n$ centre fitting gives a very large Δ_1 of 1.73×10^6 cm^{-1}, using $\zeta = -135$ cm^{-1}, the free-ion value for O^- derived from an isoelectronic sequence of ions [71]. This is the expected result, given the mathematical requirement for a non ground-state g value less than g_e noted earlier.

It is not clear what, if any, significance may be attached to the α value being greater than or less than one. The final results for the fitted crystal-field splittings are given in table 4.3. As a check that the calculations were giving sensible answers, the g values were also calculated from the derived orbital splittings using the perturbation equations 4.9 and 4.10 (and including the α factor). These values, and the rmsd between the calculated and experimental g values, are given in table 4.4.

The centres in table 4.3 are ordered by increasing range in their principal g values, which is observed to correspond to a decreasing value for Δ_2. The range in principal g values is equivalent to g_x - g_z (Δg_{xz}) which may be calculated from equations 4.10a and 4.9. If all higher-order

Table 4.4: Perturbation-calculated g values and rmsd between calculated and experimental.

Centre	Perturbation g values	RMSD
D [21]	2.010560, 2.006340, 2.003600	2.7×10^{-8}
RT [21]	2.013400, 2.006560, 2.005090	2.9×10^{-8}
SiO_4/Y [65]	2.029602, 2.008600, 2.002000	9.6×10^{-7}
$[BO_4]^0$ [36]	2.047436, 2.012713, 2.003858	3.8×10^{-6}
$[AlO_4]^0$ [37]	2.051748, 2.014979, 2.004808	4.7×10^{-6}
$[SiO_4/Y]^0$ [38]	2.062826, 2.009715, 2.003485	1.0×10^{-5}
$[SiO_4/M]^n$ [38]	2.115116, 1.997610, 1.995259	8.5×10^{-5}

terms are ignored and the normalisation constant N set to 1, the resulting equation 4.14a shows that Δg_{xz} is inversely proportional to Δ_2. A similar expression involving Δ_1 may be calculated for g_y - g_z, given in equation 4.14b.

$$g_x - g_z \approx \frac{-2\zeta}{\Delta_2} \tag{4.14a}$$

$$g_y - g_z \approx \frac{-2\zeta}{\Delta_1} \tag{4.14b}$$

Based on these equations, a plot was made of $\frac{1}{\Delta g_{xz}}$ and Δg_{xz} against $\frac{-\Delta_2}{\zeta}$ and $\frac{1}{\Delta g_{yz}}$ and Δg_{yz} against $\frac{-\Delta_1}{\zeta}$, shown in figure 4-6. The points agree very well with the plotted functions y = 2x and y = $\frac{2}{x}$. The inverse proportionality relationship is not surprising, as deviations of the principal g values from g_e requires mixing of the other states by spin-orbit coupling. The magnitude of the mixing will be greater when the pure p-orbital energy levels are closer together, so small delta values will correspond to large Δgs, and vice versa. While this approach is not rigorous, and does not include any s-orbital energies or covalency effects, these results show that the epr experiment may give an immediate estimate of the crystal-field splittings, with no requirement of extensive calculations. An experimental investigation of the crystal-field splittings for some of the investigated hole centres using optical techniques would be a good test of the validity of this model. This may prove very difficult however, as preliminary experiments carried out in Paderborn, Germany failed to produce any absorptions of appreciable intensity

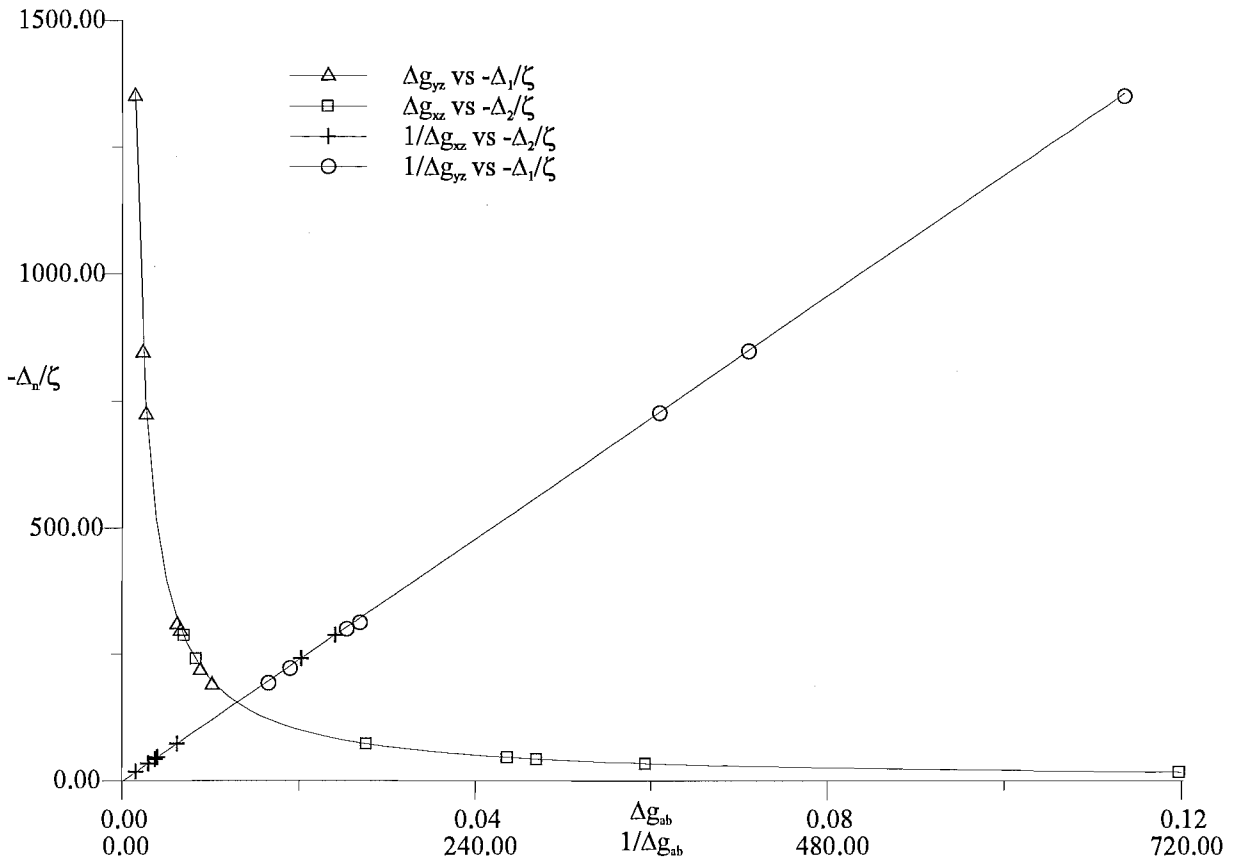

Figure 4-6: Plot of experimental principal g-value differences against calculated crystal-field splittings for assorted hole centres in zircon.

which could be attributed to p-p transitions [72].

Chapter 5

Electron centres in zircon

5.1 Introduction

As described in section 1.2.2, the electron centres include those centres which trap an electron during irradiation, such as the titanium centre described in this chapter, and also those that may be termed 'natural' electron centres. These are centres which do not require irradiation to be observed, as they already contain unpaired electrons, and which have similar properties to the irradiation-generated electron centres. The chromium (Z) centre described in this chapter is probably an example of this sort, although it is not absolutely clear in what oxidation state the chromium first enters the zircon lattice.

All of the electron centres studied in this thesis are thought to be centred on a normal zirconium or silicon position in the zircon lattice, in some cases with associated impurities in nearby positions. Three of the centres ($Si(Ti^{3+})$, Z and H) have $\bar{4}2m$ site symmetry, and are thus expected to comprise only a single foreign entity in the substitutional lattice site, as described in section 2.1. The final two electron centres described in this chapter are associated with one or more boron atoms, and have point-group symmetries $mm2$ and m, respectively. As described in section 2.1, the former point-group symmetry is very unusual in zircon, and it is the first to have been reported by the Canterbury epr group.

The $Si(Ti^{3+})$, H and boron centres are thought to have an electronic spin of $\frac{1}{2}$, as they are only moderately anisotropic, and there is no observed fine structure. The Z centre has an electronic spin of $\frac{3}{2}$, and is very anisotropic, with effective g values for the observed transition

varying between approximately 2 and 4.

5.2 The Si(Ti^{3+}) centre

5.2.1 Experimental details

The Si(Ti^{3+}) centre was first observed in a Ti^{4+}/Y^{3+}-doped synthetic crystal (growth L of table 3.1), the same crystal in which the $[SiO_4/Y]^0$ and $[SiO_4/M]^n$ centres were observed. As described in the previous chapter, the crystal was mounted on one of the naturally occurring *bc* faces, x-irradiated at 77 K and transferred cold to the previously cooled Displex head of the cavity goniometer system.

The spectrum of the Si(Ti^{3+}) centre consisted of a large central line due to the 87.2 % abundant spinless titanium isotopes, flanked by eight hyperfine lines due to the 7.3 % abundant ^{47}Ti (six lines, $S = \frac{5}{2}$), and 5.5 % abundant ^{49}Ti (eight lines, $S = \frac{7}{2}$). Eight, rather than fourteen lines are seen due to ^{47}Ti and ^{49}Ti because the inner six lines coincide due to the very similar nuclear g values of the two isotopes ($g_n(^{49}Ti) = 1.00025 \times g_n(^{47}Ti)$. The full *c*-axis spectrum is shown in figure 4-2, while an expanded view in figure 5-1 clearly shows the ^{47}Ti and ^{49}Ti hyperfine lines.

Measurements were carried out in the *bc* plane only as they were sufficient to completely determine the spin-Hamiltonian matrices, as noted in section 1.2.1. Data were taken every 5°-10° over a range of 210°.

5.2.2 Results

The overall observed spectrum of the Si(Ti^{3+}) centre is really due to three independent, but closely related centres, where each individual defect contains either a ^{47}Ti, ^{49}Ti or one of the spinless isotopes ($^{46,48,50}Ti$). The epr data are fitted separately to the appropriate spin Hamiltonian in each case, the octuplet being fitted as a ^{49}Ti centre and the sextuplet as a ^{47}Ti centre. The identity of the isotope involved in the single-line spectrum is irrelevant as the only term required in the spin Hamiltonian is the electronic Zeeman term. The three centres would be expected to have relative concentrations in the crystal in proportion to the natural abundances of the ^{47}Ti, ^{49}Ti and spinless isotopes. The signal intensity for each centre should

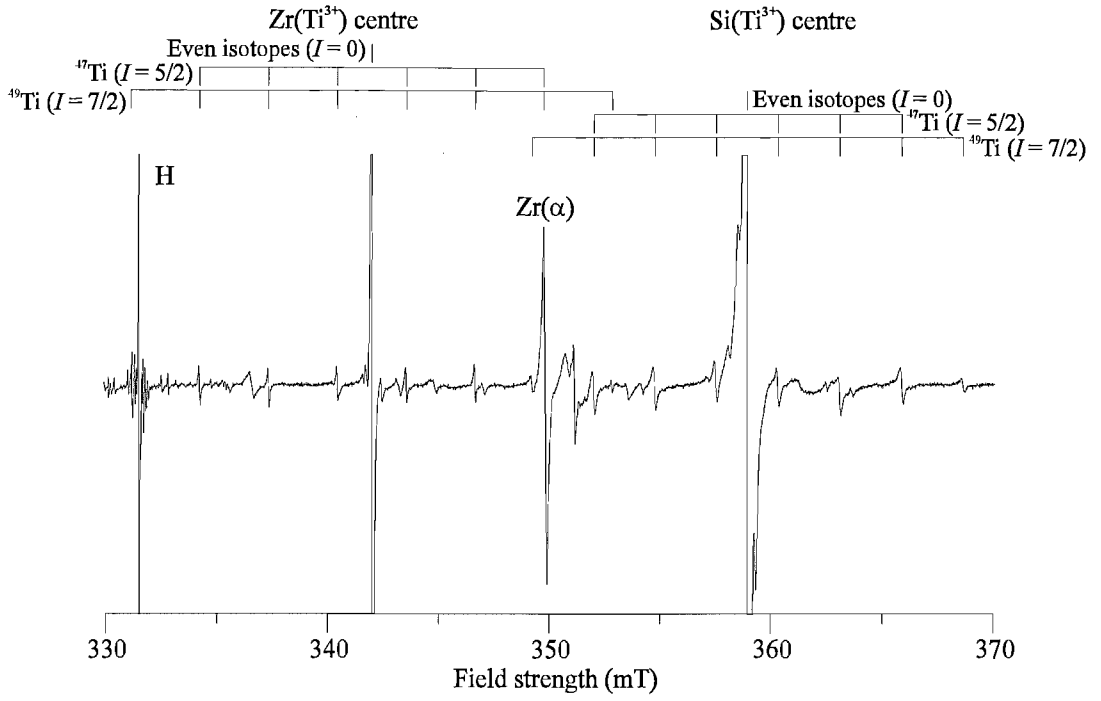

Figure 5-1: c-axis epr spectrum of Ti^{4+}/Y^{3+}-doped crystal showing $Zr(Ti^{3+})$ and $Si(Ti^{3+})$ centres in zircon at *ca* 15 K. Frequency = 9.22300 GHz.

thus also be in proportion to the natural abundances, as is observed to be the case. This characteristic pattern of lines with intensities consistent with the natural abundances of the titanium isotopes makes the assignment of a titanium atom unequivocal.

As the crystal was rotated in the bc plane, no site splitting was observed, immediately revealing the site symmetry of the defect to be $\bar{4}2m$, the site symmetry of the silicon and zirconium lattice positions. This almost certainly indicates that the defect is a single Ti^{3+} atom substituted into a normal silicon or zirconium site. Another Ti^{3+} centre with $\bar{4}2m$ symmetry containing a Ti^{3+} atom in the Zr^{4+} site was already well known [23], [24], [9], so it seemed likely that this was a Ti^{3+} species in a Si^{4+} site. Unlike the $Zr(Ti^{3+})$ centre, this centre was observed to be unstable towards annealing to room temperature, so measurements were carried out directly after irradiation and cold transfer. The earlier stacked plot in figure 4-3 showed the spectra of both Ti^{3+} centres through a rotation of 90° in the bc plane, while figure 5-2 shows the measured angular dependence of the $Si(Ti^{3+})$ centre-line positions, along with the roadmap

generated by the final fitted parameter matrices.

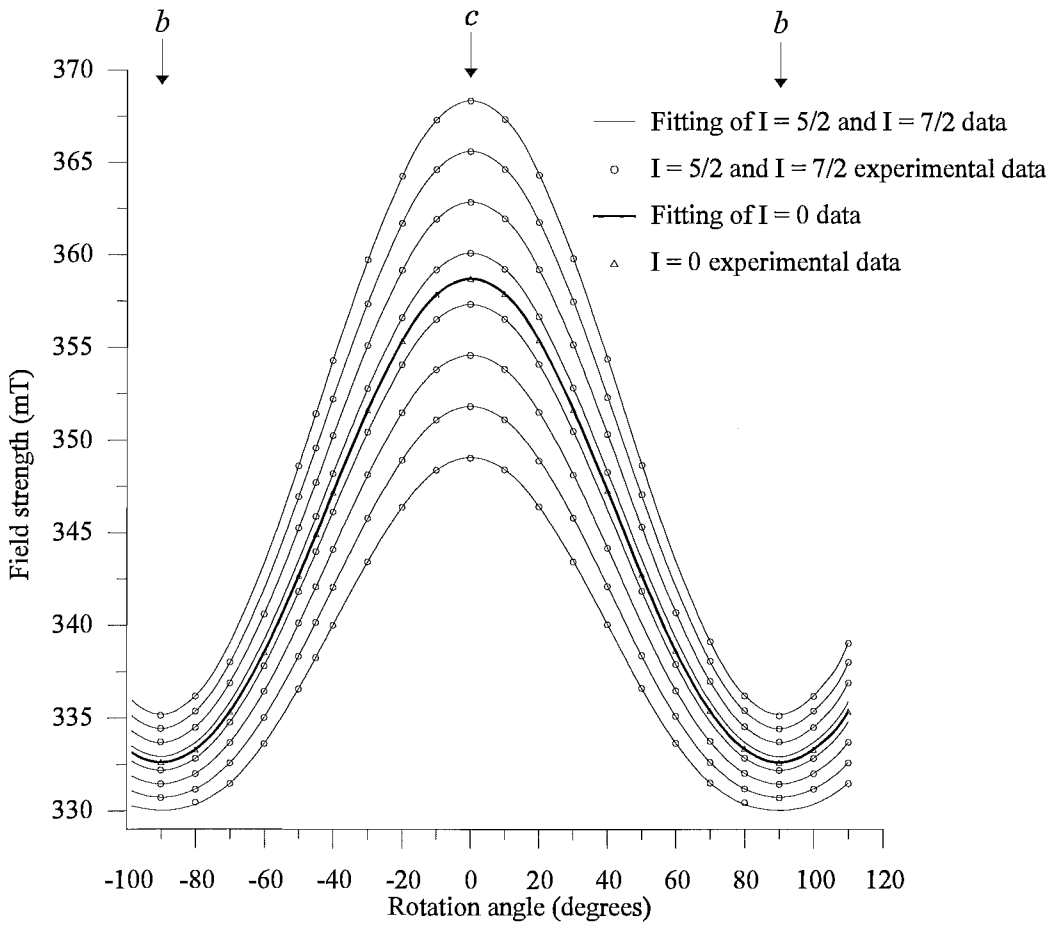

Figure 5-2: Angular dependence of Si(Ti^{3+})-centre epr spectra in zircon in the *bc* plane: experimental data and computer fitting. Average frequency $\approx$ 9.2195 GHz.

The data in all three fittings contained 23 angles in the *bc* plane over a range of 210°. The spin Hamiltonian used was of the form:

$$\widehat{\mathcal{H}} = \beta_e \mathbf{B.g.\hat{S}} + \mathbf{\hat{S}.A.\hat{I}} + \mathbf{\hat{I}.P.\hat{I}} - \beta_n \mathbf{B.g}_n\mathbf{.\hat{I}} \tag{5.1}$$

where $\mathbf{g}_n$ was set as the scalar matrix $-0.31539\mathbf{U}$ for ^{47}Ti and $-0.315477\mathbf{U}$ for ^{49}Ti. $\mathbf{U}$ is the 3×3 unit matrix, and -0.31539 and -0.315477 are the g_n values of ^{47}Ti and ^{49}Ti set internally by EPR-NMR. Only the first term of 5.1 was required for the analysis of the central-line spectra

resulting from the spinless titanium isotopes.

The analysis of the Zr(Ti^{3+}) centre had required high-spin terms in the Hamiltonian, specifically, terms of magnitude BI^3, BI^5, SI^3, SI^5 and I^4 [9]. A large nuclear quadrupole matrix was also fitted. A most striking aspect of the observed spectra was the large number of 'forbidden' lines seen in all orientations away from the c axis. These lines very quickly dominated the spectrum, and the 'allowed' transitions were soon lost as the crystal was rotated away from the c axis. In most orientations the ^{47}Ti and ^{49}Ti hyperfine lines were resolved, and could be separately measured. However, no such effects were observed in the new titanium centre. At all orientations measured, only the 6 + 8 allowed hyperfine lines were observed, and the inner six ^{49}Ti lines were always coincident with the ^{47}Ti lines within the experimental resolution. The fitted matrices are given in table 5.1.

Table 5.1: Spin-Hamiltonian parameters for the Si(Ti^{3+}) centre in zircon at *ca* 15 K. Error estimates in parentheses.

	^{47}Ti parameters		^{49}Ti parameters		Spinless isotopes	
	Principal values		Principal values		Principal values	
Matrix $\mathbf{Y}$	$Y_\parallel$	$Y_\perp$	$Y_\parallel$	$Y_\perp$	$Y_\parallel$	$Y_\perp$
$\mathbf{g}$	1.836155(9)	1.980606(9)	1.83615(1)	1.98048(1)	1.83617(2)	1.98055(2)
$\mathbf{A}/g_e\beta_e$ (mT)	2.5299(9)	0.7274(13)	2.5302(7)	0.7268(10)	-	-
$\mathbf{P}/g_e\beta_e$ (mT)	0.0157(20)	-0.0078(10)	0.0067(18)	-0.0034(9)	-	-
$\mathbf{g}_n$	-0.31539	-0.31539	-0.315477	-0.315477	-	-
Total data points	138		184		23	
Unit weighted	87		118		22	
$\sum$ weightings	95.95		126.74		22.2	
rmsd (mT)	0.0113		0.0141		0.0081	

An inner pair of hyperfine lines is also visible in the c-axis spectrum, very close to the central spinless isotope line. As the crystal is rotated in the bc plane, these lines merge into the larger central line, which broadens from 0.16 mT in the c-axis orientation to 0.20 mT after a

40° - 50° rotation. The lines do not become visible again until a rotation of nearly 90 degrees, i.e., when the crystallographic axis b is nearly parallel to the magnetic field, and the central linewidth decreases to 0.07 mT. These lines are likely to be due to hyperfine interaction with the nearby zirconium nuclei (see discussion), but there are not enough data to attempt to fit them.

5.2.3 Discussion

Location of the titanium atom

Comparison with the Zr(Ti^{3+}) centre. The assignment of the new centre to a titanium species was unequivocal, due to the unique hyperfine signature of a titanium atom. The oxidation state was also clearly 3+, being formed by the capture of an electron by diamagnetic (d^0) Ti^{4+} during irradiation, to form the paramagnetic $S = \frac{1}{2}$, d^1 species, Ti^{3+}. The centre was clearly closely related to the well-known Zr(Ti^{3+}) centre [23], [24], [9], and was observed to have the same site symmetry, indicating that perhaps this was Si-substituting analogue of that centre.

When the Zr(Ti^{3+}) centre was measured, it was assigned to a zirconium substitutional site for four reasons [24]. Firstly, because of the lack of correspondence between the fitted matrices and those of the $[TiO_4]^-$ centre in α-quartz [73], [74]. The $[TiO_4]^-$ centre of α-quartz is another Ti^{3+} centre, which is known to be located in a silicon site. While the symmetry of the two centres is different (2 for the $[TiO_4]^-$ centre of α-quartz), it was argued that the SiO_4 tetrahedron is very similar in the two cases, and hence some correspondence might be expected between the two centres if they were both located in the respective silicon sites.

Secondly, on the basis of the ionic radii of Zr^{4+}(0.79 Å), Si^{4+} (0.42 Å) and Ti^{4+}(0.68 Å), it was argued that the titanium would be more likely to occur in a zirconium site, due to their more similar size. The Si-O bonding in both crystal systems is covalent rather than ionic however, and it was noted that it is possible for Ti^{4+} to enter a Si^{4+} site, as proved by the existence of the $[TiO_4]^-$ centre of α-quartz.

The third argument was based on point-charge calculations. Following Hutchings [6], the 3d energy levels for a d^1 system were calculated by summing the contributions to the electric-field potential at the unpaired electron from a set of point charges in the oxygen atom positions.

The calculation was carried out for both the ZrO_8 dodecahedral case and the SiO_4 tetrahedral case. The calculations indicated that the ordering of the d_{xy} and $d_{xz,yz}$ orbital energy levels was reversed between the two cases. While the more recent calculations given herein have shown an error in these calculations, this conclusion remains the same. Fitting of the observed g values of the $Zr(Ti^{3+})$ centre to orbital energy-level splittings using spin-orbit crystal-field calculations revealed an ordering of the levels which agrees with the ZrO_8 calculation. The fitting of the g values follows a similar process to that described for the hole centres, and is outlined again in this chapter for the two Ti^{3+} centres and another $3d^1$ ion, V^{4+}.

The final reasoning given for the placement of Ti^{3+} at a Zr^{4+} position was the observation of probable ^{29}Si ($I = \frac{1}{2}$) hyperfine structure in limited orientations. Where the lines are visible, the intensity ratio is consistent with 4.6 % abundant ^{29}Si. There are also two sets of lines, due to the two non-equivalent sets of Si atoms surrounding a zirconium atom. For a titanium atom substituted in a silicon site, the nearest silicon atoms are too far away to be likely to result in any observable hyperfine interaction. In this case, hyperfine interaction with 11.23 % abundant ^{91}Zr ($I = \frac{5}{2}$) would be expected to be observed.

Having observed a new point-group-symmetry-$\bar{4}2m$ Ti^{3+} centre, it was then possible to check these points against the new centre in the hope of confirming the expected characteristics of a silicon-substituted Ti^{3+} centre.

Matrices. An inspection of the matrices of the $Si(Ti^{3+})$ centre and comparison with the matrices of the $Zr(Ti^{3+})$ centre and the $[TiO_4]^-$ centre of α-quartz shows that there is no better agreement between $Si(Ti^{3+})$ and $[TiO_4]^-$ than between $Zr(Ti^{3+})$ and $[TiO_4]^-$. In fact, there is poorer agreement between $Si(Ti^{3+})$ and $[TiO_4]^-$. The ordering of $g_{\|} < g_{\perp}$ and $A_{\|} > A_{\perp}$ for the $Si(Ti^{3+})$ centre is the same as the $Zr(Ti^{3+})$ centre, and the opposite of the $[TiO_4]^-$ centre[1]. The anisotropy in g for the $[TiO_4]^-$ centre is intermediate between the two zircon Ti^{3+} centres, and if anything, is closer to the $Zr(Ti^{3+})$ centre. The magnitude of the ^{47}Ti and ^{49}Ti hyperfine-matrix principal values is very similar for both $Si(Ti^{3+})$ and $Zr(Ti^{3+})$, and

[1] Although the site symmetry of the quartz $[TiO_4]^-$ centre is 2, the matrices are approximately uniaxial, so the 'unique' principal values may be compared with the parallel principal values in the zircon centres. The reversing of the order of g- and particularly the A-value magnitudes is expected for the usual b_1 ground state of zircon and a_1 ground state of α-quartz (see section 5.4.3).

neither agrees at all well with the $[TiO_4]^-$ centre matrices. Finally, the elements of the nuclear quadrupole matrix for the $Si(Ti^{3+})$ centre are approximately ten times smaller than those of the $Zr(Ti^{3+})$ and $[TiO_4]^-$ centre nuclear quadrupole matrices. This evidence would tend to suggest that a comparison between the quartz centre and the zircon centres means very little, rather than that the previous conclusions were in error. Of the four pieces of evidence for the assignment of the substitutional sites, this was probably the weakest.

Ionic radii. The assignment of the $Zr(Ti^{3+})$ centre to a zirconium substitutional site on the basis of the more similar ionic radii is probably still a valid one. The $Zr(Ti^{3+})$ centre is observed almost invariably in all the artificially grown crystals regardless of what doping, if any, took place, and also in many natural crystals. The $Si(Ti^{3+})$ centre, on the other hand, was only observed in a crystal doped with Ti^{4+}, in which both centres were observed. These observations are consistent with the requirement for high concentrations of titanium impurity to be present before any will be incorporated into silicon sites. At low levels, the titanium ions preferentially substitute into the zirconium sites only.

Point-charge calculations. The calculations reported in [24] have now been shown to be in error, however, the important conclusion of the calculation remains the same, as described below. As described in Hutchings [6], the calculations are developed from the expression for the electrostatic potential $V(r,\theta,\phi)$ at a point near the origin (the nucleus of the magnetic ion) due to a set of point charges q_j:

$$V(r,\theta,\phi) = \sum_j \frac{q_j}{|\mathbf{R}_j - \mathbf{r}|} \tag{5.2}$$

where R_j is the distance of charge q_j from the origin. Use of the spherical-harmonic addition theorem and some mathematical manipulation gives an expression for $V(r,\theta,\phi)$ in terms of spherical harmonics:

$$V(r,\theta,\phi) = \sum_{n=0}^{\infty} \sum_{\alpha} r^n \gamma_{n\alpha} Z_{n\alpha}(\theta,\phi) \tag{5.3}$$

where for k charges:

$$\gamma_{n\alpha} = \sum_{j=1}^{k} \frac{4\pi}{2n+1} q_j \frac{Z_{n\alpha}(\theta_j,\phi_j)}{R_j^{n+1}} \tag{5.4}$$

The $Z_{n\alpha}(\theta,\phi)$'s are tesseral combinations of spherical harmonics giving real numbers, and α may take values from n to $-n$. The number of terms which must be used is limited by the symmetry of the system, and is no greater than three for all cases considered here. For $\bar{4}2m$ point-group symmetry, or Laue class $4/mmm$, the $\gamma_{n\alpha}$ are restricted to γ_{20}, γ_{40} and γ_{44} (see table 4 of [75]).

The required values of $\gamma_{n\alpha}$ are evaluated for the set of θ_j, ϕ_j values describing the positions of the oxygen atoms surrounding the substitutional site. Substitution into equation 5.3 gives $V(r,\theta,\phi)$ as a sum of terms of the form:

$$V(r,\theta,\phi) = aq\frac{r^n}{R_j^{n+1}}Z_{n\alpha}(\theta,\phi) \tag{5.5}$$

for each $n\alpha$, where a is the numerical solution of $\gamma_{n\alpha}$. In order to calculate the matrix elements of $V(r,\theta,\phi)$ with the wavefunctions of the d orbitals, the $Z_{n\alpha}(\theta,\phi)$'s are written in cartesian form as defined in table IV of Hutchings [6]. They are given in the form:

$$Z_{n\alpha}(\theta,\phi) = b\frac{f_{n\alpha}(x,y,z)}{r^n} \tag{5.6}$$

where b is a constant and the function $f_{n\alpha}(x,y,z)$ is related to the commonly used Stevens operator equivalents $\hat{O}_n^m$ by:

$$\sum_i f_{nm}(x_i,y_i,z_i) = \theta_n \langle r^n \rangle \hat{O}_n^m \tag{5.7}$$

θ_n is a multiplicative factor where $\theta_2 = \alpha_J$, $\theta_4 = \beta_J$, and $\theta_6 = \gamma_J$. They are also known as reduced matrix elements as introduced in equation 1.25 (for α). These factors may be found tabulated in various sources, including [8]. For a single d electron the non-zero values are $-\frac{2}{21}$ for α and $\frac{2}{63}$ for β. The reason for doing this is that $V(r,\theta,\phi)$ may then be written in terms of Stephens operators allowing for easy calculation of the matrix elements.

As well as the ZrO_8 and SiO_4 sites, the calculations were carried out for an eightfold and fourfold cubic case, a dodecahedral distortion from the eightfold cube, and a ZrO_8 site with all bond lengths equal. The eightfold cubic case takes eight equal charges at the corners of a cube surrounding the central ion, and was calculated for a bond length of 2.20 Å, the average

Table 5.2: Polar coordinates of point charges (oxygen atoms) and resulting expressions for the electrostatic potential for various sites. The a's in the potential expressions refer to the r coordinate of the point charges. For the ZrO_8 dodecahedron, $a = 2.13$ and $b = 2.17$.

Site	Polar coordinates r (Å)	θ (°)	ϕ (°)	$\hat{V}\left(\frac{q}{d}\right)$
8-fold cube	2.20	54.74[a]	$90n^b - 45$	$-\frac{1}{81}\left(\hat{O}_4^0 + 5\hat{O}_4^4\right)\frac{q\langle r^4\rangle}{a^5}$
		125.26[a]	$90n^b - 45$	
10° dodecahedral distortion of 8-fold cube	2.20	44.74	45, 225	$-\frac{0.23960}{42}\hat{O}_2^0\frac{q\langle r^2\rangle}{a^3} - \frac{18.116}{2016}\hat{O}_4^0\frac{q\langle r^4\rangle}{a^5} - \frac{5\times 3.6578}{288}\hat{O}_4^4\frac{q\langle r^4\rangle}{a^5}$
		64.74	135, 315	
		115.26	45, 225	
		135.26	135, 315	
ZrO_8 dodecahedron with average bond length	2.20	78.62	45, 225	$-\frac{1.0257}{42}\hat{O}_2^0\frac{q\langle r^2\rangle}{a^3} + \frac{5.1682}{2016}\hat{O}_4^0\frac{q\langle r^4\rangle}{a^5} - \frac{5\times 4.0236}{288}\hat{O}_4^4\frac{q\langle r^4\rangle}{a^5}$
		101.38	135, 315	
		147.62	45, 225	
		32.38	135, 315	
ZrO_8 dodecahedron	2.13	78.62	45, 225	$\left(\frac{3.5328}{42}\frac{q\langle r^2\rangle}{a^3} - \frac{4.5585}{42}\frac{q\langle r^2\rangle}{b^3}\right)\hat{O}_2^0 + \left(\frac{7.5402}{2016}\frac{q\langle r^4\rangle}{a^5} - \frac{2.3720}{2016}\frac{q\langle r^4\rangle}{b^5}\right)\hat{O}_4^0$
		101.38	135, 315	
	2.17	147.62	45, 225	$-\left(\frac{5\times 3.6946}{288}\frac{q\langle r^4\rangle}{a^5} + \frac{5\times 0.32900}{288}\frac{q\langle r^4\rangle}{b^5}\right)\hat{O}_4^4$
		32.38	135, 315	
SiO_4 tetrahedron	1.623	48.483	45, 225	$-\frac{1.2723}{42}\hat{O}_2^0\frac{q\langle r^2\rangle}{a^3} - \frac{13.698}{2016}\hat{O}_4^0\frac{q\langle r^4\rangle}{a^5} - \frac{5\times 1.2573}{288}\hat{O}_4^4\frac{q\langle r^4\rangle}{a^5}$
		131.517	135, 315	
4-fold cube	1.623	54.74[b]	45, 225	$-\frac{1}{162}\left(\hat{O}_4^0 + 5\hat{O}_4^4\right)\frac{q\langle r^4\rangle}{a^5}$
		125.26[b]	135, 315	

[a] $\theta = \tan^{-1}\sqrt{2}$, $180 - \tan^{-1}\sqrt{2}$
[b] $n = 1 - 4$

of the ZrO_8 bond lengths. The dodecahedral case is a distortion of this situation by rotations and/or changes in bond length to produce two interlocking tetrahedra. The operation must be the same for each bond of one tetrahedron, but may be different for the two tetrahedra. In the case of the ZrO_8 dodecahedron, the two tetrahedra have differing bond lengths as described in chapter two, and the rotation angles from the cubic case are 22.4° and 23.9°. The dodecahedral distortion of the eightfold cube was calculated with an intermediate rotation of 10°, keeping the same average bond length. This average bond length was also used for the ZrO_8 site with equal bond lengths. The fourfold cube is the same as the eightfold cube with alternate corners missing, leaving a single tetrahedron, and was calculated with bond lengths identical to the SiO_4 site.

The polar coordinates of the point charges and the resulting expressions for the electrostatic potential in terms of Stephens operator equivalents are given in table 5.2 for each site. The electric-field interaction is treated as a first-order perturbation, and the energy levels are calculated by simply evaluating the matrix elements of $-|e|\hat{V}$ where e is the electronic charge, between the free-ion wavefunctions of the 3d orbitals. The matrix $-|e|\left\langle \psi_i \middle| \hat{V} \middle| \psi_j \right\rangle$ comes out in diagonal form since the d orbitals are eigenfunctions. Table 5.3 gives the calculated results of the corrections to the unperturbed energies. The wavefunctions utilised for the five 3d orbitals are as follows [68]:

$$d_{z^2} \sim |0\rangle \sim a_1 \tag{5.8a}$$

$$d_{xz} \sim \frac{1}{\sqrt{2}}(-|+1\rangle + |-1\rangle) \sim e_a \tag{5.8b}$$

$$d_{yz} \sim \frac{i}{\sqrt{2}}(|+1\rangle + |-1\rangle) \sim e_b \tag{5.8c}$$

$$d_{x^2-y^2} \sim \frac{1}{\sqrt{2}}(|+2\rangle + |-2\rangle) \sim b_1 \tag{5.8d}$$

$$d_{xy} \sim \frac{i}{\sqrt{2}}(-|+2\rangle + |-2\rangle) \sim b_2 \tag{5.8e}$$

where the group-theory labels apply under a crystal field of dodecahedral ($\bar{4}2m$) symmetry. The expressions 5.8a-5.8c were also used for the p orbitals in chapter four (equations 4.2). The matrix elements of the Stephens operator equivalents were calculated by making use of tabulations of $\langle JJ_z | O_n^0 | JJ_z \rangle$ and non-zero $\langle JJ_{z1} | O_n^m | JJ_{z2} \rangle$ matrix elements given in Hutchings [6] and

referenced therein.

Table 5.3: Crystal-field splittings of 3d energy levels in different sites from point-charge calculation. The calculations neglect the spin-orbit coupling, under which the $d_{xz,yz}$ energies are no longer degenerate (see crystal-field spin-orbit-coupling analysis in the next section).

Site	$-\lvert e\rvert \left\langle \psi \middle\lvert \widehat{V} \middle\rvert \psi \right\rangle$ (cm^{-1})			
	$d_{x^2-y^2}$	d_{z^2}	$d_{xz,yz}$	d_{xy}
8-fold cube	−2312	−2312	1541	1541
10° distortion	−2661	−1284	1321	1303
ZrO_8 2.20 Å	−3807	2187	533.6	553.0
ZrO_8	−2828	1063	−209.4	2184
SiO_4	−9363	−548.3	6519	−3127
4-fold cube	−5290	−5290	3527	3527

For the two cubic calculations, the energies may be expressed in units $\frac{eq\langle r^4\rangle}{a^5}$ and are thus independent of bond length and radial expectation values. However, as all of the other solutions contain terms in both $\frac{eq\langle r^2\rangle}{a^3}$ and $\frac{eq\langle r^4\rangle}{a^5}$, and the ZrO_8 site has two different bond lengths, numerical values were used for all quantities in the calculations of table 5.3, with the energy units converted to wavenumbers. The point charges (O^{2-}) were given a charge $q = -\lvert 2e\rvert$. Data for the 3d radial expectation values for Ti^{3+} (free ion) including relativistic corrections were taken from Fraga *et al.* [76]. The plotted energies are shown in figure 5-3. Figure 5-3 shows that the ordering of the b_2 (d_{xy}) and e ($d_{xz,yz}$) orbitals is reversed between the ZrO_8 and SiO_4 sites, still in agreement with the conclusions reached in the earlier $Zr(Ti^{3+})$ paper [24] after the corrections to those calculations. If the spin-orbit crystal-field analysis of the g values of the new Ti^{3+} centre were also to show that this was the case, it would go a long way towards confirming the location in a silicon site.

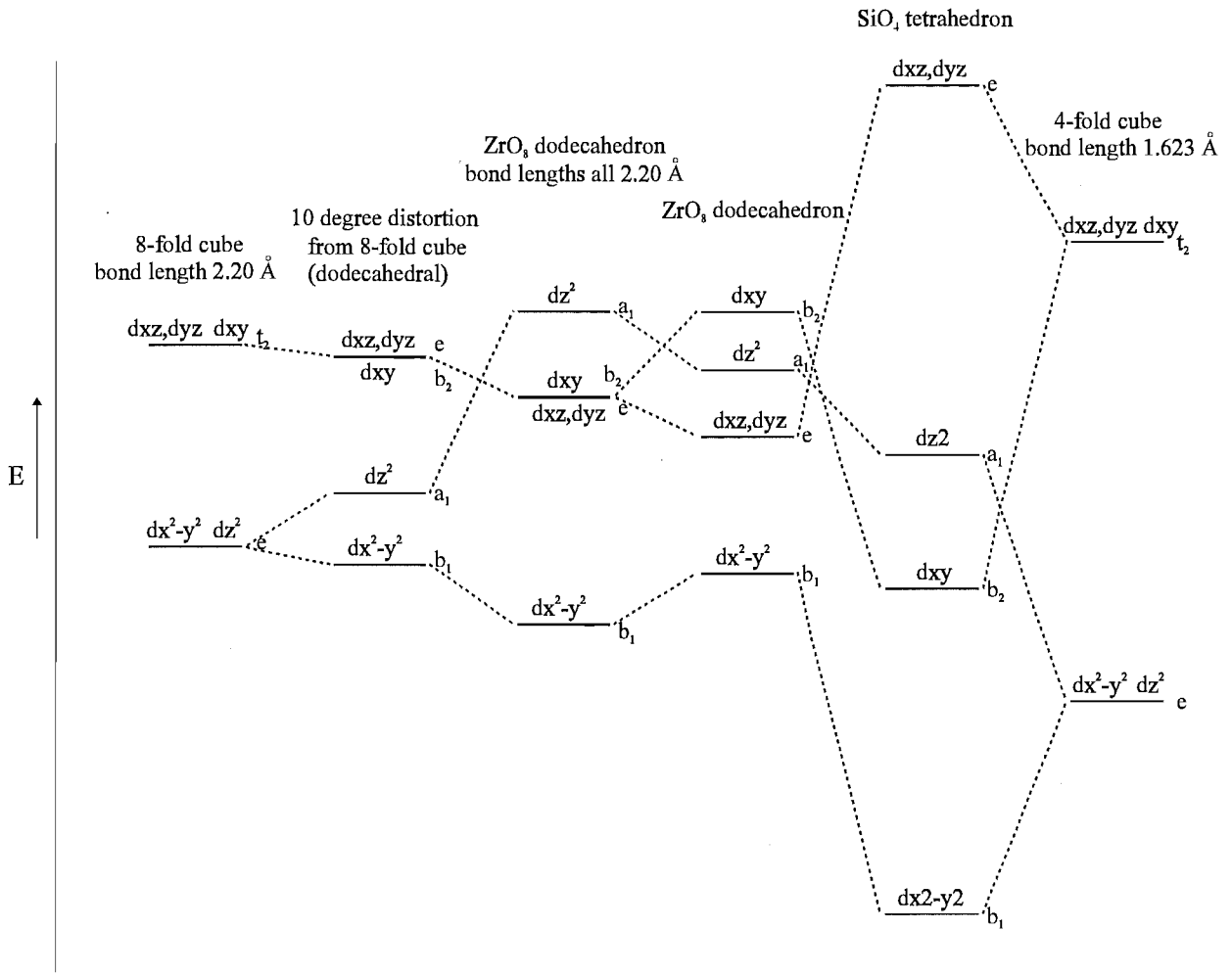

Figure 5-3: Crystal-field splitting of 3d energy levels from point-charge calculation for various sites. The labels on the right of the energy levels are the apropriate symmetry labels of the d orbitals.

Crystal-field spin-orbit-coupling analysis of g values The crystal-field spin-orbit-coupling analysis of the d^1 electron centres was carried out in a similar fashion to that described in section 4.3 for the hole centres, using the same computer programme, Pdorbit [70]. Here the crystal-field spin-orbit-coupling matrix is a 10×10 matrix which block diagonalises into two 5×5 matrices:

	$\|b_1^+\rangle$	$\|b_2^+\rangle$	$\|e_a^-\rangle$	$\|e_b^-\rangle$	$\|a_1^+\rangle$	$\|a_1^-\rangle$	$\|e_b^+\rangle$	$\|e_a^+\rangle$	$\|b_2^-\rangle$	$\|b_1^-\rangle$
$\langle b_1^+\|$	E_{b_1}	$-i\zeta$	$\frac{\zeta}{2}$	$i\frac{\zeta}{2}$	0	0	0	0	0	0
$\langle b_2^+\|$	$i\zeta$	E_{b_2}	$-\frac{i\zeta}{2}$	$\frac{\zeta}{2}$	0	0	0	0	0	0
$\langle e_a^-\|$	$\frac{\zeta}{2}$	$\frac{i\zeta}{2}$	E_e	$\frac{i\zeta}{2}$	$-\frac{\sqrt{3}\zeta}{2}$	0	0	0	0	0
$\langle e_b^-\|$	$-\frac{i\zeta}{2}$	$\frac{\zeta}{2}$	$-\frac{i\zeta}{2}$	E_e	$-\frac{\sqrt{3}i\zeta}{2}$	0	0	0	0	0
$\langle a_1^+\|$	0	0	$-\frac{\sqrt{3}\zeta}{2}$	$\frac{\sqrt{3}i\zeta}{2}$	E_{a_1}	0	0	0	0	0
$\langle a_1^-\|$	0	0	0	0	0	E_{a_1}	$\frac{\sqrt{3}i\zeta}{2}$	$\frac{\sqrt{3}\zeta}{2}$	0	0
$\langle e_b^+\|$	0	0	0	0	0	$-\frac{\sqrt{3}i\zeta}{2}$	E_e	$\frac{i\zeta}{2}$	$-\frac{\zeta}{2}$	$-\frac{i\zeta}{2}$
$\langle e_a^+\|$	0	0	0	0	0	$\frac{\sqrt{3}\zeta}{2}$	$-\frac{i\zeta}{2}$	E_e	$\frac{i\zeta}{2}$	$-\frac{\zeta}{2}$
$\langle b_2^-\|$	0	0	0	0	0	0	$-\frac{\zeta}{2}$	$-\frac{i\zeta}{2}$	E_{b_2}	$-i\zeta$
$\langle b_1^-\|$	0	0	0	0	0	0	$\frac{i\zeta}{2}$	$-\frac{\zeta}{2}$	$i\zeta$	E_{b_1}

(5.9)

where the d orbitals have been labelled by the appropriate representations under $\bar{4}2m$ symmetry. The value of ζ is again set to one in setting up the matrix so that it has effectively been divided by ζ leaving the eigenfunctions unaffected and the eigenvalues as unitless $\frac{\Delta}{\zeta}$ in the eventual output. ζ is now positive as we are dealing with a single electron, or a shell which is less than half full. The values along the diagonal are set by the user to an initial guess taking E_{b_1} (ground state) to be zero, and thus the other values become the splittings between each level and the ground state due to the crystal-field interaction. The matrix is then diagonalised numerically to obtain the combined crystal-field spin-orbit-coupling energies, and the coefficients of the new wavefunctions. The unperturbed wavefunction dominates the wavefunction, but there is a little mixing in of the other states through the spin-orbit coupling. The ground-state wavefunction is dominated by $|b_1\rangle$, and mixes with all of the unperturbed wavefunctions except $|a_1\rangle$ (see also alternate basis set used later in this section). The algebra for calculation of the magnetic-field interaction with the ground-state wavefunctions (Kramers doublet) in the x, y and z directions, and thus the g values has all been calculated and programmed into Pdorbit, so that values of g_x $(= g_y)$ and g_z are calculated according to the crystal-field splittings. The values of the crystal-field splittings are then varied from the initial guesses and the g values recalculated until the rmsd between experimental and calculated g values is minimised. Because there is no mixing of the a_1 orbital into the ground-state wavefunction, a value for $\Delta(E_{a_1} - E_{b_1})$ is not

obtained. The other two Δ values may be derived, however, giving the ordering of the e and b_2 levels.

As for the oxygen-hole case, perturbation expressions for the g values have also been developed, and are used to check the solutions fitted by Pdorbit using the numerical diagonalisation of 5.9. For the d-orbital case, the perturbation expressions have only been calculated to second degree in powers of $\frac{\zeta}{\Delta}$. The ground-state Kramers doublet perturbation wavefunctions are given by:

$$|+\rangle = N\left|b_1^+\right\rangle - \frac{i\zeta}{\Delta_1}\left|b_2^+\right\rangle - \frac{\zeta}{2\Delta_2}\left|e_a^-\right\rangle + \frac{i\zeta}{2\Delta_2}\left|e_b^-\right\rangle \tag{5.10a}$$

$$|-\rangle = N\left|b_1^-\right\rangle + \frac{i\zeta}{\Delta_1}\left|b_2^-\right\rangle + \frac{\zeta}{2\Delta_2}\left|e_a^+\right\rangle + \frac{i\zeta}{2\Delta_2}\left|e_b^+\right\rangle \tag{5.10b}$$

which leads to the equations:

$$g_{\parallel} = g_e\left(N^2 - 4yN - x^2 + y^2\right) \tag{5.11a}$$

$$g_{\perp} = g_e\left(N^2 - xN + xy - y^2\right) \tag{5.11b}$$

$$N = \left(1 - \frac{1}{2}x^2 - y^2\right)^{\frac{1}{2}} \tag{5.11c}$$

where $x = \frac{\zeta}{\Delta_2}$, $y = \frac{\zeta}{\Delta_1}$, $\Delta_1 = E_{b_2} - E_{b_1}$ and $\Delta_2 = E_e - E_{b_1}$. Some of the coefficients in the above equations have been simplified by taking $g_e = 2$. The perturbation expressions are useful in making a rough analysis of the g values. To first order, equations 5.11a and b reduce to:

$$g_{\parallel} = g_e - \frac{8\zeta}{\Delta_1} \tag{5.12a}$$

$$g_{\perp} = g_e - \frac{2\zeta}{\Delta_2} \tag{5.12b}$$

These equations show that the closer $g_{\parallel}$ is to g_e the larger Δ_1 will be, and the closer $g_{\perp}$ is to g_e the larger Δ_2 will be. In addition, for $\Delta_1 < \Delta_2$ (The SiO_4 case), $g_e - g_{\parallel} > 4\left(g_e - g_{\perp}\right)$, and conversely, for $\Delta_1 > \Delta_2$ (the ZrO_8 case), $g_e - g_{\parallel} < 4\left(g_e - g_{\perp}\right)$. Using this rule, the ordering of the b_2 and e levels may be ascertained by inspection, simply by comparing the deviations of the two g values from g_e.

The results of the calculations for both $Zr(Ti^{3+})$ and $Si(Ti^{3+})$ by matrix diagonalisation

Table 5.4: Calculated 3d-orbital crystal-field splittings from g values of d^1 centres in zircon. Absolute splittings calculated using $\zeta = 154$ cm^{-1} (see text).

Centre	$Zr(Ti^{3+})$	$Si(Ti^{3+})$	$Si(V^{4+})$
$g_{\parallel}$	1.926873	1.836155	1.889
$g_{\perp}$	1.940835	1.980606	1.9699
$\frac{\Delta_1}{\zeta}$	111.0	48.42	71.51
$\frac{\Delta_2}{\zeta}$	32.66	99.95	63.20
Δ_1 (cm^{-1})	17100	7460	11000
Δ_2 (cm^{-1})	5030	15400	9730

are given in table 5.4 as both the unitless quantities $\frac{\Delta_n}{\zeta}$ and as Δ_n in cm^{-1}, calculated using ζ = 154 cm^{-1}, an experimental Ti^{3+} hydrated-ion spin-orbit-coupling constant ([8] p378). The results of calculations for a V^{4+} centre are also included, another d^1 electron centre which was reported by Di Gregorio *et al.* [77], where V^{4+} is claimed to be substituted at a silicon site.

The calculations show that the b_2 (d_{xy}) and e ($d_{xz,yz}$) orbital energy levels are indeed swapped between the two centres according to the crystal-field spin-orbit-coupling analysis of the measured g values. The order of the two levels is consistent with the original interpretation of each centre and the predictions made by the point-charge calculations. The results for the V^{4+} centre appear to disagree with the interpretation of a silicon site, but the ordering of the levels in this case is much less certain since $\Delta_1 \approx \Delta_2$.

As noted in the earlier section on point-charge calculations, the spin-orbit coupling splits the degenerate e levels under the crystal field of $\bar{4}2m$ symmetry. The splittings given in table 5.4 are the fitted crystal-field splittings without spin-orbit coupling. The splitting of the e levels was apparent upon inspection of the numerical eigenvalues derived from matrix 5.9, and may be seen more clearly when the basis functions in the crystal-field spin-orbit-coupling matrix are changed. Two basis functions may be defined as linear combinations of the e_a and e_b

wavefunctions used above as follows:

$$|+1\rangle = -\frac{1}{\sqrt{2}}\left(|e_a\rangle - i\,|e_b\rangle\right) \tag{5.13a}$$

$$|-1\rangle = \frac{1}{\sqrt{2}}\left(|e_a\rangle + i\,|e_b\rangle\right) \tag{5.13b}$$

With these new basis functions, the crystal-field spin-orbit-coupling matrix becomes:

	$\left\|b_1^+\right\rangle$	$\left\|b_2^+\right\rangle$	$\left\|-1^-\right\rangle$	$\left\|+1^-\right\rangle$	$\left\|a_1^+\right\rangle$	$\left\|a_1^-\right\rangle$	$\left\|-1^+\right\rangle$	$\left\|+1^+\right\rangle$	$\left\|b_2^-\right\rangle$	$\left\|b_1^-\right\rangle$
$\left\langle b_1^+\right\|$	E_{b_1}	$-i\zeta$	$\frac{\zeta}{\sqrt{2}}$	0	0	0	0	0	0	0
$\left\langle b_2^+\right\|$	$i\zeta$	E_{b_2}	$-\frac{i\zeta}{\sqrt{2}}$	0	0	0	0	0	0	0
$\langle -1^-\|$	$\frac{\zeta}{\sqrt{2}}$	$\frac{i\zeta}{\sqrt{2}}$	$E_e + \frac{\zeta}{2}$	0	0	0	0	0	0	0
$\langle +1^-\|$	0	0	0	$E_e - \frac{\zeta}{2}$	$\frac{\sqrt{6}\zeta}{2}$	0	0	0	0	0
$\left\langle a_1^+\right\|$	0	0	0	$\frac{\sqrt{6}\zeta}{2}$	E_{a_1}	0	0	0	0	0
$\left\langle a_1^-\right\|$	0	0	0	0	0	E_{a_1}	$\frac{\sqrt{6}\zeta}{2}$	0	0	0
$\langle -1^+\|$	0	0	0	0	0	$\frac{\sqrt{6}\zeta}{2}$	$E_e - \frac{\zeta}{2}$	0	0	0
$\langle +1^+\|$	0	0	0	0	0	0	0	$E_e + \frac{\zeta}{2}$	$-\frac{i\zeta}{\sqrt{2}}$	$\frac{\zeta}{\sqrt{2}}$
$\left\langle b_2^-\right\|$	0	0	0	0	0	0	0	$\frac{i\zeta}{\sqrt{2}}$	E_{b_2}	$-i\zeta$
$\left\langle b_1^-\right\|$	0	0	0	0	0	0	0	$\frac{\zeta}{\sqrt{2}}$	$i\zeta$	E_{b_1}

(5.14)

The matrix now block-diagonalises into two 2×2 and two 3×3 matrices and shows clearly that the a_1 state does not mix into the ground b_1 state. In addition, spin-orbit-coupling contributions of opposite sign now appear on the two diagonal elements for the linear combinations of the e states. One could easily write down exact algebraic solutions for the energy eigenvalues and wavefunctions of the 2×2 matrices, but they would have no bearing on the analysis of the g values, as the wavefunctions would not be for the ground state.

Hyperfine structure The line structure visible on the sides of the central Si(Ti^{3+}) line in figure 5-1, and expanded in figure 5-4, first appears to be a pair of hyperfine lines which would be indicative of a nucleus with a nuclear spin of $\frac{1}{2}$, rather than the expected nuclear spin $\frac{5}{2}$ ^{91}Zr isotope. For a titanium atom substituted in a silicon position, hyperfine interaction would be expected with two sets of non-equivalent neighbouring zirconium atoms. One set of two atoms

is found half a unit cell (2.99 Å) above and below the silicon atom in the z-axis direction, and another set of four atoms is found roughly in the direction of the four Si-O bonds (3.62 Å). The natural abundance of ^{91}Zr is 11.23 %. This gives the probability of a single centre being surrounded by all spinless isotopes of zirconium of 0.489, by a single ^{91}Zr in the set of four of 0.248, and by a single ^{91}Zr in the set of two of 0.124. As the spectrum resulting from a centre with a single ^{91}Zr contains six lines, the intensity of each line is $\frac{1}{6}$ of the total. Therefore ignoring the centres containing two or more ^{91}Zr atoms, 13 lines should be present with relative intensities of 2.06 (×6), 4.13 (×6 lines) and 48.93. A simple programme was used to simulate the overall lineshape by summing all these contributions. The lineshape chosen was Lorentzian (first derivative), with a linewidth of 0.162 mT. A hyperfine splitting of 0.15 mT was chosen for the less-intense six-line spectrum to give the outer pair at the experimentally observed positions. The higher-intensity set of six lines was given a smaller hyperfine splitting of 0.13 mT, giving a reasonable fit to the experimental lineshape. This set of lines would be expected to have a smaller hyperfine splitting as the zirconium positions are further away, and would be likely to carry less spin density. The resulting plot is overlaid on an experimental spectrum in figure 5-4. The disparity on the left-hand side of the spectrum is likely to be due to interference from other centres, resulting in the non-symmetrical appearance of the experimental spectrum. The simulation clearly serves to show that the observed hyperfine lines could indeed be accounted for by the zirconium atoms neighbouring the silicon site.

Summary The observation of the Si(Ti^{3+}) centre has allowed the evidence for the location of the well-known Zr(Ti^{3+}) centre in a zirconium site to be more thoroughly investigated. The major quoted characteristics of the Zr(Ti^{3+}) which lead to the identification of the zirconium site and the predictions made for a theoretical Si(Ti^{3+}) centre [24] have been borne out in the analysis of the new centre.

Further analysis of parameter matrices

Hyperfine matrix As noted earlier, the ordering of the magnitudes of the principal values of **g** and **A** for Si(Ti^{3+}) is identical to Zr(Ti^{3+}). The principal values of **A** themselves are also very similar between the two centres, $\frac{A_\parallel}{g_e\beta_e} = 2.5299$ mT, $\frac{A_\perp}{g_e\beta_e} = 0.7274$ mT for Si($^{47}Ti^{3+}$), and

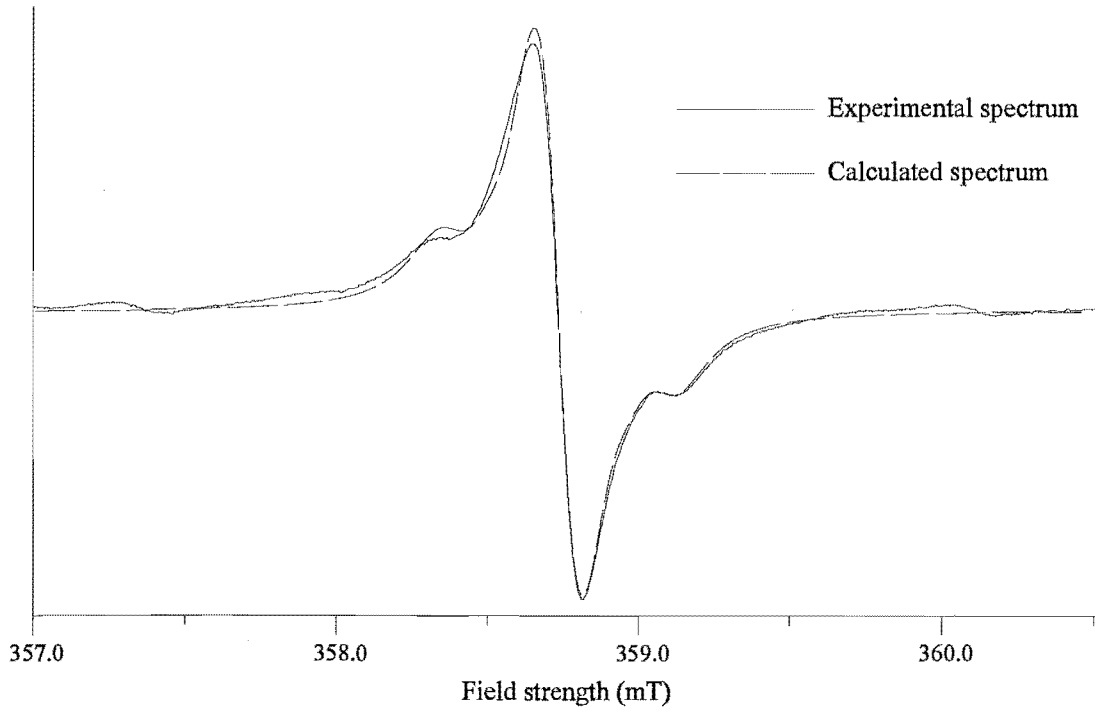

Figure 5-4: Experimental and simulated epr spectra of Si(Ti^{3+}) centre with ^{91}Zr hyperfine. Frequency $\approx$ 9.2195 GHz.

$\frac{A_\parallel}{g_e\beta_e} = 2.9714$ mT, $\frac{A_\perp}{g_e\beta_e} = 0.8986$ mT for B($^{47}Ti^{3+}$). However, in most other ways, the two sets of matrices are quite different.

From a hyperfine matrix, three parameters may be derived, which describe different parts of the hyperfine interaction, and reflect the symmetry of the interaction. They are the isotropic parameter, a, the uniaxiality parameter, b, and the rhombicity parameter c. They are defined (in magnetic-field units) as [3]:

$$a = \frac{\mathrm{tr}(\mathbf{A})}{3g_e\beta_e} \tag{5.15a}$$

$$b = \frac{A_1 - \frac{1}{2}(A_2 + A_3)}{3g_e\beta_e} \tag{5.15b}$$

$$c = \frac{|A_2 - A_3|}{2g_e\beta_e} \tag{5.15c}$$

where tr($\mathbf{A}$) is the trace of $\mathbf{A}$, or $A_1 + A_2 + A_3$ where A_i (i = 1 - 3) are the principal values

of $\mathbf{A}^2$. The principal values are ordered such that $|A_1 - A_2|$ and $|A_1 - A_3|$ are greater than or equal to $|A_2 - A_3|$, and $|A_2| - |A_3|$ is positive or zero. Similar equations may also be defined for the g matrix (omitting the $g_e\beta_e$).

For Si(Ti^{3+}), the uniaxiality parameter of the g matrix is much larger than for Zr(Ti^{3+}), 0.04815 compared to 0.00465. This increase in g anisotropy is consistent with the qualitative result noted earlier as a result of the perturbation expressions 5.11a-5.11b reduced to first-order. The silicon-substituted centre is predicted to have a $g_{\|}$ which deviates from g_e by over four times the deviation of $g_\perp$ from g_e.

The A matrix may be used to estimate the electron spin density contained in the orbitals of the hyperfine atom. The matrix is decomposed into an isotropic part $a\mathbf{U}$, where $\mathbf{U}$ is the identity matrix and a is the isotropic hyperfine parameter defined above, and a traceless anisotropic part, $\mathbf{T}$, which sum to give the complete matrix:

$$\frac{\mathbf{A}}{g_e\beta_e} = a\mathbf{U} + \frac{\mathbf{T}}{g_e\beta_e} \tag{5.16}$$

For a uniaxial matrix the anisotropic parameter b comes directly from the anisotropic part of the matrix, which has diagonal elements $\pm b$, $\pm b$ and $\mp 2b$. The isotropic part corresponds to the contact interaction due to non-zero spin density at the nucleus for s orbitals, and the anisotropic part arises from the dipolar term (see equations 5.20 and discussion). Following Morton and Preston (1978) [78], the isotropic and anisotropic components of $\mathbf{A}$ are compared with theoretical parameters A_{corr} and P (table 1 of [78]) for unit spin density in an s orbital or p, d, f orbital, respectively. For titanium, the parameters are listed as -728.0 MHz and -73.64 MHz.

For Si(Ti^{3+}), the decomposition is:

$$\mathbf{A} = 37.224 \begin{pmatrix} 1 & & \\ & 1 & \\ & & 1 \end{pmatrix} + \begin{pmatrix} -16.838 & & \\ & -16.838 & \\ & & 33.677 \end{pmatrix} \text{ MHz} \tag{5.17}$$

[2]It is not necessary to use the principal values to calculate the trace of the matrix (and hence a), as the trace is invariant under diagonalisation. However, the principal values must be used to calculate b and c.

so that $a = 37.224$ MHz and $b = 16.838$ MHz. The units have been converted from mT to MHz ($\times$ 28.0249) as used by Morton and Preston. Assuming that all of the possible hyperfine interactions of the defect centre can be associated with one unit of spin density, the proportion of that spin density which is associated with titanium s electrons is then assumed to be:

$$sd_{ns} = \left| \frac{a}{A_{corr}} \right| = 0.048 \ (4.8\%) \tag{5.18}$$

and similarly for the 3d electrons:

$$sd_{3d} = \left| \frac{b}{\alpha \times P} \right| = 0.800 \ (80.0\%) \tag{5.19}$$

where α is an angular factor listed in table 2 of Morton and Preston for an nl ($l \neq 0$) orbital. This leaves 15 % of the spin density unaccounted for, which may lie on the surrounding Zr^{4+} ions, for which hyperfine structure is also observed. It is assumed that the negatively charged oxygen atoms immediately surrounding the Ti^{4+} ion will not take on any spin density. It should also be noted that the parameter P involves a free-ion radial expectation value $\langle r^{-3} \rangle$, which is likely to be reduced for the covalently bound atom, as will be discussed later. This would result in a higher value calculated in equation 5.19, meaning that less spin density is left unaccounted for.

If it is assumed that the ratio of a and b is similar for the zirconium hyperfine structure as for the titanium, a hyperfine matrix may be estimated from the simulated splitting in the c-axis orientation (figure 5-4). Given the splittings 0.15 mT for the closer two zirconium atoms, and 0.13 mT for the more-distant four zirconium atoms the decompositions will be:

$$\mathbf{A}_{Zr(2)} = 0.075 \begin{pmatrix} 1 & & \\ & 1 & \\ & & 1 \end{pmatrix} + \begin{pmatrix} -0.0375 & & \\ & -0.0375 & \\ & & 0.075 \end{pmatrix} \text{mT}$$

$$\mathbf{A}_{Zr(4)} = 0.065 \begin{pmatrix} 1 & & \\ & 1 & \\ & & 1 \end{pmatrix} + \begin{pmatrix} -0.0325 & & \\ & -0.0325 & \\ & & 0.065 \end{pmatrix} \text{mT}$$

Conversion to MHz and calculation of the spin density as for equations 5.19 and 5.18 gives a spin density of 2.4% and 0.08% in the 4d and 5s orbitals of the closer zirconiums, and 2.0% and 0.07% for the more-distant zirconiums ($A_{corr} = -2753$ MHz, $P = -155.6$ MHz for zirconium, from table 1 of [78]). Multiplying by the number of zirconium atoms in each set gives a total of 13%, in reasonable agreement with the spin density unaccounted for in equations 5.19 and 5.18.

This is in contrast to the calculation for the $Zr(Ti^{3+})$ centre, which gives 92.0% spin density in the 3d orbital and 5.7% in the s orbitals, leaving only 2% unaccounted for. In this case the small amount of spin density might be accounted for by a rarely observable hyperfine interaction with neighbouring silicon atoms.

The approach of Morton and Preston [78] is designed to calculate the relative proportions of s and p, d, f character in a molecular-orbital description of the free radical. It has been applied here to estimate the amount of spin density which would be required, assuming a total spin density of one, in the distinct orbitals of single isolated atoms, to account for the observed hyperfine interactions. This may not be a valid interpretation of the Morton-and-Preston procedure. The nature of the isotropic hyperfine interaction as a result of spin polarisation is discussed in more detail below, with a model which does not require spin density to be 'borrowed' from the d orbital.

The Kramers-doublet ground-state wavefunction calculated earlier from the crystal-field spin-orbit-coupling matrix and used to calculate the g values may also be used to calculate A values. Once again, comparison with the experimental values allows a number of parameters to be determined.

Following Golding [68], the Hamiltonian interaction for the magnetic moment of a nucleus with nuclear spin I interacting with the magnetic field due to the orbital and spin angular momentum of the electrons is written:

$$\widehat{\mathcal{H}} = \widehat{\mathcal{H}}_1 + \widehat{\mathcal{H}}_2 \tag{5.20a}$$

$$\widehat{\mathcal{H}}_1 = g_e g_n \beta_e \beta_n \sum_i \left(\frac{\left(\hat{\mathbf{l}}_i - \hat{\mathbf{s}}_i\right).\hat{\mathbf{I}}}{\hat{\mathbf{r}}_i^3} + \frac{3\left(\hat{\mathbf{r}}_i.\hat{\mathbf{s}}_i\right)\left(\hat{\mathbf{r}}_i.\hat{\mathbf{I}}\right)}{\hat{\mathbf{r}}_i^5} \right) \tag{5.20b}$$

$$\widehat{\mathcal{H}}_2 = \frac{8\pi}{3} g_e g_n \beta_e \beta_n \sum_i \delta\left(r_i\right) \hat{\mathbf{s}}_i.\hat{\mathbf{I}} \tag{5.20c}$$

where r_i is the distance of the ith electron from the hyperfine nucleus, and $\delta(r_i)$ is the s-electron spin density at the nucleus. When written as a summation over single electrons as in equation 5.20c, $\delta(r_i)$ may be considered as an electron density at the nucleus, but with a positive or negative sign for an alpha (spin 'up') or beta (spin 'down') electron. The overall contribution is a spin density which is non-zero only when the alpha and beta electron densities at the nucleus are not equal. This 'core polarisation' is due to the interaction between the core electrons and the unpaired electron(s) in the outer shells. The interaction between an unpaired alpha electron and the core alpha electrons will be different to that between the unpaired alpha electron and core beta electrons, so that the radial functions of a core alpha and beta electron pair in a single s orbital may be different.

The two parts of the Hamiltonian in equations 5.20 correspond to the 'contact' interaction (named because the electrons have a finite probability *at* the nucleus) ($\widehat{\mathcal{H}}_2$) and the dipolar interaction ($\widehat{\mathcal{H}}_1$). Using operator equivalents to replace the r's with angular-momentum operators gives:

$$\widehat{\mathcal{H}}_1 = g_e g_n \beta_e \beta_n \left\langle r^{-3} \right\rangle \sum_i \left[\hat{\mathbf{l}}_i.\hat{\mathbf{I}} + \xi \left(l\,(l+1)\,\hat{\mathbf{s}}_i.\hat{\mathbf{I}} - \frac{3}{2}(\hat{\mathbf{l}}_i.\hat{\mathbf{s}}_i)(\hat{\mathbf{l}}_i.\hat{\mathbf{I}}) - \frac{3}{2}(\hat{\mathbf{l}}_i.\hat{\mathbf{I}})(\hat{\mathbf{l}}_i.\hat{\mathbf{s}}_i) \right) \right] \quad (5.21a)$$

$$\xi = \frac{2}{(2l-1)\,(2l+3)} \quad (5.21b)$$

For d electrons, $l = 2$, and equations 5.21 give:

$$\widehat{\mathcal{H}}_1 = g_e g_n \beta_e \beta_n \left\langle r^{-3} \right\rangle \sum_i \left[\hat{\mathbf{l}}_i.\hat{\mathbf{I}} + \frac{1}{7} \left(4\hat{\mathbf{s}}_i.\hat{\mathbf{I}} - \left(\hat{\mathbf{l}}_i.\hat{\mathbf{s}}_i\right) \left(\hat{\mathbf{l}}_i.\hat{\mathbf{I}}\right) - \left(\hat{\mathbf{l}}_i.\hat{\mathbf{I}}\right) \left(\hat{\mathbf{l}}_i.\hat{\mathbf{s}}_i\right) \right) \right] \quad (5.22)$$

This may then be expanded for a single d electron into x, y z components to give:

$$\widehat{\mathcal{H}}_1 = g_e g_n \beta_e \beta_n \left\langle r^{-3} \right\rangle \left(\widehat{\mathcal{H}}_x \hat{I}_x + \widehat{\mathcal{H}}_y \hat{I}_y + \widehat{\mathcal{H}}_z \hat{I}_z \right) \quad (5.23a)$$

where:

$$\widehat{\mathcal{H}}_x = \hat{l}_x + \frac{1}{7} \left(4s_x - 2\hat{l}_x^2 s_x - \left(\hat{l}_x\hat{l}_y + \hat{l}_y\hat{l}_x\right) \hat{s}_y - \left(\hat{l}_x\hat{l}_z + \hat{l}_z\hat{l}_x\right) \hat{s}_z \right) \quad (5.24a)$$

$$\widehat{\mathcal{H}}_y = \hat{l}_y + \frac{1}{7} \left(4s_y - 2\hat{l}_y^2 s_y - \left(\hat{l}_x\hat{l}_y + \hat{l}_y\hat{l}_x\right) \hat{s}_x - \left(\hat{l}_y\hat{l}_z + \hat{l}_z\hat{l}_y\right) \hat{s}_z \right) \quad (5.24b)$$

$$\widehat{\mathcal{H}}_z = \hat{l}_z + \frac{1}{7}\left(4s_z - 2\hat{l}_z^2 s_z - \left(\hat{l}_x\hat{l}_z + \hat{l}_z\hat{l}_x\right)\hat{s}_x - \left(\hat{l}_y\hat{l}_z + \hat{l}_z\hat{l}_y\right)\hat{s}_y\right) \tag{5.24c}$$

If the Hamiltonian of equation 5.20a, written in its component parts, is compared with the hyperfine term in the experimental Hamiltonian 1.12, also written in its component parts, we have:

$$A_x\hat{s}_x\hat{I}_x = g_e g_n \beta_e \beta_n \left(\left\langle r^{-3}\right\rangle \widehat{\mathcal{H}}_x + \frac{8\pi}{3}\delta(r)\, s_x\right)\hat{I}_x \tag{5.25a}$$

$$A_y\hat{s}_y\hat{I}_y = g_e g_n \beta_e \beta_n \left(\left\langle r^{-3}\right\rangle \widehat{\mathcal{H}}_y + \frac{8\pi}{3}\delta(r)\, s_y\right)\hat{I}_y \tag{5.25b}$$

$$A_z\hat{s}_z\hat{I}_z = g_e g_n \beta_e \beta_n \left(\left\langle r^{-3}\right\rangle \widehat{\mathcal{H}}_z + \frac{8\pi}{3}\delta(r)\, s_z\right)\hat{I}_z \tag{5.25c}$$

where $A_{x,y,z}$ are the principal values of the experimentally determinable hyperfine interaction tensor. Equating the terms to the left of the $\hat{I}_{x,y,z}$, and evaluating the matrix elements $\langle + \,||\, - \rangle$ using the operator forms on the left and right of equation 5.25a for the x components gives:

$$\frac{1}{2}A_x = g_e g_n \beta_e \beta_n \left(\left\langle r^{-3}\right\rangle \left\langle + \left|\widehat{\mathcal{H}}_x\right| - \right\rangle + \frac{1}{2}\frac{8\pi}{3}\overline{\delta(r)}\right) \tag{5.26a}$$

$$A_x = g_e g_n \beta_e \beta_n \left(\left\langle r^{-3}\right\rangle 2\left\langle + \left|\widehat{\mathcal{H}}_x\right| - \right\rangle + \frac{8\pi}{3}\overline{\delta(r)}\right) \tag{5.26b}$$

since $\langle + \,|s_x|\, - \rangle = \frac{1}{2}$. Evaluation of the $\langle - \,||\, + \rangle$ matrix elements gives an equivalent expression, and $\langle - \,||\, - \rangle = \langle + \,||\, + \rangle = 0$. Similarly:

$$-\frac{i}{2}A_y = g_e g_n \beta_e \beta_n \left(\left\langle r^{-3}\right\rangle \left\langle + \left|\widehat{\mathcal{H}}_y\right| - \right\rangle - \frac{i}{2}\frac{8\pi}{3}\overline{\delta(r)}\right) \tag{5.27a}$$

$$A_y = g_e g_n \beta_e \beta_n \left(\left\langle r^{-3}\right\rangle 2i\left\langle + \left|\widehat{\mathcal{H}}_y\right| - \right\rangle + \frac{8\pi}{3}\overline{\delta(r)}\right) \tag{5.27b}$$

and:

$$\frac{1}{2}A_z = g_e g_n \beta_e \beta_n \left(\left\langle r^{-3}\right\rangle \left\langle + \left|\widehat{\mathcal{H}}_z\right| + \right\rangle + \frac{1}{2}\frac{8\pi}{3}\overline{\delta(r)}\right) \tag{5.28a}$$

$$A_z = g_e g_n \beta_e \beta_n \left(\left\langle r^{-3}\right\rangle 2\left\langle + \left|\widehat{\mathcal{H}}_z\right| + \right\rangle + \frac{8\pi}{3}\overline{\delta(r)}\right) \tag{5.28b}$$

Here evaluation of $\langle - \,||\, - \rangle$ would give an equivalent expression multiplied on both sides by -1. Equations 5.26b-5.28b may be written:

$$A_x = \wp\left(2\left\langle + \left|\widehat{\mathcal{H}}_x\right| - \right\rangle - \kappa\right) \tag{5.29a}$$

$$A_y = \wp\left(2i\left\langle + \left|\widehat{\mathcal{H}}_y\right| - \right\rangle - \kappa\right) \tag{5.29b}$$

$$A_z = \wp\left(2\left\langle + \left|\widehat{\mathcal{H}}_z\right| + \right\rangle - \kappa\right) \tag{5.29c}$$

where[3]:

$$\wp = g_e g_n \beta_e \beta_n \left\langle r^{-3} \right\rangle \tag{5.30a}$$

$$\kappa = -\frac{8\pi\overline{\delta\left(r\right)}}{3\left\langle r^{-3}\right\rangle} \tag{5.30b}$$

and both parameters may be determined by solving the simultaneous equations 5.29 which become two independent equations for a uniaxial matrix.

$\wp$ is a factor which has little meaning on its own; it is simply a product of three constants g_e, β_e and β_n, the well-known g_n factor for a given element, and $\left\langle r^{-3}\right\rangle$, the average value of the inverse cube of the distance of the unpaired electron from the nucleus. Calculated values of $\left\langle r^{-3}\right\rangle$ for free ions may be found tabulated in various places, such as Fraga *et al.* [76], which was used for the point-charge calculations. However, the value of $\left\langle r^{-3}\right\rangle$ for an unpaired electron on an atom in a molecule or crystal lattice is largely an unknown, so calculation of $\wp$ is not trivial. Multiplication of equation 5.30a by $\frac{\mu_0}{4\pi}$ (10^{-7}), where μ_0 is a fundamental constant representing the permeability of free space, gives $\wp$ in joules when β_e and β_n are in JT^{-1} and $\left\langle r^{-3}\right\rangle$ is in m^{-3}.

The definition of κ in equation 5.30b demonstrates that it is proportional to the spin density at the nucleus, as described earlier in this section. It is a unitless parameter, as both the spin density and radial expectation value have units of $(\text{volume})^{-1}$. The product of κ and $\wp$ is more meaningful than κ itself, as it gives the contact interaction energy

$$-\kappa\wp = \frac{2\mu_0}{3} g_e g_n \beta_e \beta_n \overline{\delta\left(r\right)} \tag{5.31}$$

[3] κ is defined with the opposite sign by Golding [68], but has been chosen here and in the Pdorbit calculations to be consistent with Abragam and Bleaney [8].

in SI units. $\kappa\wp$ is often divided by $2g_n\beta_n$, giving the hyperfine field at the nucleus due to the core polarisation

$$H_{cp}^{hf} = \frac{-\kappa\wp}{2g_n\beta_n} = \frac{\mu_0}{3} g_e \beta_e \overline{\delta(r)} \tag{5.32}$$

The computer programme Pdorbit [70] described in section 4.3 and earlier in this section also calculates $\wp$ (and thus $\langle r^{-3} \rangle$) and κ from the input principal A values for a d^1 electron centre under $\bar{4}2m$ symmetry. Golding [68] has tabulated the matrix elements of $\widehat{\mathcal{H}}_{x,y,z}$ (equations 5.24) with the 3d wavefunctions (equations 5.8). These are used to calculate the three matrix elements which appear in equations 5.29 using the coefficients of the ground-state wavefunctions calculated to agree with the observed g values. The solutions to these simultaneous equations are then given by:

$$\wp = \frac{A_z - A_x}{2\left(\langle + |H_z| + \rangle - \langle + |H_x| - \rangle\right)} \tag{5.33a}$$

$$= \frac{A_z - A_y}{2\left(\langle + |H_z| + \rangle + \langle + |H_y| - \rangle_r\right)} \tag{5.33b}$$

where $\langle + |H_y| - \rangle_r$ represents the real coefficients of this matrix element, and:

$$\kappa = 2\langle + |H_x| - \rangle - \frac{A_x}{\wp} \tag{5.34}$$

$\langle r^{-3} \rangle$ is readily obtained from $\wp$ using equation 5.30a.

Once again, expressions have also been developed using the perturbation wavefunctions 5.10, which lead to the formulae listed in Claridge *et al.* [39]:

$$A_\perp = \frac{1}{7}\wp\left(2N^2 - 11Nx - 2y^2 + 11xy - 7\kappa\right) \tag{5.35a}$$

$$A_\parallel = -\frac{1}{7}\wp\left(4N^2 + 56Ny + 6Nx + 4y^2 + 8x^2 + 6xy + 7\kappa\right) \tag{5.35b}$$

These equations agree with the first-order equations given by Abragam and Bleaney [8], page 456.

The results of these calculations for the three point-group-symmetry $\bar{4}2m$ d^1 centres in zircon whose g values were analysed earlier in this section are given in table 5.5. Also included for comparison are theoretical free-ion values $\langle r^{-3} \rangle_{th}$ taken from Fraga *et al.* [76], and a theoretical

value of the hyperfine field at the nucleus due to core polarisation ($\equiv \frac{-\wp\kappa}{2g_n\beta_n}$) for d^1 ions.

This theoretical hyperfine field was calculated using a theoretical value of the parameter χ per unit spin which is related to κ by [8]:

$$\chi = -\frac{3}{2}\kappa \left\langle r^{-3} \right\rangle \tag{5.36}$$

Using equations 5.36 and 5.30b:

$$\frac{\chi}{a_0^3} = 4\pi\overline{\delta(r)} \tag{5.37}$$

where χ is in atomic units, and division by the Bohr radius, a_0, gives the right-hand side in SI units. By comparison with equation 5.32, H_{cp}^{hf} per unit spin (S) in tesla is given by

$$H_{cp}^{hf} = \frac{\mu_0 g_e \beta_e}{6\pi a_0^3}\chi \tag{5.38a}$$

$$= 8.3542\chi \tag{5.38b}$$

with χ expressed in atomic units. The theoretical value of χ for d^1 ions (-2.8 au) was taken from the 3d-ion plot in figure 4 of Watson and Freeman [79], calculated using a exchange-polarised Hartree-Fock (EPHF) method for free ions.

The values of $\left\langle r^{-3} \right\rangle$ and $-\wp\kappa/2g_n\beta_n$ calculated from the experimental data are all smaller than the theoretical values calculated for free ions. The smaller radial expectation values suggest that the unpaired d electron is on average further away from the nucleus than would be predicted for the free ion, which is not unexpected. Secondly, the reduction in $\left\langle r^{-3} \right\rangle$ for the covalently bound Si(Ti^{3+}) centre is greater than for the ionically bound Zr(Ti^{3+}) centre, which also seems reasonable given that electron density will be drawn away from the ion in the covalent case. The calculated value for the V^{4+} ion is very low, and would seem to be rather suspect. It is difficult to comment on this value since the experimental data were not collected by the Canterbury epr group.

The hyperfine fields calculated from the experimental data follow the same pattern as the $\left\langle r^{-3} \right\rangle$ values. This is not surprising, because even though the hyperfine field at the nucleus is ostensibly independent of $\left\langle r^{-3} \right\rangle$ (equation 5.32), the spin density at the nucleus which arises through spin polarisation will have some kind of dependence on the unpaired electron distri-

Table 5.5: Fitted and theoretical parameters from analysis of principal values of hyperfine matrices.

	$Zr(Ti^{3+})$	$Si(Ti^{3+})$	V^{4+}
$A_{\parallel}$ (mT)	2.9714	2.5299	8.729
$A_{\perp}$ (mT)	0.8986	0.7274	3.092
$\wp$ (10^{-4} cm^{-1})	−21.300	−16.583	55.178
κ	0.6326	0.6799	0.7847
$\langle r^{-3} \rangle$ (au)	2.1196	1.6502	1.1794
$-\wp\kappa/2g_n\beta_n$ (T)	−8.3914	−7.0214	−5.7920
$\langle r^{-3} \rangle_{th}$ (au)	2.54512	2.54512	3.67197
H_{cp}^{hf} (T)	−11.70	−11.70	−11.70

bution. The value for the hyperfine field at the nucleus calculated from experiment may be used to calculate an experimental χ from equation 5.38b. The calculation gives $\chi = -2.01$ for $Zr(Ti^{3+})$ and $\chi = -1.68$ for $Si(Ti^{3+})$. The former value compares well with the trend shown by experimental points for oxygen-coordinated 3d ions in salts in figure 4 of Watson and Freeman [79]. The authors note that covalency reduces core polarisation, and state that a crude account of covalency in their calculations gave good agreement with the experimental results. The lower value of χ for the $Si(Ti^{3+})$ centre probably implies more covalency than was present in the salts used for the experimental work quoted by Watson and Freeman (see references therein).

A simple alternative calculation of the hyperfine field due to core polarisation may also be carried out. This approach is relied on in the case of the d^3 Cr^{3+} work in section 5.3.3, as the above theory used in Pdorbit does not apply in the d^3 case. It is used here for a comparison with the results from the more complex calculations carried out above.

The experimental hyperfine fields at the nucleus along the principal directions are given by $\frac{A_{\parallel}}{g_n\beta_n} = -29.49$ T and $\frac{A_{\perp}}{g_n\beta_n} = -8.479$ T. These represent the sum of core polarisation, orbital and dipolar contributions, as may be surmised by an inspection of equations 5.20. A detailed discussion of the interpretation of hyperfine data is contained in Freeman and Watson [80]. The

orbital hyperfine field is given by [5], [81]:

$$H_{orb}^{hf} = g_e \beta_e \left\langle r^{-3} \right\rangle \Delta g_L \tag{5.39}$$

where Δg_L is the shift of the g values from g_e due to admixture of other orbital states only; admixture of spin states can arise only when the ground state is orbitally degenerate. For the orbital-singlet $^4A_1$ ground state of Cr^{3+}, Δg may be taken to be entirely due to orbital admixture. If $\left\langle r^{-3} \right\rangle$ is given in atomic units, the orbital hyperfine field in tesla will then be given by:

$$H_{orb}^{hf} = 12.5314 \left\langle r^{-3} \right\rangle \Delta g_L \tag{5.40}$$

For the Si(Ti^{3+}) centre, using $\left\langle r^{-3} \right\rangle$ for Ti^{3+} from Fraga *et al.* [76] quoted in table 5.5, $H_{orb}^{hf} = -5.300$ T for $g_{\|}$ and -0.693 T for $g_{\perp}$. The hyperfine field due to core polarisation and dipolar interaction only must then be -24.19 T in the z direction, and -7.787 T in the x and y directions. If it is assumed that the remaining hyperfine field is made up of an isotropic contribution due to the core polarisation field, and a uniaxial contribution due to the dipolar interaction, then $H_{cp}^{hf} = -13.26$ T, and $H_{dip}^{hf} = -10.94$ T in the z direction, and $+5.468$ T in the x and y directions.

The result for H_{cp}^{hf} is significantly larger than even the theoretical value calculated in table 5.5, which is not likely to be the case. As noted previously, covalency is known to reduce the core polarisation, so the experimental value would be expected to be less than the free-ion calculation, as was found for the Pdorbit calculations. It is likely that these alternative calculations will be more valid when the core polarisation is dominant, as is the case for the Cr^{3+} centre for which it will be used in the next section.

Nuclear quadrupole matrix For a single d electron the experimental parameter $P_{\|}$ should be given by ([8], p456):

$$P_{\|} = \frac{3e^2 Q \left\langle r_q^{-3} \right\rangle_{3d}}{7I(2I-1)} \tag{5.41}$$

where e is the electronic charge, Q is the nuclear quadrupole moment, and $\left\langle r_q^{-3} \right\rangle_{3d}$ differs from $\left\langle r^{-3} \right\rangle_{3d}$ because of electrostatic shielding (or antishielding) of the nucleus. Alternatively ([8],

p167):

$$P_{\|} = \frac{3e^2Qq}{4I(2I-1)} \tag{5.42}$$

where eq is the z component of the electric-field gradient (efg) at the nucleus, due to electronic and lattice contributions. The contribution to q by the unpaired (valence) electron in the $d_{x^2-y^2}$ orbital, q_{val}, is given by:

$$q_{val} = +\frac{4\langle r^{-3}\rangle_{3d}}{7} \tag{5.43}$$

resulting in a contribution to $P_{\|}$ of $3e^2Qq_{val}/40$ for a nucleus with spin $I = \frac{5}{2}$ (equation 5.42). For the Zr(Ti^{3+}) centre, this gives a value of +0.2211 mT [9], using the experimentally determined value of $\langle r^{-3}\rangle_{3d}$ quoted therein. However, this value is lowered by the Sternheimer shielding (see [79], p71 and references therein) due to a distortion of the charge cloud of the inner electron shells which changes the efg at the nucleus due to the unpaired electron. This effect is accounted for by rewriting $\langle r^{-3}\rangle_{3d}$ in equation 5.43 as $\langle r_q^{-3}\rangle_{3d} = (1-R)\langle r^{-3}\rangle_{3d}$. The value of R is usually of the order 0.1 - 0.2 [8], p708, and was estimated in [9] to have a value of +0.28, to agree with the experimental results. The (negative) contribution to q by the surrounding oxygen ions was calculated to be negligible in comparison to the valence contribution, as is usually found to be the case for paramagnetic ions [8], p708. Because $P_{\|}$ is mostly due to q_{val} in the case of Zr(Ti^{3+}), knowing the sign of q_{val} and Q to be positive for ^{47,49}Ti allowed the sign of the experimental $P_{\|}$ to be made positive, according to equation 5.42.

However, for the Si(Ti^{3+}) centre, the experimental value of $P_{\|}$ is considerably smaller, meaning that either the valence contribution to the efg at the nucleus is smaller, the (negative) lattice contribution is greater, or a mixture of both. Hence, the sign of $P_{\|}$ is also not as clear cut as the Zr(Ti^{3+}) case. The valence contribution would be reduced if the local symmetry of the silicon site was close to tetrahedral, being zero for exact tetrahedral symmetry, with an orbitally degenerate ground state . However, the symmetry of both sites is dodecahedral, and neither is very close to tetrahedral, despite the silicon site being surrounded by an approximate tetrahedron of oxygen atoms. The point-charge and crystal-field spin-orbit-coupling calculations presented earlier demonstrate this fact, with the latter giving the crystal-field splitting between the b_1 ground state and next highest energy (b_2) state as *ca* 7500 cm^{-1} (table 5.4).

The valence contribution may also be reduced by increasing the shielding factor R, although

the value is already outside the usual range of 0.1 - 0.2 quoted above. For Si(Ti^{3+}), the valence contribution to $P_{\|}$ using the value for $\langle r^{-3} \rangle_{3d}$ given in table 5.5 is calculated to be +0.179 mT. With the shielding taking into account by using the same R factor as used for Zr(Ti^{3+}), this value is lowered to +0.129 mT. This is still an order of magnitude too large in comparison with the experimental value of 0.0157 mT. Using a simple point-charge model containing only oxygen atoms with a charge of −1, the lattice contribution to $P_{\|}$ for the silicon site is −0.00858 mT, as reported in [39] (−0.008042 mT using a value of Q consistent with that used later, and oxygen positions as in table 5.2). The oxygen charge of −1 was used to reflect the covalency of the SiO_4^{4-} unit, as reduced from the −2 value which would be expected for an ionic structure. The anti-shielding effect of the polarisation of the closed shells, in this case caused by external charges, is again taken into account using the formulation developed by Sternheimer $q^*_{lat} = q_{lat}\,(1 - \gamma_\infty)$ where q^*_{lat} is the efg actually experienced at the nucleus due to the external charges ([79], p71 and references therein). Unlike the R factor, γ_∞ is found to be large and negative, magnifying the efg contribution that would be expected in the absence of polarisation. For Ti^{3+}, $1 - \gamma_\infty$ has been estimated to lie between +10 and +15 [82], giving a contribution to $P_{\|}$ of −0.0858 - −0.129 mT. Thus the calculated total $P_{\|}$ due to both the valence and lattice contributions was reported to range from 0 - +0.043 mT, encompassing the true experimental value. With this model, the calculated lattice contribution to $P_{\|}$ is directly proportional to the charge assigned to the oxygen atoms. Thus taking a value between −1 and −2 would increase the contribution calculated above, and make $P_{\|}$ more negative.

These calculations have been revisited with an inclusion of the two nearest-neighbour zirconium atoms in the point-charge lattice contribution to the efg. It was expected that due to the increased distance of these atoms from the titanium atom, the effect of this addition would be relatively minor. However, the calculation shows that the inclusion of the two zirconium atoms with a charge of +4 changes the sign of the lattice contribution, giving a contribution to $P_{\|}$ of +0.00814 mT before shielding is taken into account. When added to the value for the valence contribution, which is already too large and positive, this newly calculated lattice contribution will clearly make the agreement between the calculated and experimental values of $P_{\|}$ even worse. If the charge on the oxygen atoms is assigned a value of −2, as would be the case for an ionic structure, the lattice contribution to $P_{\|}$ becomes very small, due to the

near cancellation of positive and negative terms. In this case a value of $+0.37 \times 10^{-5}$ mT is obtained. The lattice contribution is then negligible in comparison to the valence contribution, but the valence contribution remains too large in comparison with the experimental value.

The failure of these calculations to reproduce the experimental results for the Si(Ti^{3+}) centre when they were successful for the Zr(Ti^{3+}) centre can probably be attributed to the effect of covalency in the silicon site, which is not taken into account. The zirconium site is principally ionic in the ideal zircon structure, and would be likely to remain so when the similar titanium atom is substituted into this site. The TiO_4^{4-} entity may be less covalent than the normal SiO_4^{4-} group, but is likely to be forced to be somewhat more covalent than titanium in the zirconium site. An investigation of other substitutional transition-metal electron centres which are observed in both the silicon and zirconium sites would make a useful comparison.

Equations 5.41 and 5.42 show that the ratio of the principal values of the nuclear quadrupole matrix for the ^{47}Ti and ^{49}Ti data should be given by

$$\frac{^{47}P_{\|}}{^{49}P_{\|}} = \frac{^{49}I\left(2^{49}I-1\right)}{^{47}I\left(2^{47}I-1\right)} \times \frac{^{47}Q}{^{49}Q} = \frac{21}{10} \times \frac{^{47}Q}{^{49}Q} \tag{5.44}$$

where $\langle r^{-3} \rangle_{3d}$ is assumed to be equal for the two isotopes. Substituting in values for the electric quadrupole moment of $0.29 \times |e| \times 10^{-24}$ cm^2 for ^{47}Ti and $0.24 \times |e| \times 10^{-24}$ cm^2 for ^{49}Ti [83] gives a theoretical ratio of 2.54. This agrees with the experimental ratio of 2.3 within the limits of experimental error, 1.6 - 3.5. For the Zr(Ti^{3+}) centre, initial disagreement between the predicted and experimental ratio of $P_{\|}$ for the two isotopes was shown [24], [9] to be the result of the neglect of high-spin terms in the Hamiltonian which were later fitted. There are apparently no such terms required to fit the Si(Ti^{3+}) centre.

5.3 The Cr^{3+} (Z) centre

5.3.1 Experimental details

In the Canterbury laboratory, the Z centre was first observed, along with the C centre, in an artificially grown undoped crystal supplied by Aerospace Corporation [25]. The centres were observed after x-irradiation at 77 K and cold transfer to the previously cooled Displex head.

Annealing of the crystal to room temperature removed the prominent Zr(α), the $[AlO_4]^0$ and a number of other centres, leaving behind the C and Z centres and the Zr(Ti^{3+}) centre [25]. In this crystal, the C centre had much greater intensity than the Z centre, and the two centres were thought to be part of the same defect, since they appeared together, had similar stability to annealing, and were coincident within the experimental resolution in the c-axis orientation.

In all of the zircon crystals subsequently grown as a part of this work, the relative intensities of the two centres were swapped, and it was possible to record some much better spectra of the Z centre. All of the figures and results described in this section are the result of measurement of the Z centre in a crystal from the M growth run (table 3.1) which had been gamma irradiated for *ca* 48 hours at room temperature. Spectra were measured in both the *bc* and *ab* planes. For the *bc*-plane data, the crystal was mounted on one of the naturally occurring *bc* faces. For measurement in the *ab* plane, the crystal was mounted by glueing two adjacent *bc* faces to a vertical corner mount (top right of figure 1-3a). The c-axis spectrum of this crystal is dominated by intense Z-centre and Zr(Ti^{3+})-centre signals, and a weak C-centre signal may be observed away from the c axis. Alignment of the crystal in the c-axis orientation was confirmed by observing the exact turning point of the Z centre. All measurements were carried out at *ca* 15 K.

5.3.2 Results

The Z centre is highly anisotropic, with apparent g values of 1.9991 and 3.9118 [25], corresponding to a change in the resonant field of around 160 mT when the crystal is rotated between the c and b axes. In the c-axis orientation, it is observed to coincide with the isotropic C centre to within the limits of experimental resolution of around 0.02 mT, which is now known to be simply a coincidence. No site splitting of the Z-centre signal is observed within the experimental linewidth, indicating a point-group symmetry of $\bar{4}2m$.

The first indication that the two centres might be independent came when the intensity ratio was observed to be different in the new artificially grown crystals. More compelling evidence came when an undoped crystal (growth K of table 3.1) was measured at low temperature in Paderborn, Germany [72]. The saturation behaviour of the two centres as a function of both temperature and microwave power was studied [26], with access to temperatures lower than were

obtainable in the Canterbury laboratory. It was discovered that at these lower temperatures, the saturation behaviour of the two centres was quite different. Below 14 K, the C centre begins to rapidly lose intensity at low power, while the Z centre continues to gain intensity (see figure 2, [26]).

The increased intensity of the Z centre in the new crystals allowed all of the associated hyperfine lines to be observed, where some had previously been overlooked due to both the lack of intensity and interference from the structure associated with the C centre. In particular, there was a set of four hyperfine lines indicative of a nuclear spin of $\frac{3}{2}$ [26][4]. These hyperfine lines are clearly visible in figure 5-5, a stacked plot of spectra taken every degree of rotation up to 5 degrees in either direction from the c axis. The hyperfine lines marked in this figure clearly follow the more intense central line due to the spinless isotopes, as the crystal is rotated away from the c axis. Also visible in this figure, and marked in figure 5-6 is a sextet of hyperfine lines due to interaction with ^{91}Zr. These lines had been very weak in the original crystal, but had been correctly assigned to ^{91}Zr [25].

A long scan of the Z centre and all of the hyperfine lines was made to increase the signal-to-noise ratio and allow an accurate calculation of the intensity ratio of both the sextet and quadruplet of hyperfine lines to the central line. The intensity of the quartet of hyperfine lines is 9.67 % of the total intensity of the quartet plus the central line, in good agreement with the natural abundance of ^{53}Cr of 9.55 %, which has the required nuclear spin of $\frac{3}{2}$. No other element has a single nuclear spin $\frac{3}{2}$ isotope with the same natural abundance. The intensity of the sextet was initially calculated to be significantly lower than the 20.19 % expected for the two nearest-neighbour zirconium atoms. However, it was later discovered that some of the lower-intensity lines present in the c-axis spectrum are ^{91}Zr forbidden hyperfine lines, as discussed later. A recalculation of the intensity including the forbidden lines gave a figure of 22.6 %, in reasonable agreement with the expected value. Figure 5-6 is a spectrum of the Z and C centres rotated 1.5° away from the c axis, showing all of the ^{53}Cr and ^{91}Zr hyperfine lines.

The effective g values of 2.0 and 4.0 suggest that the observed spectrum is a transition between one of the doublets of an $S = \frac{3}{2}$ system with a large zero-field splitting (zfs) (Hutton

[4]The ^{53}Cr and ^{91}Zr matrices reported in this paper are derived from measurement of the c- and b-axis splittings only, and are superceded by the data-fitted hyperfine matrices reported herein.

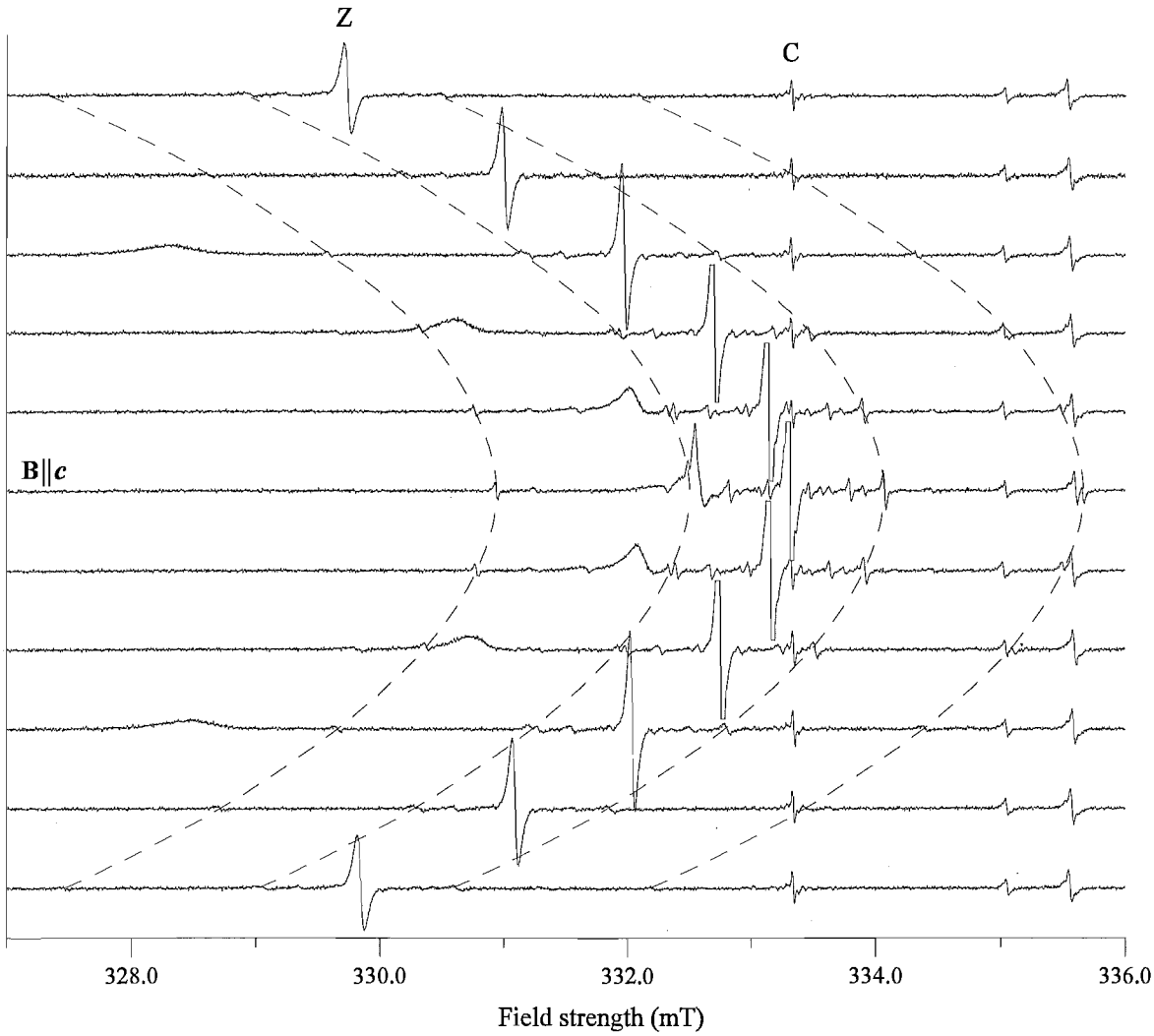

Figure 5-5: Stacked plot of Z-centre epr spectra near the c axis at *ca* 15 K showing ^{53}Cr hyperfine structure (dashed lines). Average frequency $\approx$ 9.3268 GHz. Successive spectra correspond to crystal rotation by one degree. The central line has been clipped in some orientations for clarity.

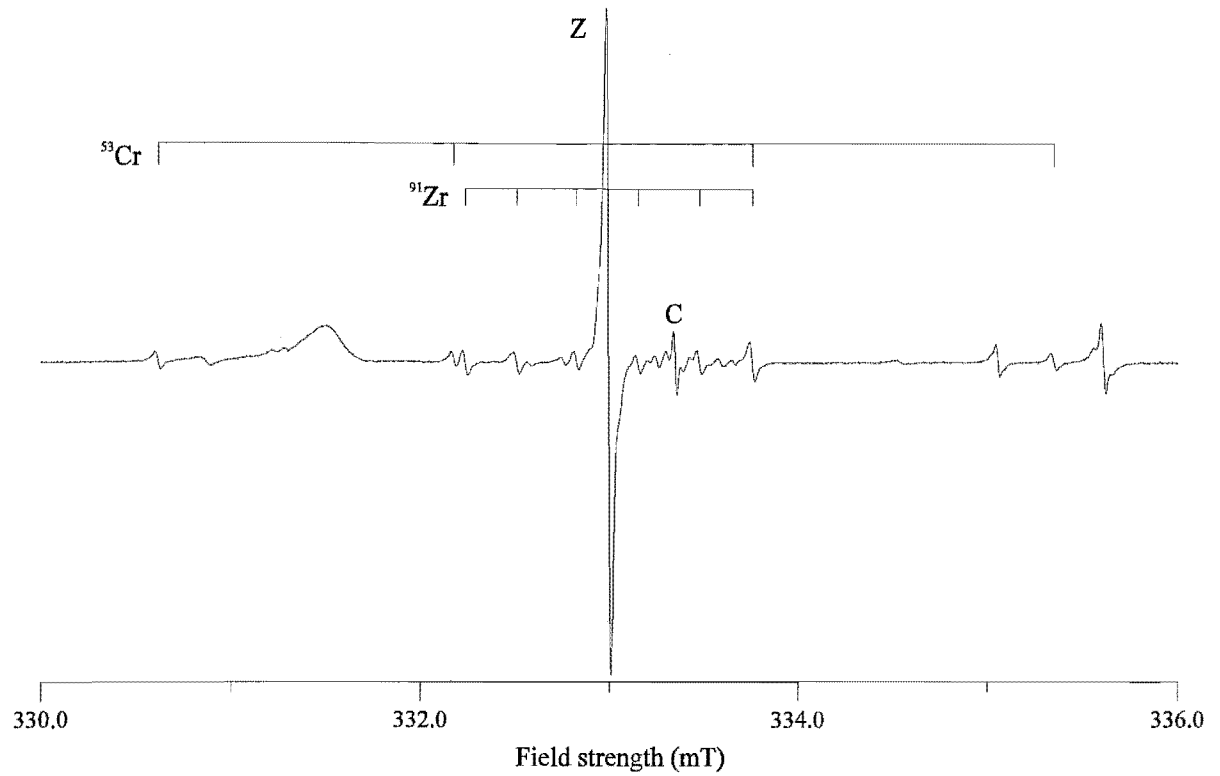

Figure 5-6: Epr spectrum of C and Z centres in zircon at *ca* 15 K 1.5° from the *c* axis. Frequency = 9.32701 GHz.

(1969) [84], Pilbrow (1978) [85], see discussion). This would require the chromium ion to have an oxidation state of +3, a common state for chromium. A Cr^{3+} centre with a large zero-field splitting is reported in Krasnobaev *et al.* [63], where transitions were also observed in only one doublet. However, no fitted parameter matrices were given, other than a value of $A_{\|}$ (1.92 mT) and $A_{\perp}$ (1.45 mT), a fairly poor agreement with the Z centre fitted values (5.7).

Two growths of chromium-doped crystals were attempted, one with chromium in a +3 oxidation state, and one with chromium in a +6 oxidation state, growth runs 99G and 99H of table 3.1 respectively. Epr measurements were made for both sets of crystals prior to any irradiation, and both revealed a reasonably intense Z centre. The intensity was not as high as might have been hoped for a doped crystal, but more surprising was the presence of the Z centre in the unirradiated 99H crystal. Apparently during the incorporation of the chromium into the zircon lattice during growth, the oxidation state is changed to +3. It is unclear what

species in the growth mixture may have been responsible for this reduction, although it may have been an impurity.

It was suggested in the earlier paper [25] that the chromium may exist in the unirradiated crystal in the +4 oxidation state, and only become readily visible to epr after trapping an electron, similar to the titanium centres. There has been no evidence of a d^2 Cr^{4+} centre in any of the zircons studied, but such a centre could be epr silent, as discussed in [25]. Secondly, attempts to anneal the Z centre in both the original doped crystal and new doped crystals have proved unsuccessful, even after heating to 900° C for over 15 hours. This evidence seems to support the inclusion of chromium into the zircon lattice only in the +3 oxidation state.

The linewidth of the Z centre changes considerably as it is rotated in the *bc* plane. In the *c*-axis orientation, the linewidth is *ca* 0.020 mT. As the crystal is rotated away from the *c* axis, the line rapidly broadens to 0.086 mT at 10° rotation, and to a maximum of *ca* 0.11 mT near 20°. The linewidth then narrows to 0.038 mT in the *a*- or *b*-axis orientation. The *ab*-plane data were collected with a higher modulation amplitude to improve the signal-to-noise ratio, which resulted in an instrumental increase of the linewidth. In the *a*- or *b*-axis orientation the linewidth was 0.050 mT, which decreased to 0.036 mT near the [110] orientation.

As the crystal is rotated in the a*b* plane towards the [110] direction, not only is there is a narrowing in the linewidth, but also the appearance of a number of extra lines in the ^{91}Zr hyperfine region. Figure 5-7 shows a stacked plot of the Z centre and associated hyperfine lines as the crystal is rotated in 10° steps from **B**|| **a** to **B**|| **b**. The *a* and *b* orientations are only approximate as there is not a good reference signal to observe. The figure shows that the increase in the number of lines is clearly not due simply to improved resolution because of the reduced linewidth. Some of the extra lines occur between the pairs of the usual sextet, and rapidly lose intensity away from the intermediate orientation.

These extra lines strongly resembled forbidden hyperfine lines, which had been observed and interpreted before, such as for the Zr(Ti^{3+}) centre [24], [9]. The presence of such lines in the ^{91}Zr hyperfine structure implied that a significant non-uniaxial ^{91}Zr quadrupole interaction was present. Such an interaction could also explain a hyperfine pattern which was not evenly spaced. As can be seen in figure 5-6 upon close inspection, the outer two splittings are significantly smaller than the inner three. Line positions recorded from a long run-time spectrum 2° from

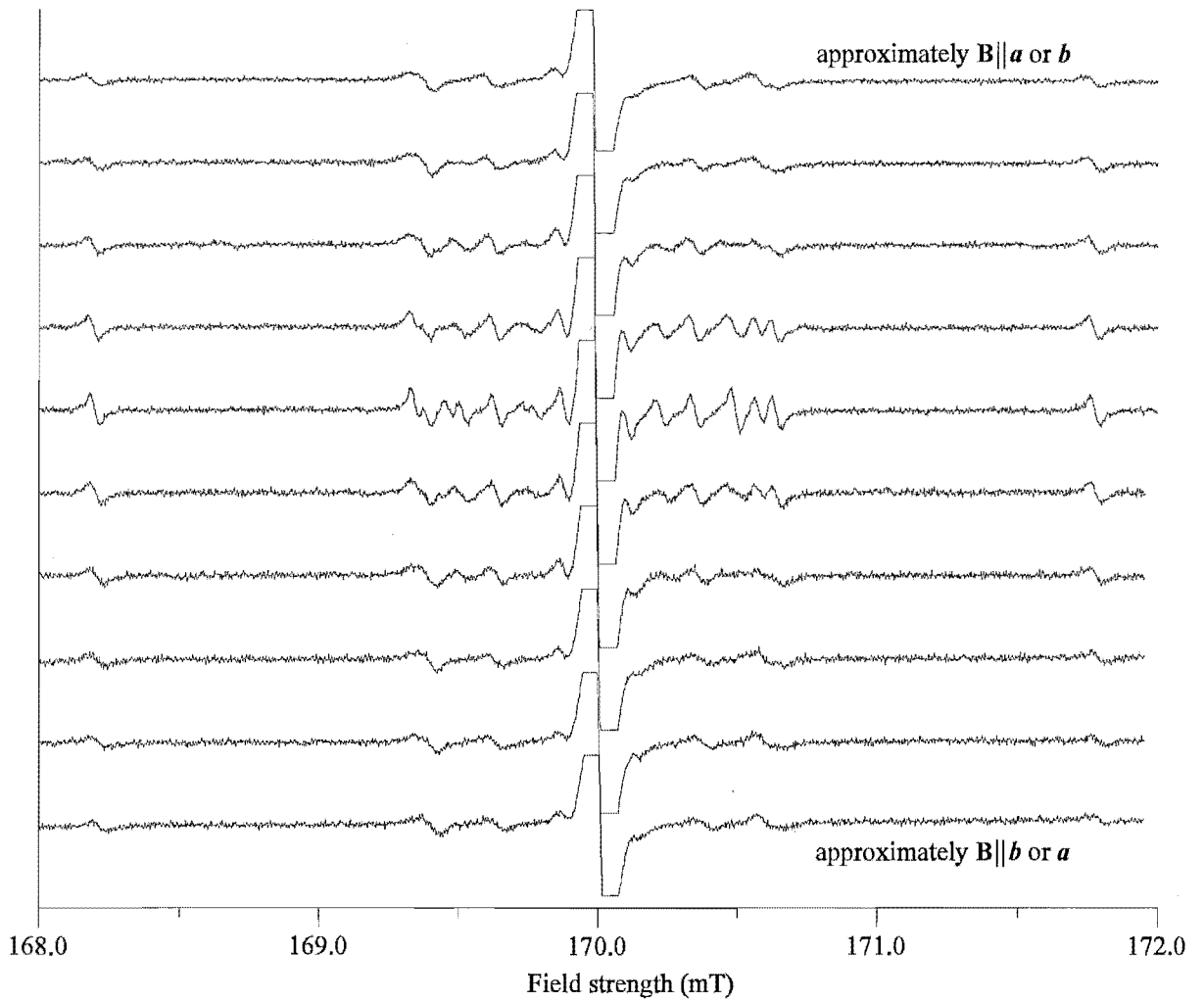

Figure 5-7: Stacked plot of Z-centre epr spectra in zircon at *ca* 15 K in the *ab* plane. Average frequency $\approx$ 9.3099 GHz. The central line has been clipped for clarity.

the c axis yielded the splittings 0.270 mT, 0.318 mT, 0.328 mT, 0.325 mT and 0.281 mT with an experimental error of approximately $\pm$ 0.005 mT. The fitted matrices (with a quadrupole matrix which was zero within the uncertainty) did not initially reproduce this pattern of hyperfine lines, but rather a very gradually increasing splitting from the low-field to high-field end of the spectrum. This is the usual pattern observed for hyperfine lines in the absence of quadrupolar effects.

To collect more data for the extra lines, the crystal was mounted on a 45° mount, as in figure 1-3a, where $\alpha = 45°$. This mount allowed spectra to be recorded from the c-axis orientation to the [110] orientation. It also provided a more precise alignment in the [110] orientation than the ab-plane data. A long run-time spectrum in this orientation is shown in figure 5-8, with very good resolution of the forbidden ^{91}Zr lines.

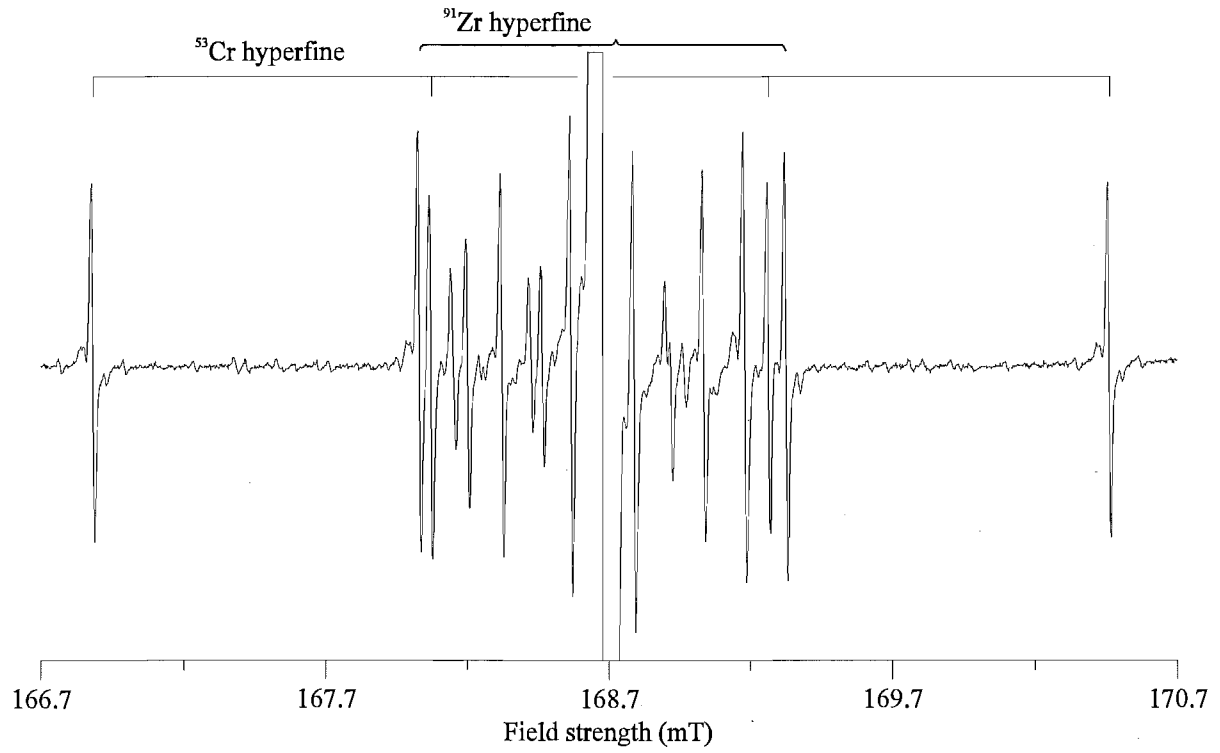

Figure 5-8: Epr spectrum of Z centre in zircon at 15 K, in [110] orientation, frequency = 9.23762 GHz. The central line has been clipped. The very small lines seen in the relatively flat region between the outer chromium lines are zirconium hyperfine lines on the chromium hyperfine lines.

The extra data allowed a non-zero P matrix to be fitted for the zirconium lines. The spin Hamiltonian used for the fitting of the Z centre lines was of the form:

$$\widehat{\mathcal{H}} = \beta_e \mathbf{B.g.\hat{S}} + \mathbf{\hat{S}.D.\hat{S}} + \mathbf{\hat{S}.A.\hat{I}} + \mathbf{\hat{I}.P.\hat{I}} - \beta_n \mathbf{B.g}_n\mathbf{.\hat{I}} \tag{5.45}$$

where $\mathbf{g}_n$ was set as the scalar matrix $-0.3147\mathbf{U}$ for ^{53}Cr and $-0.521448\mathbf{U}$ for ^{91}Zr. $\mathbf{U}$ is the 3×3 unit matrix, and -0.3147 and -0.521448 are the g_n values of ^{53}Cr and ^{91}Zr set internally by EPR-NMR. Only the first two terms were required for the analysis of the central-line spectra resulting from the spinless chromium isotopes.

The data were fitted in two ways for the spinless isotopes. In the first fitting, only the *bc*-plane data were used, and were fitted to uniaxial parameter matrices. With this symmetry, there should be no anisotropy in the *ab* plane. Experimental measurements do show a slight anisotropy in this plane, but this might be interpreted as a slight misalignment of the crystal on its mount. The anisotropy is < 0.03 mT in the most recent measurements, and is not readily apparent in figure 5-7. Simulations using the fitted uniaxial matrices showed that the observed anisotropy in the most recent set of data may be reproduced by a crystal tilt of about 1.2°. In the second fitting, the anisotropy in the *ab* plane was treated as a real effect, and included in the fit. It is accounted for in this fit by allowing only the electronic quadrupole matrix to become slightly non-uniaxial.

The ^{53}Cr fitting used only the *bc*-plane data, while the ^{91}Zr fitting used data from both the *bc* and 45° planes. The ^{91}Zr quadrupole matrix had to be fitted without the restriction of uniaxiality, in order to account for the observed anisotropy in the hyperfine spectrum. The final fits are given in tables 5.6 and 5.7. The differences in the values of $\mathbf{g}$ and $\mathbf{D}$ in the different fits are more likely to be due to the different data sets used than any real isotope effects. The uncertainties output by EPR-NMR [28], especially for $\mathbf{D}$, should probably be a little larger. Very small changes in anisotropy which might be found in separately collected data sets can lead to large changes in the fitted D matrix. Figure 5-9 shows a comparison between the experimental spectra and spectra simulated from the matrices of table 5.7, for the zirconium lines in the *c*-axis and [110] orientations.

Table 5.6: Spin-Hamiltonian parameters for the spinless isotope line of the Z centre in zircon at *ca* 15 K. Error estimates in parentheses.

	Spinless isotopes				
	bc only		*ab* and *bc*		
	Principal values		Principal values		
Matrix $\mathbf{Y}$	$Y_\parallel$	$Y_\perp$	Y_x	Y_y	Y_z
$\mathbf{g}$	1.99927(7)	1.9580(1)	1.9578(1)	1.9578(1)	1.99926(7)
$\mathbf{D}/g_e\beta_e$ (mT[a])	−1980(100)	990(100)	928.0(50.0)	928.4(50.0)	−1860(100)
Total data points	23		35		
Unit weighted	19		31		
$\sum$ weightings	19.04		31.13		
RMSD (mT)	0.0190		0.0177		

Table 5.7: Spin-Hamiltonian parameters for the Z centre in zircon at *ca* 15 K, ^{53}Cr and ^{91}Zr. Error estimates in parentheses.

	^{53}Cr		^{91}Zr		
	Principal values		Principal values		
Matrix $\mathbf{Y}$	$Y_\parallel$	$Y_\perp$	Y_x	Y_y	Y_z
$\mathbf{g}$	1.99924(4)	1.95817(8)	1.9581(1)	1.9581(1)	1.99932(4)
$\mathbf{D}/g_e\beta_e$ (mT[a])	−1740(50)	870(50)	960(120)	960(120)	−1910(120)
$\mathbf{A}/g_e\beta_e$ (mT)	1.575(5)	1.165(3)	0.241(2)	0.241(2)	0.290(3)
$\mathbf{P}/g_e\beta_e$ (mT)	0.0067(18)	-0.0034(9)	0.022(2)	-0.016(2)	-0.007(2)
Total data points	97		156		
Unit weighted	43		96		
$\sum$ weightings	49.32		106.16		
RMSD (mT)	0.0218		0.0257		

[a] multiply by $\frac{g_e\beta_e}{10^9 h} = 28.0249$ for units of MHz

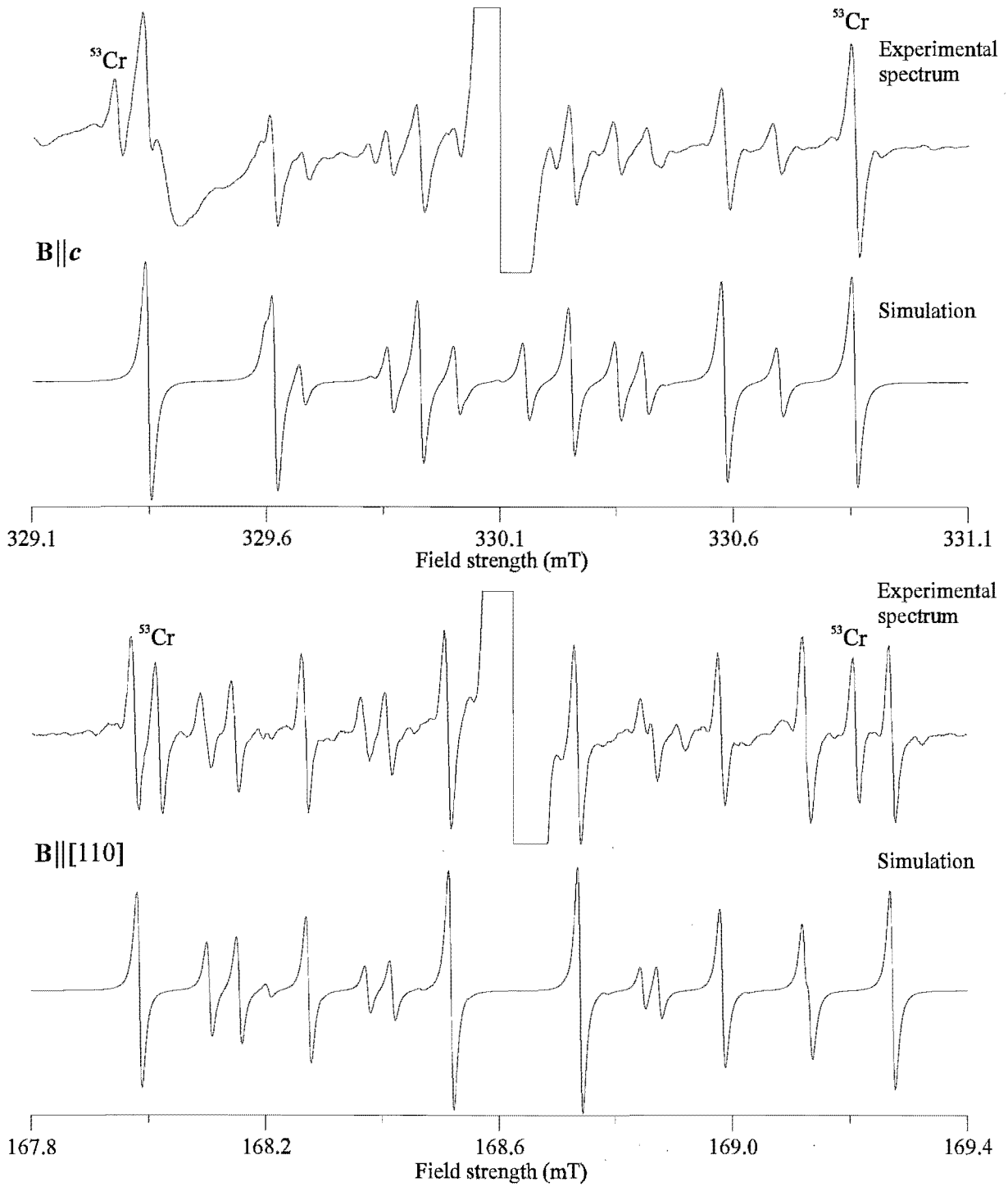

Figure 5-9: Experimental and simulated epr spectra of ^{91}Zr lines of the Z centre in zircon at 15 K, in the c-axis (top, 9.23719 GHz) and [110] (bottom, 9.23762 GHz) orientations. The simulated spectra show only the ^{91}Zr lines. The central line has been clipped in the experimental spectra.

5.3.3 Discussion

Effective g values

The effective g values of 1.9991 and 3.9118 when the line positions of the Z centre are fitted to an $S = \frac{1}{2}$ system are suggestive of an $S = \frac{3}{2}$ centre with a large zfs [84], [85]. The zero-field Hamiltonian is given by [3]:

$$\widehat{\mathcal{H}}_{zf} = D\left(\hat{S}_z^2 - \frac{1}{3}\hat{S}^2\right) + E\left(\hat{S}_x^2 - \hat{S}_y^2\right) \tag{5.46}$$

where:

$$D = \frac{3}{2}D_z \tag{5.47a}$$

$$E = \frac{1}{2}\left(D_x - D_y\right) \tag{5.47b}$$

where the principal values of $\mathbf{D}$ are labelled so that

$$|D_z| > |D_x| \geq |D_y| \tag{5.48}$$

The matrix elements of the zero-field Hamiltonian between the four eigenfunctions of the $\hat{S}_z$ operator for an $S = \frac{3}{2}$ system are:

$$\begin{array}{c|cccc} & \left|\frac{3}{2}\right\rangle & \left|-\frac{3}{2}\right\rangle & \left|\frac{1}{2}\right\rangle & \left|-\frac{1}{2}\right\rangle \\ \left\langle\frac{3}{2}\right| & D & 0 & 0 & \sqrt{3}E \\ \left\langle-\frac{3}{2}\right| & 0 & D & \sqrt{3}E & 0 \\ \left\langle\frac{1}{2}\right| & 0 & \sqrt{3}E & -D & 0 \\ \left\langle-\frac{1}{2}\right| & \sqrt{3}E & 0 & 0 & -D \end{array} \tag{5.49}$$

For a system which is exactly uniaxial, $E = 0$. The matrix 5.49 then reduces to a diagonal matrix with the eigenvalues D for the $\left|\pm\frac{3}{2}\right\rangle$ doublet, and $-D$ for the $\left|\pm\frac{1}{2}\right\rangle$ doublet. For a large zfs, the magnetic-field interaction is given by $g_e\beta_e B_i\hat{S}_i$ where $i = x, y, z$ may then be treated as a perturbation. The fitted spin-Hamiltonian parameters of tables 5.6 and 5.7 give $\frac{D}{g_e\beta_e} \approx 2800$ mT, or $\frac{D}{h} = 78.5$ GHz, more than 8× the microwave energy. The perturbation treatment is

thus a valid one. For the magnetic field in the z direction, the zfs - magnetic-field-interaction matrix is:

$$\begin{array}{cccccc} & \left|\frac{3}{2}\right\rangle & & \left|-\frac{3}{2}\right\rangle & \left|\frac{1}{2}\right\rangle & \left|-\frac{1}{2}\right\rangle \\ \left\langle\frac{3}{2}\right| & D+\frac{3}{2}g_e\beta_e B_z & & 0 & 0 & 0 \\ \left\langle-\frac{3}{2}\right| & 0 & & D-\frac{3}{2}g_e\beta_e B_z & 0 & 0 \\ \left\langle\frac{1}{2}\right| & 0 & & 0 & -D+\frac{1}{2}g_e\beta_e B_z & 0 \\ \left\langle-\frac{1}{2}\right| & 0 & & 0 & 0 & -D-\frac{1}{2}g_e\beta_e B_z \end{array} \tag{5.50}$$

Thus the splitting of the $\left|\pm\frac{3}{2}\right\rangle$ doublet is given by $3g_e\beta_e B_z$, and the splitting of the $\left|\pm\frac{1}{2}\right\rangle$ doublet by $g_e\beta_e B_z$. Equating these expressions with equation 1.6 for the resonance condition with $\mathbf{B}\|\,\mathbf{z}$ gives:

$$g_z = g_\| = 3g_e \qquad \left(\left|\pm\frac{3}{2}\right\rangle\right) \tag{5.51a}$$

$$g_z = g_\| = g_e \qquad \left(\left|\pm\frac{1}{2}\right\rangle\right) \tag{5.51b}$$

For the magnetic field in the x direction, the zfs - magnetic-field-interaction matrix is:

$$\begin{array}{cccccc} & \left|\frac{3}{2}\right\rangle & & \left|-\frac{3}{2}\right\rangle & \left|\frac{1}{2}\right\rangle & \left|-\frac{1}{2}\right\rangle \\ \left\langle\frac{3}{2}\right| & D & & 0 & \frac{\sqrt{3}}{2}g_e\beta_e B_x & 0 \\ \left\langle-\frac{3}{2}\right| & 0 & & D & 0 & \frac{\sqrt{3}}{2}g_e\beta_e B_x \\ \left\langle\frac{1}{2}\right| & \frac{\sqrt{3}}{2}g_e\beta_e B_x & & 0 & -D & g_e\beta_e B_x \\ \left\langle-\frac{1}{2}\right| & 0 & & \frac{\sqrt{3}}{2}g_e\beta_e B_x & g_e\beta_e B_x & -D \end{array} \tag{5.52}$$

The elements between the $\left|\pm\frac{3}{2}\right\rangle$ and $\left|\pm\frac{1}{2}\right\rangle$ wavefunctions may be ignored if D is sufficiently large. This leaves the matrix block diagonalised into one 2×2 and two 1×1 matrices yielding the identical eigenvalues D for the $\left|\pm\frac{3}{2}\right\rangle$ wavefunctions, and $-D+\beta B g_e$, $-D-\beta B g_e$ for the mixed $\left|\pm\frac{1}{2}\right\rangle$ wavefunctions. Thus the $\left|\pm\frac{3}{2}\right\rangle$ doublet is unsplit by the magnetic field under this approximation, and the doublet described by the mixed $\left|\pm\frac{1}{2}\right\rangle$ wavefunctions is split by $2g_e\beta_e B_x$.

Equating these expressions with the resonance condition as before yields the g values:

$$g_x = g_\perp = 0 \qquad \left(\left|\pm\frac{3}{2}\right\rangle\right) \tag{5.53a}$$

$$g_x = g_\perp = 2g_e \qquad \frac{1}{\sqrt{2}}\left(\left|\frac{1}{2}\right\rangle \pm \left|-\frac{1}{2}\right\rangle\right) \tag{5.53b}$$

The equivalent expression of 5.52 for $\mathbf{B}\|\ \mathbf{y}$ is only changed by a factor i in each off-diagonal element, with $H_{ij} = H_{ji}^*$, and must lead to the same expressions for g_y under uniaxial symmetry.

These calculations show that the effective principal g values for an $S = \frac{3}{2}$ system with a large zfs will be approximately 6 and 0 for one of the doublets, and 2 and 4 for the other. The transition which is observed for the Z centre corresponds to the doublet with g values 2 and 4, while the other is not observed.

Intensity calculations may be carried out to show that transitions within the observed doublet will be strong, while those within the other doublet will be very weak. The intensity of a transition between two states $|\phi_i\rangle$ and $|\phi_j\rangle$ is given by:

$$\mathcal{I} = \left|\left\langle \phi_i \left| \widehat{\mathcal{H}_1} \right| \phi_j \right\rangle\right|^2 + \left|\left\langle \phi_j \left| \widehat{\mathcal{H}_1} \right| \phi_i \right\rangle\right|^2 \tag{5.54}$$

where:

$$\widehat{\mathcal{H}_1} = \beta_e B_1 \cos(\omega t)\left(l g_x \hat{S}_x + m g_y \hat{S}_y + n g_z \hat{S}_z\right) \tag{5.55}$$

B_1 is the magnitude of the oscillating magnetic-field component of the microwave radiation, and l, m and n are the direction cosines of $\mathbf{B}_1$.

The experimental measurements were carried out with $\mathbf{B}_1 \parallel \mathbf{x}$, thus in this case:

$$\widehat{\mathcal{H}_1} = \beta_e B_1 \cos(\omega t) g_x \hat{S}_x \tag{5.56}$$

For $\mathbf{B}\|\ \mathbf{z}$ the appropriate $|\phi_i\rangle$ and $|\phi_j\rangle$ are given by $\left|\pm\frac{3}{2}\right\rangle$ for one doublet and $\left|\pm\frac{1}{2}\right\rangle$ for the other as shown above. Thus:

$$\begin{aligned} \mathcal{I} &\propto \left|\left\langle +\frac{3}{2}\left|\hat{S}_x\right|-\frac{3}{2}\right\rangle\right|^2 + \left|\left\langle -\frac{3}{2}\left|\hat{S}_x\right|+\frac{3}{2}\right\rangle\right|^2 \\ &= 0 \end{aligned} \tag{5.57}$$

for the $\left|\pm\frac{3}{2}\right\rangle$ doublet, and:

$$\begin{aligned} \mathcal{I} &\propto \left|\left\langle +\frac{1}{2}\left|\hat{S}_x\right|-\frac{1}{2}\right\rangle\right|^2 + \left|\left\langle -\frac{1}{2}\left|\hat{S}_x\right|+\frac{1}{2}\right\rangle\right|^2 \\ &= 2 \end{aligned} \tag{5.58}$$

for the $\left|\pm\frac{1}{2}\right\rangle$ doublet.

For $\mathbf{B}\|\,\mathbf{y}$ the appropriate $|\phi_i\rangle$ and $|\phi_j\rangle$ are given by $\left|\pm\frac{3}{2}\right\rangle$ for one doublet and $\frac{1}{\sqrt{2}}\left(\left|+\frac{1}{2}\right\rangle \pm i\left|-\frac{1}{2}\right\rangle\right)$ or $\frac{1}{\sqrt{2}}\left(i\left|+\frac{1}{2}\right\rangle + \left|-\frac{1}{2}\right\rangle\right)$ and $\frac{1}{\sqrt{2}}\left(\left|+\frac{1}{2}\right\rangle + i\left|-\frac{1}{2}\right\rangle\right)$ for the other taking the equivalent matrix to 5.52 for the y direction. Operation of $\hat{S}_x$ as above then gives the same results as for $\mathbf{B}\|\,\mathbf{z}$.

The true intensity of transitions in the $\left|\pm\frac{3}{2}\right\rangle$ doublet are not exactly zero. They are calculated by EPR-NMR as the matrix elements of a transition operator between the eigenstates of the diagonalised spin Hamiltonian. These calculations show that the intensity is essentially zero when the resonance is at low field values (larger effective g values), but becomes larger as the resonance occurs at higher field values (smaller effective g values) near the b axis. The intensities are still very weak, and are likely to be detectable only when the predicted resonance-field position climbs to a value above the capabilities of the spectrometer electromagnet described in section 1.3.

Parameter matrices

The zfs parameter $D \approx 2600$ - 3000 mT (multiply by $\frac{g_e\beta_e}{10^9 h} = 28.0249$ to convert to MHz) fitted in tables 5.6 and 5.7 is much larger than for most other Cr^{3+} centres reported in the literature. Large D values usually fall within the range 650 - 900 mT. Cr^{3+} centres in GeO_2 [86], SnO_2 [87], TiO_2 [88], TeO_2 [89] and $ZnWO_4$ [90] are examples. A large value of D implies a strong crystalline electric field at the site of the unpaired electrons. Watterich *et al.* [89] report the zfs for Cr^{3+} substituted for Te^{4+} in TeO_2 as 831 mT. Here the Cr^{3+} is surrounded by four oxygen atoms and two positively charged Te ions along the c-axis direction, analogous to the silicon site in zircon. In zircon however, the Zr^{4+} ions carry more positive charge than the covalently bound Te ions, and are only 2.99 Å from the Cr^{3+} site compared to 7.61 Å for TeO_2. Thus it might be expected qualitatively that the crystal field at the substitutional site, and thus the zfs, would be greater in the zircon case. Watterich *et al.* [89] note a trend in the size of D for

Cr^{3+} in GeO_2, TiO_2, SnO_2 and TeO_2, which increases as the lattice spacing decreases.

The uncertainty in the D matrix is reasonably high because data are only available for transitions within one of the Kramers doublets. The inclusion of transitions between the doublets would allow a much more precise determination of $\mathbf{D}$, but they are inaccessible at X band for such a large zfs. Transitions within the other doublet would also assist the determination to a lesser extent, but are either too weak, or occur at a resonant field too high to be observed, as described above.

Because of the large uncertainty in the matrix $\mathbf{D}$, the E term required to fit the observed anisotropy in the *ab* plane is many times smaller than its uncertainty, thus any attempted fitting of an E term will be dubious. It is also difficult to fit such a small anisotropy in the *ab* plane alongside a very large anisotropy in the *bc* plane without putting very large weightings on the *ab*-plane data. As EPR-NMR [28] fits by minimising the disagreement between experimental and fitted line positions, the *ab*-plane data can be fitted poorly without affecting the rmsd. The fit in table 5.6 is for unit weightings of the *ab*-plane data, and gives an E term which generates too much anisotropy in the *ab* plane. If all the data points in the *ab* plane are given a weighting of 100, the fitted E term is smaller, and the *ab*-plane data well fitted. However, the accuracy of these data points is questionable, as different degrees of anisotropy in the *ab*-plane have been measured in different crystals, which is almost certainly due to slight differences in alignment.

If a small E term was present, it would generate a small site splitting. However, simulation shows that the site splitting from the E term required to fit the observed *ab*-plane anisotropy would be smaller than the observed linewidths. The splitting would thus only be observed as a line broadening. The site splitting is at its largest in the *a*- and *b*-axis orientations, and in most of the *bc* plane, at *ca* 0.25 mT. These are the orientations in which the observed linewidth is at its greatest. The site splitting is zero in the *c*-axis and [110] orientations, where the observed linewidth is the smallest. This evidence suggests that the E term may be real. The ^{91}Zr nuclear quadrupole matrix is certainly non uniaxial, as will be discussed later, and indeed much further removed from uniaxial symmetry than the electronic quadrupole matrix required to fit the observed *ab*-plane anisotropy, so it is not inconceivable that the electronic quadrupole matrix could also be non uniaxial.

However, if the anisotropy is at least partly due to a slight tilt of the crystal, as indicated

by the different anisotropies measured in different experiments, it seems possible that it may be the only reason. As described earlier, the *ab*-plane data used in these fittings came from a synthetic crystal mounted on two adjacent perpendicular faces. This is likely to give a more accurate orientation of the crystal in the *ab*-plane than mounting on a single face, as was the case for earlier measurements in the cut crystal. Indeed, the anisotropy measured in the double-face-mounted crystal (*ca* 0.026 mT) was smaller than any previous measurements. However, a reasonably large tilt of 1.2° is still required to account entirely for this anisotropy. This is slightly above the estimated uncertainty given in table 1.3, which is itself considered a quite generous overestimation. It may be necessary to devise a system by which the crystal may be mounted very precisely and accurately in a given plane in order to establish the nature of the anisotropy beyond doubt.

The isotropic part of the ^{53}Cr hyperfine matrix is substantially less than has been found for other Cr^{3+} centres, while the anisotropic part is greater. Studies of Cr^{3+} in Al_2O_3 [91], $ZnWO_4$ [90], MgO [92], $LiNbO_3$ [93],[94], $AlCl_3.6H_2O$ [95], and TiO_2 [88] all give an isotropic, or very nearly isotropic ^{53}Cr A matrix with $\frac{A}{g_e\beta_e} \approx 1.8$ mT. A small anisotropy in the ^{53}Cr hyperfine interaction was found for Cr^{3+} in GeO_2 [86] and SnO_2 [87] where the isotropic and anisotropic parameters (as defined in equations 5.15) were $|a| = 1.74$, 1.81 mT and $|b| = 0.033$, 0.030 mT, respectively. The largest anisotropies were found for Cr^{3+} in CaF_2, SrF_2 [96] and in $ZrSiO_4$ itself [63], later reported in [97], where $|a| = 1.80$, 1.85 and 1.61 mT and $|b| = 0.093$, 0.083 and 0.157 mT, respectively. The decomposition of **A** into isotropic and anisotropic parts for the Z centre gives $|a| = 1.30$ mT and $|b| = 0.14$ mT. Interestingly, the other reported Cr^{3+} centre in $ZrSiO_4$ [63], [97] is the only example of Cr^{3+} in an inorganic oxide with a comparable anisotropy in **A**; it is in fact larger than for the Z centre. In contrast to the Z centre, this centre is reported to be located at the zirconium site, based on optical spectroscopy results [97]. The epr results are only reported very briefly, with no indication of effective g values or fitted g and D matrices. The magnitude of the isotropic component of **A** is similar to the other examples, all larger than the Z centre.

The isotropic component of **A** for the Z centre is still dominant, despite its small value, and can be attributed almost entirely to core polarisation [8]. The contributions to the hyperfine field at the nucleus may be calculated as outlined in the latter part of section 5.2.3 for the $Si(Ti^{3+})$

centre. The experimental hyperfine fields at the nucleus along the principal directions are given by $\frac{A_\parallel}{g_n\beta_n} = -18.40$ T and $\frac{A_\perp}{g_n\beta_n} = -13.61$ T. Equation 5.40 gives the orbital contribution to the hyperfine field at the nucleus $H^{hf}_{orb} = -0.15$ T for $g_\parallel$ and -2.19 T for $g_\perp$, using $\langle r^{-3} \rangle = 3.96444$ au for Cr^{3+} from Fraga *et al.* [76].

The hyperfine field due to core polarisation and dipolar interaction only must then be -18.25 T in the z direction, and -11.42 T in the x and y directions. If it is assumed that the remaining hyperfine field is made up of an isotropic contribution due to the core-polarisation field, and a uniaxial contribution due to the dipolar interaction, then $H^{hf}_{cp} = -13.69$ T, and $H^{hf}_{dip} = -4.55$ T in the z direction, and $+2.28$ T in the x and y directions.

A value of H^{hf}_{cp} for the free ion may be calculated using a theoretical value of χ as described in section 5.2.3. The Watson-and-Freeman [79] calculated value of χ for $3d^3$ ions is about -3.0 au, only slightly larger than the $3d^1$ value of -2.8 au used for Ti^{3+} in section 5.2.3. For $\chi = -3.0$, and $S = \frac{3}{2}$, equation 5.38b gives $H^{hf}_{cp} = -37.6$ T.

This experimental core-polarisation field for the Z centre is much smaller than both the values calculated from the other epr results of Cr^{3+} centres of *ca* -20 T and the free-ion value calculated above. One possible explanation for this reduction of H^{hf}_{cp} may be increased covalency of the SiO_4 substitutional site relative to those of the other crystal hosts. As noted in section 5.2.3, covalency is known to reduce core polarisation [79]. An epr study of Cr^{3+} in SiC [98], a more covalent material, reports an isotropic ^{53}Cr hyperfine matrix with $\frac{A}{g_e\beta_e} = 0.928$ mT for a hexagonal silicon site. If it is assumed that the core-polarisation field is dominant, as for other Cr^{3+} species, then $H^{hf}_{cp} \approx -10.8$ T. A more useful comparison could be made with a Cr^{3+} centre in quartz, as it also contains covalent SiO_4 units, however, no such centre is known.

The non-uniaxial nature of the ^{91}Zr nuclear quadrupole matrix is very puzzling. It is almost as far removed from uniaxial symmetry as it is possible to be, with a small value in the *c*-axis direction, and larger, almost equal and opposite values, in the *a*- and *b*-axis orientations. However, it is the only possible way of accounting for the observed spectra.

If this form of the nuclear quadrupole matrix is due to the efg at the zirconium site due to the usual surrounding atoms, and a +3 ion substituting for one of the nearest-neighbour silicon sites, then one might have expected something similar to be observed for the ^{91}Zr hyperfine on the $Si(Ti^{3+})$ centre (section 5.2). However, in this case the zirconium hyperfine is hidden

underneath the zero isotope line, so it is not possible to see whether a similar effect is present. A more thorough point-charge-based calculation of the efgs at the zirconium nucleus than undertaken in section 5.2.3 and [24], [9] may be required to help understand what is going on.

It is difficult to imagine how the efg could be so different in the a- and b-axis orientations unless there is more involved in the defect than simply a chromium atom substituting for a silicon atom. However, **g** and **D** appear to be either exactly, or very close to uniaxial. It may be that another impurity, possibly providing charge-balancing, is present in a position close enough to the zirconium atoms to affect the efg at the zirconium positions, while not having much effect at the site of the chromium atom.

5.4 The "H" centre

5.4.1 Experimental details

The H centre was first seen in the Ti^{4+}/Y^{3+}-doped crystals in which both the Si(Ti^{3+}) centre and hole centres of chapter four were observed (growth L of table 3.1). All four centres were observed after x-irradiation at 77 K and cold transfer. The location of the H centre relative to the Si(Ti^{3+}) and hole centres may be seen in the earlier figures 4-2 and 5-1. All of the figures and data in this section are a result of measurement of a crystal from a subsequent crystal growth run (growth R) identical to growth L. The crystal was gamma irradiated at room temperature for 48 hours, which produced a number of stable centres including a high-intensity H-centre signal. The only other crystals in which the H centre has been observed thus far are the boron-doped crystals 99B, although a thorough search for H in other crystals has not been undertaken.

The H centre was stable at room temperature, as proved by its persistence in the gamma-irradiated crystal which was irradiated more than a year before the most recent measurements were made. Data were collected in the bc plane only, in 5° intervals between the b and c-axis orientations.

5.4.2 Results

The H-centre spectrum in the c-axis orientation consisted of an intense central line which was flanked by at least 11 weaker lines within a range of ± 0.5 mT, and an outer two matching lines on each side with an average separation of 1.05 mT and 1.34 mT from the central peak. The spectrum is shown in figure 5-10. As the crystal was rotated, all of these lines appeared

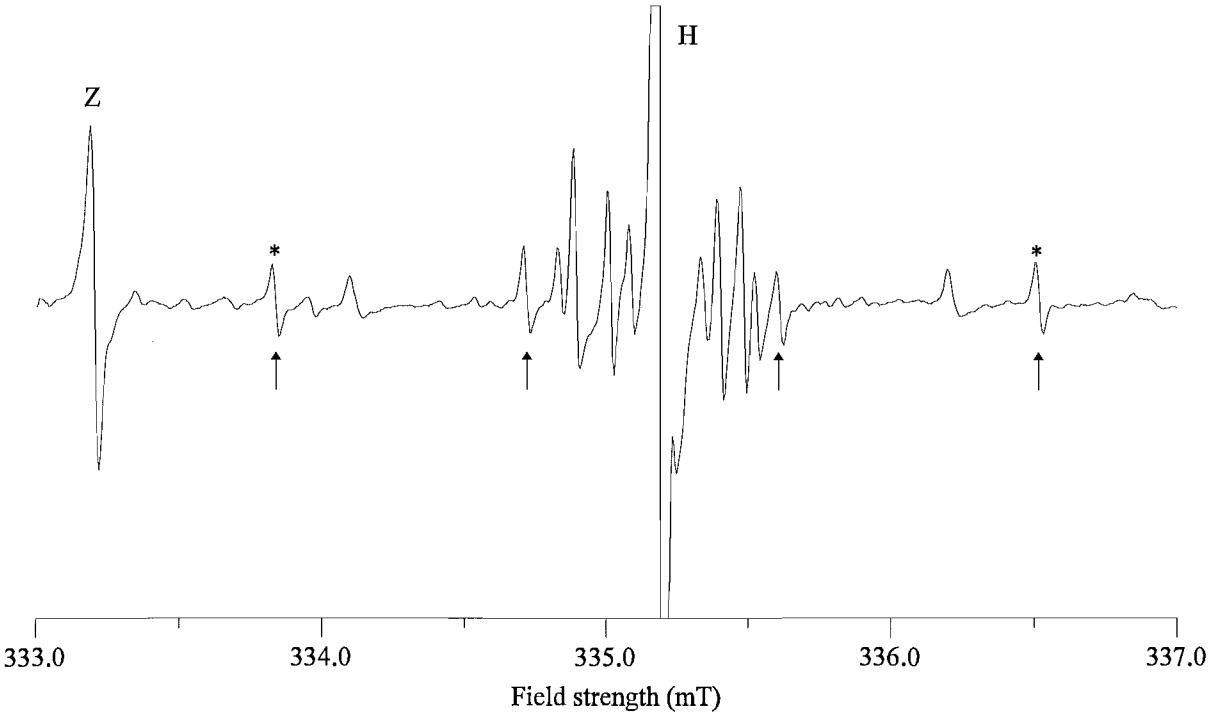

Figure 5-10: c-axis epr spectrum of H centre in zircon at *ca* 15 K. Frequency = 9.32408 GHz. The lines marked with an asterisk were fitted as nuclear spin $\frac{1}{2}$ hyperfine interaction as described in the text. The significance of the arrows is described later in the discussion section.

to remain centred about the main line, indicating that they are likely to be hyperfine lines associated with the H centre. The change in the spectrum as the crystal is rotated may be seen in the stacked plot of figure 5-11.

It was clear from the stacked plot that there was no site splitting in the bc plane, indicating that the H centre has Laue symmetry $4/mmm$ ([12] and table 1.2). The true point-group symmetry of the defect will be $\bar{4}2m$.

The only analysis which has been carried out using the H-centre data is a fitting of the g

matrix assuming an electronic spin of $\frac{1}{2}$, and fitting of the outer pair of lines, marked in figure 5-10, as a possible ^{29}Si hyperfine pair. The intensity of these lines is not exactly right, but they are difficult to interpret any other way, as discussed later. The spin Hamiltonian used for the fitting of the proposed ^{29}Si lines was of the same form as that used for the $[SiO_4/Y]^0$ hole centre (equation 4.1), where $\mathbf{g}_n$ was set as the scalar matrix -1.1106**U**, where **U** is the 3×3 unit matrix and -1.1106 is the g_n value of ^{29}Si set internally by EPR-NMR. Fitting of the g matrix for the central line required only the electronic Zeeman term. The fitted matrices are given in table 5.8.

The ^{29}Si hyperfine lines were only visible up to 35° away from the c-axis. Fitting of only the experimental points gave a very poor value for $A_\perp$, so an estimate was made of the line positions in the b-axis orientation. A stacked plot of the spectra was made with each spectrum shifted to place the central line in the same position, so as to create an effective roadmap of the hyperfine splittings (figure 5-12). It showed that there was a turning point (maximum) in the magnitude of the observed splitting in the c-axis orientation. It was assumed that there would be a minimum in the b-axis orientation, with an inflection point at the 45° orientation. The line positions in the b-axis orientation could then be estimated from the size of the splitting in the 45° orientation, which in turn was extrapolated from the observed splittings up to 35°. The value of $A_\perp$ obtained this way may be subject to a reasonable error, but allows a approximate determination of the spin density on the silicon atoms to be made.

5.4.3 Discussion

The $\bar{4}2m$ symmetry of the H centre indicates that it is almost certainly an impurity substituted into a silicon or zirconium site in the zircon lattice. The g values, which are considerably less than the free-electron value, indicate that H is an electron centre. This evidence points very clearly towards the H centre being a single substitutional metal atom with no nearby impurities, similar to the two Ti^{3+} centres substituted in a zirconium [9] and silicon [39] site.

The titanium centres are easily identified by their distinctive pattern of eight well-spaced hyperfine lines in the c-axis orientation, which occur in a symmetrical pattern around the zero-isotope line. The H-centre c-axis spectrum is much more difficult to interpret. There seem to be no hyperfine lines more than 1.34 mT from the central peak, the spectrum is not entirely

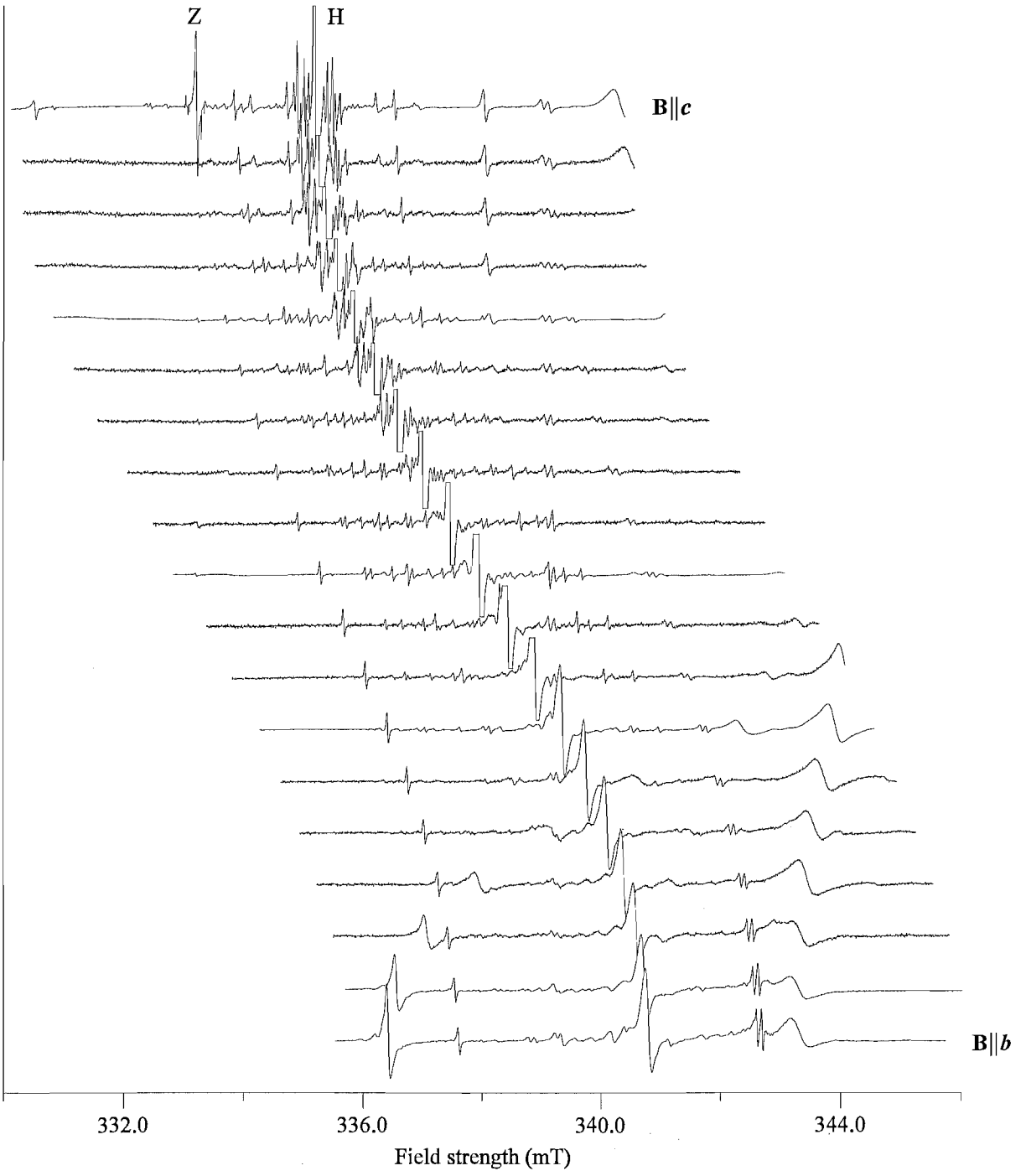

Figure 5-11: Stacked plot of H-centre epr spectra in zircon at *ca* 15 K in the *bc* plane. Frequency $\approx$ 9.3245 GHz.

Figure 5-12: Stacked plot of hyperfine splittings of H centre in zircon at *ca* 15 K. The epr spectra have been field-shifted to keep the central line in the same position. The magnetic-field strength scale is appropriate for the *c*-axis (top) spectrum. Broken lines mark the signals fitted as possible ^{29}Si hyperfine.

Table 5.8: Spin-Hamiltonian parameters for the H centre in zircon at it ca 15 K. Error estimates in parentheses.

	Central line		^{29}Si fitting	
	Principal values		Principal values	
Matrix $\mathbf{Y}$	$Y_\parallel$	$Y_\perp$	$Y_\parallel$	$Y_\perp$
$\mathbf{g}$	1.98753(1)	1.95503(1)	1.9876(1)	1.9553(3)
$\mathbf{A}(^{29}\mathrm{Si})/g_e\beta_e$ (mT)	-	-	2.49(4)	0.22(11)
Total Data points	19		17	
Unit weighted	17		16	
$\sum$ weightings	17.2		16.5	
rmsd (mT)	0.0057		0.0689	

symmetrical, and there are no obvious groups of evenly spaced lines.

The complicated pattern of lines close to the central line may be due to a number of low-abundance isotopes of the metal ion which have different nuclear spins. However, as it is assumed that most of the spin density will lie on the metal centre of this defect, the hyperfine splittings would be expected to be larger. If these lines are due to superhyperfine interaction with nearby nuclei, then the splittings would be smaller, but such a complicated appearance is not very likely. For a single metal atom in a silicon site with no other impurities, the only superhyperfine structure likely to be seen is six evenly-spaced lines due to hyperfine interaction with the two equivalent nearest-neighbour zirconium atoms, as is the case for the Z centre. Similarly, in a zirconium site, the main superhyperfine interaction observed will be a pair of lines due to the two equivalent nearest-neighbour silicon atoms. Even if both ^{29}Si and ^{91}Zr hyperfine was observed, it is unlikely that such a complicated pattern of lines would result.

Krasnobaev *et al.* [63] reported a centre with the same g values as H, which they interpreted as a Cr^{5+} centre. However, the H-centre spectrum does not appear to have a regular $I = \frac{3}{2}$ hyperfine spectrum due to 9.55 % abundant ^{53}Cr. In the c-axis orientation, the outermost pair of hyperfine lines and the outer pair of the inner set (see arrows in figure 5-10) seem to comprise

a set of four equally spaced hyperfine lines of roughly equal intensity. The intensity ratio of these four lines to the main line is appropriate for the natural abundance of ^{53}Cr, with $I = \frac{3}{2}$. However, as the crystal is rotated away from the c axis, the outer two lines move towards the central line, while the inner two move away, indicating that they are not part of the same set of hyperfine lines (see figure 5-12). The inner two lines appear not to be related to each other, as one loses intensity after only a 20° rotation, while the other may be observed through 50°. The intensity of the outer two lines changes in the same way as the crystal is rotated, and they remain approximately evenly spaced around the central line. Treating the two lines as hyperfine structure due to a low-abundance $I = \frac{1}{2}$ nucleus, with no other isotopes with $I \neq 0$, an intensity ratio calculation gives the abundance as 5.45 %. The closest match among the elements is ^{29}Si, with a natural abundance of 4.67 %. However, a silicon interaction would be expected to involve two equivalent nearest-neighbour atoms, which should give an apparent abundance of 8.90 %, unless the unpaired electron is actually located on a silicon atom.

If the element which carries the bulk of the spin density has several different isotopes with a nuclear spin, including one with $I = \frac{1}{2}$, then the calculation of the abundance from the experimental spectrum should take into account the intensity of the other isotopes. In this case, the experimental calculation would give an abundance value for the $I = \frac{1}{2}$ isotope lower than 5.45 %, as the percentage must be taken from the total intensity of all the isotopes. However, there are no elements which have either a single $I = \frac{1}{2}$ isotope with a natural abundance of around 5-6 %, or an $I = \frac{1}{2}$ isotope with a lower natural abundance, in addition to other significant isotopes with a nuclear spin. The only elements other than silicon which have a nuclear spin of $\frac{1}{2}$ with a natural abundance between 2 % and 10 % are iron (2.15 %), selenium (7.6 %), tin (7.75 %, 8.6 %) and tellurium (7.0 %).

Aside from a single silicon atom, tellurium gives the closest agreement with the observed intensity ratio. Tellurium has another $I = \frac{1}{2}$ isotope, with lower abundance (0.89 %). There is a pair of equally spaced lines around the central line that have an intensity corresponding to 0.76 % abundance if all the isotopes of tellurium are taken into account. If the two pairs of lines are due to hyperfine interaction with ^{125}Te and ^{123}Te then the ratio of the hyperfine splitting for the two isotopes should be approximately equal to the ratio of their g_n values, as can be seen from the dependence on $\wp$ in equation 1.19. This was found to be the case for epr

measurements of substitutional Te^+ in silicon [99]. However, the ratio of the two splittings for the H centre is 0.478, well removed from the g_n ratio of 0.829. The splittings are also very small for a tellurium atom which would be carrying most of the spin density, so H is unlikely to be a tellurium centre.

The lineshape of the H-centre central line in the spectrum used to extract these data indicates some power saturation. It is possible that this has affected the intensity-ratio calculations somewhat, resulting in values that do not agree particularly well with natural isotopic abundances. If the outer pair of lines is due to hyperfine interaction with an $I = \frac{1}{2}$ nucleus, then silicon is the most likely possibility, despite the lack of agreement with the experimental intensities. A study of the effect of microwave power on the H-centre spectrum might be useful, to see if an unsaturated spectrum could be obtained, and check whether the associated structure has the same saturation characteristics as the central line.

The g values of the H centre were analysed using the same crystal-field spin-orbit-coupling calculations as were detailed in section 5.2.3. This analysis is appropriate for a d^1 (or d^9) ion, which seems the most likely possibility for the H centre. If this turns out not to be the case, then the following analysis would of course be made meaningless. The approach also assumes a b_1 ground state, which has almost always been found to be the case for d^1 centres in zircon. The unitless orbital energy-level splittings calculated were $\frac{\Delta_1}{\zeta} = 603$ and $\frac{\Delta_2}{\zeta} = 42.3$, with the same definitions as used in the previous analysis.

The first splitting is very large in comparison to the unitless splittings calculated for the titanium centres in table 5.4, but it is difficult to make a direct comparison when the absolute value is not known. If the ion present in the H centre has a smaller ζ than titanium, the difference might not be so great. The large difference in the two splittings calculated for the H centre can be understood by examining the g-value perturbation equations 5.12. When $\Delta_1 < 4\Delta_2$ with a b_1 ground state, these equations show that $g_\parallel$ is less than $g_\perp$. This is usually the situation for point-group symmetry $\bar{4}2m$ centres in zircon. The H centre has $g_\parallel > g_\perp$, which is only possible for a b_1 ground state if $\Delta_1 > 4\Delta_2$. For the H centre $g_\parallel$ is substantially less than $g_\perp$, so the ratio is much higher than four.

If the ground state is not b_1, the appropriate analysis may give orbital energy-level splittings which are not so large. Greenblatt *et al.* [100] reported a Cr^{5+} centre in YPO_4, a crystal which

has the same structure as zircon, where an a_1 ground state was inferred from the relationships $g_{\|} < g_{\perp}$ and $A_{\|} < A_{\perp}$. The perturbation equations 5.35 for the A values show that, for a b_1 ground state, $A_{\|}$ can only be less than $A_{\perp}$ if κ is negative. Theoretical and experimental studies have shown that the κ is positive (or χ negative) for 3d and 4d ions (see [79] and references therein). Hence the ordering observed by Greenblatt *et al.* indicates a different ground state. An a_1 ground state is usually observed in α-quartz, but there have apparently been no reports of such in zircon. Point-charge calculations of some possible distortions of the usual zircon structure might indicate whether a_1 might possibly be the ground state in some circumstances.

In the absence of any fitted hyperfine parameter matrices relevant to the ion carrying the spin density, it is not possible to say for sure what the ground state of the H centre is. Without any evidence to prove otherwise, a b_1 ground state will be assumed, in agreement with other point-group symmetry $\bar{4}2m$ d^1 centres in zircon.

The A matrix for the ^{29}Si fitting of table 5.8 has an isotropic parameter $|a| = 0.977$ mT, and a uniaxiality parameter $|b| = 0.757$ mT (defined in equations 5.15). Following the procedure of Morton and Preston [78], the spin density on the silicon 3s orbital is calculated as 0.60 %, and the spin density on the 3p orbital 18.6 %. This would mean 38.2 % spin density in total on the two equivalent silicon atoms. This is much higher than would be expected for an electron centre trapped on a metal ion, and much lower than would be expected for a silicon electron centre.

Another unexplained aspect of the H-centre spectra is the number of lines which appear to be associated with the central line in the intermediate orientations of the *bc* plane, as seen in the 45° spectrum of figure 5-13. These lines are mostly observable as the crystal is rotated in the region 15° - 50° away from the c axis, as though they were forbidden hyperfine lines. They are numerous and occur both inside and outside the so-called $I = \frac{1}{2}$ line, and so cannot be explained as forbidden transitions within the $I = \frac{1}{2}$ hyperfine energy-level manifold. These lines seem to indicate the presence of a higher nuclear spin, but there is no evidence of such in the c-axis spectrum.

Until the nature of the H centre is better understood, there is little analysis which can be made. The multitude of associated lines may offer a lot of structural information about this defect if they could be interpreted and fitted.

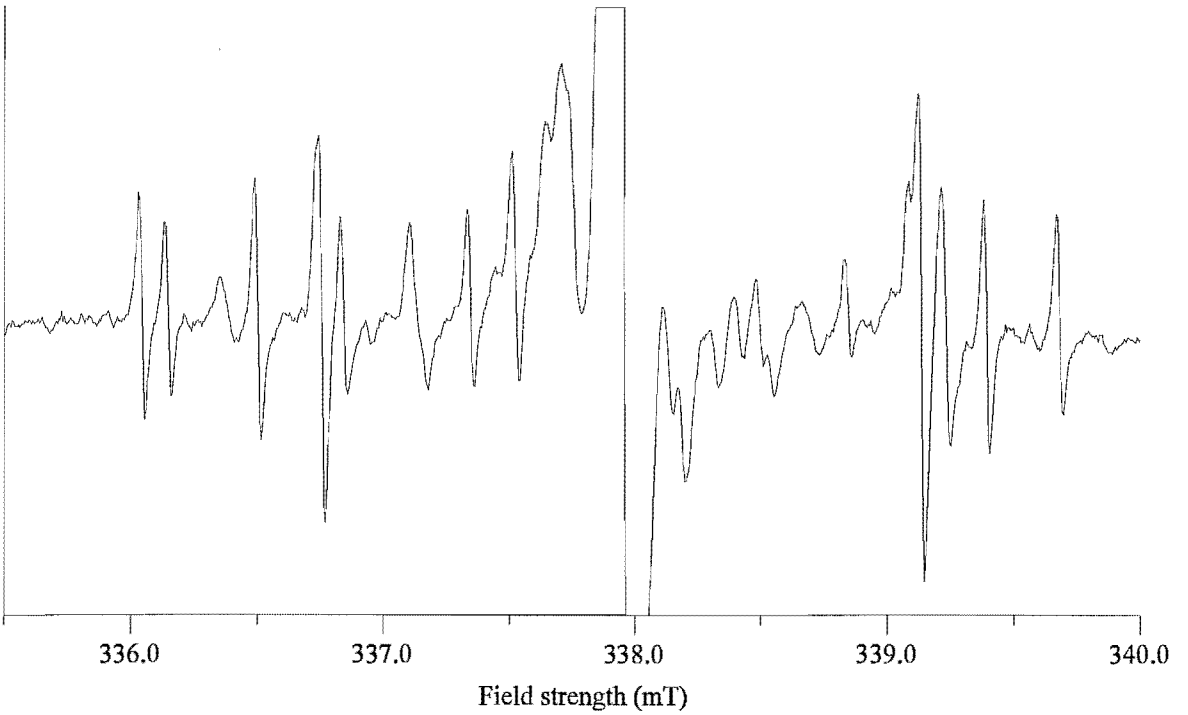

Figure 5-13: Epr spectrum of H centre in zircon at *ca* 15 K in [011] orientation showing associated structure. The central line has been clipped. Frequency = 9.32407 GHz.

5.5 Two boron centres

5.5.1 Experimental details

Zircon crystals doped with boron were grown following the discovery of a boron hole centre [36] in the nominally undoped zircon crystal grown by Aerospace Corporation (see section 3.2 for details). The first boron-doped growth run, 99B of table 3.1, contained 0.1 molar % B_2O_3, and produced a number of average-sized crystals with well-defined *bc* faces. Epr measurements at 15 K in the *bc* plane following x-irradiation at room temperature revealed the boron hole centre, and an unidentified set of signals centred at $g = 1.9686$. The signals were weak, and were not very distinct in any orientation other than the *c* and *b* axes, where one and two sites were visible, respectively. Subsequent room-temperature irradiations of other 99B crystals gave similar results.

One striking aspect of the irradiations was the colouration of the zircon crystals after irradia-

tion at room temperature. All other zircon crystals became coloured only after irradiation under liquid nitrogen, and lost their colour upon warming to room temperature. The boron-doped crystals retained a reasonably intense purple colouration for several days at room temperature, and slowly returned to their unirradiated colour over a week or more. These observations prompted an investigation of the epr spectrum of one of these crystals at room temperature, to see if the defect responsible for the colouration was visible to epr. Most of the epr centres studied in the Canterbury laboratory have been observable only at low temperature. However, there were weak signals visible in the 99B crystal at room temperature, which corresponded to the unidentified lines seen at low temperature.

A temperature-dependence study of the intensity of the new centre was then carried out, which revealed that there was an approximately threefold increase in intensity as the temperature was raised from 15 K to *ca* 100 K. Subsequent measurements were carried out at this optimum temperature, where the intensity was high enough to allow a full set of spectra in the *bc* plane to be recorded.

5.5.2 Results

The initial spectra of the boron centres in the *c*- and *b*-axis orientations showed what appeared to be a single centre consisting of four lines, one of which was of greater intensity (figure 5-14). In the *b*-axis orientation the line pattern was similar, but there were two sites, and a smaller fourfold splitting was visible for one of them.

In the first study of the epr spectra as the temperature was raised from 15 K to room temperature, the intensity ratio of the larger line to the smaller ones remained constant, as though they were a single centre. However, an overnight spectrum at room temperature showed only the single-line spectrum, indicating that the lower intensity lines, later seen to be a set of four, were unstable at room temperature. When the temperature was then lowered again to raise the intensity of the signals, it was evident that the four-line spectrum had indeed been irreversibly annealed. It was obvious from this evidence that the original epr spectrum was due to two independent, but closely related centres.

Data were collected for the single-line spectrum alone at 60 K. Figure 5-15 is a stacked plot of the spectra collected. The crystal was then annealed at 900 °C, reirradiated at room

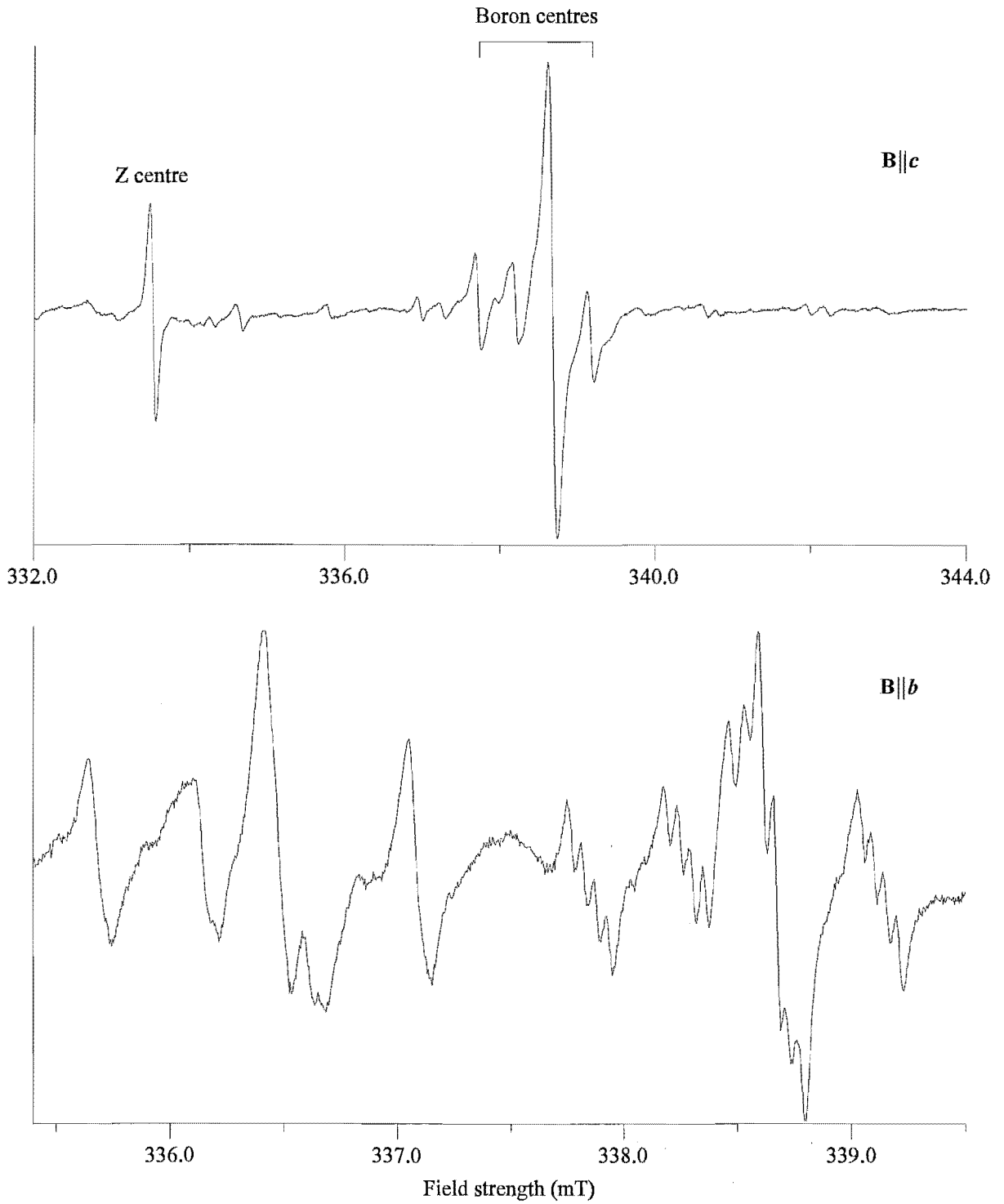

Figure 5-14: Epr spectra of boron centres in zircon at *ca* 70 K with **B**||**c** (frequency $\approx$ 9.330 GHz, top) and at *ca* 100 K with **B**||**b** (frequency = 9.32945 GHz, bottom). All signals in the bottom spectrum are attributable to the boron centres.

temperature and data collected for the four-line spectrum at 100 K [5]. Figure 5-16 is a stacked plot of this data, overlaid with the fitted line positions.

The two stacked plots in figures 5-15 and 5-16 revealed that the site splitting for the two centres was different. The single-line spectrum of figure 5-15 showed only two sites in the bc plane, including the b axis itself. The four-line spectrum of figure 5-16 showed three sites in the bc plane, of which only two can be seen at the same time in almost all orientations, and two sites in the b-axis orientation. The fitted line positions are included in figure 5-16 to make the location of the three sites clearer. From [12] and table 1.2 these site splittings indicated a site of Laue class $2/m^2$ for the four-line spectrum, and either mmm^2 or $2/m^1$ for the single-line spectrum. However, the $2/m^1$ possibility for the single-line spectrum would require either a mirror plane perpendicular to the c axis, or a twofold axis parallel to the c axis with no mirror planes at all. The former symmetry is impossible, as there are no mirror planes in zircon in this orientation. The latter is unlikely because the lack of mirror planes would imply an interstitial atom, and then the twofold axis would require two interstitial atoms. The true point-group symmetries of the two centres which are available in the zircon lattice and consistent with the observed site splitting are almost certainly m and $mm2$ as described in section 2.1.

The spin Hamiltonian used to fit the observed line positions for the four-line spectrum, and the single-line spectrum including the smaller hyperfine was of the same form as 5.1, which was used to fit the Si(Ti^{3+}) centre. In this case $\mathbf{g}_n$ was set as the scalar matrix 1.792424**U** where **U** is the 3×3 unit matrix and 1.792424 is the value of g_n for ^{11}B set internally by EPR-NMR. Boron was assumed to be the species responsible for the observed hyperfine as it has the correct nuclear spin of $\frac{3}{2}$, and the centre is only seen in a reasonably highly boron-doped crystal. For the fitting of the single-line spectrum without the hyperfine structure, only the electronic Zeeman term was required.

An attempt to fit the smaller hyperfine splitting due to a nuclear spin $\frac{3}{2}$ species which is only well resolved in a few orientations was made only for the single-line spectrum. Its higher intensity meant that the partially resolved hyperfine structure could be recorded more reliably in more orientations. The smaller splitting on the four-line spectrum seemed to behave in an

[5] Measurements of the two centres were carried out at various times over a range 60 - 120 K, within which there was very little variation in the spectra. The most pronounced change in intensity occurs between 15 K and 60 K.

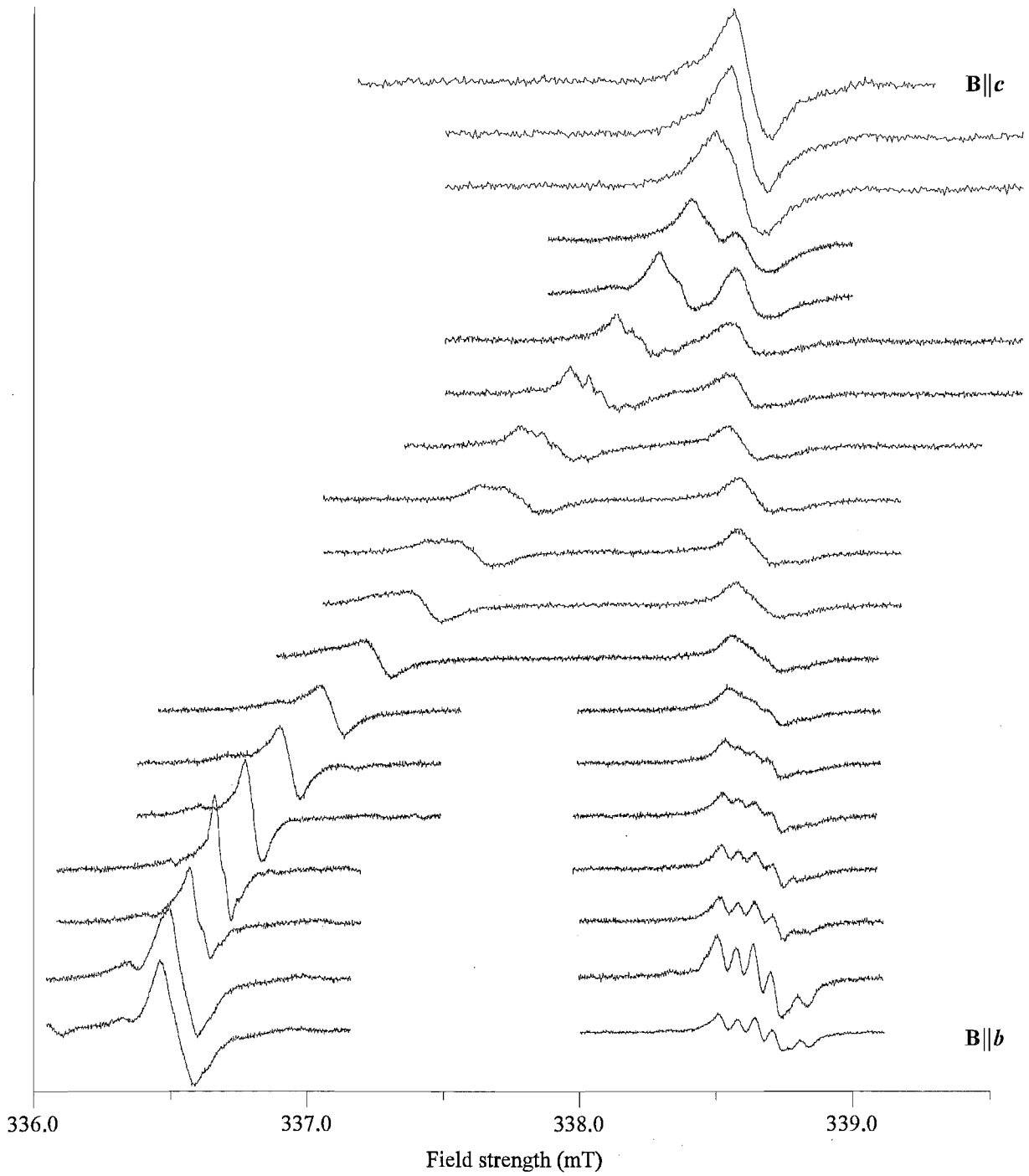

Figure 5-15: Stacked plot of single-boron-centre epr spectra in zircon at *ca* 60 K in the *bc* plane. Frequency $\approx$ 9.3305 GHz.

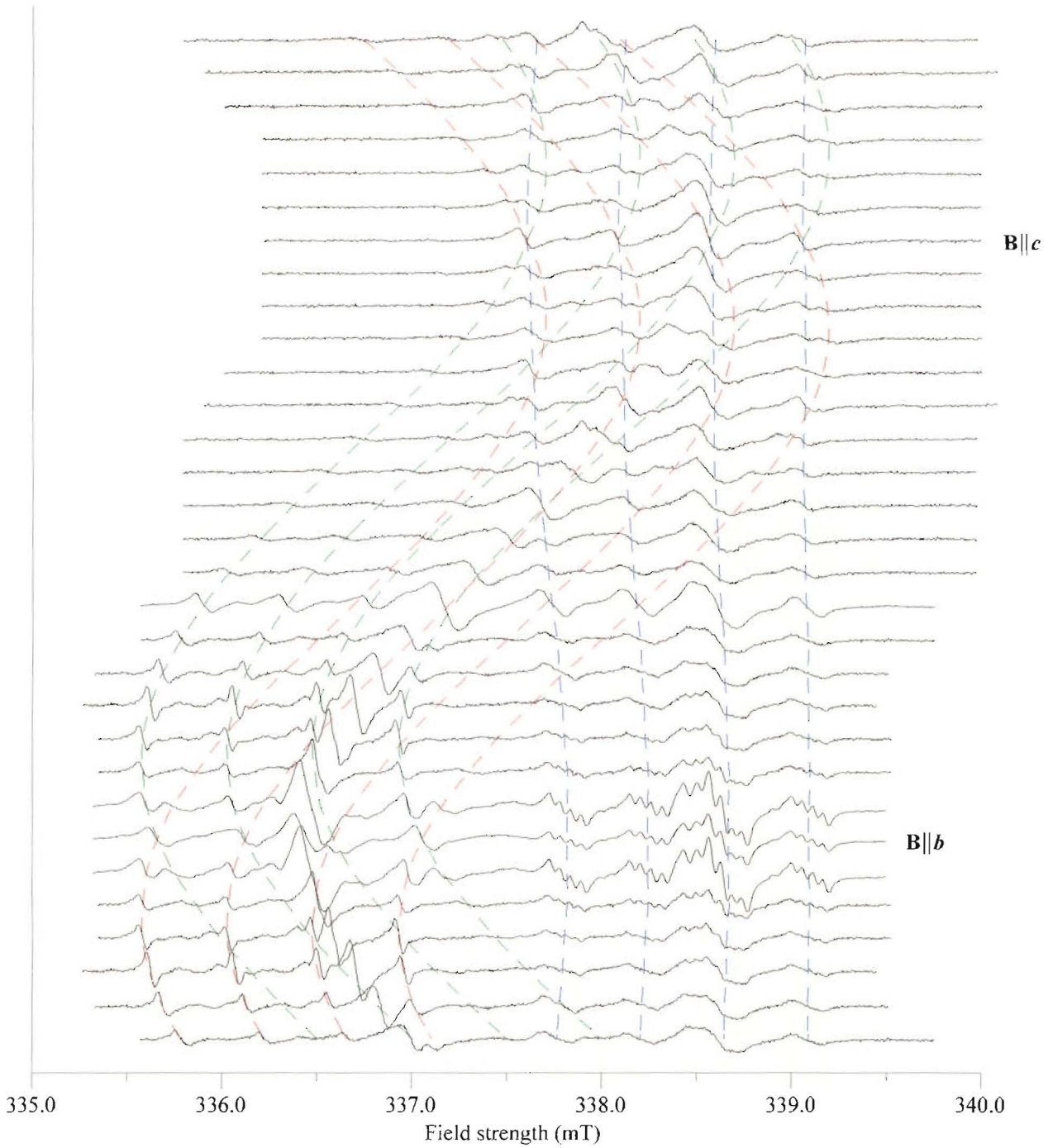

Figure 5-16: Stacked plot of two-boron-centre (and overlapping one-boron-centre) epr spectra in zircon at *ca* 100 K in the *bc* plane. Frequency $\approx$ 9.3285 GHz. Successive spectra correspond to rotations of 5°. Plotted lines are generated by the fitted parameters in table 5.10.

almost identical fashion to the splitting on the single-line spectrum, and would presumably give a fairly similar matrix if it could be fitted.

Where the hyperfine splitting was unresolved, line positions were estimated using a simple formula which was derived using the resolved line positions. It was found that the observable hyperfine line positions were given approximately by:

$$B_i = l + 0.017 + n_i \left(\frac{w - 0.034}{3} \right) \tag{5.59}$$

where B_i (in mT) is the resonant field, l is the position of the lower-field peak, w is the overall peak-to-peak linewidth, 0.017 mT is the average field shift between the upper-field or lower-field peak and the closest hyperfine position, and $n_i = 0 - 3$. Thus the unresolved line positions were estimated by measuring the overall peak-to-peak linewidth.

This method assumes that changes in the overall linewidth where the hyperfine structure is unresolved are due solely to changes in the magnitude of the hyperfine splittings, rather than changes in the linewidth itself. If the linewidth was changing significantly, and alternatively enhancing and opposing the effect of the hyperfine splitting in different orientations, the magnitude of the resultant hyperfine splittings fitted by equation 5.59 might increase and decrease more than expected. However, the splittings followed a smooth trend, with a single minimum and maximum value for each site over the 90° rotation. All points generated by this method were given a weighting factor of 0.2 in the fitting, while the measured lines were unit-weighted.

The resulting fitting appears to have a very low rmsd, with all the matrix elements well determined, but this will be partly due to the low weighting of a large proportion of the data points. The results of all the fittings are given in tables 5.9 and 5.10.

5.5.3 Discussion

Site symmetry

The point-group symmetry m of the two-boron centre is very common, requiring only that the impurities which comprise the defect are located in a single mirror plane. By contrast, the point-group symmetry $mm2$ of the two-boron centre is very unusual. This is a little surprising, as a centre does not have to be particularly complex to have this point-group symmetry. The

Table 5.9: Spin-Hamiltonian parameters for the single-boron centre in zircon at *ca* 60 K, fitted with and without the small hyperfine interaction included. Error estimates in parentheses.

	Without hyperfine			With hyperfine		
	Principal values			Principal values		
Matrix **Y**	Y_x	Y_y	Y_z	Y_x	Y_y	Y_z
g	1.96874(2)	1.98091(2)	1.96865(2)	1.968755(5)	1.98092(1)	1.96859(1)
$\mathbf{A}/g_e\beta_e$ (mT) (^{11}B)	-	-	-	0.0638(8)	0.017(2)	0.019(2)
Total data points		76			208	
unit weighted		54			48	
$\sum$ weightings		58.8			80	
rmsd (mT)		0.0124			0.00889	

Table 5.10: Spin-Hamiltonian parameters for the two-boron centre in zircon at *ca* 100 K. Error estimates in parentheses.

Y		Matrix **Y**		k	Principal value Y_k	Principal direction θ_k (deg)	Principal direction ϕ_k (deg)
g	1.98152(1)	0	0.00275(2)	1	1.982145(9)	77.27(0)	0
		1.969251(8)	0	2	1.96936(1)	167.27(0)	0
			1.969985(9)	3	1.969251(8)	90	90
$\mathbf{A}/g_e\beta_e$ (^{11}B) (mT)	0.459(2)	0	0.032(2)	1	0.499(2)	141.5(1)	0
		0.416(1)	0	2	0.434(2)	51.5(1)	0
			0.474(1)	3	0.416(1)	90	90
$\mathbf{P}/g_e\beta_e$ (^{11}B) (mT)	-0.0072(36)	0	0.0017(24)	1	0.0040(29)	90	90
		0.0040(29)	0	2	0.0035(26)	8.8(12.9)	0
			0.0032(27)	3	-0.0075(35)	98.8(12.9)	0

Data points: 172 Unit weighted: 151 $\sum$ Weightings: 157.8 rmsd (mT): 0.00804

$\bar{4}2m$ point-group symmetry of a centre located on a silicon or zirconium position can be reduced to $mm2$ simply by removing the $\bar{4}$ symmetry element without destroying either the twofold axis parallel to c, or either of the two mirror planes perpendicular to a and b. This may be achieved by introducing another impurity on the same $\bar{4}$ axis.

It seems likely that the single-boron centre comprises a boron atom in a silicon substitutional site, with some other impurity on which most of the spin density lies in the adjacent zirconium position along the $\bar{4}$ axis. The similarity of the spectra for the two centres, as shown in figures 5-15 and 5-16 suggests that they are probably very closely related, perhaps only being different due to the presence of an extra boron atom in the two-boron centre. If this is the case, then the single-boron centre probably comprises the same impurity-boron structure along one $\bar{4}$ axis, with another boron in an adjacent silicon site on a neighbouring $\bar{4}$ axis. The second boron could also be interstitially located, provided it was within one of the mirror planes.

The nature of the defect

The observation of two different hyperfine nuclei with a highly abundant nuclear spin $I = \frac{3}{2}$ isotope does not unequivocally establish their identity. Although it is very likely that they will both be boron atoms, as this centre only occurs in a reasonably highly boron-doped crystal, there are a number of nuclei which have the required spin.

The nuclei could be confirmed as boron if hyperfine lines due to the minor isotope could be observed. Boron has two isotopes with a non-zero nuclear spin: the major isotope, ^{11}B (80.2 %), with $I = \frac{3}{2}$, and ^{10}B (19.8 %), which has $I = 3$. The ratio of the hyperfine splitting for the two isotopes should be approximately equal to the ratio of their nuclear g values, as discussed in section 5.4.3. As the ratio of the nuclear g values $\frac{g_n(^{10}B)}{g_n(^{11}B)} = 0.335$, the seven ^{10}B hyperfine lines will be found within the range of the larger four lines due to ^{11}B. Thus the ^{10}B lines will only be seen if the ^{11}B lines are well resolved. This means that these lines will not be visible within the smaller hyperfine splitting which is common to both centres, but may be seen within the larger splitting of the proposed two-boron centre.

A slow spectrum taking 4×10^5 samples per data point was recorded at an orientation 70° from the c axis in the bc plane, where the ^{11}B lines are sharp and well resolved. The spectrum is shown in figure 5-17, and it clearly shows five of the seven lines of the ^{10}B spectrum. The other

two lines are hidden by the much more intense single-boron centre. The ratio of the observed hyperfine splittings from this spectrum is 0.338, in good agreement with the g_n ratio. As a further check, the intensity ratio of the two spectra was calculated, and found to correspond to an abundance of 10 %, much smaller than the expected value of 19.8 %. The intensities of the minor isotope lines are subject to considerable error due to their poor signal-to-noise ratio, and the five measured intensities varied by a factor of two from largest to smallest. However, even assuming all of the lines were the same intensity as the largest measured, the result of the abundance calculation was only raised to 13.4 %. It is possible that the minor-isotope lines are superimposed on broader lines which distort their apparent intensity. The observation of the set of lines with the correct splitting alone is fairly convincing evidence that one of the two hyperfine nuclei is boron.

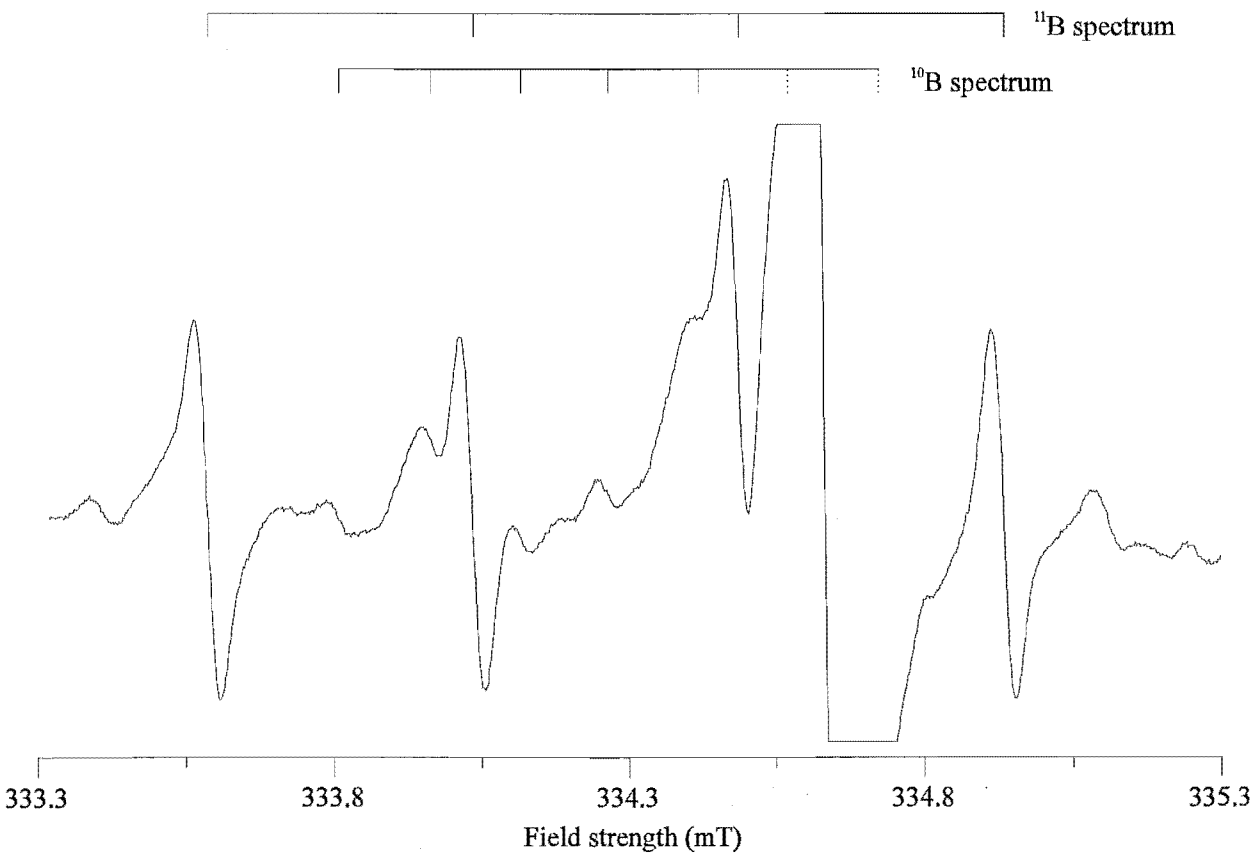

Figure 5-17: Experimental epr spectrum of two-boron centre in zircon at *ca* 80 K showing ^{11}B and minor isotope ^{10}B spectra. Frequency = 9.27327 GHz.

The 'common' boron atom which seems to be present in both centres must generate the smaller hyperfine splitting which manifests itself in the spectra in an almost identical fashion for the two centres. The amount of spin density on the two boron atoms may be estimated from the ^{11}B hyperfine interaction matrices by using the technique of Morton and Preston [78] as described earlier in the chapter for Si(Ti^{3+}). The matrices in tables 5.9 and 5.10 yield a total estimated spin density of 7 % on the common boron atom, and 16 % on the second boron in the two-boron centre. These calculations indicate that the electron spin density is mostly located away from both of the boron atoms. For the single-boron centre to have orthorhombic symmetry, the location of the bulk of the spin density must be on the same fourfold screw axis as the common boron atom, as discussed above. The observation of only a single electronic Zeeman transition with low anisotropy indicates that the system probably has $S = \frac{1}{2}$, and could be a d^1 or d^9 ion in a silicon or zirconium substitutional position, or a single electron trapped in a vacancy on the axis. Krasnobaev *et al.* [63] reported a centre with identical g values $g_x = g_z = 1.969$, $g_y = 1.981$, which was tentatively assigned as a d^1 ruthenium-lithium centre, but the spectrum appeared to be quite different to the boron centres.

If there is an impurity present, then it is probably one with a low abundance of isotopes with a nuclear spin, as there is no detectable hyperfine other than ^{11}B. This leaves relatively few possibilities. Calcium is one example, as the only isotope with nuclear spin has a very low abundance of 0.135 %. If calcium were to enter the lattice as Ca^{2+}, it could possibly gain an electron during x-irradiation to form an s^1 species which would be visible to epr. However, there is no reason in terms of charge balancing why a Ca^{2+} impurity should occur next to at least one substitutional boron atom, with a formal oxidation number of +3. There are several examples of substitutional +3 ions in zircon, including boron itself, which stabilise a nearby oxygen hole centre [37], [36], [38]. In this case the excess negative charge of a +3 ion substituting for a +4 ion is balanced by the loss of an electron from a nearby oxygen. Substitution of a Ca^{2+} ion for another +4 ion would have the opposite effect of increasing the charge imbalance.

If charge balancing of the single boron atom in a silicon or zirconium position is to occur via another substitution in a nearby zirconium or silicon site, then the oxidation state would be expected to be +5. Other ions which have larger natural abundances of nuclear-spin isotopes than calcium but may still be too low to observe are nickel and iron, but these would be unlikely

to have an oxidation number of +5. The spectra would also be expected to be more complicated than observed, as Ni^{5+} is d^5 and Fe^{5+} is d^3. Chromium, molybdenum and tungsten are d^1 ions in the +5 oxidation state, but they all have hyperfine which would probably be observable.

Of these three possibilities, chromium seems the most likely , as it is known to be present in the same crystal through observation of the Cr^{3+} Z centre (section 5.3). The lack of observed hyperfine might possibly be explained by a very small hyperfine splitting, which is non-resolvable within the linewidth. Bates *et al.* [101] reported a d^9 Cu^{2+} ion which had no measurable hyperfine splitting due to the two $I = \frac{3}{2}$ isotopes which have a total abundance of 100 %. They interpreted this result as an admixture of an excited state $3d^84p$ wavefunction into the ground state, which was shown to drastically reduce the hyperfine values calculated without the p-orbital admixture. However, this would not explain the lack of isotropic hyperfine interaction in the present case, which is expected to be large.

The electron in a vacancy model would also explain the lack of hyperfine. These F-centre-type defects are well known and studied, particularly in the alkali halides [102], but they occur at anion vacancies. There is no obvious reason why in this case an electron would occupy a cationic vacancy. Secondly, the g values of F centres are usually fairly isotropic, with all three values close to g_e. F centres are well known for being the cause of visible colouration in many crystals because they often absorb light in the visible region, but they are by no means the only kind of defect to do so. The boron epr centres are probably not responsible for the unusual colouration of the boron-doped zircon crystals after room-temperature irradiation because the centre may still be observed after the colour has faded.

If the two boron centres only differ by the second boron atom, then the observed instability of the two-boron centre around room temperature might not be due to the electron trap being destroyed. If this were the case, then both centres would probably be destroyed at the same temperature. The loss of the two-boron spectrum might be explained by the second boron atom being able to move away from the defect at room temperature, converting the two-boron centre into the single-boron centre. If this is the case, then the intensity of the single-line spectrum should increase after the four-line spectrum is annealed out. Experimentally, it was found that the single-line spectrum actually decreased after some time at room temperature, but this may merely indicate that neither centre is completely stable at room temperature. Alternatively, the

single-boron centre may simply be more stable than the two-boron centre in the paramagnetic state, possibly due to charge balancing. More comment on this possibility may be found later in the discussion.

If the second boron atom does move away from the defect at room temperature, it is probably not in a lattice site in the crystal, but located interstitially. This is very unusual in zircon, because the interstitial spaces are much smaller than those in quartz, where small interstitial ions are quite common. If there is a vacancy present, as suggested previously, then this may allow more room for the boron atom to move about. However, as shown in the next section, the hyperfine matrix of the two-boron centre seems to suggest a lattice position for the second boron atom.

Analysis of matrices

The matrices of the point-group-symmetry $mm2$ single-boron centre in zircon are required by symmetry to be diagonal, with three different principal values. The principal directions lie along the crystallographic axes, as discussed in section 2.1. Inspection of the fitted matrices of table 5.9 shows that the symmetry appears to be very close to uniaxial, as two of the principal directions are almost identical. However, one must be careful with the use of the term uniaxial here, which is often used interchangeably with $\bar{4}2m$ point-group symmetry in zircon. As described in section 2.1, the silicon and zirconium sites in zircon have $\bar{4}2m$ point-group symmetry, and so will a defect located entirely on one of these sites. In this case the 'unique' principal direction is along the c axis, and the other two principal directions are along the crystallographically indistinguishable a and b axes. Only one site is observed in all orientations. For the boron centre, there are two clearly distinguishable sites in the a and b orientations, and the two g values which are nearly identical correspond to the c- and a-axis orientations for one site, and the c- and b-axis orientations for the other. These orientations are certainly crystallographically distinguishable, but in this case the g values happen to be almost identical. In this way the parameter matrices can be uniaxial, but the site symmetry clearly orthorhombic, a most unusual situation.

Another unusual aspect is that the 'unique' principal directions of the g and A matrices for the single-boron centre are along the a and b axes, respectively (or equivalently along b and a,

respectively). Thus for one site, the g value remains isotropic as one rotates in the bc plane, while the A value changes, and for the other site, A remains isotropic while g varies.

The matrices of the m symmetry two-boron centre have the same form as those fitted for other centres with m site symmetry, where the only off-diagonal element is Y_{xz}. The P matrix is barely defined within the experimental uncertainty and could be set to zero with little effect on the rmsd. The principal directions of the A and g matrices may be compared with those of the other m centres, especially the hole centres listed in table 4.2.

The g-matrix principal directions are not within the cluster of values observed for the hole centres of table 4.2, and illustrated in figure 4-5. However, the principal directions do agree very closely with the one centre of figure 4-5 which does not resemble the others, the D centre [21]. The two principal directions in the mirror plane only differ by 1.9°. As noted in section 4.2.3, one of the D-centre g-matrix principal directions agreed very well with the short O-Zr bond direction. Likewise, one of the two-boron-centre g-matrix principal directions is only 1.3° from the Zr-O direction, as shown in figure 5-18. This evidence helps confirm that the source of the spin density in both boron centres is on a zirconium atom, and also suggests that there is something significant about the oxygen atom.

The significance of the oxygen atom is also indicated by the principal directions of the A matrix. It has principal directions which agree very closely with those of the boron hole centre, [36] and table 4.2. The two directions in the mirror plane only differ by 0.4°. This direction was interpreted as pointing from the boron substitutional site in a silicon position to the oxygen hole in the $[BO_4]^0$ centre. In this case, the hyperfine matrix reveals the site of the boron atom not common to the two boron electron centres, which has the larger hyperfine splittings. As discussed above, this boron atom must be located away from the $\bar{4}$ axis containing the spin density site and the common boron atom. Figure 5-18 shows the g-matrix principal direction, which deviates from the Si-O direction by only 3°.

The reason for the apparent significance of the oxygen atom is unclear. It is not likely to be the site of the spin density, firstly because the g values are too low for an oxygen hole centre. Secondly, the two-boron centre bears a very strong resemblance to the single-boron centre, so they are almost certainly the same type of centre. The single-boron centre cannot be an oxygen hole centre on the basis of its site symmetry.

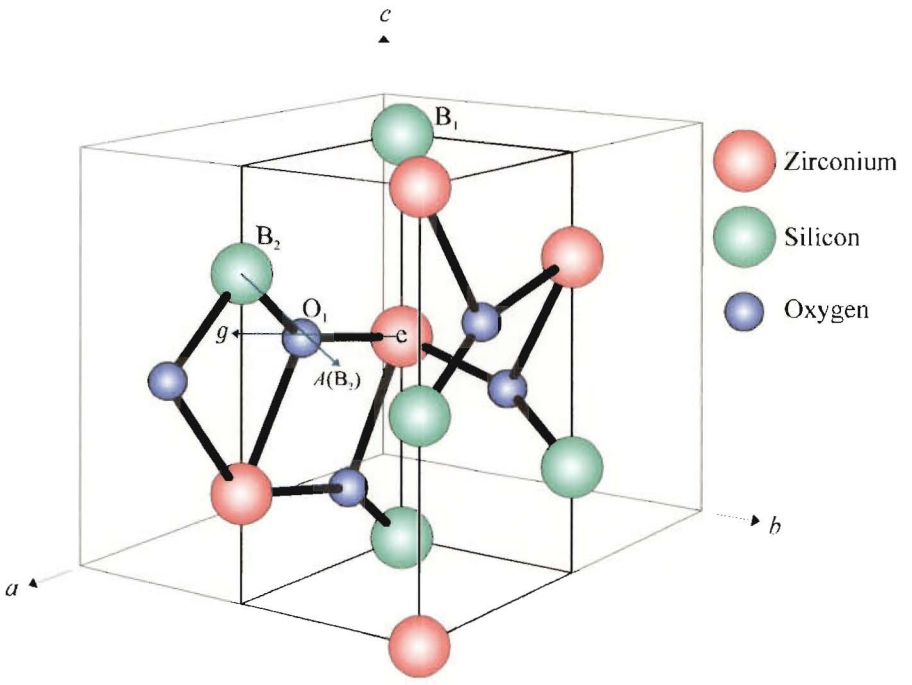

Figure 5-18: Model of boron centres showing **g** and **A** principal directions of two-boron centre which point towards O_1. The centre of electron spin density is labelled e. In the single-boron centre B_2 is a normal silicon site.

However, by the same argument, there can be nothing significant about the oxygen atom at all, unless it is repeated by operation of the two fold axis of the $mm2$ point group. If an oxygen vacancy was present, i.e., a +2 hole, then replacement of two Si^{4+} by B^{3+} would balance the charges with no other requirements. But if one oxygen vacancy was present then the orthorhombic site symmetry would require a second vacancy, leading to a +4 charge imbalance, or overall +3 for the single-boron centre, and +2 for the two-boron centre. If the electron centre in a Zr^{4+} position were to then balance the charges, it would have to have a charge of +1 or +2, respectively.

This may be suggestive of Ca^{2+}, which was noted earlier in the discussion to have very low abundance nuclear spin isotopes, which would explain the lack of observed hyperfine. This model would suggest that $[CaB_2V(O)_2]^0$ and $[CaBV(O)_2]^+$ diamagnetic centres exist prior to irradiation, with Ca^{2+} in the zirconium site. After irradiation, Ca^+ paramagnetic electron centres $[CaB_2V(O)_2]^-$ and $[CaBV(O)_2]^0$ form at low temperature. The unstable $[CaB_2V(O)_2]^-$

Table 5.11: Crystal-field splittings of orbital energy levels for two boron centres in zircon, calculated from experimental g values.

Centre	g_x	g_y	g_z	$\frac{\zeta}{\Delta_1}$	$\frac{\zeta}{\Delta_2}$	$\frac{\zeta}{\Delta_3}$
single boron	1.96874	1.98091	1.96865	242	93.9	59.6
two boron	1.96936	1.982145	1.969251	246	99.7	60.8

is then observed to disappear following annealing, presumably to revert back to diamagnetic form $[CaB_2V(O)_2]^0$. The excess electrons may form new $[CaBV(O)_2]^0$ centres, or annihilate irradiation-generated hole centres.

While this model seems to fit some of the experimental observations, it is more complicated than one would normally expect based on all the other defects which have been characterised in zircon. There is probably a simpler explanation for the two-boron centre, which does not involve so many defect components.

If the source of the electron spin density in the boron centres is a d^1 ion, a nearly identical crystal-field spin-orbit-coupling analysis of the g values may be carried out as was performed for the $Si(Ti^{3+})$ centre in section 5.2.3. As for the H centre, the analysis will be meaningless if the defect turns out not to be a single-d-electron centre. For this centre, the lower point-group symmetry means that the d_{xz} and d_{yz} levels labelled e in the previous treatment are non degenerate under the crystal-field interaction. Thus three orbital energy-level splittings must be fitted, rather than the previous two. The principal g values may then be all different, although the g matrices of the two boron centres are almost uniaxial. The results of the fitting are shown in table 5.11, where $\Delta_1 = E_{d_{xy}} - E_{d_{x^2-y^2}}$, $\Delta_2 = E_{d_{xz}} - E_{d_{x^2-y^2}}$ and $\Delta_3 = E_{d_{yz}} - E_{d_{x^2-y^2}}$. The ordering of Δ_2 and Δ_3 is not important, and could be reversed with a different choice for the site-one matrix, equivalent to swapping g_x and g_y.

The unitless splittings are larger than those fitted for the titanium centres in table 5.4, but it is not possible to comment on the absolute splittings without knowing the identity of the ion carrying the spin density, and thus the appropriate ζ.

Chapter 6

Two defect centres in α-quartz

6.1 Introduction

The piezoelectric nature of quartz coupled with its stability and ease of synthesis in very pure form leads to its usage in a wide range of technological applications. It is well-known that the properties of a quartz crystal which are utilised in these applications may be strongly affected by the number and type of defects present [60]. Natural quartz is also very common, being the dominant form of silica, SiO_2, which takes up around 12 % of the earth's lithosphere. These two factors have lead to the detailed study of the defect centres of quartz. The two review articles [103] and [104] cover the known magnetic defect centres in α-quartz up to 1992.

The first of the two centres described in this chapter is postulated to be an oxygen hole next to a silicon vacancy, with charge compensation by an H^+ and two Li^+ ions. This particular centre has not been reported in the literature, but appears to be closely related to two silicon vacancy/oxygenic hole centres previously reported [105], which respectively contain three and four H^+ ions.

These centres are derivatives of the hydrogarnet defect, $[H_4O_4]^0$, a cluster of four OH units replacing a silicon atom in a silicate crystal. The defect is so-named as it was discovered in varieties of hydrogarnet, and has been well characterised in such crystals by both neutron and x-ray diffraction experiments, e.g. [106]. No such data exist for the hydrogarnet defect in quartz, but its existence has been postulated for some time. The epr data presented in [105] provide very strong evidence that the defect does exist in quartz.

The hydrogarnet defect may be a crucial form of storage of "water" in "wet" quartz, describing any quartz sample that shows an IR signal in the 3-μm range, indicative of O-H bonds. It is well known that quartz rock may be plastically deformed under the moderate stresses it is subjected to in the Earth's crust (≤ 0.2 GPa, with $T \leq 700$ °C) [107]. This is a process by which deformation occurs by generation and motion of dislocations, so that the applied stress does not lead to brittle failure. The first testing of the mechanical properties of quartz at raised temperatures was carried out by Griggs and Blacic who realised the importance of water [108]. Testing of synthetic and natural samples of both wet and dry quartz have shown that their mechanical behaviour is very different. Dry quartz, as either a gem-quality natural sample, or high-quality synthetic crystal, is very strong, and cannot be plastically deformed, even at *ca* 1600 K and under a differential stress of *ca* 3 GPa. However, wet quartz is ductile under moderate stresses of *ca* 0.1 GPa at $T \geq 400$ °C [107]. This phenomenon is known as hydrolytic weakening, and its exact nature has been the subject of much study, as has the possible role of the hydrogarnet defect.

Purton *et al.* [109] modelled the neutral hydrogarnet defect in quartz using local density functional (LDF) pseudopotential calculations on a 36-atom cluster. This work was extented by Lin *et al.* [110], who calculated the energy of formation of the hydrogarnet defect from interstitial water, and found this to be thermodynamically favourable. The *ab-initio* stress calculations indicate that there is a substantial stess in the vicinity of the defect, which is likely to be minimised by the segregation of the defects into $(10\bar{1}0)$ planes. Lin *et al.* and McConnell *et al.* [111] suggest that this is the nature of the crystallographically oriented lattice defects observed in the $(10\bar{1}0)$ planes by McLaren *et al.* [112] using electron microscopy on reasonably wet, unheated crystals.

McConnell *et al.* used the calculations of Lin *et al.* to calculate the solubility of water in quartz in the form of the hydrogarnet defect as temperature is varied, under isobaric conditions. They concluded that the solubility has a maximum at a temperature which depends on the external water pressure, and then decreases as the temperature is raised further, in contrast to the earlier results of Paterson [113]. This leads to the conclusion that wet quartz reacts to produce quartz and molecular water upon heating. The water bubbles so produced lead to nucleation of dislocation loops and promote dislocation climb [112], [114], [115], resulting in

hydrolytic weakening. As the reaction of the hydrogarnet defects to form quartz and water requires diffusion of the defects, their rate of diffusion could be the rate-controlling process of the deformation of quartz in nature [116].

The hydrogarnet defect $[H_4O_4]^0$ was converted into the first of the epr-active centres reported in [105] by x-irradiation at 77 K or room temperature, and transfer to the instrument for measurement at *ca* 25 K. The irradiation is thought to remove an electron from an oxygen atom adjacent to the defect, leaving a $[H_4O_4]^+$ species. After a sufficiently long period at room temperature, the spectrum due to $[H_4O_4]^+$ is replaced by a three-hydrogen centre, $[H_3O_4]^0$. Thus charge neutrality is restored by the presumed diffusion of one H^+ ion away from the defect at sufficiently high temperature. It is probable that the new centre, with the characteristics of an oxygen hole centre compensated by one H^+ and two Li^+ ions, is an analogue of the $[H_3O_4]^0$ centre.

The second centre described in this chapter is an H^+-compensated Fe^{3+} centre, $[FeO_4/H]^0$ [49]. It is one of a number of iron centres in quartz of the form $[FeO_4/M]^0$, where[1] $M = H^+$, Li^+, Na^+, which have been studied by epr. An uncompensated centre $[FeO_4]^-$ is also known. As well as the general reviews cited earlier [103], [104], there is a specific review of the paramagnetic iron centres in α-quartz [19].

The first studies of the Fe^{3+} centres in α-quartz appear in the 1960s ([19] and references therein). Early studies were made on the natural coloured quartz crystals citrine and amethyst [117], [118]. In these crystals, iron centres compensated by alkali metal ions were found, and designated S_1 centres [119], to indicate a substitutional site for the iron. Measurements carried out around the same time on iron-doped "synthetic brown quartz" revealed an uncompensated iron centre initially designated *I*, to indicate an interstitial site for the iron [120], [121]. In the following years there has been much controversy about this assignment (see discussion and references in [19]). There has been strong evidence provided which points towards a substitutional site for the iron. Among these is the pseudocube calculation, which is described in the iron-centre section of this chapter, and is used to analyse the $[FeO_4/H]^0$ centre.

The various iron centres have epr spectra with narrow linewidths, are visible even at room temperature, and display great anisotropy (see figure 6-16). The large number of lines which

[1] See earlier footnote, p36.

may be observed for each centre, and the complicated angular-dependence curves yield more detailed information which cannot not be extracted from other centres with low electronic spin and correspondingly simpler spectra.

The centre described in this chapter was found, when the final matrices were compared with the literature, to be one which had already been characterised. However, the pseudocube analysis of the fitted spin-Hamiltonian parameter matrices for this centre had not yet been carried out, and is reported herein.

6.2 The $[HLi_2O_4]^0$ centre

6.2.1 Experimental details

The $[HLi_2O_4]^0$ (and $[FeO_4/H]^0$) centre was observed in a right-hand α-quartz crystal supplied by Professor J. A. Weil during a visit to Canterbury in 1998. It was grown by Sawyer Research Products in 1975 using hydrothermal techniques as described in section 3.1.2.

The handedness of the crystal was determined by Professor Weil's group[2] by experiments determining the optical rotation of plane-polarised white light as described in [42], using the fact that right-quartz is dextrorotatory. The crystal was cut by them with faces perpendicular to the crystallographic *c (z)* axis, one of the crystallographic *a (x)* axes, and a mutually perpendicular *y* axis. The dimensions were 5.02 mm × 4.27 mm × 5.25 mm in the *x*, *y*, and *z* directions, respectively.

The crystal had been gamma-irradiated at room temperature for *ca* 18 hours at 2687 rads per minute, and qualitatively examined by epr spectroscopy before and after irradiation, before it was supplied to the Canterbury epr group. All measurements were carried out without further irradiation or annealing treatment. In addition to the $[FeO_4/H]^0$ and $[HLi_2O_4]^0$ centre spectra described herein, spectra from the three-hydrogen centre, $[H_3O_4]^0$ [105] and the aluminium oxygen-hole centre $[AlO_4]^0$ [42] were also observed in this crystal. Experiments were carried out with the crystal mounted on one of the faces perpendicular to the two-fold a_1 *(x)* axis. The crystal was mounted on the adjustable mount described earlier (figure 1-3), as the faces of the cut crystal were not precisely perpendicular to the crystallographic axes. Precise alignment in

[2] With thanks to Mr J. A. S. Williams.

the yz plane was achieved by observing the collapse of the aluminium centre $[AlO_4]^0$ lines at *ca* 15 K as the mount was tilted by small amounts in two perpendicular directions as described in section 1.3. The $[AlO_4]^0$ centre has site symmetry 1, and therefore shows six sites in a general orientation which collapse to three when the applied field is precisely perpendicular to the a_1 axis, and one when it is parallel to the c axis. The collapse of six site spectra to three allowed the precise alignment of the rotation plane by adjusting the mount until nearby pairs of signals on an oscilloscope collapsed to single lines.

Following precise alignment of the crystal in the yz plane using the $[AlO_4]^0$ lines, the crystal was warmed to *ca* 100 K for measurement of the $[HLi_2O_4]^0$ centre. At lower temperatures this low-intensity centre is completely obscured by the much-higher-intensity $[AlO_4]^0$ centre. Fortunately, the $[AlO_4]^0$ lines rapidly broaden as the temperature is raised, a phenomenon which has been proposed to be due to the rapid exchange of the spin density between the oxygen atoms surrounding the aluminium ion [122]. Data for analysis were recorded at 5° intervals over 180° in the yz plane beginning in the c-axis orientation. Measurement of spectra for both the $[AlO_4]^0$ and $[HLi_2O_4]^0$ centres in the same crystal orientation allowed the final fitted parameter matrices for $[HLi_2O_4]^0$ to be checked for consistency of rotational sense with the system established by Weil's group [42].

6.2.2 Results

The $[HLi_2O_4]^0$ spectra collected over 180° were gathered in a stacked plot, shown in figure 6-1. This plot is a good visual demonstration of the large number of lines present, and the anisotropy in the hyperfine interaction. There were clearly three distinct site spectra observable in the plane measured, indicating that the point-group symmetry was 1. The complicated lineshape of the spectra, which appeared to be due to several small hyperfine interactions, hinted at a relationship to the multiple-hydrogen centres [105], though there were clearly more hyperfine lines present in this case.

On the basis that this was another silicon-vacancy/oxygen-hole centre with several compensatory +1 ions, an attempt was made to approximately reproduce the c-axis spectrum (see figure 6-4, later in the chapter) using several spins of $\frac{1}{2}$ and/or $\frac{3}{2}$. These nuclear spins were considered to be more likely than any other, as the +1 compensators known for other cen-

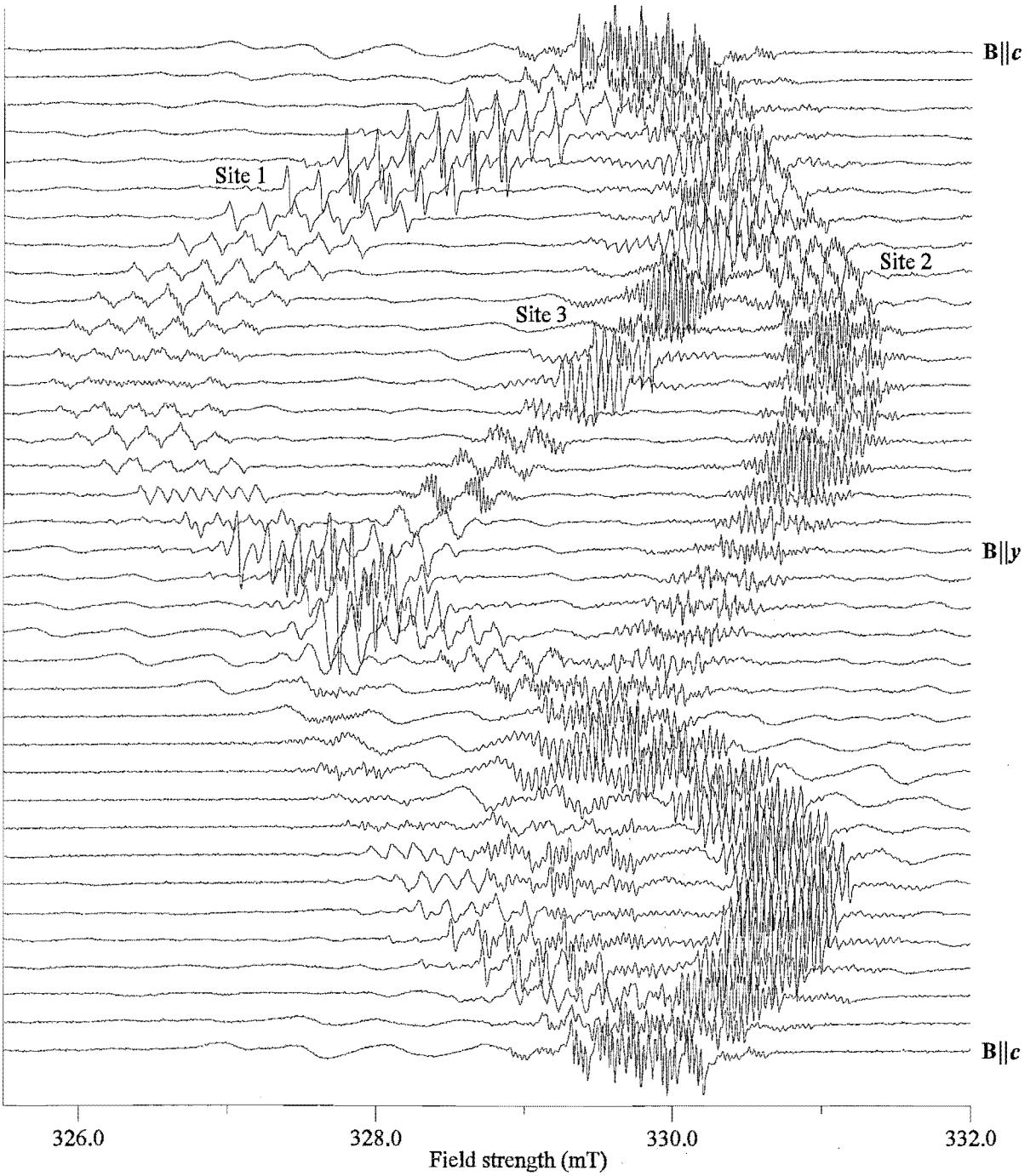

Figure 6-1: Stacked plot of $[HLi_2O_4]^0$-centre epr spectra in α-quartz at *ca* 100 K with **B** in the yz plane. Frequency $\approx$ 9.2832 GHz.

tres in α-quartz (H^+, Li^+, Na^+, Ag^+) have no other spins amongst the principal isotopes. Simulation of the spectrum was carried out using Winepr Simfonia [123], a software package designed to simulate solution or powder epr spectra using perturbation theory up to third order. The simulation-of-solution-spectra option using first-order perturbation theory proved to be a quick and easy way to experiment with various spins and hyperfine splittings until a reasonable spectrum was obtained.

The c-axis spectrum was found to be reasonably well simulated by three hydrogen ions (principal spin $\frac{1}{2}$) and one lithium ion (principal spin $\frac{3}{2}$) with hyperfine splittings of 0.357 mT, 0.246 mT, 0.178 mT and 0.031 mT, respectively. To prove that this agreement for the c-axis spectrum was not coincidental, the same process was repeated for all the site-resolved spectra obtained. If most of the spectra could be reproduced using the same number and type of atoms, and if a plot of the extracted splittings against the rotation angle followed a smooth trend with no discontinuities, then the assignment would be reasonably secure. This was indeed found to be the case. A plot of the extracted splittings is overlaid on the final fitted hyperfine splittings in figure 6-2. As discussed below, however, the hyperfine nuclei were eventually identified as two Li^+ and one H^+.

The hyperfine splittings were used to generate individual artificial data sets for four one-nucleus 'centres', one for each hyperfine nucleus, where the g value was taken as 2.0 for all orientations. Hence the artificial line positions were given by:

$$B_H = \frac{h\upsilon}{2\beta_e} \pm \frac{a}{2} \tag{6.1}$$

$$B_{Li} = \frac{h\upsilon}{2\beta_e} \pm n\frac{a}{2} \tag{6.2}$$

where a is the extracted hyperfine splitting, and $n = 1$ or 3. Each of these data sets was fitted to obtain an approximate hyperfine matrix for each nuclide according to the derived splittings.

A true g matrix for the $[HLi_2O_4]^0$ centre was also obtained, using the centre position of the set of hyperfine lines for each site in each orientation. The four hyperfine matrices and the g matrix were then used together to simulate the spectrum and allow the true observed line positions to be matched with the correct transition labels. This was the only way in which this could be done, as the spin-Hamiltonian energy-level manifold for this centre contained 64 levels

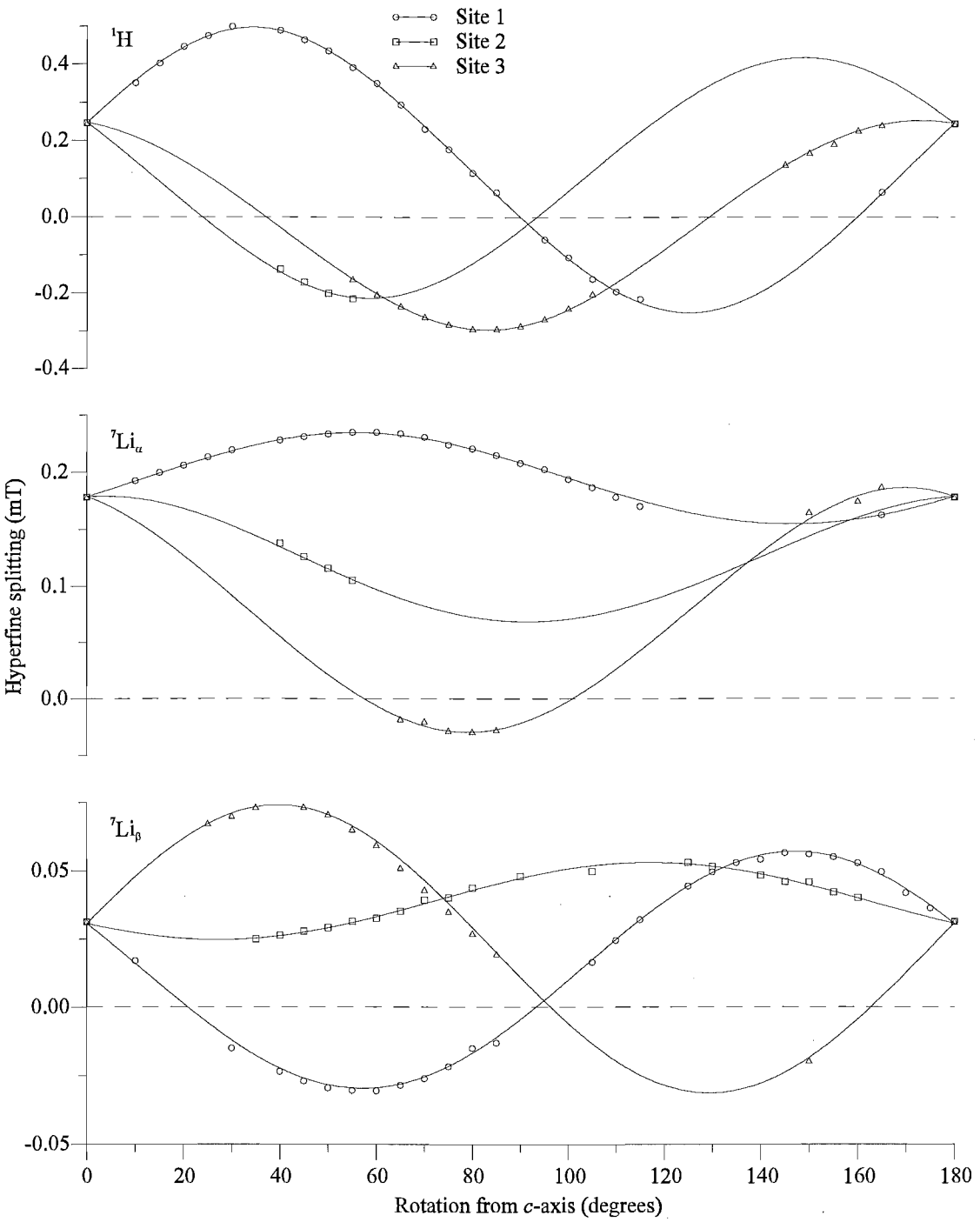

Figure 6-2: Variation of observed hyperfine splitting for the three hyperfine nuclei of the $[HLi_2O_4]^0$ centre in α-quartz at *ca* 100 K in the *yz* plane. The experimental points were derived as discussed in the text and the solid curves were calculated from the fitting of the artificial data set.

generating 1024 possible epr transitions, and the anisotropy of the hyperfine matrices led to levels continually crossing in different crystal orientations. Eventually a process of simulating, entering data, fitting the data, and resimulating with new matrices lead to the inclusion of 1243 data points in the fitting, covering all three sites and 180° of rotation.

The agreement between experimental and observed spectra was reasonable for the higher-intensity allowed lines, but was not very good for the forbidden lines involving simultaneous changes in the electronic and nuclear spin z-component quantum numbers M_S and M_I which were observed on the outsides of the allowed lines. In some orientations the intensity of these secondary lines constituted a significant fraction of the allowed lines, and they also had an influence on the main spectrum lineshape. The failure of the $3H^+$-Li^+ model to account for these lines led to the reinvestigation of this assignment of the hyperfine nuclei. Closer inspection of two of the fitted hydrogen hyperfine matrices revealed that one was almost exactly double the other. The line pattern produced by two doublet splittings with a ratio of magnitudes of two, is four evenly spaced lines with a splitting equal to the smaller of the two doublet splittings. Thus it was possible that the two fitted doublet hydrogen splittings were in fact a single hyperfine interaction with a spin $\frac{3}{2}$ nucleus.

To test this possibility, some of the angles where the agreement between simulated and observed spectra had been quite poor were resimulated after replacing the two hydrogen hyperfine matrices by a lithium matrix identical to the hydrogen matrix which had the lesser-magnitude elements. The resultant spectra agreed very well with the observed spectra, confirming the new assignment. Simulation using other nuclei with the correct nuclear spin failed to give a good agreement with the experimental spectra. The correct value of g_n clearly is crucial to an accurate simulation. Figure 6-3 shows an experimental spectrum of site two, 55° from the c axis, with the simulations using $3H^+/Li^+$ and $2Li^+/H^+$.

The change in the model changed all of the transition labels of the observed lines, so that all spectra had to be resimulated and the data reassigned. It was also possible to add more data points as the higher-intensity forbidden lines could now be included where they were observed. The final fitting was made to a spin Hamiltonian of the form:

$$\hat{H} = \beta_e \mathbf{B}.\mathbf{g}.\hat{\mathbf{S}} + \sum_i \left(\hat{\mathbf{S}}.\mathbf{A}_i.\hat{\mathbf{I}} + \hat{\mathbf{I}}.\mathbf{P}_i.\hat{\mathbf{I}} - \beta_n \mathbf{B}.\mathbf{g}_{ni}.\hat{\mathbf{I}} \right) \tag{6.3}$$

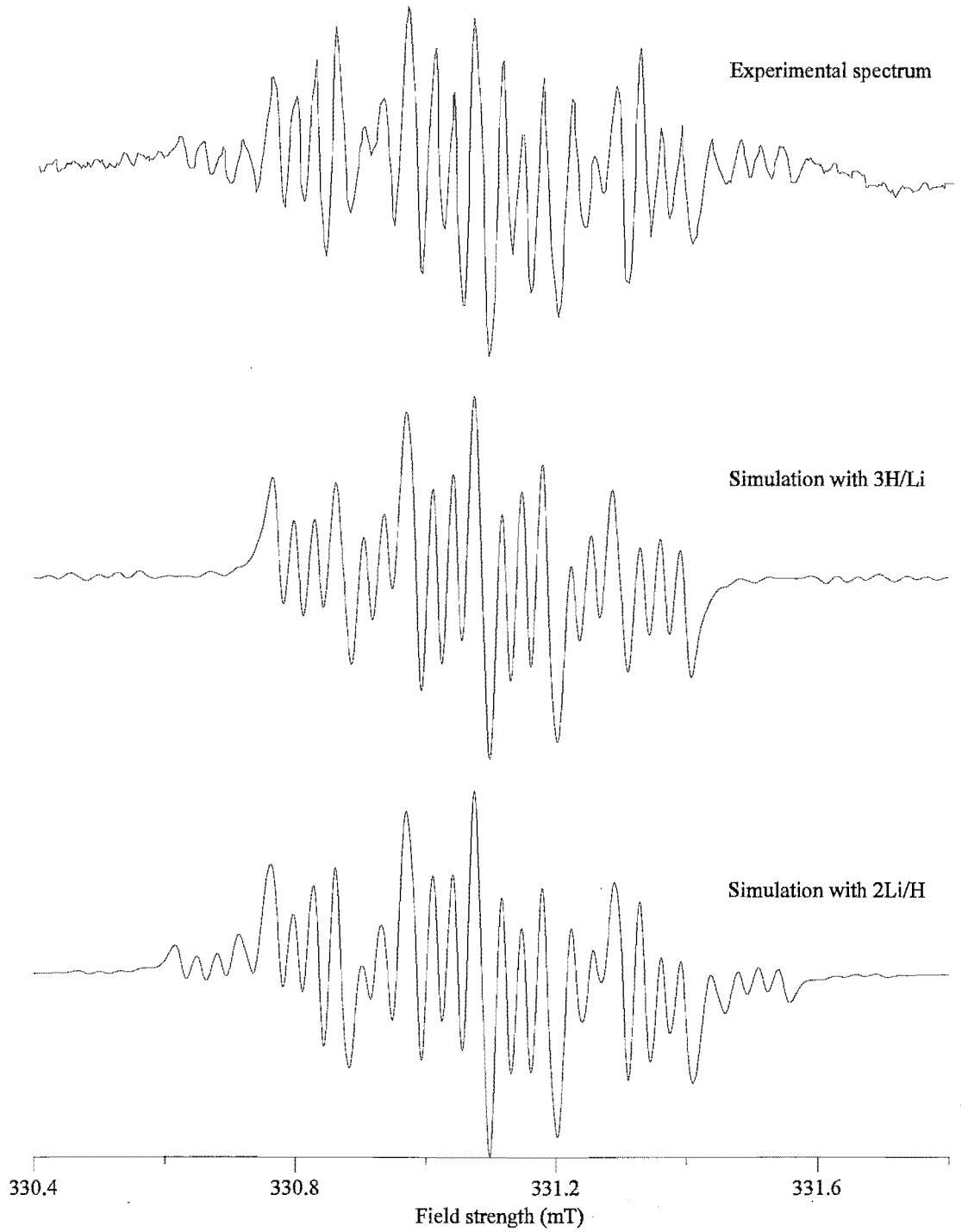

Figure 6-3: Experimental (top) and simulated epr spectra of $[HLi_2O_4]^0$ centre in α-quartz at *ca* 100 K using 3H/Li and 2Li/H models. Frequency = 9.28315 GHz. The spectra are for site 2, 55° from the c axis.

where the sum is over the three hyperfine nuclei. The quadrupole term applies only to the lithium nuclei. The $\mathbf{g}_{ni}$ were set as the scalar matrices 5.5856912**U** for the hydrogen nucleus and 2.170961**U** for the lithium nuclei. **U** is the 3×3 unit matrix, and 5.5856912 and 2.170961 are the g_n values of ^{1}H and ^{7}Li set internally by EPR-NMR. The contribution due to ^{6}Li (7.5 % abundant) was not taken into account in the fitting because it had only a minor effect on the spectrum, and produced no resolved lines. The ^{7}Li P matrices were found to be zero within the uncertainty of the fitted values, so were set to be exactly zero in the final fit.

Site one was chosen as the 'unique' site observed in the stack plot of figure 6-1, the site which is most unlike the other two, as discussed in section 2.2. As also discussed in that section, the degenerate nature of the site-one spectra (sites 1 and 1′) in the plane of measured data allows two identical fittings (line positions + intensities) to be produced without changing the assignment of site one. The principal directions of all of the parameter matrices for the two fittings are given by θ_1, ϕ_1, θ_2, ϕ_2, θ_3, ϕ_3 and θ_1, $180° - \phi_1$, θ_2, $180° - \phi_2$, θ_3, $180° - \phi_3$. The matrices reported in table 6.1 have the principal directions which best agree with those of one of the aluminium oxygen-hole centres, corresponding to placing the electron hole on either O_2 or O_3 of figure 2-2.

A simulation of the c-axis spectrum using these matrices proved to be in excellent agreement with the experimental spectrum. The most significant difference was a set of four very-low-intensity lines on the very outside of the spectrum, which were appreciably higher in intensity and in slightly different positions to the simulated lines. These lines were interpreted as silicon hyperfine lines. This was confirmed by measurement of the intensity ratio which corresponded to a natural abundance of 4.78 %, assuming a low-abundance nuclear spin $\frac{1}{2}$ isotope, in good agreement with the natural abundance of ^{29}Si of 4.7 %. This single silicon atom would most likely be the one which is bonded to the oxygen hole. The other silicon atoms are much further away from the oxygen hole both in terms of physical distance and through bonding. The position of the hyperfine lines indicated a hyperfine splitting of 1.21 mT at the c-axis orientation, but no hyperfine matrix was fitted, as there were no other data collected.

A final simulation was produced which included the contributions from the minor lithium isotope, ^{6}Li, 7.5 % abundant with $I = 1$, as well as the silicon hyperfine. This was taken into account by simulating the spectra for the five dominant combinations of isotopes, and adding

Table 6.1: Spin-Hamiltonian parameters for the $[HLi_2O_4]^0$ centre in α-quartz at *ca* 100 K. The hyperfine matrix signs are arbitrarily given such that the isotropic component a is positive. Error estimates in parentheses.

Y		Matrix **Y**		k	Principal value Y_k	Principal direction θ_k (deg)	Principal direction ϕ_k (deg)
g	2.009839(2)	0.008334(2)	-0.000650(1)	1	2.034377(2)	115.05(0)	70.57(0)
		2.025822(2)	-0.011332(1)	2	2.009657(2)	128.37(1)	182.28(1)
			2.0110472(8)	3	2.002674(1)	131.29(1)	316.33(1)
$\mathbf{A}/g_e\beta_e$	-0.2177(6)	-0.1459(5)	0.1299(4)	1	0.5619(5)	142.1(1)	112.8(2)
(^{1}H)(mT)		-0.0027(6)	-0.3608(4)	2	-0.2145(5)	55.7(2)	141.3(4)
			0.2643(3)	3	-0.3035(5)	104.0(2)	221.5(3)
$\mathbf{A}/g_e\beta_e$	-0.0383(3)	-0.0549(3)	-0.0242(2)	1	0.2437(2)	118.37(8)	98.4(3)
(^{7}Li$_\alpha$)(mT)		0.2148(3)	-0.0379(2)	2	0.1676(2)	29.60(6)	116.5(1)
			0.1807(1)	3	-0.0540(2)	97.7(1)	192.6(3)
$\mathbf{A}/g_e\beta_e$	0.0408(3)	-0.0210(2)	0.0368(2)	1	0.0752(2)	136.5(3)	195.9(3)
(^{7}Li$_\beta$)(mT)		-0.0045(3)	0.0399(2)	2	0.0395(2)	66.3(3)	133.5(3)
			0.0313(1)	3	-0.0472(3)	56.0(2)	240.7(2)

Data points: 1886 Unit weighted: 469 $\sum$ weightings: 1124.3 rmsd (mT): 0.00346

the spectra after multiplication by appropriate scaling factors. The combinations ^{6}Li$_\alpha$, ^{7}Li$_\beta$, ^{29}Si, and ^{7}Li$_\alpha$, ^{6}Li$_\beta$, ^{29}Si, and ^{6}Li$_\alpha$, ^{6}Li$_\beta$, ^{29}Si, were not included as the simulations are time consuming and would have made a negligible contribution to the spectrum. The ^{6}Li hyperfine matrices were calculated by multiplying the ^{7}Li matrix by the isotopic g_n ratio, while the ^{29}Si spectrum was simulated simply by using the estimated c-axis hyperfine splitting. Slight adjustments of the hyperfine splittings were then made for all of the minor spectra to obtain the best simulation.

The simulation is shown in figure 6-4, and includes all possible epr transitions. Flanking the 32 allowed lines which are due to transitions with no changes in any nuclear spin quantum number, there are some weaker 'spin-flip' transitions, which involve a simultaneous change in both the electronic and one nuclear spin component quantum numbers relevant in a strong magnetic field [124]. The nature of these lines was determined by identifying the transition labels from the simulation output, and checking these against an energy-level plot, also calculated

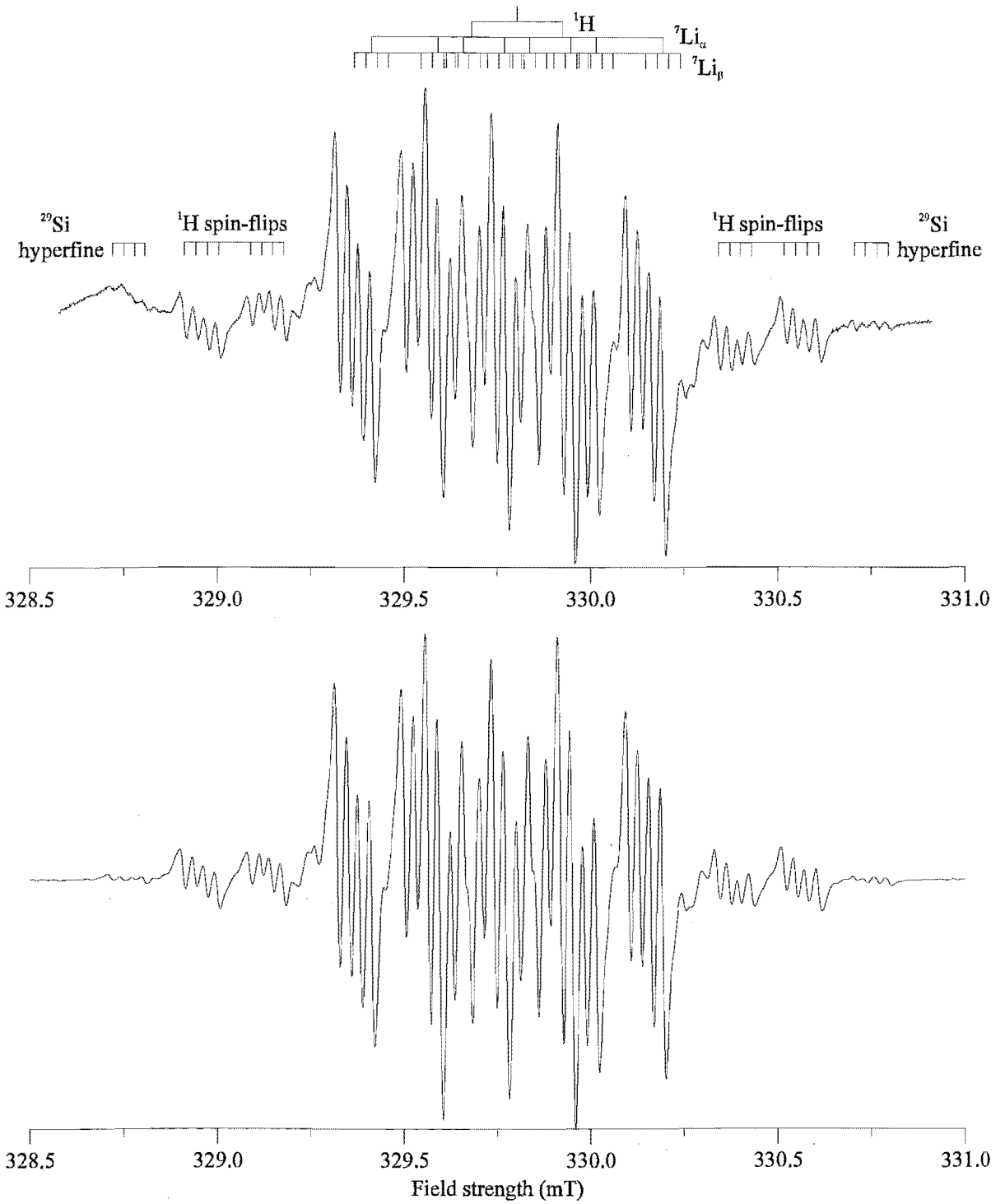

Figure 6-4: Experimental (top) and simulated epr spectrum of $[HLi_2O_4]^0$ centre in α-quartz at *ca* 100 K with $\mathbf{B}\|\mathbf{c}$. Frequency = 9.28188 GHz. The fitted hyperfine splitting due to each nucleus is shown above the experimental spectrum. Broad lines are due to $[AlO_4]^0$.

using EPR-NMR. This plot is shown in figure 6-5, with all nuclear spin quantum numbers M_I shown. Also indicated are the 32 allowed transitions, and 16 of the most clearly visible spin flips, placed at their resonant field positions (i.e., all transition images are the same length, as they are all stimulated by the same frequency of microwave radiation).

The position of the various spin-flip lines depends on the g value of the nucleus undergoing the change in M_I. These lines are thus useful indicators of the nuclei present. It is clear from the agreement between the experimental and simulated spectra that the assignment of the nuclei present in this centre is correct. The lithium spin flips are not visible as resolved lines (as the hydrogen spin flips marked in figure 6-4 are), but they make a contribution to the spectrum in excellent agreement with the experimental spectrum.

6.2.3 Discussion

Formation and nature of the defect

The centre $[HLi_2O_4]^0$ can be fairly confidently assigned as an oxygen hole centre due to the similarity of the g-matrix principal directions to those of other holes in α-quartz, as discussed below. The identity of the three hyperfine nuclei which are associated with the hole have been firmly established by the excellent simulations of the experimental spectra. The small magnitude of the hyperfine interaction matrices suggests that they carry only a minor part of the spin density, and are most likely to be in the $+1$ oxidation state, in which they have no directly associated unpaired electrons. These two aspects of the defect centre (an oxygen hole, and three $+1$ charges), imply a net charge imbalance of $+4$ with respect to the normal α-quartz lattice. The overall charge of the defect is likely to be neutral with respect to the normal α-quartz lattice as it is very stable, and does not decay after long periods at room temperature. This requires a -4 charge to be present in the defect also, which could be provided by an interstitial ion(s) with a charge of -4, or either a neutral atom substituted in the silicon site, or a silicon vacancy (both equivalent to replacement of a $+4$ ion by a neutral species).

There is no evidence, by way of hyperfine splittings, for any foreign atoms in the $[HLi_2O_4]^0$ defect other than the hydrogen and lithium ions, which leaves few possibilities for either an interstitial or a substitutional impurity to provide the necessary charge balancing described above. Neither of these two possibilities is as plausible as a silicon vacancy, which is thought to

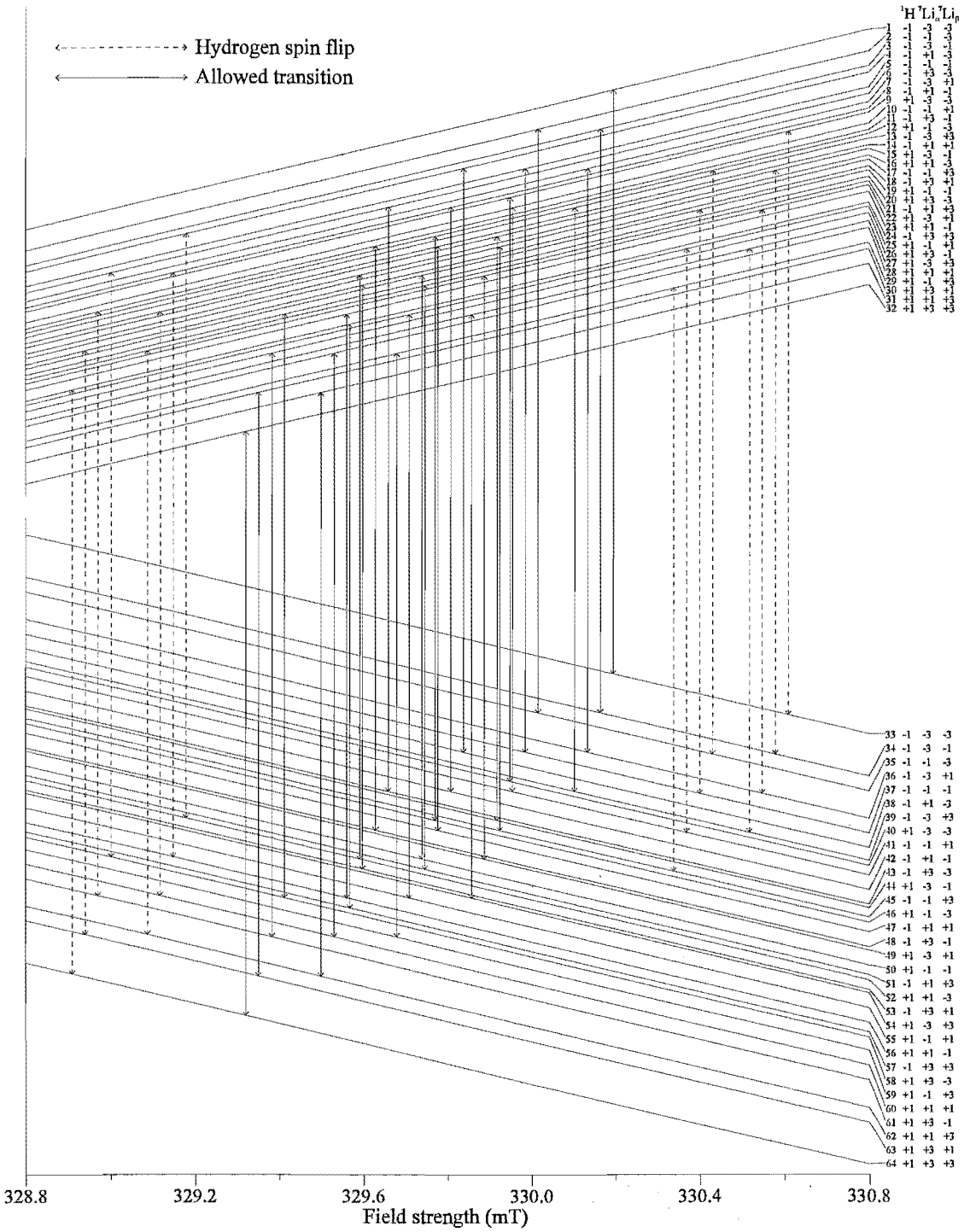

Figure 6-5: Zeeman energy-level plot for centre $[HLi_2O_4]^0$ in α-quartz in the c-axis orientation showing 32 allowed transitions and several proton spin-flip transitions, corresponding to a frequency of 9.28188 GHz.

be common in quartz, as briefly reviewed at the beginning of this chapter. If the hydrogarnet defect exists in α-quartz, there seems no reason why an equivalent centre with different +1 compensators could not be formed. However, this raises the question of why only $[HLi_2O_4]^0$ has been observed, in addition to the multi-hydrogen centres. As both lithium and hydrogen ions are present in this crystal, there is no obvious reason why a centre with one hydrogen and two lithium ions should occur exclusively in preference to a $[H_2LiO_4]^0$ or $[Li_3O_4]^0$ centre.

Secondly, if the $[HLi_2O_4]^0$ centre is an analogue of the hydrogarnet defect and the multi-hydrogen epr centres, then one would expect there to be a precursor to this centre. The $[H_4O_4]^+$ epr centre is thought to be generated from the hydrogarnet defect by the loss of an electron from an oxygen atom upon irradiation [105]. As the defect then contains an excess positive charge, one of the H^+ ions would likely migrate away from the defect at sufficiently high temperature, leaving the $[H_3O_4]^0$ centre. The $[HLi_2O_4]^0$ centre may similarly be the final stage of a transition from an epr-silent $[XHLi_2O_4]^0$ defect in the undisturbed crystal to a $[XHLi_2O_4]^+$ epr centre following irradiation, and finally to the $[HLi_2O_4]^0$ epr centre following annealing. The X ion in the precursor could be another hydrogen or lithium ion, or something else entirely, provided it had a charge of +1.

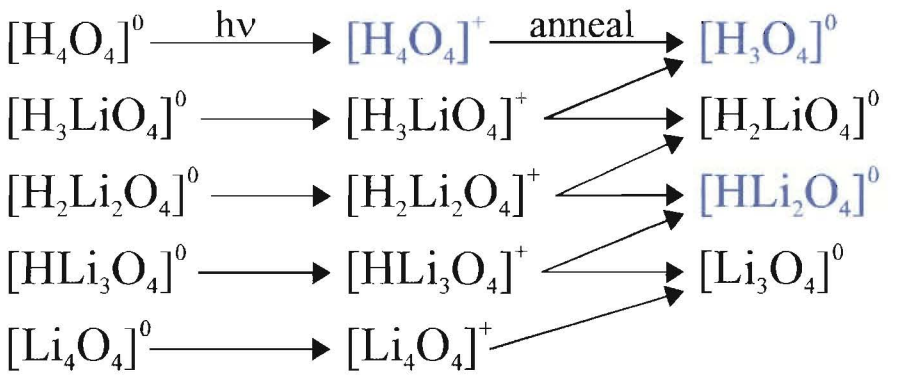

Figure 6-6: Summary of possible variations of the diamagnetic hydrogarnet defect, involving only H^+ and Li^+, and the paramagnetic species which could be generated from them. The known paramagnetic centres are shown in blue.

Even if one only assumes the possibility of H^+ and Li^+ ions, this still leaves many possible centres which have not been observed, as summarised in figure 6-6. However, every starting point other than $[Li_4O_4]^0$ in figure 6-6 can lead to one of the two paramagnetic centres observed

in this crystal after a long time at room temperature. This may suggest that these two centres are the most stable forms of the paramagnetic hydrogarnet defect, and that their final relative concentrations in the annealed crystal may depend on the relative concentrations of H^+ and Li^+ in the crystal. As the $[HLi_2O_4]^0$ centre has not been observed before, it may only form when reasonably high concentrations of Li^+ are present. The crystal in which $[HLi_2O_4]^0$ was observed was not grown under any special conditions which might lead to a higher concentration of Li^+ than is usual, but perhaps the mineraliser used contained more lithium impurity than normal. However, if this were the case, then one might expect to observe other paramagnetic centres involving lithium. The crystal contains a hydrogen-compensated iron centre, but no lithium-compensated iron centres were observed. It appears that all of the lithium ions are either bound in the $[HLi_2O_4]^0$ centres, or are not associated with paramagnetic centres. If the proposed $[XHLi_2O_4]^+$ precursor to $[HLi_2O_4]^0$ was ever present, the X ion may have become associated with any uncompensated iron centres, $[FeO_4]^-$, which are also not observed in this crystal. This would tend to suggest that X was H^+. Careful epr measurements on a gamma-irradiated virgin α-quartz crystal from the same synthetic growth would be useful, to see what centres are present initially, and after annealing. It would also be useful to study a crystal which was deliberately grown with a high proportion of Li^+ ions.

It is quite possible that the $[Li_4O_4]^0$ species, which would not lead to either of the two known neutral paramagnetic centres, is unlikely to form when H^+ ions are present, due to the steric factors involved. A Li^+ ion, with a filled 1s electron shell, is clearly much larger than a single proton. Secondly, the analysis of the hyperfine matrices for $[HLi_2O_4]^0$ later in this chapter suggests that the lithium ions bridge between two oxygen atoms in the oxygen tetrahedron surrounding the silicon vacancy. It may be that the bridging of three or four of the six edges in a tetrahedron would cause too much distortion to be energetically favourable.

It is harder to explain why the species $[H_2LiO_4]^0$ might not be formed, but it is also very difficult to imagine what the exact nature of the bonding would be in any of these species. *Ab-initio* calculations could perhaps offer some clue as to which configurations out of the multitude of possibilities might have lower energies.

Various experiments were carried out on a piece of the gamma-irradiated crystal which contained the $[HLi_2O_4]^0$ centre in the hope of finding a paramagnetic precursor. Initial exper-

iments involved x-irradiation of the crystal without any previous high-temperature anneal. If there were any diamagnetic $[XHLi_2O_4]^0$ defects left in the crystal which survived the original gamma irradiation, it was hoped that this treatment would generate a $[XHLi_2O_4]^+$ precursor. The irradiations produced some unidentified signals, but they appeared too simple to be the desired centre. The crystal was annealed several times at increasing temperature until the $[HLi_2O_4]^0$ centre was no longer visible. This was eventually achieved by annealing for several hours at *ca* 400 °C, which removed all signals in the region around $g = 2$. Subsequent x-irradiations did not produce any centres which looked worthy of further investigation. The $[HLi_2O_4]^0$ was never successfully regenerated, even after a long time at room temperature following irradiation, although the region of the spectrum containing $[HLi_2O_4]^0$ was somewhat obscured by a room-temperature-stable $[AlO_4/Li]^+$ centre [125], [126].

The failure of these experiments to generate a precursor for $[HLi_2O_4]^0$ cannot be considered as proof that such a centre does not exist. As proposed earlier, a more telling experiment would require the gamma-irradiation of a piece of virgin crystal from the same growth under similar conditions, and epr measurement immediately following irradiation and cold transfer. As the gamma irradiations were not carried out in the Canterbury lab, such an experiment has not been performed.

No other presently proposed model of the current centre seems to fit all of the experimental data as well as the silicon-vacancy/oxygen-hole model. Suspected silicon vacancy centres are not the only centres known in α-quartz which are associated with multiple +1 compensatory ions, but these other centres are very different in all other respects. The $GeHLi_2$ centre [127] contains the same +1 ions as $[HLi_2O_4]^0$, but this is the only similarity. The $GeHLi_2$ centre is formed from a diamagnetic precursor comprising a Ge^{2+} ion substituting for Si^{4+} with two Li^+ compensators in opposite-side channels. Room-temperature x-irradiation is thought to produce hydrogen atoms which readily diffuse through the crystal and react with the Ge^{2+} ions to produce Ge^{3+} and a hydride ion, H^-, by electron transfer. As would be expected for an electron centre such as this, the g-matrix principal directions do not fit as well into the pattern shown by the hole centres (see discussion below and table 6.2). Secondly, the principal g values are all less than the free-electron value, in contrast to those of all of the hole centres, including $[HLi_2O_4]^0$. The H^- ion also carries a lot more spin density than the hydrogen ion in

the $[HLi_2O_4]^0$ centre, with hyperfine splittings of the order of 8 mT compared to a maximum of around 0.05 mT in $[HLi_2O_4]^0$, and the two lithium ions are nearly equivalent, which is not true for $[HLi_2O_4]^0$.

In light of the proposed importance of the hydrogarnet defect in quartz degradation and plasticity, it is interesting to speculate about the effect that $[XHLi_2O_4]^0$ defects might have. As described earlier, the hydrogarnet defect, $[H_4O_4]^0$, is thought to react on heating to produce quartz and molecular water [111]. The energetics of formation of Li_2O from lithium-containing hydrogarnet-type defects would be quite different to H_2O formation from the $[H_4O_4]^0$ hydrogarnet defect. The presence of the lithium may help stabilise the defect, and perhaps resist the processes leading to dislocation production in heated quartz. Similar calculations to those carried out for the hydrogarnet defect need to be undertaken to give some idea as to the affect of the lithium. Electron-microscopy experiments and mechanical testing on a crystal known to contain a high concentration of $[HLi_2O_4]^0$ defects would also be useful.

Location of the hole

The principal directions of the g matrix of table 6.1 fall into the same pattern as other hole centres in quartz, including the aluminium hole centres [42], [128], [17], and the multi-hydrogen centres [105]. All of these centres are generated by irradiation, and are thought to involve the trapping of an electron hole on an oxygen atom adjacent to a pre-existing crystal defect. In the case of the aluminium centres, the stabilising defect is an aluminium ion substituted in a silicon position, while the multi-hydrogen centres are thought to comprise a silicon vacancy accompanied by compensating H^+ ions.

The g-matrix principal directions of all of these centres are approximately related by a rotation about the c axis, as may be seen in table 6.2. All of the polar angles θ are approximately the same, while the azimuthal angles ϕ are related approximately by an additive constant (which changes from each centre to the next), as discussed below.

The $[AlO_4/M]^+$ centres may be grouped together, as they have very similar g-matrix principal directions. These are related to the $[AlO_4]^0$-centre directions by a rotation of approximately 110° about the c axis. The major difference in the structure of the $[AlO_4/M]^+$ and $[AlO_4]^0$ centres, other than the presence of the compensator, is the location of the oxygen hole rela-

Table 6.2: g-matrix principal directions for aluminium and silicon vacancy hole centres in α-quartz, ordered by rotation about the c-axis with positive $\Delta\phi$.

k		$[AlO_4]^0$	$[HLi_2O_4]^0$	$[H_3O_4]^0$	$[H_4O_4]^+$	$[AlO_4/H]^+$	$[AlO_4/Li]^+$	$[AlO_4/Na]^+$
1	θ_k	119.25*	115.05*	119.54	124.18	120.13	116.44	113.41
	ϕ_k	57.62*	70.57*	141.99	146.18	167.70	168.36	168.99
2	θ_k	124.43	131.29	123.23	124.46	127.62	130.23	134.10
	ϕ_k	305.05	316.33	30.20	28.41	51.14	53.48	54.18
3	θ_k	131.65	128.37	132.52*	127.13*	127.79*	128.33*	126.74*
	ϕ_k	177.49	182.28	263.29*	267.12*	284.44*	281.51*	277.85*

* 'unique' principal direction

tive to the aluminium atom. As described in section 2.2, there are two types of oxygen atoms bonded to any given silicon atom, which have slightly different bond lengths. In the unit-cell diagram of figure 2-2, the short Si-O bonds are shaded. Analysis of the principal directions of the spin-Hamiltonian parameter matrices of the aluminium centres has shown that the hole is located on a long-bonded oxygen atom in the $[AlO_4]^0$ centre, and on a short-bonded oxygen atom in the $[AlO_4/M]^+$ centres.

Of particular importance are the ^{17}O hyperfine data collected for the $[AlO_4]^0$ centre [42], [129], since here the oxygen atom carries the majority of the spin density. The ^{17}O hyperfine matrix was found to be coaxial with the g matrix [42], though the 'unique' principal values correspond to different directions. The unique principal direction of the ^{17}O hyperfine matrix is expected to indicate the direction of the oxygen p-orbital component of the unpaired-electron wavefunction, and was found to be perpendicular to the Si(Al)-O-Si plane containing the oxygen long-bonded to the aluminium site. The other perpendicular directions were necessarily close to the Si(Al)-O-Si plane, with one direction close to an Si(Al)-Si direction. The same comparisons could, of course, be made with the g-matrix principal directions, as the two matrices are nearly coaxial. The 'unique' principal directions of the other parameter matrices could also be rationalised in terms of a hole on a long-bonded oxygen. The principal directions of the $[AlO_4/M]^+$-centres g and A(Al) matrices were found to be related to interatomic directions in the same manner as $[AlO_4]^0$, with the hole placed on a short-bonded oxygen atom in this case.

The g-matrix principal directions of the $[HLi_2O_4]^0$ centre are close to the $[AlO_4]^0$-centre

directions, while the $[H_3O_4]^0$ and $[H_4O_4]^+$ centres are close to the $[AlO_4/M]^+$-centre directions. They are related to the repective aluminium centres by a rotation of approximately 10° and 20° about the c axis, respectively. This correlation strongly suggests that these centres are oxygen holes. It also suggests that the location of the oxygen hole may be the same as the corresponding aluminium centre. The terms 'short-bonded' and 'long-bonded' oxygen hole may have little meaning with respect to a silicon vacancy, but the terms still serve as useful labels for oxygens 2 and 3 of figure 2-2. There is certain to be significant relaxation of the crystal structure surrounding the vacancy to new positions, but the surrounding lattice is likely to prevent major rearrangements. The similarity of the g-matrix principal directions with the aluminium centres supports this argument.

Purton *et al.* [109] carried out an LDF pseudopotential calculation of pure α-quartz and the hydrogarnet defect $[H_4O_4]^0$ in α-quartz, using 33-atom and 36-atom clusters, respectively. For the calculation of the pure structure, the 33-atom cluster included terminating hydrogen atoms fixed in position with an O-H bond length of 1.0 Å, and the inner 9 atoms were allowed to relax from the crystallographic positions. Their results agreed well with the published crystallographic data for α-quartz, so the hydrogarnet defect was modelled by replacing the central silicon atom by four hydrogen atoms and allowing the new structure to relax. Figure 6-7 shows the resulting structure, produced from the published cartesian coordinates. The orientation has been adjusted to match figure 2-2, with the oxygen atom labels as used in the aluminium-centre publications [42], [128].

The compensating protons are found to lie slightly outside the faces of a tetrahedron formed by the four oxygen anions. The shortest O-H bonds are 0.99 Å, but each proton is also 1.83 - 1.97 Å from the other two oxygen atoms which make up the tetrahedral face.

The calculated positions of the silicon and oxygen atoms surrounding the hydrogarnet defect are not very different from the crystallographic positions in pure α-quartz, though this may be partly an artefact of the number of atoms allowed to relax. The Si_2-O_2 (see labels in figure 2-2) bond direction changes from $\theta = 136.48°$, $\phi = 272.97°$ to $\theta = 136.52°$, $\phi = 267.13°$, while the O_3-Si_3 bond direction changes from $\theta = 113.00°$, $\phi = 69.08°$ to $\theta = 111.24°$, $\phi = 65.72°$. The Si-O directions from either the crystallographic α-quartz or calculated hydrogarnet defect data are close to the g-matrix 'unique' principal directions of the silicon defect centres listed in

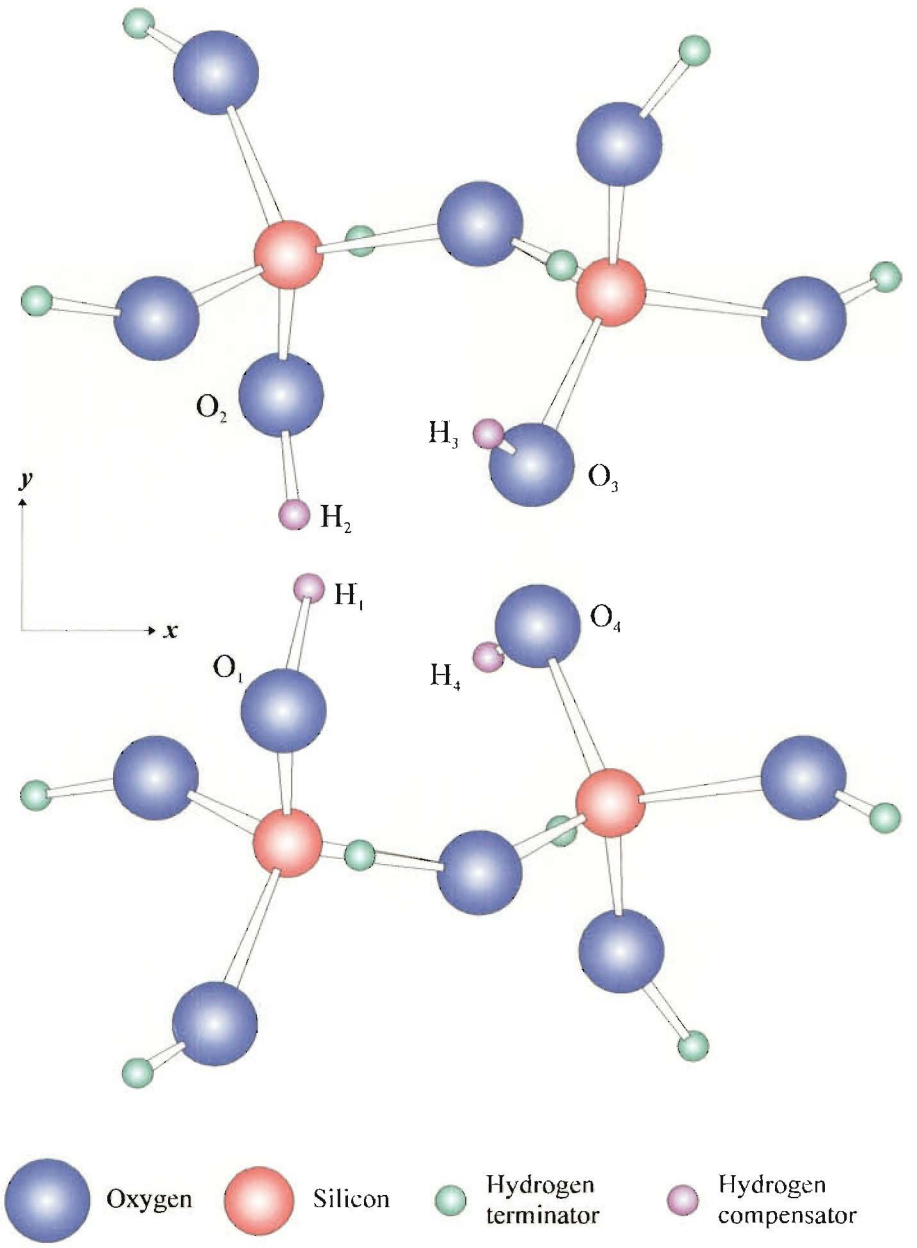

Figure 6-7: Calculated structure of hydrogarnet defect $[H_4O_4]^0$ in α-quartz from Purton *et al* [109].

table 6.2. The deviations are given in table 6.3.

Table 6.3: Deviations of silicon-vacancy centre g-matrix unique principal directions from crystallographic interatomic directions in quartz.

Centre	Direction	Deviation (°)
$[HLi_2O_4]^0$	Si_3-O_3 [a]	2.5
	Si_3-O_3 [b]	5.9
$[H_3O_4]^0$	Si_2-O_2 [a]	7.9
	Si_2-O_2 [b]	4.8
$[H_4O_4]^+$	Si_2-O_2 [a]	10.3
	Si_2-O_2 [b]	9.4

a crystallographic data
b hydrogarnet calculation

The differences between the g-matrix principal directions of the aluminium centres and the crystallographic directions given above are considerably larger than those of table 6.3. Better agreements for the aluminium centres may be found with directions and planes involving the central silicon atom, as shown in table 4 of [42] and [128]. This is to be expected, as the aluminium atom substitutes at this site. As this atom is postulated to be absent in the silicon vacancy centres, it is not surprising that the g-matrix principal directions are significantly changed, but they are still close enough to identify a relationship with the appropriate short-bonded or long-bonded aluminium centre. The 'unique' principal direction apparently shifts from the approximate Si_0-Si_n direction to the approximate O-Si_n direction in the absence of the central silicon atom. This evidence suggests that the $[HLi_2O_4]^0$ centre has the oxygen hole located on O_3, as for the $[AlO_4]^0$ centre, and the $[H_3O_4]^0$ and $[H_4O_4]^+$ centres have the oxygen hole located on O_2, as for the $[AlO_4/M]^+$ centres.

Location of the hyperfine nuclei

The narrow linewidths of the $[HLi_2O_4]^0$ spectra suggest that the positions of the three hyperfine nuclei are well defined at the temperature at which the data were collected, and on the epr timescale. It should thus be possible to extract information about the location of the nuclei from the well-defined hyperfine matrices. However, this has proved to be a difficult, and as yet

not completely resolved, problem.

The locations of the M^+ ions of the $[AlO_4/M]^+$ centres where $M^+ = H^+$, Li^+ was estimated using a simple uniaxial magnetic point-dipole - point-dipole approximation [128]. Under this approximation, the hyperfine nucleus is treated as a point charge which carries no spin density, and the atom carrying the spin density is treated as another (electronic) point charge. The dipolar hyperfine matrix $\mathbf{T}$ (see equation 5.16) is then given in magnetic-field units by:

$$\frac{\mathbf{T}}{g_e\beta_e} = \frac{\mu_0}{4\pi} g_n \beta_n R^{-3} |c_x|^2 \begin{pmatrix} 2 & 0 & 0 \\ & -1 & 0 \\ & & -1 \end{pmatrix} \tag{6.4}$$

where R is the distance between the electronic and nuclear dipoles and $|c_x|^2$ is the coefficient of the orbital x in the unpaired-electron wavefunction. It is assumed that one orbital, in this case the oxygen 2p orbital, carries the bulk of the spin density. For the $[AlO_4/M]^+$ centres, $|c_{2p}|^2$ was taken as the value found for $[AlO_4]^0$. This was determined using the ^{17}O hyperfine data and the relations [129]:

$$|c_s|^2 = \frac{a}{a_0} \tag{6.5a}$$

$$|c_p|^2 = \frac{b}{b_0} \tag{6.5b}$$

where a and b are the isotropic and uniaxial components of the hyperfine matrix as defined in equations 5.15, and a_0 and b_0 are the "free"-ion parameters. These were calculated using SCF Hartree-Fock wavefunctions with a computer programme as described in Nuttall and Weil [129]. Using a charge of +0.5 for the oxygen atom carrying the electron hole, the calculated free-ion parameters lead to a value for $|c_p|$ of 0.87, supporting the assumption that most of the spin density is on the oxygen 2p orbital. This value may in fact be higher, as calculations show [125] that the charge on the oxygen atom is likely to be more negative than +0.5, leading to a significantly smaller value of b_0. This could also account for the missing spin density discussed in [42].

Solving equation 6.4 for R gives the distance of the hyperfine nucleus from the source of the spin density. The direction is assumed to be the unique principal direction of the hyperfine

Table 6.4: Principal values of the anisotropic part of the $[HLi_2O_4]^0$ centre hyperfine matrices, and hyperfine parameters a, b, c (see text).

Nucleus	Principal values $\frac{\mathbf{T}}{g_e\beta_e}$ (mT)	$\lvert a\rvert$ (mT)	$\lvert b\rvert$ (mT)	c (mT)
^{1}H	0.5473 −0.2291 −0.3182	0.0147	0.2736	0.0451
$^7Li_\alpha$	0.1246 0.0485 −0.1730	0.1191	0.0865	0.0381
$^7Li_\beta$	0.0527 0.0170 −0.0697	0.0225	0.0348	0.0179

matrix.

The magnetic point-dipole - point-dipole model described above assumes a uniaxial hyperfine matrix. For a low-symmetry centre in a crystalline system, the matrix is likely to deviate from uniaxiality. The M^+ hyperfine matrices of the $[AlO_4/M]^+$ centres and the ^{1}H hyperfine matrix of the $[HLi_2O_4]^0$ centre are close to uniaxial, but the two ^{7}Li matrices of $[HLi_2O_4]^0$ are quite distorted from the uniaxial case. The principal values of the matrix $\mathbf{T}$ are listed in table 6.4 for each of the hyperfine nuclei, along with the isotropic component a, and the uniaxiality and rhombicity parameters b and c (equations 5.15).

Despite this deviation from uniaxiality, the point-dipole - point-dipole calculation was applied to all three nuclei. The value of $|c_p|$ was assumed to be similar to the value calculated for $[AlO_4]^0$. Calculations have shown that the charge on the hole-bearing oxygen atom is likely to be very similar in the two cases [130]. Table 6.5 shows the calculated O(hole)-M distances taking $|c_p| = 0.9 \pm 0.1$, corresponding to an O_{2p} spin density from 0.64 - 1.0, within which range the true value will almost certainly lie for a localised hole centre. As described earlier,

Table 6.5: O-M^+ distances for $[HLi_2O_4]^0$ centre calculated using equation 6.4, and unique principal directions. H_{1-4} are the calculated hydrogarnet positions.

M^+	O-M distance (Å)	Unique principal direction θ	ϕ
^1H	2.03 ± 0.15	37.9 (142.1)*	292.8 (112.8)
$^7Li_\alpha$	2.17 ± 0.16	82.3 (97.7)	12.6 (192.6)
$^7Li_\beta$	2.94 ± 0.22	124.0 (56.0)	60.7 (240.7)
$^1H_1$	1.98	78.1	209.5
$^1H_2$	2.89	39.5	191.4
$^1H_3$	1.00	23.8	143.9
$^1H_4$	2.17	44.4	257.6

* equivalent (opposite) direction, $180° - \theta$, $180° + \phi$

the g-matrix principal directions appear to support this model. Table 6.5 also gives the unique principal directions of the three hyperfine matrices, and the distances and directions from O_3 to the H^+ positions in $[H_4O_4]^0$, as calculated by Purton *et al.* [109].

The unique principal direction of the hydrogen atom agrees best with the H_4 direction from the hydrogarnet calculation, but the agreement is not very good. The 'unique' principal direction of the Li_β hyperfine matrix surprisingly agrees better with this direction, though the calculated distance is somewhat larger. The positions of the three hyperfine nuclei given by the data in table 6.5 are shown in figure 6-8.

The limits indicated in figure 6-8 show the the uncertainty in the O-M distance due to the choice of $|c_p|$ has very little effect on the calculated position relative to the surrounding lattice. The only position which might be may be questioned on the basis of proximity to an atomic position is the upper proton position in figure 6-8, which is 0.77 Å away from an oxygen atom. However, a slight distortion of the atomic positions from their pure-quartz crystallographic positions could easily increase this distance to a more reasonable size.

The point-dipole - point-dipole approximation is likely to be more reliable for the more uniaxial ^1H hyperfine matrix. Of the two positions indicated in figure 6-8, the lower seems most likely, as the H^+ ion is associated with one of the oxygen atoms immediately surrounding

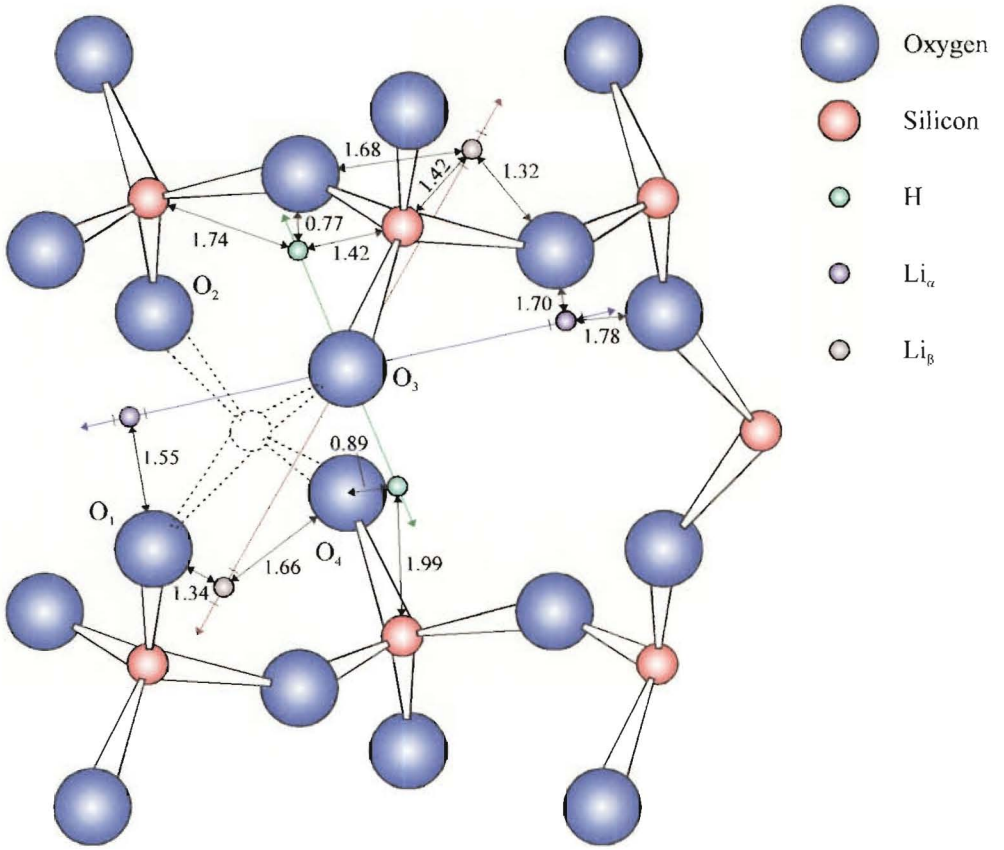

Figure 6-8: Calculated positions of hyperfine nuclei of $[HLi_2O_4]^0$ centre in α-quartz using the point-dipole - point-dipole model. Black arrows give distances to nearest atoms in Å, and coloured arrows point in the unique principal directions of the A matrices used to define the O-M direction in this model. The perpendicular marks either side of the hyperfine nuclei positions mark the quoted error limits in $|c_p|$ discussed in the text. The marks for H are hidden within the outline of the atom.

the oxygen vacancy. As noted previously, this position does not agree with the H_4 position of the hydrogarnet calculation, figure 6-7. The calculated H_4 position lies slightly outside one of the tetrahedral faces formed by the four oxygen atoms surrounding the silicon vacancy, as do the other three hydrogen ions. This may be seen in figure 6-9a, where the tetrahedral face formed by $O_{1,3,4}$ is in the plane of the page. The H position is plotted for both the hydrogarnet calculation, and the point-dipole - point-dipole calculation, using the hydrogarnet calculated oxygen positions. The point-dipole - point-dipole solution is virtually identical when the pure-quartz oxygen positions are used, as seen in 6-9b. 6-9c shows the point-dipole - point-dipole solution relative to the adjoining $O_{2,3,4}$ face, also using the pure-quartz positions. The numbers in the figure indicate the perpendicular distance of the proton from the plane of the tetrahedral face.

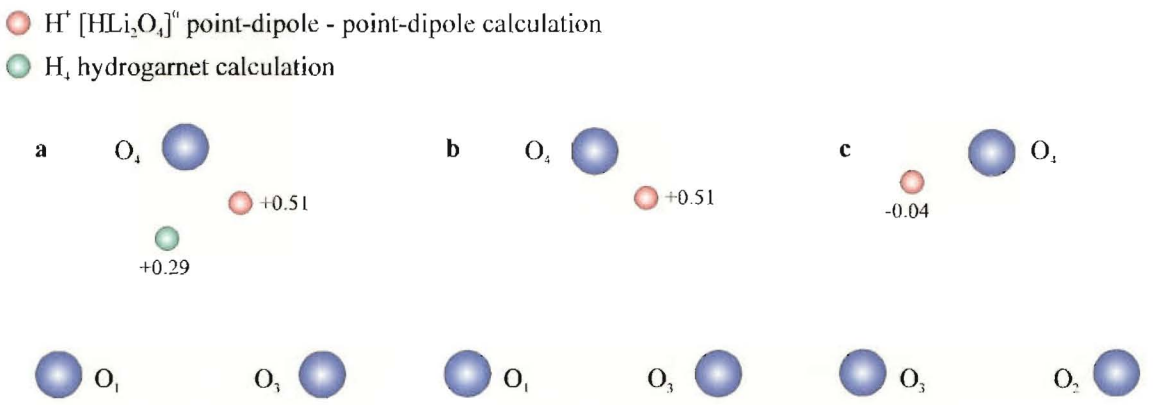

Figure 6-9: Proton positions from hydrogarnet calculation (H_4) and point-dipole - point-dipole calculation for $[HLi_2O_4]^0$. Numbers indicate $\perp$ distance from the ion to the O_{abc} plane, where the positive direction points away from the tetrahedron. **a** O_{134} plane using hydrogarnet-calculation oxygen positions. **b** O_{134} plane using pure-quartz crystallographic oxygen positions. **c** O_{234} plane using pure-quartz crystallographic oxygen positions.

The proton position for the $[HLi_2O_4]^0$ centre is outside the boundaries of the $O_{1,3,4}$ tetrahedral face, closest to the O_3 - O_4 edge. It is also further away in a direct line from the plane defined by the face than the H_4 position. 6-9c shows that the position is also well outside the adjoining $O_{2,3,4}$ face, but is almost exactly in the plane defined by this face, as the unique principal direction only deviates from the $O_{2,3,4}$ plane by 1.2°.

The point-dipole - point-dipole calculation for the two lithium ions places Li_α, which has

the larger-magnitude hyperfine interaction, in one of the main c-axis channels on either side of the silicon vacancy (in the x axis direction), and Li_β in one of the smaller side channels. The assumption that the ions are likely to be located close to the silicon vacancy indicates that the positions on the lower left of figure 6-8 are more likely. This Li_α position also seems more likely as it is close to the a_1 axis which runs through the centre of the main c-axis channel, and is on the opposite side from the oxygen hole. This was found to be the case for the Li^+ and H^+ ions in the $[AlO_4/M]^+$ centres [128]. The oxygen atom nearest to Li_α in this position is 1.55 Å away. The two Li_β positions are located within a small c-axis channel in almost identical positions in the x and y dimensions, but differ in their positioning along the channel in the z-axis direction. Both positions are located *ca* 1.3 Å from the nearest oxygen atom, giving little reason prefer one position over the other, other than that the lower position of figure 6-8 is within a channel adjacent to the silicon vacancy. Interstitial ions in quartz contained within the smaller c-axis channels are less common than those in the larger channels, but have been postulated before (for example [127], [131]). The silicon vacancy may facilitate the inclusion of ions in these spaces.

The second approach taken to solve the locations of the hyperfine nuclei was a more general point-dipole - point-dipole calculation, where both the distance and direction of the O-M vector are fitted to the diagonal matrix **T**, having principal axes which are not parallel to the g-matrix principal axes. The theory behind this approach is contained in Mabbs and Collison (1992) [132], pp 1233-1235.

The diagonal dipolar matrix **T** (in J) is fitted using the following equations, from [132] A11.46-48:

$$T_{xx} = -\frac{\mu_0 g_n \beta_n \beta_e}{4\pi R^3}\left(g_{xx}\left(1-3l^2\right) - 3lmg_{yx} - 3lng_{zx}\right) \tag{6.6a}$$

$$T_{yy} = -\frac{\mu_0 g_n \beta_n \beta_e}{4\pi R^3}\left(g_{yy}\left(1-3m^2\right) - 3lmg_{xy} - 3mng_{zy}\right) \tag{6.6b}$$

$$T_{zz} = -\frac{\mu_0 g_n \beta_n \beta_e}{4\pi R^3}\left(g_{zz}\left(1-3n^2\right) - 3lng_{xz} - 3mng_{yz}\right) \tag{6.6c}$$

where the g values refer to the g matrix transformed into the A-matrix principal-axis system, the l, m, n are the direction cosines of the M-O vector in the A-matrix principal-axis system, and R is the M-O distance (figure 6-10). The units may be converted to tesla by dividing both

sides by $g_e\beta_e$.

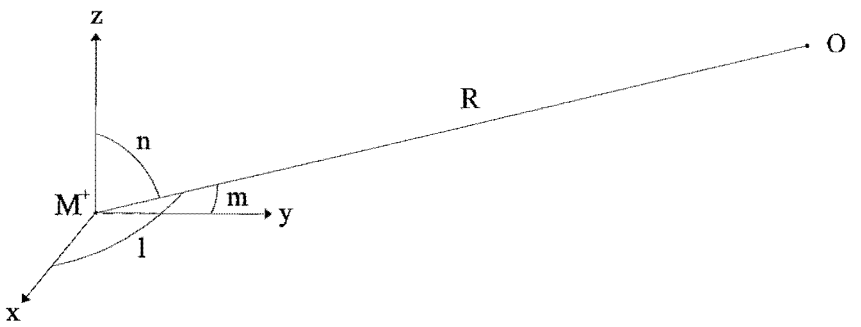

Figure 6-10: Model used in programme Dipole. Direction cosines l, m, n give the direction from the hyperfine nucleus to the oxygen atom in terms of the principal-axis system of the A matrix, x, y, z. R is the interatomic distance.

The programme Dipole has been written [133] to fit the parameters l, m, n and R to input experimental data using equations 6.6 and the direction-cosines relation:

$$l^2 + m^2 + n^2 = 1 \tag{6.7}$$

The experimental data required to run Dipole are the principal values of the dipolar hyperfine matrix and the six elements of the g matrix transformed into the principal-axis system of the A matrix. The transformation is carried out using the same similarity transformation (equation 1.33) which diagonalises **A**. The first step in the fitting is to find an approximate minimum by carrying out a grid search over a sphere in 10 degree increments of the polar coordinates $0° \leq \theta \leq 180°$ and $0° \leq \phi \leq 360°$ for a fixed R, which is also input. The rmsd between the experimental hyperfine-matrix principal values and the values calculated by equations 6.6 is printed in a 18×37 grid for the various combinations of θ and ϕ as incremented above. The minima are located by inspection, and the appropriate direction cosines may then be calculated and input along with R for a minimisation run. Three of the four parameters are varied (two direction cosines and R), where the third direction cosine is given by equation 6.7, until the rmsd reaches a minimum. The minimisation package used is Minpack [134], which is also utilised by EPR-NMR. The l, m, n values which are output describe the M-O vector in terms of the principal-axis system of the hyperfine matrix, as shown in figure 6-10. These values are

then transformed back into the crystal coordinate system ($x \equiv a_1$, $z \equiv c$), and converted into polar coordinates. The transformation of the unit vector represented by lmn is carried out by multiplication on the left by the inverse of the matrix whose columns represent the unit vectors of the axes of the new (crystal) coordinate system in the old (A matrix) coordinate system. Equivalently, one can multiply on the left by the matrix whose columns represent the unit vectors of the axes of the old (A matrix) coordinate system in the new (crystal) coordinate system. This is simply the principal axes of the A matrix in the crystal coordinate system, or the eigenvector matrix which is output by EPR-NMR for each fitted matrix, which diagonalises that matrix.

In every fitting, the grid search was found to produce a number of approximate minima related by symmetry. When the polar coordinates were converted to direction cosines, it was obvious that the eight general solutions were the eight possible sign combinations of the three cosines, provided none of the cosines was zero. This result is not surprising, as the major contribution to the calculated hyperfine principal value comes from the $g_{aa}\left(1-3b^2\right)$ term, which is independent of the sign of the direction cosine.

Several problems arose in the minimisation runs, possibly because the functions 6.6 are not well suited for minimisation using the Minpack package. The minimised values of the parameters often varied considerably from the values which were initially entered, and the final rmsd was sometimes greater than that reached several iterations earlier in the minimisation. Many of the problems seemed to arise when one of the cosines became close to zero. However, a number of solutions were found for each hyperfine nucleus which produced hyperfine principal values in agreement with the experimental values.

After carrying out eight minimisations starting with each of the approximate solutions, there were never more than two exact solutions (and their exact negatives) found, where the rmsd in mT was zero within the specified limit of 7 decimal places, well beyond the error in the experimental values that were being fitted. Some of the starting points resulted in a solution with an rmsd of around 0.0005 - 0.001 mT, which could apparently be reduced no further. Minimising from random starting values always produced one of the solutions which had been obtained from the initial eight approximate solutions.

The fittings were carried out using both positive and negative experimental A matrices, as

the sign is indeterminate from the EPR-NMR fitting of the epr data. The fitted positions were quite different for the two possibilities. For the hydrogen fitting, all of the eight approximate solutions minimised to one of the two exact solutions with the sign of the matrix such that the unique principal value is positive. When the opposite sign was given to the hyperfine matrix, only half of the approximate solutions minimised to one of two more exact solutions. For the lithium fittings, the opposite was true. Fitting the matrix with the unique principal value negative gave only exact solutions, while the opposite sign only gave an exact solution for half of the approximate starting points.

Surprisingly, none of the solutions gave a direction which agreed very well with the unique principal direction, which was assumed to be the correct direction in the earlier point-dipole - point-dipole calculation. If the M-O vector was along one of the principal axes of the hyperfine matrix, then the fitted l, m, n values should have been approximately 1, 0, 0, the position of the one depending on which of the x, y or z axes was defined as the unique principal direction. It is possible that the problems which seemed to occur when cosines approached zero may have prevented fitting of such a solution.

The other solutions cannot be ignored, however, as they do produce the correct dipolar hyperfine matrix. Table 6.6 lists the two exact solutions found for each hyperfine nucleus and matrix sign choice in terms of polar coordinates θ and ϕ in the crystal coordinate system, and the M-O distance R in Å. The resulting positions are also plotted in figures 6-11 and 6-12.

This method of determining the hyperfine-nuclei positions would clearly be more useful if there were already some information about their location. It is quite possible that none of the 'exact' solutions listed in table 6.6 are close to the true positions. If all solutions within a certain rmsd limit were permitted, there would be a continuum of possible positions covering a wide area.

The closest of the exact solutions for hydrogen in table 6.6 to the unique principal direction ($\theta = 37.9°$, $\phi = 292.8°$) is $\theta = 14.6°$, $\phi = 304.1°$, which differs by 23.7° followed by $\theta = 55.9°$, $\phi = 319.5°$, which differs by 26.3°. The M-O distances of the two solutions, 1.99 Å and 1.94 Å, are only slightly smaller than the 2.03 Å derived using equation 6.4. The first solution has a smaller θ than the unique principal direction, and thus points more along the c-axis direction from O_3. The resultant position, marked 1 in figure 6-11, is still closely associated with O_4 (0.94

Table 6.6: Polar coordinates of hyperfine nuclei relative to O_3, determined using programme Dipole (exact solutions only).

Nucleus	Sign*	Polar coordinates θ (deg)	ϕ (deg)	R (Å)
H	+	55.9 (124.1)	319.5 (139.5)	1.943
		165.4(14.6)	124.1(304.1)	1.989
	−	66.3(113.7)	87.9(267.9)	1.665
		70.4(109.6)	12.2(192.2)	1.687
Li_α	+	114.5(65.5)	11.7(191.7)	1.940
		115.8(64.2)	217.4(37.4)	2.005
	−	101.9(78.1)	285.8(105.8)	1.853
		157.2(22.8)	139.3(319.3)	1.589
Li_β	+	104.3(75.7)	12.9(192.9)	1.815
		154.8(25.2)	19.9(199.9)	2.325
	−	61.1(118.9)	317.1(137.1)	1.877
		118.6(61.4)	254.4(74.4)	1.877

* Sign of the 'unique' principal value

Å), as was the case in the earlier calculation (0.89 Å), figure 6-8. However, the position with respect to O_4 is quite different. The polar coordinates of the two positions with respect to O_4 are $\theta = 116.3°$, $\phi = 70.6°$ and $\theta = 146.6°$, $\phi = 7.1°$, respectively. The second solution, marked 2 in figure 6-11, is very different to the earlier calculation. It is not closely associated with any oxygen atom, and is located away from the oxygen tetrahedron, in the *c*-axis channel closer to the oxygen hole. Once again, none of the other solutions can be disregarded on account of being to close to other atoms, but solutions 1 and 2 seem more likely. The other solutions are not closely associated with any of the tetrahedron of oxygen atoms, nor are they close to the centre of one of the *c*-axis channels.

For Li_α, the solutions with the θ and ϕ closest to the unique principal direction ($\theta = 97.7°$, $\phi = 192.6°$) are $\theta = 115.8°$, $\phi = 217.4°$, and $\theta = 65.5°$, $\phi = 191.7°$, which deviate by 29.7° and 32.3° respectively. The M-O distances of 2.01 Å and 1.94 Å are a little smaller than the 2.17

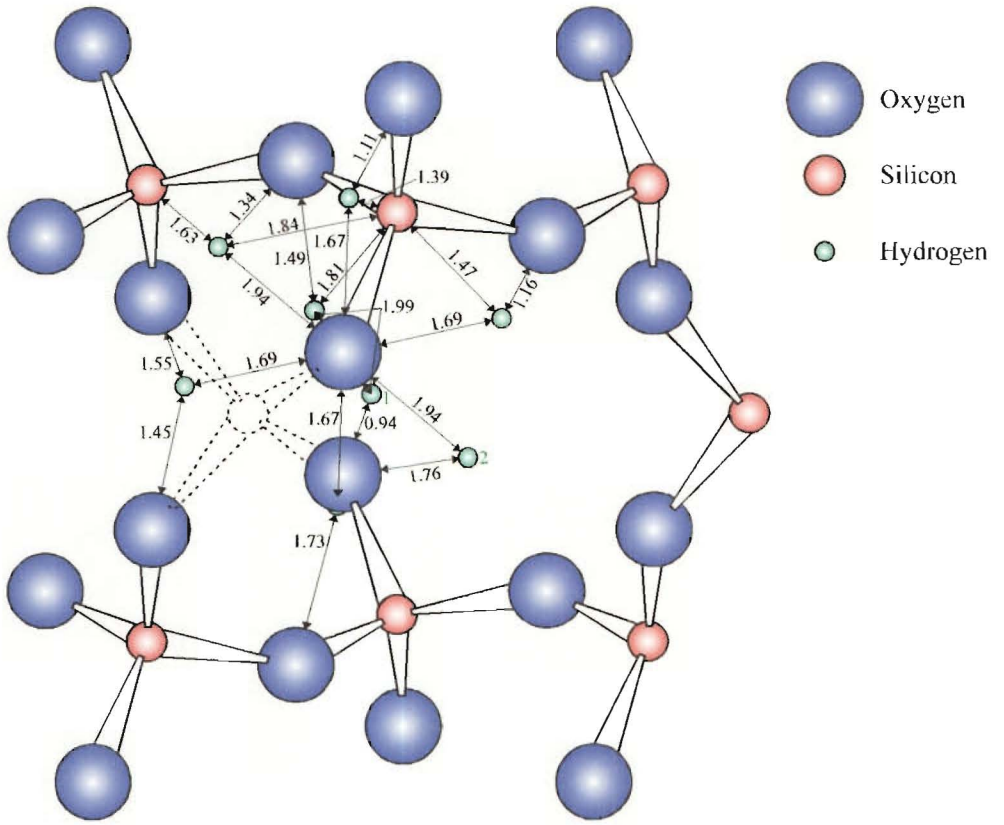

Figure 6-11: Calculated positions of the hydrogen nucleus in $[HLi_2O_4]^0$ centre in α-quartz using programme Dipole. Distances less than 2 Å to the nearest atoms are indicated.

Å derived using equation 6.4. The first of these solutions, labelled 1 in the top of figure 6-12, locates the lithium nucleus 1.62 Å from O_1, 'underneath' the oxygen tetrahedron, as viewed in figure 6-12. The second solution, labelled 2, more closely resembles the simple point-dipole - point-dipole calculated position, shifted along the c axis towards the oxygen tetrahedron. It is located close to the a_1 axis in the c-axis channel opposite the oxygen hole, as was the earlier calculation, and is almost equidistant from O_1 (1.43 Å) and O_2 (1.35 Å).

The Li_β hyperfine matrix is the most removed from uniaxial symmetry, and the general point-dipole - point-dipole solutions show the least agreement with the unique principal axis, as might be expected. The closest agreement in table 6.6 with the unique principal direction ($\theta = 56.0°$, $\phi = 240.7°$) is $\theta = 25.2°$, $\phi = 199.9°$, a 39.4° deviation. This solution also has the closest M-O distance of 2.33 Å, but is still much smaller than the 2.94 Å derived using equation

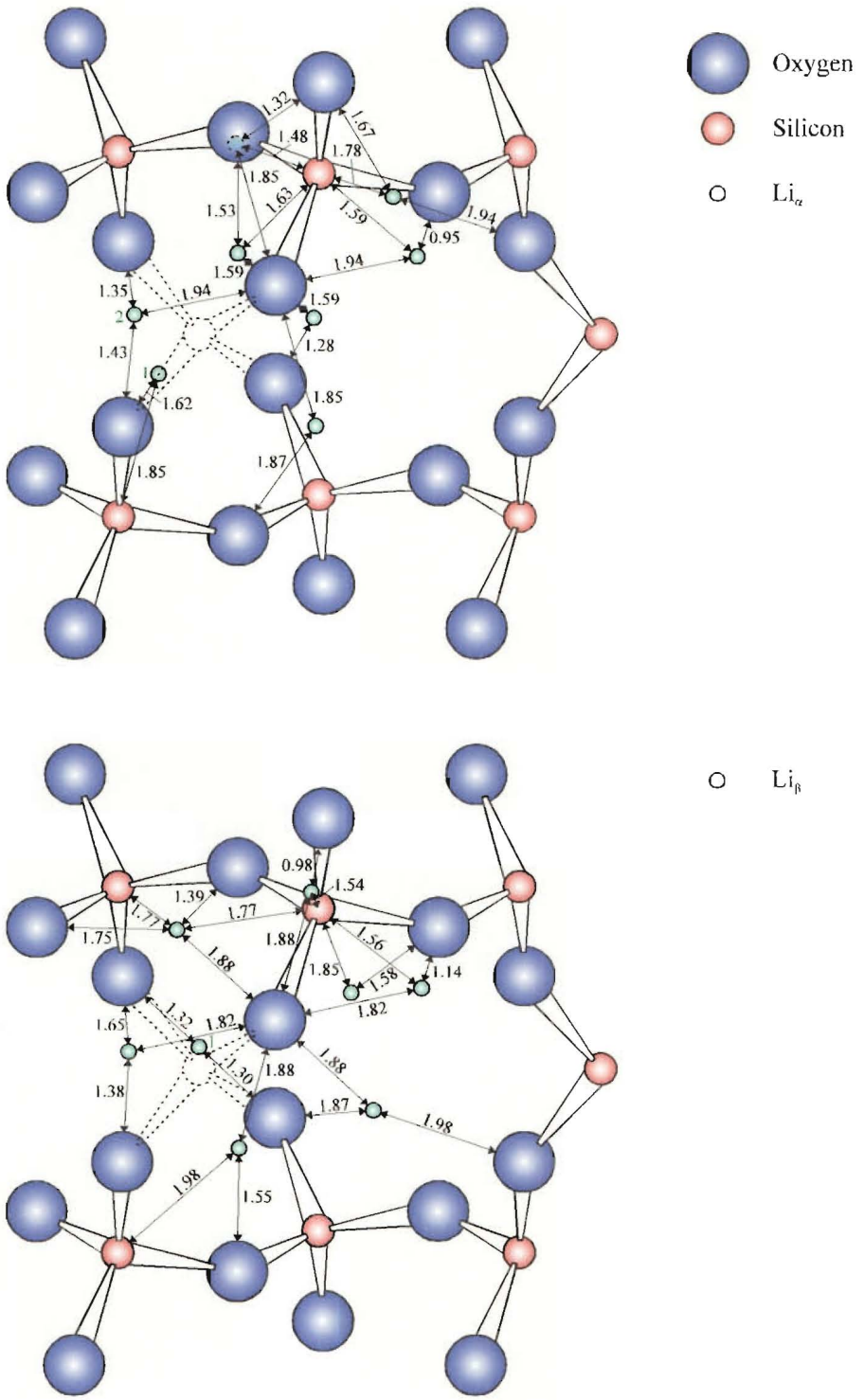

Figure 6-12: Calculated positions of the lithium nuclei in $[HLi_2O_4]^0$ centre in α-quartz using programme Dipole (Li_α top and Li_β bottom). Distances less than 2 Å to the nearest atoms are indicated.

6.4. The position given by this solution, labelled 1 in the bottom of figure 6-12, is almost in a direct line along the c axis from the centre of the oxygen tetrahedron, where the normal silicon position would be. It is almost equidistant from O_2 and O_4, and is only 0.03 Å away from the tetrahedral edge between these two atoms.

The Dipole approach has yielded solutions which agree more closely with the simpler point-dipole - point-dipole approximation as the experimental hyperfine matrix involved becomes more uniaxial, which may be taken as an encouraging sign that the calculations have some meaning. As noted earlier, this approach is more useful if there is already some indication of where the hyperfine nucleus might be located, in order to reduce the multitude of possibilities which may be fitted to equations 6.6. Ignoring those solutions which do not agree moderately well with the unique principal direction has allowed a tentative position to be postulated for each nucleus, labelled 1, 2, and 1 for H, Li_α, and Li_β, respectively, in figures 6-11 and 6-12.

The final approach taken in solving the hyperfine-nuclei positions involved the use of the programme Fitpkl [135], [136]. Fitpkl is designed to calculate $\mathbf{T}$, the traceless anisotropic part of the hyperfine matrix, using the interaction between an unpaired electron in one or more ns and/or np hydrogenic orbitals ($n = 2 - 4$) on a set of N1 nuclei and a bare point nucleus. The equations used in this programme were developed following the work of McConnell and Strathdee (1959) [137], as corrected by Pitzer, Kern and Lipscomb (1962) [138]. The equations are given in reference [139] for $n = 2, 3$, and [140] for $n = 4$ (note also correction of [139]). Fitpkl varies selected parameters which may include the atomic positions of the atoms carrying the unpaired-electron orbitals and the hyperfine nuclei, the effective charge associated with the unpaired-electron orbitals, and the admixture coefficient a_{np} of the p orbital where $(a_{np})^2 + (a_{ns})^2 = 1$, until the best agreement between the experimental and calculated $\mathbf{T}$ is reached.

The data required by Fitpkl to calculate a matrix $\mathbf{T}$ are the cartesian coordinates of the atoms with the electronic and nuclear spins, the orientation of any p orbitals to be used in polar angles θ and ϕ, the coefficient a_{np} and effective nuclear charge as described above, the spin density associated with each orbital, and the nuclear g values of the hyperfine nuclei. Fitting of parameters of course requires an experimental matrix to be included also.

The first fits were carried out using a pure p orbital on O_3, with an effective charge 3.815, as

used for the aluminium centres in quartz [139], derived using the empirical rules given in [141]. The p-orbital orientation would normally be expected to be perpendicular to the Si-O-Si plane containing the oxygen hole, but there is no central silicon atom in this case, so no such plane exists. It was initially assumed that the orbital carrying the spin density would be perpendicular to the remaining Si-O bond, thus allowing the normal Si-O-Si perpendicular orientation, and any rotation of this vector about the Si-O bond. Polar coordinates were calculated for such rotations in 10° increments up to 180°, which is equivalent to the original direction. A refinement of the hyperfine-nucleus position was carried out for each of these calculated p-orbital orientations, and the rmsd between the experimental and calculated T matrix recorded. The matrices were initially given the same sign as had generated the more significant solutions when Dipole was used.

For the hydrogen nucleus, the rmsd ranged from a maximum 0.0215 mT 10° away from the normal Si-O_3-Si plane perpendicular direction to 0.0078 mT 100° away from this direction (90° from the maximum rmsd), or almost in the Si-O_3-Si plane. The fits of Li_α yielded rmsds ranging between 0.0167 mT and 0.0132 mT, again separated by 90°. The minimum in this case was 70° from the quartz Si-O_3-Si plane perpendicular direction. The Li_β fittings ranged from 0.0085 mT to 0.0074 mT, also 90° apart, with the mimimum at the same orientation as the hydrogen-fitting minimum. The fitted position of each hyperfine nucleus was not greatly affected by the orientation of the p orbital. When the fittings were repeated with the opposite choice of sign of the matrix, the rmsds were much higher in all cases. The lowest rmsd values found for H, Li_α and Li_β were 0.169 mT, 0.0442 mT and 0.0191 mT, respectively.

The orbital direction must be the same in all three fittings, as the location of the spin density in the defect centre will be the same regardless of the hyperfine nucleus considered. To find a minimum for all three hyperfine nuclei, they were fitted simultaneously, using the original matrix signs which gave the lower rmsds in the initial individual fits. The calculated perpendicular orbital directions were first used, with Z fixed at 3.815. The minimum rmsd of 0.00948 mT was predictably found with the orbital 100° from the normal of the Si-O_3-Si plane, the same orientation as had provided the best individual fit for both H and Li_β. The rmsd is only directly comparable with other fittings of all three nuclei as there are more experimental values to fit, and two exact-fitting dummy atoms were also used. The same set of calculated

orbital directions was then used, this time fitting both the coordinates of the hyperfine nuclei fitted and the Z value for the oxygen p orbital. The minimum of 0.00802 mT was then 70° from the normal of the Si-O_3-Si plane, and the fitted Z was lowered to 2.315. The orbital direction was then systematically varied in the region close to this minimum, and the hyperfine-nuclei coordinates and Z fitted. The lowest rmsd found was 0.00764 mT with the orbital direction $\theta = 145°$, $\phi = 300°$, almost exactly perpendicular to the crystallographic Si-O_3 bond direction, making an angle of 89.27°. The fitted Z was 2.122. The experimental and calculated matrices from this fitting are given in table 6.7, with the fitted hyperfine-nuclei positions and errors.

The best agreement between the experimental and calculated matrices is for Li_α, but the fitted coordinates have large uncertainties. The hydrogen-nucleus position appears to be fitted more precisely, even though the agreement between the matrices is not as good. The Li_β matrix is not very well fitted and has the least-precise fitted coordinates.

The position fitted for the hydrogen nucleus agrees with the Dipole position of 3.51, 0.19, 0.75 (position 1, figure 6-11) within the quoted uncertainties. The x and y coordinates of the Li_α position agree with the Dipole solution 1.50, 0.25, −0.36 (position 2, top of figure 6-12) within the quoted uncertainties, but the z coordinate is much more negative. Similarly, the x and z coordinates of the Li_β position agree with the Dipole solution 2.30, 0.27, 0.93 (position 1, bottom of figure 6-12) within the quoted uncertainties, but the y coordinate is much more negative.

No better fitting could be found by introducing some s character into the spin density, or by placing some of the spin density in an orbital on another atom. All of these fits produced higher rmsd values and moved the p-orbital orientation out of the plane perpendicular to Si-O_3.

A number of exact fits using only a pure p orbital on the oxygen atom could be found for each nucleus individually, by systematically varying the orientation of the orbital and the effective charge, Z. The calculated matrices in these fits agreed exactly with the experimental matrices to the number of figures that were entered[3]. An example for each of the hyperfine nuclei is given in table 6.8.

The fits all use different orientations of the p orbital, and thus cannot represent the true

[3]The zz element was actually fitted to a value one figure different in the last decimal place each time because the fitted matrix was always traceless while the experimental matrix was not because of rounding.

Table 6.7: Experimental and calculated T matrices for $[HLi_2O_4]^0$ centre in α-quartz using programme Fitpkl, and fitted coordinates of the hyperfine nuclei.

	Matrix $\frac{\mathbf{T}}{g_e\beta_e}$ (mT)			k	Principal value T_k	Principal direction θ_k (deg)	Principal direction ϕ_k (deg)
^{1}H	-0.2323	-0.1459	0.1299	1	0.5473	37.9	292.8
experimental		-0.0173	-0.3608	2	-0.2291	124.3	321.3
			0.2497	3	-0.3182	76.0	41.5
calculated	-0.2383	-0.1232	0.1510	1	0.5467	37.7	293.2
		-0.0090	-0.3571	2	-0.2546	127.6	298.3
			0.2473	3	-0.2921	87.5	26.4
coordinates	x	y	z				
	3.5(2)	-0.1(4)	0.75(9)				
Li_α	0.1574	0.0549	0.0242	1	0.1730	82.3	12.6
experimental		-0.0957	0.0379	2	-0.0485	150.4	296.5
			-0.0616	3	-0.1246	61.6	278.4
calculated	0.1570	0.0542	0.0273	1	0.1737	81.3	13.0
		-0.0919	0.0442	2	-0.0461	145.7	295.9
			-0.0651	3	-0.1276	57.1	277.3
coordinates	x	y	z				
	1.6(6)	0.0(6)	-1.7(1.0)				
Li_β	-0.0183	0.0210	-0.0368	1	0.0697	56.0	240.7
experimental		0.0270	-0.0399	2	-0.0170	113.7	313.5
			-0.0088	3	-0.0527	136.5	195.9
calculated	-0.0208	0.0320	-0.0250	1	0.0702	57.9	241.3
		0.0246	-0.0393	2	-0.0309	137.2	288.6
			-0.0038	3	-0.0393	115.0	168.3
coordinates	x	y	z				
	2.0(1.0)	-1.3(1.3)	0.6(1.3)				

Table 6.8: Selected Fitpkl exact fits to individual hyperfine matrices of $[HLi_2O_4]^0$ centre in α-quartz.

	p-orbital direction		Calculated matrix $\frac{\mathbf{T}}{g_e\beta_e}$ (mT)			k	Principal value	Principal direction	
	θ (deg)	ϕ (deg)					T_k	θ_k (deg)	ϕ_k (deg)
^{1}H	50.07	143.61	-0.232300	-0.145899	0.129902	1	0.54728	37.9	292.8
(Z = 2.0)				-0.017299	-0.360800	2	-0.22916	124.3	321.4
					0.249599	3	-0.31812	76.0	41.5
fitted	x	y	z	rmsd (mT)					
coordinates	3.235(2)	-0.063(2)	0.586(2)	0.0000011					
Li_α	28.82	109.29	0.157396	0.054903	0.024205	1	0.17306	82.3	12.6
(Z = 2.0)				-0.095703	0.037894	2	-0.04854	150.4	296.5
					-0.061693	3	-0.12452	61.6	278.4
fitted	x	y	z	rmsd (mT)					
coordinates	1.44(1)	0.46(1)	-0.95(2)	0.0000045					
Li_β	68.95	129.89	-0.018298	0.020999	-0.036798	1	0.06966	56.0	240.7
(Z = 1.5)				0.027001	-0.039902	2	-0.01701	113.7	313.5
					-0.008703	3	-0.05265	136.5	196.0
fitted	x	y	z	rmsd (mT)					
coordinates	1.90(4)	-0.66(3)	0.37(4)	0.0000017					

nature of the $[HLi_2O_4]^0$ centre, but the fitted coordinates of the nuclei are similar to those of the best simultaneous fit in table 6.7.

The three techniques used to investigate the locations of the hyperfine nuclei have produced results which may be interpreted such as to indicate an approximate position for each which is reasonably consistent. All of the results appear to indicate that the hydrogen ion is bonded to O_4, while one of the lithium ions is probably at the edge of the main c-axis channel opposite to the oxygen hole. The second lithium-ion position cannot be as confidently assigned, but the Dipole results indicate that it may be located near the O_2-O_4 tetrahedral edge, equidistant from these two atoms. The first lithium ion may be similarly located near the O_1-O_2 tetrahedral edge which is adjacent to the main c-axis channel. These positions are indicated in figure 6-13. *Ab initio* calculations of the $[HLi_2O_4]^0$ defect could show whether these sites are viable, and perhaps suggest a more precise location. This could in turn make the task of interpreting the fitted epr data easier.

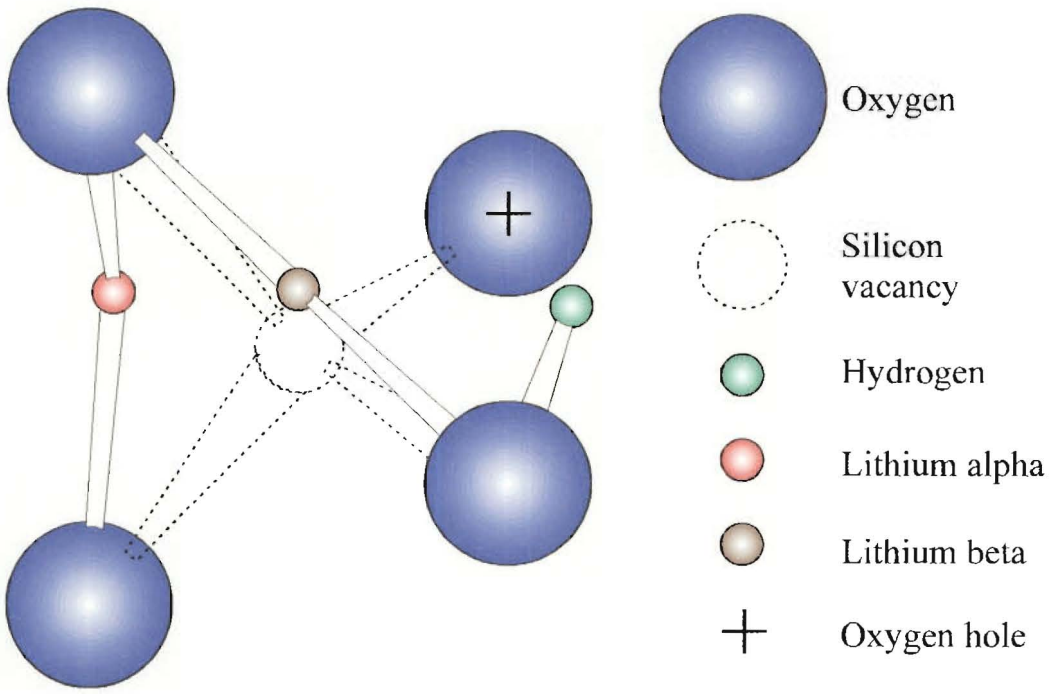

Figure 6-13: Final tentative compensator positions indicated by the combination of hyperfine matrix analyses described in the text. Only the four oxygens of the tetrahedron surrounding the silicon vacancy are shown (oriented as in all other quartz diagrams in this thesis).

6.3 The $[FeO_4/H]^0$ centre

6.3.1 Experimental details

The $[FeO_4/H]^0$ centre was observed in the same gamma-irradiated α-quartz crystal as the $[HLi_2O_4]^0$ centre. The first spectrum was observed in the c-axis orientation at 15 K at a resonant field of *ca* 150 mT at 9.281 GHz, $g_{eff} \approx 4.4$. Orientation of the crystal had been achieved as previously described utilising the $[AlO_4]^0$ signals.

The new centre was found to be much more sensitive to misalignment than $[AlO_4]^0$. The c-axis spectrum was different each time the crystal was aligned in a new experiment, even though the $[AlO_4]^0$ centre appeared to be identical in each case. Alignment of the crystal using the screwdriver apparatus could not be carried out using the $[FeO_4/H]^0$ centre as a guide as the intensity was too low for observation on the oscilliscope in any orientation other than the c-axis. The c-axis spectrum could be changed simply by the application of slight pressure on

the Displex head. As a result of these problems, spectra were collected in a plane which was not perfectly oriented. This was evident in the slight splitting of the degenerate sites as the crystal was rotated in the yz plane. Experimental line positions in these circumstances were taken to be the midpoint of the split spectrum.

Data were collected in the yz plane over 180° for the 150 mT signal, and signals due to other transitions which were subsequently discovered as the spectral measurement and fitting progressed.

6.3.2 Results

The 150 mT signal consisted of three equally spaced lines when the crystal was well aligned (figure 6-14). The intensity of the outer two lines was not the same as the inner line, and the intensity ratio could be changed by adjusting the microwave power (figure 6-15). Low-intensity hyperfine lines were visible flanking the main lines, due to a nuclear spin of $\frac{1}{2}$ with low abundance. The intensity ratio corresponded to a natural abundance of 2.21 %, in agreement with ^{57}Fe, 2.19 % abundant.

The iron centres which have been characterised in α-quartz by epr are almost exclusively d^5 Fe^{3+} centres [19], with five unpaired electrons. The centres are invariably highly anisotropic, as was found to be the case for $[FeO_4/H]^0$. The signal at 150 mT was found to be the 3-4 transition among the six non-degenerate levels of the electronic ground state in a strong magnetic field. Experimental data were eventually collected for every transition between adjacent levels except 5-6, where the energy levels are labelled from highest energy to lowest.

The spin Hamiltonian used for the analysis of the centre was of the form:

$$\widehat{\mathcal{H}} = \beta_e \mathbf{B}.\mathbf{g}.\hat{\mathbf{S}} + \hat{\mathbf{S}}.\mathbf{D}.\hat{\mathbf{S}} + \sum_{m=-4}^{4} B_{4,m}\Im_{4,m} \tag{6.8}$$

where the last term represents a linear combination of spherical tensor operators, defined in [75], for which there are nine parameters under point-group symmetry 1. Terms of the type BS^3 and BS^5 are also allowed for $S = \frac{5}{2}$, but these were found to be negligible in this case. The final results of the fitting are given in table 6.9, with the same site assignment as the published $[FeO_4/H]^0$ results [49].

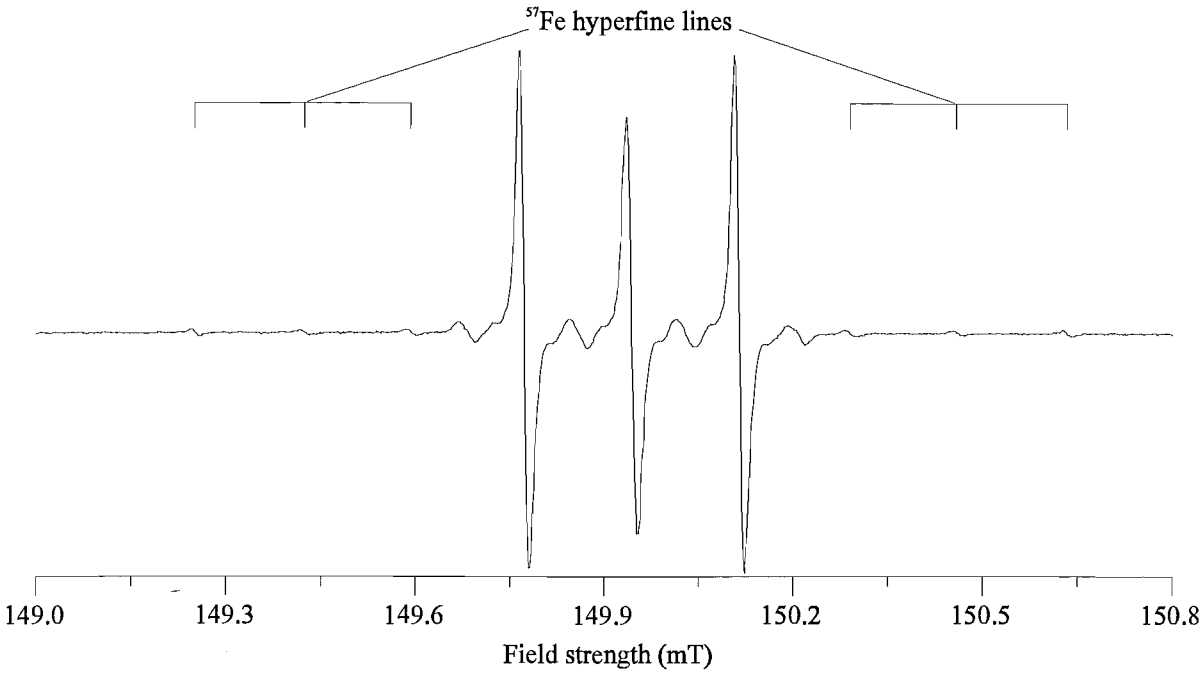

Figure 6-14: c-axis epr spectrum of $[FeO_4/H]^0$ centre in α-quartz at *ca* 15 K. Microwave power 0.1 mW, frequency = 9.28106 GHz.

The complete roadmap generated using these matrices is shown in figure 6-16. Despite the problems with alignment and the resulting relatively high rmsd of 0.19 mT for the fitting, none of the experimental points would visibly deviate from the simulated curves on the scale of figure 6-16. The regions for which experimental data points were obtained have been indicated in the figure by bold lines.

6.3.3 Discussion

After the iron centre had been fitted, it was discovered to be one which was already known [49]. It is an iron centre associated with a proton compensator, which is responsible for the observed hyperfine. The central peak of the c-axis spectrum is the sum of two overlapping 'forbidden' lines, equivalent to the hydrogen spin flips of the $[HLi_2O_4]^0$ centre. The different saturation properties of these lines leads to the change in appearance of the spectrum as the microwave power is varied.

This centre is sometimes referred to as $[FeO_4/H]^0_\alpha$, to distinguish it from another proton-

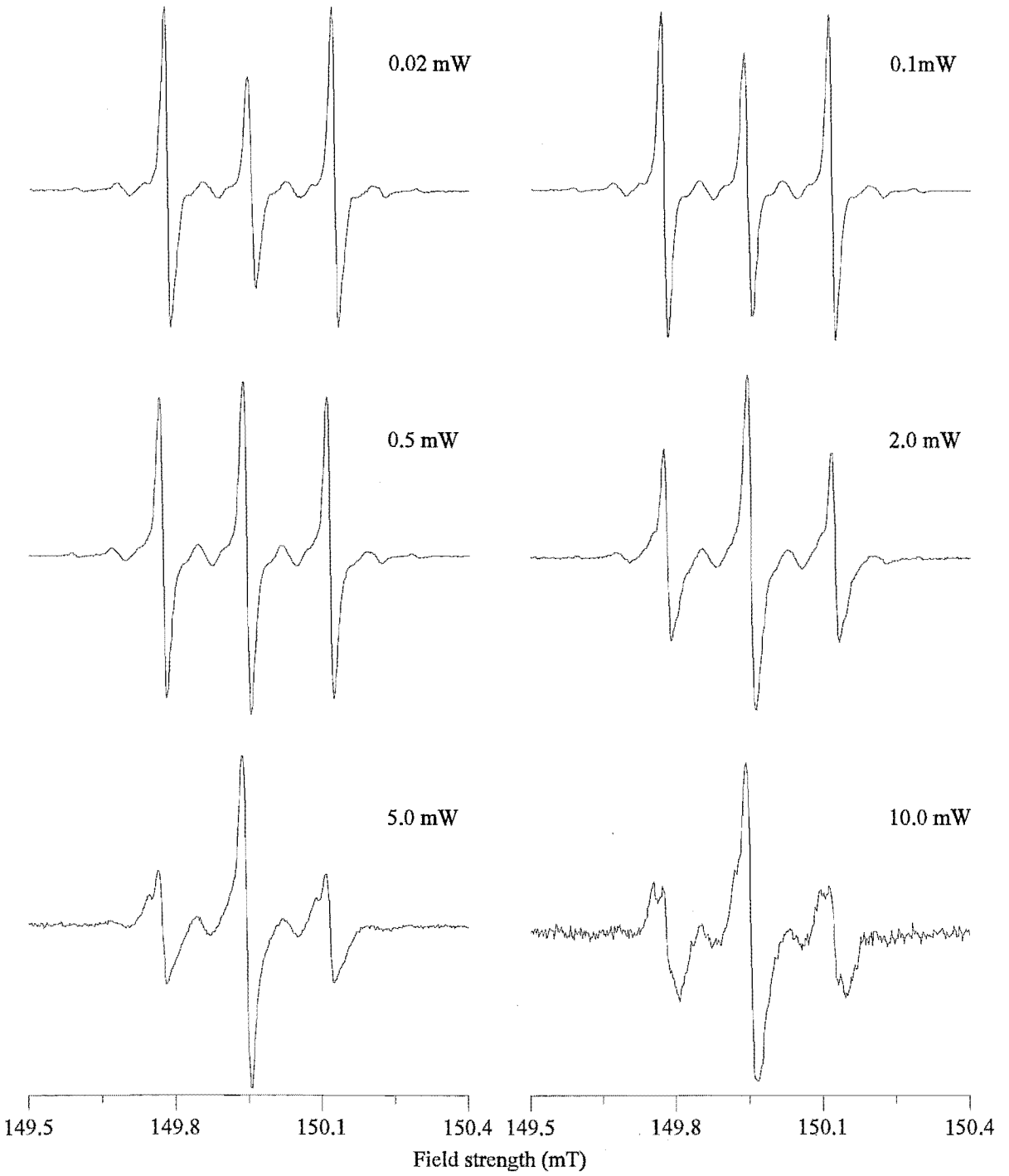

Figure 6-15: c-axis epr spectra of $[FeO_4/H]^0$ centre in α-quartz at *ca* 15 K under different microwave power levels. Average frequency = 9.28108 GHz.

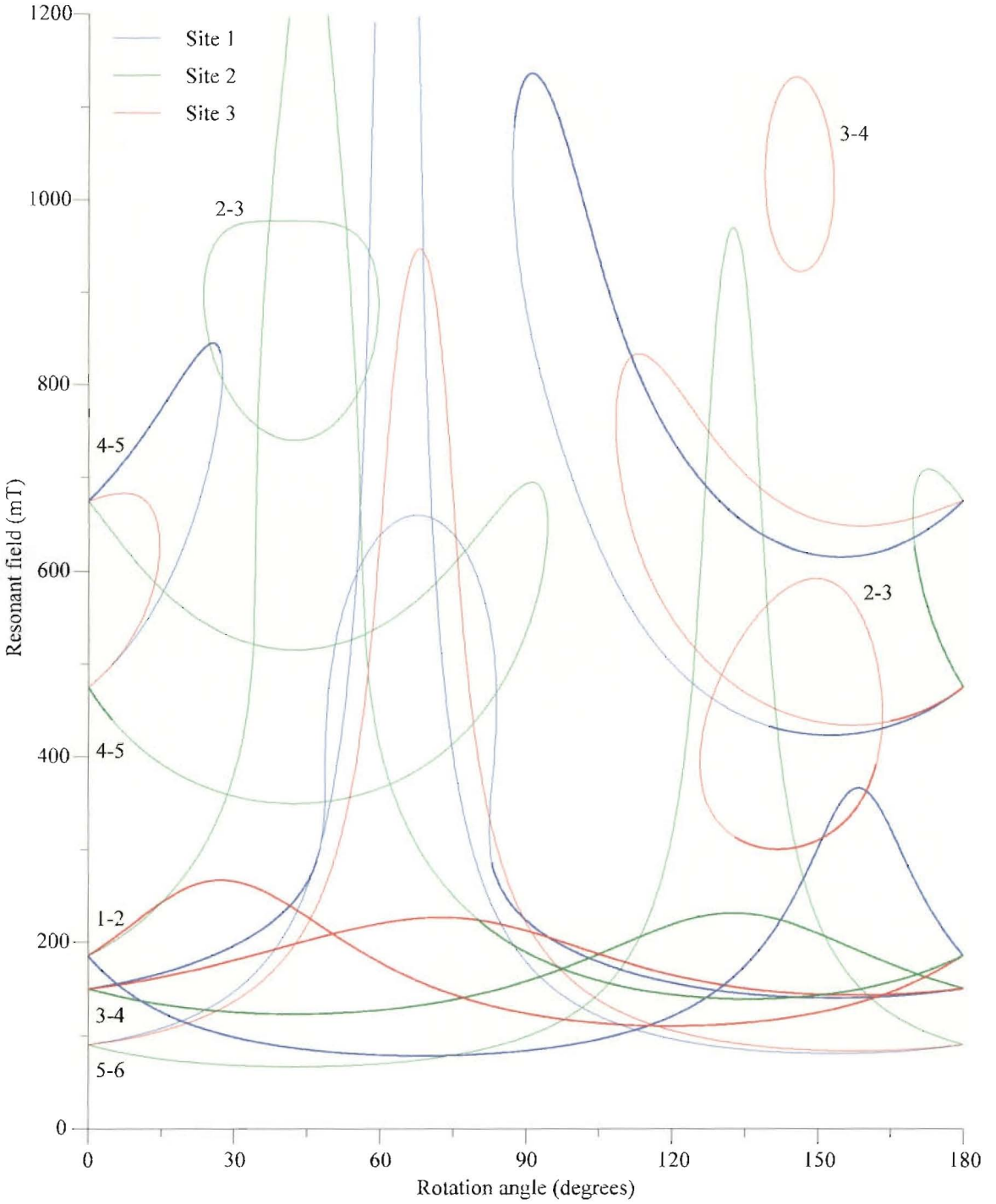

Figure 6-16: Roadmap of $[FeO_4/H]^0$ centre in α-quartz at *ca* 15 K, simulated using matrices of table 6.9 with microwave frequency 9.281 GHz. Bold curves indicate regions where experimental line positions were obtained. The plotted points would not visibly deviate from the simulated lines on the scale of the figure.

Table 6.9: Spin-Hamiltonian parameters for the $[FeO_4/H]^0$ centre in α-quartz at *ca* 15 K. Error estimates in parentheses.

Y	Matrix **Y**			k	Principal value Y_k	Principal direction θ_k (deg)	ϕ_k (deg)
g	2.0047(5)	-0.0005(3)	-0.0002(3)	1	2.0060(3)	14.62(1)	142.55(2)
		2.0037(2)	0.0003(2)	2	2.0048(5)	76.0(7)	339.8(10.2)
			2.0059(2)	3	2.0035(2)	94.2(2.4)	68.7(9.6)
$\mathbf{D}/g_e\beta_e$ (mT)	-33.46(9)	94.26(3)	-148.65(3)	1	207.14(3)	69.00(1)	81.36(2)
		137.20(6)	143.27(6)	2	82.65(3)	55.05(2)	186.92(3)
			-103.74(8)	3	-289.80(4)	42.51(1)	326.61(2)

$B_{4,m}/g_e\beta_e$ (mT)	m		m		m		m		m	
	0	0.24(2)	+1	−0.015(17)	+2	−0.28(2)	+3	−0.05(2)	+4	0.45(1)
			−1	0.37(2)	−2	0.29(1)	−3	0.17(2)	−4	0.14(1)

Data points: 293 Unit weighted: 278 $\sum$ weightings: 283.23 rmsd (mT): 0.19

compensated iron centre, labelled $[FeO_4/H]^0_\beta$ [142], which was not observed in this crystal. As discussed earlier, no lithium-compensated iron centres were observed either, despite the presence of lithium in the crystal, as proved by the $[HLi_2O_4]^0$ centre. The uncompensated iron centre, $[FeO_4]^-$, was also not observed.

As described in the introduction to this chapter, the $[FeO_4]^-$ centre was initially known as the *I* centre, as the Fe^{3+} ion was thought to be interstitially located [119]. Evidence for its location in a silicon substitutional site was provided in part by a pseudocube analysis (Scala and Hutton (1976) [143], and later Mombourquette *et al.* (1986) [144]), whereby structural information is extracted from the fitted $B_{4,m}$ parameters as described by Michoulier and Gaite (1972) [145]. This analysis had not yet been carried out on the $[FeO_4/H]^0$ centre, and thus was performed here using the fitted parameters of table 6.9.

Under exact cubic symmetry, the nine $B_{4,m}$ parameters reduce to three non-zero parameters when an appropriate coordinate system is chosen, with the polar axis along one of the three fourfold or four threefold axes (figure 6-17). The pseudocube analysis assumes that the $B_{4,m}$ parameters are largely dependent on the positions of the nearest-neighbour ions. In this case, an approximately tetrahedral or octahedral site will approximate cubic symmetry regardless of

the often lower symmetry of the crystal system. In α-quartz, a defect centred at a relatively undistorted silicon site surrounded by a distorted oxygen tetrahedron would be expected to have approximate cubic symmetry, as shown in figure 6-17.

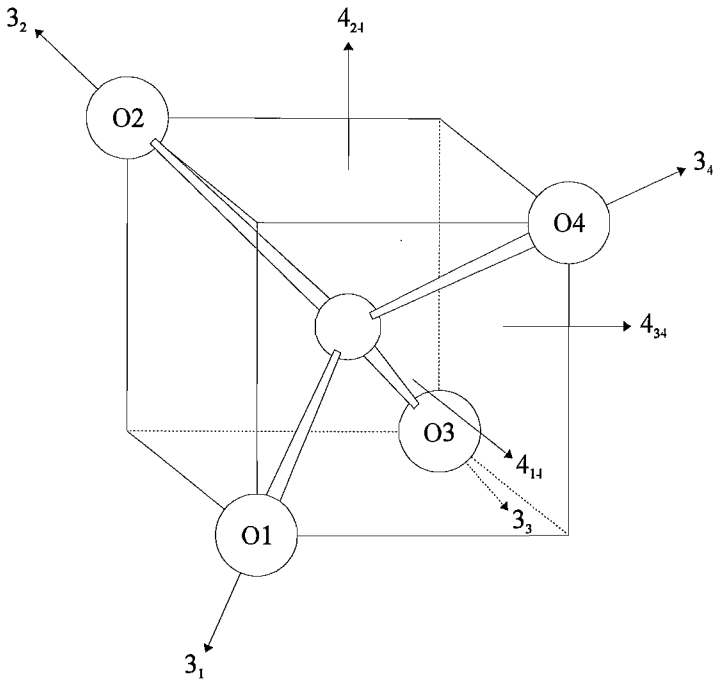

Figure 6-17: Perfect tetrahedron showing cubic-symmetry fourfold and threefold axes, labelled 4 and 3 respectively. The threefold axes are bond directions and the fourfold axes are bisectors of these bonds. The true α-quartz SiO_4 'tetrahedron' has 5 independent 'fourfold axes', as neither 4_{24} and 4_{13} nor 4_{14} and 4_{23} are exactly parallel.

A programme Rotsto (Rotation of Spherical Tensor Operators) has been developed [146], one of the functions of which is to find the coordinate system under which the experimental $B_{4,m}$ or other fourth-rank or sixth-rank tensor parameters (given in crystal coordinate system) best approximate cubic symmetry. This requires axis-transformation operations to be carried out, which is the main purpose of the programme. In the pseudosymmetry search, the search parameters

$$\varepsilon_4^{(k)} = \frac{\sum_q (B_{k,q})^2}{N_k} \qquad q \neq 0, \pm 4 \tag{6.8a}$$

$$\varepsilon_3^{(k)} = \frac{\sum_q (B_{k,q})^2}{N_k} \qquad q \neq 0, \pm 3 \tag{6.8b}$$

where:

$$N_k = \sum_q (B_{k,q})^2 \qquad -k \leq q \leq k \tag{6.9}$$

are calculated for the tensor of rank k expressed in coordinate systems where the polar axis is varied over a hemisphere ($0° \leq \theta \leq 180°$, $0° \leq \phi \leq 360°$). The $B_{k,q}$ parameters referred to in these equations are equivalent to the $B_{4,m}$ parameters, and are merely a different notation. If the defect site approximates cubic symmetry, then minima will be found in $\varepsilon_4^{(k)}$ when the polar axis is parallel to one of the fourfold axes, and minima in $\varepsilon_3^{(k)}$ will be found when the polar axis is parallel to one of the threefold axes. Under perfect cubic symmetry, these parameters would go to zero with the appropriate axis system, as the $B_{k,q}$ elements summed in the numerator of equations 6.8 would all equal zero. For a slightly distorted site, a total of seven minima for the two parameters should be found.

The threefold and fourfold axes found for $[FeO_4/H]^0$ and the minimisation parameters $\varepsilon_{3,4}$ are given in table 6.10. The results of the pseudocube analysis on the $[FeO_4]^-$ centre at 295 K and the calculated pseudocube axes of the undisturbed α-quartz SiO_4 tetrahedron $[SiO_4]^0$ from [144] are also included.

The pseudosymmetry axes of the $[FeO_4/H]^0$ centre are in reasonable agreement with the SiO_4 bond directions and bisectors, but such agreement is also expected in the case of an interstitial site of the type I_c [144]. Pseudocube analysis of a calculated fourth-degree tensor for both the substitutional and interstitial sites in [144] yielded similar pseudosymmetry axes in both cases. The more conclusive evidence for the substitutional site in the analysis of $[FeO_4]^-$ came from comparison of the parameter ε (and others), giving a measure of the distortion from cubic symmetry. The values for the experimental tensor were of the order of those of the tensor calculated for a substitutional site, and at least an order of magnitude smaller than those of the tensor calculated for an interstitial site. For the $[FeO_4/H]^0$ centre, the values of the parameters ε are around an order of magnitude larger than those from the $[FeO_4]^-$ analysis as seen in table 6.10, and are more like those of the theoretical analysis of the interstitial site.

The value of the pseudocube analysis is questionable in this case, as the symmetry of

Table 6.10: Comparison of pseudosymmetry axes for $[FeO_4/H]^0$ centre with $[FeO_4]^-$ centre and the $[SiO_4]^0$ site, all in α-quartz. The Si_0 results were obtained from a pseudocube analysis of a fourth-degree tensor generated from a point-charge calculation.

	Threefold pseudosymmetry axes			Fourfold pseudosymmetry axes		
	θ (deg)	ϕ (deg)	ε_3	θ (deg)	ϕ (deg)	ε_4
$[FeO_4/H]^0$	111.8	232.0	0.148	86.2	358.4	0.147
	73.9	127.2	0.139	10.8	98.0	0.149
	135.4	28.2	0.071	69.5	246.8	0.148
	37.7	323.3	0.032			
$[FeO_4]^-$	112.2	232.1	0.0117	90.0	0.0	0.0066
	68.3	128.4	0.0058	18.1	90.0	0.0072
	136.6	32.8	0.0055	71.8	270.0	0.0075
	43.4	327.2	0.0055			
$[SiO_4]^0$ in	113.9	231.7 (3_1)	0.0028	90.0	0.0 (4_{34})	0.0006
α-quartz	66.8	128.8 (3_2)	0.0006	16.2	89.7 (4_{24})	0.0004
	135.6	34.4 (3_3)	0.0012	73.7	270.0 (4_{14})	0.0003
	44.5	325.4 (3_4)	0.0013			

the $[FeO_4/H]^0$ centre (1) is lower than that of the $[FeO_4]^-$ centre (2) because of the nearby compensating ion. This lower-symmetry site is certain to be more distorted from the ideal local-cubic case. It is likely that the interstitial and substitutional sites are virtually indistinguishable to the pseudocube analysis for such a low-symmetry defect.

Chapter 7

Summary and conclusions

The doping of synthetic zircon crystals by various impurity elements has produced a number of defect centres not seen in nominally undoped synthetic zircon crystals. While not all elements may be easily introduced into the zircon lattice, the results of the synthetic work described in this thesis suggest that many more defects could be generated by doping with other impurities. Of the dopants used in this work, titanium, chromium, yttrium, aluminium and boron all seemed to be easily incorporated into the crystals by the addition of around 0.1 weight percent of the dopant in the flux-growth mixture.

Strangely, attempted doping with phosphorus was not successful (or perhaps too successful), producing poor quality crystals, despite the well-established fact that phosphorus is commonly found in zircon [125]. Variation of the amount or the form of the dopant might solve this problem. Iron doping also proved unsuccessful, but this may again have been the result of the chemicals used for doping. A recent publication by Ball and Van Wyk [62] reports the successful growth of synthetic zircons doped with iron. Crystals have been provided by these authors for future work in the Canterbury laboratory.

The Ti^{4+}/Y^{3+}-doped crystals produced a wealth of centres which had not been observed in nominally undoped synthetic zircons. The two hole centres reported in chapter four add to the large number which have been previously reported, some of which are doubtless the same centre, shown in figure 4-1. The hole centre showing the doublet hyperfine splitting, $[SiO_4/Y]^0$, is almost certainly associated with Y^{3+}, which is presumably present in high concentrations in these crystals, and has the correct oxidation state for charge-balancing of an oxygenic-hole

centre. The chemical similarity of the Y^{3+} ion with Zr^{4+}, as opposed to Si^{4+}, and the A-matrix principal directions suggests that the yttrium substitution occurs at a zirconium lattice site. The other hole centre, $[SiO_4/M]^n$, remains largely a mystery, because of its apparent lack of hyperfine structure and unusually large anisotropy. The crystal-field spin-orbit-coupling analysis suggests a small crystal-field splitting between the ground state and first excited state for this centre, but a large splitting between the ground state and the next excited state. Point-charge calculations might offer some clues as to how this might occur. The large range in oxygenic-hole g anisotropies suggests that a wide range of lattice environments must be possible for these centres. It is difficult to account for these without invoking vacancies in the zircon lattice, as suggested by the assignments made by Krasnobaev *et al.* [63].

The observation of the $Si(Ti^{3+})$ centre in the Ti^{4+}/Y^{3+}-doped crystals allowed the hypotheses presented in the $Zr(Ti^{3+})$ publication [24], regarding the likely differences between such centres, to be tested. The important prediction made on the basis of point-charge calculations, that the ordering of the orbital energy levels split by the crystal-field interaction would be changed, was found to be correct. The crystal-field spin-orbit-coupling analysis of the new centre gave the e and b_2 d orbital levels under $\bar{4}2m$ symmetry swapped with respect to the $Zr(Ti^{3+})$ centre, as was previously calculated. Analysis of the hyperfine structure of the $Si(Ti^{3+})$ centre also indicated increased covalency in comparison to that of the $Zr(Ti^{3+})$ centre, as would be expected for an ion substituted in the covalent SiO_4^{4-} unit of the zircon lattice. There seem to be relatively few examples of transition-metal ions which have been observed to be located in both silicon and zirconium lattice sites in zircon. It is probable that in most cases, one site is preferred over the other. The $Si(Ti^{3+})$ centre has only been observed in the titanium-doped crystals, while the $Zr(Ti^{3+})$ centre is seen in nominally undoped crystals, suggesting that the zirconium site is preferred in this case.

The H centre, also observed in the Ti^{4+}/Y^{3+}-doped crystals, has thus far defied interpretation, but looks to be a very worthy centre to analyse. It has an apparent rich hyperfine structure, the complicated appearance of which suggests significant quadrupole interaction, or perhaps even high spin terms, as were found significant for the $Zr(Ti^{3+})$ centre. Until the nature of the hyperfine structure can be understood, little progress can be made. The observation of the centre in titanium-doped crystals suggests some connection with titanium, but there is no

obvious ^{47}Ti or ^{49}Ti hyperfine structure. Curiously, a weak H centre was also observed in some of the boron-doped crystals.

The Z centre was observed in almost all of the synthetic crystals produced, with a signal intensity greater than the C centre, a reversal of relative intensities observed in the original synthetic crystal from Aerospace Corporation. The greater intensity of the Z centre in these crystals allowed the ^{53}Cr and ^{91}Zr hyperfine structure to be clearly seen and fitted. The observed spectrum was attributable to a transition within one Kramers doublet of a system with $S = \frac{3}{2}$ (Cr^{3+}), with a large zero-field splitting.

It is not entirely certain whether a slight anisotropy observed in the *ab* plane is due to crystal misalignment alone, or crystal misalignment in addition to a slight deviation from uniaxiality in the D matrix. Forbidden lines within the ^{91}Zr hyperfine structure can only be fitted with a non-uniaxial P matrix, which suggests that there may be another unidentified impurity in the Z-centre defect. This impurity would have to be close enough to the zirconium atoms to affect the ^{91}Zr P matrix, but be far enough from the chromium to have little effect on matrix **D**.

The two boron centres observed in the boron-doped crystals are not completely understood, but the identification of the two boron atoms can be made with some confidence. One hyperfine nucleus in the two-boron centre is almost certainly boron, as proved by the identification of the signals due to the minor isotope, ^{10}B. The second I = $\frac{3}{2}$ spin nucleus cannot be identified in the same way due to the smaller size of the hyperfine interaction, but it is very likely to be another boron atom. The centre is only observed in a relatively highly boron-doped crystal, not being observed in the 99E crystals of table 3.1, which had 0.02 weight percent B_2O_3 doping. Boron was certainly incorporated in the 99E crystals, as a boron hole centre [36] was observed, but evidently not enough to produce the two boron centres observed in the more highly-doped (0.1 weight percent) 99B crystals. The g values of the centres suggest that they are electron centres, but the identity of the ion carrying the spin density is unknown. Long run-time spectra have shown no obvious hyperfine structure which would allow identification of the ion. The point-group symmetry of the single-boron centre is unusual for defects in zircon, but can be explained by a model involving two adjacent impurities along a single fourfold rotation-inversion axis. It is somewhat surprising that more compensated electron centres do not have this point-group symmetry. The phosphorus-compensated centres Zr(α) [22] and P(Ti^{3+}) [39] both contain

phosphorus in a lattice site on a different axis from the zirconium or titanium ion carrying the spin density, and thus have point-group symmetry m and 2, respectively.

The $[HLi_2O_4]^0$ centre in α-quartz has been interpreted as a silicon-vacancy centre compensated by one hydrogen, and two lithium ions. The oxygenic-hole nature of the centre is supported by the g-matrix principal directions, and the identity of the hyperfine nuclei is firmly established by the excellent agreement of the experimental and simulated spectra, including many forbidden lines. The centre is probably an analogue of the hydrogarnet defect, which could play a crucial role in the geology of quartz rock. Analysis of the hyperfine matrices using a combination of techniques of varying complexity has produced possible locations for the compensating nuclei. Theoretical calculations should be carried out to investigate the feasibility of these locations.

The $[FeO_4/H]^0$ centre in α-quartz was unfortunately not a new centre [49], so there was little analysis that could be carried out. Pseudocube calculations were not able to confirm the location of the iron ion in a silicon lattice site due to the increased distortion of the local environment from cubic symmetry, in comparison to the uncompensated iron centre [144].

There are clearly many unanswered questions which have arisen from the work detailed in this thesis, which need to be addressed. The $[SiO_4/M]^n$ hole centre shows no hyperfine structure, but must be charge compensated in some way, possibly by a distant +3 ion. ENDOR experiments might be undertaken in the hope of identifying any foreign nuclei not seen by the epr experiment. The unusual g values of this centre also remain to be explained, and obviously require a more rigorous approach than the crystal-field spin-orbit-coupling analysis described herein. The same could be said for all of the hole centres, which could not be fitted exactly without using the α factor. No attempt has yet been made to explain the meaning of this factor.

The range in g anisotropies in the hole centres also needs to be investigated further. Point-charge calculations could be used as a preliminary approach to determining what kind of lattice defects could generate such an apparent range in crystal-field splittings. Oxygen vacancies may be one answer. These calculations could be followed by more advanced theoretical calculations using a small cluster model of the oxygen hole and its immediate surroundings.

There are several issues regarding the Z centre to be addressed. The nature of the ab-plane

anisotropy needs to be understood. It would be useful to find a way of mounting the crystal very precisely in the *ab* plane, or to at least determine by experiment the degree of misalignment in the normal mounting procedure. This might be done using x-ray crystallography, which has been used before to orient irregular crystals. If the exact misalignment could be determined, then its effect on the *ab* plane measurements could be taken into account, and reveal whether any anisotropy would be present in a perfectly aligned crystal.

It would also be very useful to carry out high-field epr experiments on the Z centre, in order to search for transitions within the other Kramers doublet, or even transitions between the doublets, if possible. If these could be found, then the D matrix could be determined much more precisely. This would make the fitting of a small E term in the D matrix much more significant.

The large deviation of the ^{91}Zr P matrix from uniaxial symmetry also needs to be understood. Point-charge calculations could offer a clue as to what might generate the efg at the zirconium positions necessary to produce such a matrix. If a reasonable guess could be made about the nature of any other impurity, synthetic crystals could be grown with the appropriate impurities present.

The complicated H-centre spectrum needs to be understood before any detailed analysis of this defect may take place. The spectrum is rich in structure, but with no obvious patterns, it is very difficult to identify what nuclei are present. If some possible candidates could be proposed, the growth of doped crystals might be the best way of identifying the correct species. A ^{29}Si-enriched crystal would also be useful in confirming or disproving the tentative identification of ^{29}Si hyperfine structure. If the hyperfine structure is due to silicon, high-intensity epr signals in an enriched crystal would probably reveal whether the electron spin density was mostly located on, or away from the silicon atoms. Even if such a crystal did not help with the analysis of the H centre, it would quite likely allow a new analysis of some of the other known centres, and thus not be a wasted exercise. The potential gains would have to be weighed up against the expense before attempting this experiment. The growth mixtures given in table 3.1 mostly use about one gram of the silicon-containing compound.

The two boron centres are another example of a centre where there appears to be an unidentified ion which shows no hyperfine structure. ENDOR measurements could help confirm the

identity of the boron nuclei, and possibly reveal any other nuclei not identified from the epr experiments. Further epr experiments in different planes should also be undertaken, to confirm the unusual symmetry of the single-boron centre.

The $[HLi_2O_4]^0$ centre compensator positions are still tentative, and need to be more thoroughly investigated. The model which has been proposed should certainly be tested by *ab initio* calculations. The proton position is the most confidently assigned, as all of the methods used to fit the position are in reasonable agreement. It would be hoped that theoretical calculations would allow the proton to be located in a similar position. The lithium positions are less confident, but the bridging positions which come out of the analysis seem quite reasonable. In addition to *ab initio* calculations of the defect structure, further modelling of the hyperfine matrices should be undertaken. A thorough research of epr literature could reveal alternative ways in which other workers have approached similar problems.

As explained in the quartz chapter, further experiments should be undertaken in the hope of producing other centres related to $[HLi_2O_4]^0$. In the first instance, a virgin piece of crystal from the same quartz growth should be gamma irradiated, and immediately studied thoroughly by epr at low temperature, before any unstable centres might be lost. If $[HLi_2O_4]^0$ is observed without any precursor having been seen, then the current model for the centre might need to be reconsidered. However, if an $[XHLi_2O_4]^+$ centre could be observed, which loses intensity as $[HLi_2O_4]^0$ gains intensity, then it would lend strong support to the current model.

Secondly, the question of why other forms of the hydrogarnet centre have not been observed, including $[HLi_2O_4]^0$ itself up until now, could be addressed by growing some new synthetic quartz crystals doped with lithium. If quartz crystals with a high lithium content do not reveal any lithium-containing hydrogarnet-type defects, but $[H_4O_4]^+$ and $[H_3O_4]^0$ are observed, then it would tend to suggest that such centres do not form, and the model for $[HLi_2O_4]^0$ would again come into question. If the current model is correct, one might expect to see some of the previously unobserved multiple lithium centres in figure 6-6. After a length of time at sufficiently high temperatures, these might revert to the known stable centres $[H_3O_4]^0$ and $[HLi_2O_4]^0$.

In final summary, this work has attempted to characterise the structure of a number of defects in zircon and α-quartz using epr 'crystallography'. Much progress has been made in

the understanding of these centres, but questions remain. The interpretation of epr data can potentially reveal much about the nature of paramagnetic defects in crystals, but can often be a most challenging task.

Bibliography

[1] E. Zavoiski. Paramagnetic relaxation of liquid solutions for perpendicular fields. *J. Phys. U.S.S.R.*, 9:211–216, 1945.

[2] V. Rojansky. *Introductory Quantum Mechanics.* Blackie and Son, Ltd., London, U.K., 1939.

[3] J. A. Weil, J. R. Bolton, and J. E. Wertz. *Electron Paramagnetic Resonance : Elementary Theory and Practical Applications.* John Wiley and Sons, New York, NY, 1994.

[4] M. H. L. Pryce. A Modified Perturbation Procedure for a Problem in Parmagnetism. *Proc. Phys. Soc.*, A63:25–29, 1950.

[5] A. Abragam and M. H. L. Pryce. Theory of the nuclear hyperfine structure of paramagnetic resonance spectra in crystals. *Proc. Roy. Soc.*, A205:135–153, 1951.

[6] M. T. Hutchings. Point-Charge Calculations of Energy Levels of Magnetic Ions in Crystalline Electric Fields. *Solid State Phys.*, 16:227–73, 1964.

[7] J. R. Pilbrow. *Transition Ion Electron Paramagnetic Resonance.* Clarendon Press, Oxford, U.K., 1990.

[8] A. Abragam and B. Bleaney. *Electron Paramagnetic Resonance of Transition Ions.* Clarendon Press, Oxford, U.K., 1970.

[9] W. C. Tennant and R. F. C. Claridge. Large-Magnitude High-Spin Nuclear Parameters in a Ti^{3+} centre from X-band EPR Measurements at 10 K. *J. Magn. Reson.*, 137:122–131, 1999.

[10] J. A. Weil, T. Buch, and J. E. Clapp. Crystal point-group symmetry and microscopic tensor properties in magnetic resonance spectroscopy. *Adv. Magn. Reson.*, 6:183–256, 1973.

[11] J. F. Nye. *Physical Properties of Crystals. Their Representation by Tensors and Matrices.* Clarendon Press, Oxford, U.K., 1957.

[12] A. D. Rae. Relationship between the Experimental Hamiltonian and the Point Symmetry of a Paramagnetic Species in a Crystal. *J. Chem. Phys.*, 50(6):2672–2685, 1969.

[13] R. J. Strutt. Note on Colour of Zircons, and its Radioactive Origin. *Proc. Roy. Soc. (A)*, 89:405–407, 1914.

[14] J. Lietz. Colouring of zircon by light. *Naturwissenschaften*, 25:415–416, 1937.

[15] P. E. Fielding. Colour centres in zircon containing both Eu^{3+} and U^{4+} ions. *Aust. J. Chem.*, 23:1513–1521, 1970.

[16] K. Eftaxias, P. E. Fielding, and G. Lehmann. Mo^{5+} in synthetic zircon crystals. *Chem. Phys. Lett.*, 160:36–38, 1989.

[17] R. H. D. Nuttall and J. A. Weil. The magnetic properties of the oxygen-hole aluminum centres in crystalline SiO_2. III. $[AlO_4]^+$. *Can. J. Phys.*, 59:1886–1892, 1981.

[18] J. Isoya, W. C. Tennant, Y. Uchida, and J. A. Weil. Biradical Center in α-Quartz. *J. Magn. Reson.*, 49:489–497, 1982.

[19] J. A. Weil. EPR of Iron Centres in Silicon Dioxide. *Appl. Magn. Reson.*, 6:1–16, 1994.

[20] V. P. Solntsev and M. Ya. Shcherbakova. ESR study on the structural defects in irradiated zircons. *Translated from Dokl. Akad. Nauk SSSR*, 1:156–158, 1972.

[21] R. F. C. Claridge, K. M. Mackle, G. L. A. Sutton, and W. C. Tennant. Zircon EPR revisited: 10 K EPR of three low-symmetry centres in irradiated zircon (zircon silicate). *J. Phys.: Condens. Matter*, 6:3429–3436, 1994.

[22] R.F.C. Claridge, W.C. Tennant, C.J. Walsby, S. Schweizer, and J-M. Spaeth. An EPR/ENDOR investigation of a $[ZrPO_4]^0$ centre in x-irradiated zircon: the Zr(α) centre. *J. Phys.: Condens. Matter*, 12:1421–1430, 2000.

[23] V. P. Solntsev and M. Ya. Shcherbakova. Electron spin resonances of Ti^{3+} in α-quartz and zircon. *Zh. Struct. Khim.*, 13:924–927, 1972.

[24] R. F. C. Claridge, D. G. McGavin, and W. C. Tennant. 10 K electron paramagnetic resonance of a d^1 Ti^{3+} centre in x-irradiated zircon (zirconium silicate). *J. Phys.: Condens. Matter*, 7:9049–9060, 1995.

[25] R. F. C. Claridge, G. L. A. Sutton, and W. C. Tennant. X-band EPR Study of an Unusual Center in X-Irradiated Zircon at 10 K. *J. Magn. Reson.*, 125:107–113, 1997.

[26] R. F. C. Claridge, W. C. Tennant, S. Schweizer, and J-M. Spaeth. Structural models for room temperature stable radiation-induced centres in zircon. *J. Phys.: Condens. Matter*, 11:8579–8589, 1999.

[27] B. E. Williamson and K. L. Taylor. Programme ESR. 1996-98.

[28] D G McGavin, M J Mombourquette, and J A Weil. *Computer Program EPR-NMR.* Department of Chemistry, University of Saskatchewan, Canada, 1995.

[29] L. Vegard. Results of crystal analysis, Part II, The zircon group. *Phil. Mag., Ser. 7*, 1:1158–1168, 1926.

[30] W. Binks. The crystalline state of zircon. *Mineral. Mag.*, 21:176, 1926.

[31] O. Hassel. Die Kristallstruktur einiger Verbindungen von der Zusammensetzung MRO_4-I. Zirkon $ZrSiO_4$. *Z. Kristallogr.*, 63:247–254, 1926.

[32] K. Robinson, G. V. Gibbs, and P. H. Ribbe. The structure of zircon: a comparison with garnet. *Amer. Mineral.*, 56:782–790, 1971.

[33] R. M. Hazen and L. W. Finger. Crystal structure and compressibility of zircon at high pressure. *Am. Mineral.*, 64:196–201, 1979.

[34] R. W. G. Wyckoff. *Crystal Structures*, volume 4. Interscience Publishers, New York, NY, 1963.

[35] W. C. Tennant, R. F. C. Claridge, N. S. Lees, and C. J. Walsby. Point defects in crystalline zircon (zircon silicate), $ZrSiO_4$: a review of electron paramagnetic studies. To be published.

[36] C. J. Walsby, N. S. Lees, W. C. Tennant, and R. F. C. Claridge. 15 K EPR of an oxygen-hole boron centre, $[BO_4]^0$, in x-irradiated zircon. *J. Phys.: Condens. Matter*, 12:1441–1450, 2000.

[37] R. F. C. Claridge, K. M. Mackle, G. L. A. Sutton, and W. C. Tennant. 10 K EPR of an oxygen-hole aluminium centre, $[AlO_4]^0$, in x-irradiated zircon, $ZrSiO_4$. *J. Phys.: Condens. Matter*, 6:10415–10422, 1994.

[38] R. F. C. Claridge, N. S. Lees, W. C. Tennant, and C. J. Walsby. Oxygenic-hole centres in x-irradiated zircon: 10 K EPR studies. *J. Phys.: Condens Matter*, 12:1431–1440, 2000.

[39] R. F. C. Claridge, N. S. Lees, W. C. Tennant, and C. J. Walsby. Two Ti^{3+} centres studied by X-band electron paramagnetic resonance at 10 K in zircon. *J. Phys.: Condens. Matter*, 11:3571–3580, 1999.

[40] P. R. Barker and D. R. Hutton. A colour centre in natural zircon. *Phys. Stat. Sol. (b)*, 60:K109–K111, 1973.

[41] J. D. H. Donnay and Y. LePage. The Vicissitudes of the Low-Quartz Crystal Settings or the Pitfalls of Enantiomorphism. *Acta Cryst.*, A 34:584–594, 1978.

[42] R. H. D. Nuttall and J. A. Weil. The magnetic properties of the oxygen-hole aluminum centers in crystalline SiO_2. I. $[AlO_4]^0$. *Can. J. Phys.*, 59:1696–1708, 1981.

[43] R. W. G. Wyckoff. *Crystal Structures*, volume 1. Interscience Publishers, New York, NY, 2nd edition, 1963.

[44] Y. Le Page, L. D. Calvert, and E. J. Gabe. Parameter Variation in Low-Quartz between 94 and 298 K. *J. Phys. Chem. Solids*, 41:721–725, 1980.

[45] S. Danielsson, I. Grenthe, and A. Oskarsson. A Low-Temperature Apparatus for Single-Crystal Diffractometry. The Unit-Cell Dimensions of α-Quartz in the Temperature Range 86-298 K. *J. Appl. Cryst.*, 9:14–17, 1976.

[46] G. A. Lager, J. D. Jorgensen, and F. J. Rotella. Crystal structure and thermal expansion of α-quartz SiO_2 at low temperatures. *J. Appl. Phys.*, 53(10):6751–6756, 1982.

[47] R. C. Vogel and G. Gibson. Migration of Sodium Ions through Quartz Plates in an Electric Field. I. *J. Chem. Phys.*, 18(4):490–494, 1950.

[48] G. Gibson and R. C. Vogel. Migration of Lithium and Several Multicharged Ions through Quartz Plates in an Electric Field. II. *J. Chem. Phys.*, 18(8):1094–1097, 1950.

[49] M. J. Mombourquette, J. Minge, M. R. Hantehzadeh, J. A. Weil, and L. E. Halliburton. Electron paramagnetic resonance study of Fe^{3+} in α-quartz: Hydrogen-compensated center. *Phys. Rev. B*, 39(7):4004–4008, 1989.

[50] R. A. Laudise. *The Growth of Single Crystals.* Prentice-Hall, Inc., Englewood Cliffs, NJ, 1970.

[51] R. Dharmarajan, R. F. Belt, and R. C. Puttbach. Hydrothermal and flux growth of zircon crystals. *J. Cryst. Growth*, 13/14:535–539, 1972.

[52] R. Uhrin, R. F. Belt, and R. C. Puttbach. The hydrothermal growth of zircon. *J. Cryst. Growth*, 21:65–68, 1974.

[53] P. Hautefeuille and A. Perrey. Synthesis of emerald and of phenacite. *Compt. Rend.*, 106:1800, 1888.

[54] B. R. Pamplin, editor. *Crystal Growth.* Pergamon Press Ltd., Oxford, U.K., 1975.

[55] J. C. Brice. *The Growth of Crystals from Liquids.* North-Holland Publishing Company, Amsterdam, Netherlands, 1973.

[56] A. A. Ballman and R. A. Laudise. Crystallisation and Solubility of Zircon and Phenacite in Certain Molten Salts. *J. Am. Ceram. Soc.*, 48(3):130–133, 1965.

[57] A. B. Chase and J. A. Osmer. Growth and Preferential Doping of Zircon and Thorite. *J. Electrochem. Soc.*, 113:198–199, 1966.

[58] B. M. Wanklyn. Growth of silicate and germanate crystals from PbO-SiO_2(GeO_2) fluxes. *J. Cryst. Growth*, 37:51–56, 1977.

[59] A. A. Ballman and R. A. Laudise. Hydrothermal Growth. In J. J. Gilman, editor, *The Art and Science of Growing Crystals*, chapter 13, pages 231–251. John Wiley and Sons, Inc., New York, NY, 1963.

[60] J. C. Brice. Crystals for quartz resonators. *Rev. Mod. Phys.*, 57(1):105–146, 1985.

[61] N. S. Lees. B.Sc Honours Research Project: Growth of Doped Single Crystals for EPR Analysis. Technical report, University of Canterbury, Christchurch, New Zealand, September 1997.

[62] D. Ball and J. A. Van Wyk. The Electron Paramagnetic Resonance of Fe^{3+} Observed in Two Axial Sites in Synthetic Single Crystals of Zircon ($ZrSiO_4$). *Phys. Stat. Sol. (b)*, 218:545–551, 2000.

[63] A. A. Krasnobaev, S. L. Votyakov, and V. Ya. Krochalev. *Specktroskopya Tsirconov.* Nauka, Moscow, 1988.

[64] V. M. Vinokurov, N. M. Gainullina, L. A. Evgrafova, N. M. Nizamutinov, and A. N. Suslina. $Zr^{+4} \rightarrow Y^{3+}$ isomorphism in zircon and the associated charge compensation. *Sov. Phys. - Crystallogr.*, 16(2):262–265, September-October 1971.

[65] R. J. Danby and D. R. Hutton. A new radiation defect centre in natural zircon. *Phys. Stat. Sol. (b)*, 98:K125–K128, 1980.

[66] R.C. Weast, editor. *CRC Handbook of Chemistry and Physics.* CRC Press Inc., Boca Raton, FL, 61st edition, 1980-1981.

[67] L. E. Vannotti and J. R. Morton. Paramagnetic-Resonance Spectra of S^- Trapped in Alkali Halide Crystals. *Phys. Rev.*, 174(2):448–453, 1968.

[68] R. M. Golding. *Applied Wave Mechanics.* D. Van Nostrand Company Ltd, London, U.K., 1969.

[69] M. Stapelbroek, R. H. Bartram, O. R. Gilliam, and D. P. Madacsi. ESR investigation of the $[Al]^0$ center in tetragonal GeO_2. *Phys. Rev. B*, 13(5):1960–1966, 1976.

[70] W. C. Tennant. Programme Pdorbit.for, 2000.

[71] R. H. Bartram, C. E. Swenberg, and J. T. Fournier. Theory of Trapped-Hole Centers in Aluminium Oxide. *Phys. Rev.*, 139:A941–A951, 1965.

[72] R. F. C. Claridge. Personal communication. 1999.

[73] J. Isoya and J. A. Weil. Uncompensated titanium(3+) center in α-quartz. *Phys. Stat. Sol. A*, 52(2):K193–196, 1979.

[74] P. Bailey, T. Pawlik, H. Sothe, J.-M. Spaeth, and J. A. Weil. $[TiO_4]^-$ in α-quartz studied by low temperature electron paramagnetic resonance. *J. Phys.: Condens. Matter*, 4(15):4063–4073, 1992.

[75] D. G. McGavin and W. C. Tennant. Coordinate rotations and relations amongst spin-hamiltonian parameters in E.P.R. spetroscopy. *Mol. Phys.*, 55(4):853–866, 1985.

[76] S. Fraga, J. Karwowski, and K. M. S. Saxena. *Handbook of atomic data*, volume 5 of *Physical sciences data.* Elsevier, Amsterdam, Netherlands, 1976.

[77] S. Di Gregorio, M. Greenblatt, J. H. Pifer, and M. D. Sturge. An ESR and optical study of V^{4+} in zircon-type crystals. *J. Chem. Phys.*, 76(6):2931–2937, 1982.

[78] J. R. Morton and K. F. Preston. Atomic Parameters for Paramagnetic Resonance Data. *J. Magn. Reson.*, 30:577–582, 1978.

[79] R. E. Watson and A. J. Freeman. Hatree-Fock Theory of Electric and Magnetic Hyperfine Interactions in Atoms and Magnetic Compounds. In A. J. Freeman and R. B. Frankel, editors, *Hyperfine Interactions*, chapter 2, pages 53–94. Academic Press, New York, NY, 1967.

[80] A. J. Freeman and R. E. Watson. Hyperfine Interactions in Magnetic Materials. In G. T. Rado and H. Suhl, editors, *Magnetism (IIA)*, chapter 4, pages 167–305. Academic Press, New York, NY, 1965.

[81] S. Geschwind. Special Topics in Hyperfine Structure in EPR. In A. J. Freeman and R. B. Frankel, editors, *Hyperfine Interactions*, chapter 6, pages 225–286. Academic Press, New York, NY, 1967.

[82] H. Rinneberg and J. A. Weil. EPR Studies of Ti^{3+}-H^{+} Centers in X-Irradiated α-Quartz. *J. Chem. Phys.*, 56(5):2019–2028, 1972.

[83] Bruker Almanac 2000. 2000.

[84] D. R. Hutton. Rotational properties of electron spin resonance spectra. *J. Phys. C*, 2:673–679, 1969.

[85] J. R. Pilbrow. Effective g Values for $S = \frac{3}{2}$ and $S = \frac{5}{2}$. *J. Mag. Res.*, 31:479–490, 1978.

[86] D. P. Madacsi, M. Stapelbroek, and O. R. Gilliam. Paramagnetic resonance of Cr^{3+} in tetragonal GeO_2. *Phys. Rev. B*, 9(5):2023–2029, 1974.

[87] S. L. Hou, R. W. Summitt, and R. F. Tucker. Electron-Paramagnetic-Resonance and Optical Spectra of Cr^{3+} in SnO_2 Single Crystals. *Phys. Rev.*, 154(2):258–265, 1967.

[88] H. J. Gerritsen, S. E. Harrison, and H. R. Lewis. Chromium-Doped Titania as a Maser Material. *J. Appl. Phys.*, 31(9):1566–1571, 1960.

[89] A. Watterich, K. Raksányi, O. R. Gilliam, R. H. Bartram, L. A. Kappers, H. Söthe, and J.-M. Spaeth. Electron spin resonance of Cr^{3+} and perturbed Cr^{3+} centers in α-TeO_2:Cr. *J. Phys. Chem. Solids*, 53:189–195, 1992.

[90] S. K. Kurtz and W. G. Nilsen. Paramagnetic Resonance Spectra of Cr^{3+} in $ZnWO_4$. *Phys. Rev.*, 128(4):1586–1588, 1962.

[91] R. W. Terhune, J. Lambe, C. Kikuchi, and J. Baker. Hyperfine Spectrum of Chromium 53 in Al_2O_3. *Phys. Rev.*, 123(4):1265–1268, 1961.

[92] D. H. Dickey and J. E. Drumheller. Angle Dependence of Paramagnetic-Resonance Line Intensities of Trivalent Cr^{53} in MgO. *Phys. Rev. B*, 1(9):3582–3587, 1970.

[93] D. G. Rexford, Y. M. Kim, and H. S. Story. Electron-Spin Resonance Studies of Cr^{3+} in $LiNbO_3$. *J. Chem. Phys.*, 52(2):860–863, 1970.

[94] G. Corradi, H. Söthe, J.-M. Spaeth, and K. Polgár. Electron spin resonance and electron-nuclear double-resonance investigation of a new Cr^{3+} defect on an Nb site in $LiNbO_3$:Mg:Cr. *J. Phys.: Condens. Matter*, 3:1901–1908, 1991.

[95] K. Pack and A. Manoogian. Electron spin resonance studies of $^{53}Cr^{3+}$ and VO^{2+} ions in $AlCl_3.6H_2O$. *Can. J. Phys.*, 54:217–222, 1976.

[96] R. Alcalá, P. J. Alonso, V. M. Orera, and H. W. Den Hartog. Cr^{+} and Cr^{3+} defects in CaF_2 and SrF_2. *Phys. Rev. B*, 32(6):4158–4163, 1985.

[97] M. Gaft, G. Boulon, G. Panczer, Y. Guyot, R. Reisfeld, S. Votyakov, and G. Bulka. Unexpected luminescence of Cr^{5+} and Cr^{3+} ions in $ZrSiO_4$ zircon crystals. *J. Lumin.*, 87-89:1118–1121, 2000.

[98] P. G. Baranov, V. A. Khramtsov, and E. N. Mokhov. Chromium in silicon carbide: electron paramagnetic resonance studies. *Semicond. Sci. Technol.*, 9:1340–1345, 1994.

[99] H. G. Grimmeiss, E. Janzen, H. Ennen, O. Schirmer, J. Schneider, R. Woerner, C. Holm, E. Sirtl, and P. Wagner. Tellurium donors in silicon. *Phys. Rev. B: Condens. Matter*, 24(8):4571–4586, 1981.

[100] M. Greenblatt, J. H. Pifer, B. R. McGarvey, and B. M. Wanklyn. Electron spin resonance of Cr^{5+} in YPO_4 and YVO_4. *J. Chem. Phys.*, 74(11):6014–6017, 1981.

[101] C. A. Bates, W. S. Moore, K. J. Standley, and K. W. H. Stevens. Paramagnetic Resonance of a Cu^{2+} Ion in a Tetrahedral Crystal Field. *Proc. Phys. Soc.*, 79:73–83, 1962.

[102] J. H. Schulman and W. D. Compton. *Color Centers in Solids*, volume 2 of *International series of monographs on solid state physics*. Pergamon Press, Oxford, U.K., 1962.

[103] J. A. Weil. A Review of Electron Spin Spectroscopy and Its Application to the Study of Paramagnetic Defects in Crystalline Quartz. *Phys. Chem. Minerals*, 10:149–165, 1984.

[104] J. A. Weil. A review of the EPR spectroscopy of the point defects in α-quartz: the decade 1982-1992. In C. R. Helms and B. E. Deal, editors, *Phys. Chem. SiO_2 Si-SiO_2 Interface 2*, pages 131–144. Plenum, New York, N. Y., 1993.

[105] R. H. D. Nuttall and J. A. Weil. Two hydrogenic trapped-hole species in α-quartz. *Solid State Commun.*, 33:99–102, 1980.

[106] D. W. Foreman. Neutron and X-ray Diffraction Study of $Ca_3Al_2(O_4D_4)_3$, a Garnetoid. *J. Chem. Phys.*, 48:3037–3041, 1968.

[107] P. Cordier and J. C. Doukhan. Plasticity and dissociation of dislocations in water-poor quartz. *Phil. Mag. A*, 72(2):497–514, 1995.

[108] D. T. Griggs and J. D. Blacic. Quartz: Anomalous Weakness of Synthetic Crystals. *Science*, 147:292–295, 1965.

[109] J. Purton, R. Jones, M. Heggie, S. Oberg, and C. R. A. Catlow. LDF Pseudopotential Calculations of the α-Quartz Structure and Hydrogarnet Defect. *Phys. Chem. Minerals*, 18:389–392, 1992.

[110] J. S. Lin, M. C. Payne, V. Heine, and J. D. C. McConnell. *Ab Initio* Calculations on $(OH)_4$ Defects in α-Quartz. *Phys. Chem. Minerals*, 21:150–155, 1994.

[111] J. D. C. McConnell, J. S. Lin, and V. Heine. The Solubility of $[4H]_{Si}$ Defects in α-Quartz and their Role in the Formation of Molecular Water and Related Weakening on Heating. *Phys. Chem. Minerals*, 22:357–366, 1995.

[112] A. C. McLaren, R. F. Cook, S. T. Hyde, and R. C. Tobin. The Mechanisms of the Formation and Growth of Water Bubbles and Associated Dislocation Loops in Synthetic Quartz. *Phys. Chem. Minerals*, 9:79–94, 1983.

[113] M. S. Paterson. The Thermodynamics of Water in Quartz. *Phys. Chem. Minerals*, 13:245–255, 1986.

[114] A. C. McLaren, J. D. FitzGerald, and J. Gerretsen. Dislocation Nucleation and Multiplication in Synthetic Quartz: Relevance to Water Weakening. *Phys. Chem. Minerals*, 16:465–482, 1989.

[115] P. Cordier and J. C. Doukhan. Water solubility in quartz and its influence on ductility. *Eur. J. Mineral.*, 1:221–237, 1989.

[116] P. Cordier, J. A. Weil, D. F. Howarth, and J. C. Doukhan. Influence of the $(4H)_{Si}$ defect on dislocation motion in crystalline quartz. *Eur. J. Mineral.*, 6:17–22, 1994.

[117] T. I. Barry and W. J. Moore. Amethyst: Optical Properties and Paramagnetic Resonance. *Science*, 144:289–290, 1964.

[118] D. R. Hutton. Paramagnetic resonance of Fe^{+++} in amethyst and citrine quartz. *Phys. Lett.*, 12:310–311, 1964.

[119] G. Lehmann and W. J. Moore. Optical and Paramagnetic Properties of Iron Centers in Quartz. *J. Chem. Phys.*, 44(5):1741–1745, 1966.

[120] L. M. Matarrese, J. S. Wells, and R. L. Peterson. EPR Spectrum of Fe^{3+} in Synthetic Quartz. *Bull. Am. Phys. Soc.*, 9:502, 1964.

[121] L. M. Matarrese, J. S. Wells, and R. L. Peterson. EPR Spectrum of Fe^{3+} in Synthetic Brown Quartz. *J. Chem. Phys.*, 50(6):2350–2360, 1969.

[122] R. Schnadt and J. Schneider. The Electronic Structure of the Trapped-Hole Center in Smoky Quartz. *Phys. Kondens. Materie*, 11:19–42, 1970.

[123] R. T. Weber. *WIN-EPR SimFonia User's Manual (software version 1.2)*. EPR Division, Bruker Instruments, Inc., Billerica, MA USA, 1995.

[124] J. A. Weil and J. H. Anderson. Direct Field Effects in Electron Paramagnetic Resonance Hyperfine Spectra. *J. Chem. Phys.*, 35(4):1410–1417, 1961.

[125] C. J. Walsby. *Theoretical and Experimental Electron Paramagnetic Resonance Studies of Single Crystals*. PhD thesis, University of Canterbury, Christchurch, New Zealand, March 1999.

[126] C. J. Walsby, N. S. Lees, R. F. C. Claridge, and J. A. Weil. The magnetic properties of oxygen-hole aluminum centres in crystalline SiO_2. VI. A new stable $[AlO_4/Li]^+$ centre. To be published.

[127] J. A. Weil. Germanium-Hydrogen-Lithium Center in α-Quartz. *J. Chem. Phys.*, 55(10):4685–4698, 1971.

[128] R. H. D. Nuttall and J. A. Weil. The magnetic properties of the oxygen-hole aluminum centers in crystalline SiO_2. II. $[AlO_4/H^+]^+$ and $[AlO_4/Li^+]^+$. *Can. J. Phys.*, 59:1709–1718, 1981.

[129] R. H. D Nuttall and J. A. Weil. Oxygen-17 Hyperfine Structure of Trapped Holed Centre $[AlO_4]^0$ in α-Quartz. *Solid State Commun.*, 35:789–, 1980.

[130] R. G. A. R. MacLagan. Private communication. 1998-99.

[131] J. Isoya, J. A. Weil, and P. H. Davis. EPR of atomic hydrogen ^1H and ^2H in α-quartz. *J. Phys. Chem. Solids*, 44(4):335–343, 1983.

[132] F. E. Mabbs and D. Collison. *Electron Paramagnetic Resonance of d Transition Metal Compounds.* Elsevier Science Publishers B. V., Amsterdam, Netherlands, 1992.

[133] W. C. Tennant. Programme Dipole.for, 1999.

[134] J. J. Moré, B. S. Garbow, and K. E. Hillstrom. *User Guide for MINPACK-1.* Argonne National Laboratory, Argonne, IL, 1980.

[135] M. J. Mombourquette. *Program MSPKL.FOR.* PhD thesis, University of Saskatchewan, Saskatoon, Canada, 1986.

[136] M. J. Mombourquette, R. J. McEachern, and J. A. Weil. Atom positions from hyperfine data for germanium centres in α-quartz. *J. Magn. Reson.*, 33:570–580, 1995.

[137] H. M. McConnell and J. Strathdee. Theory of anisotropic hyperfine interactions in π-electron radicals. *J. Mol. Phys.*, 2:129–138, 1959.

[138] R. M. Pitzer, C. W. Kern, and W. N. Lipscomb. Evaluation of Molecular Integrals by Solid Spherical Harmonic Expansions. *J. Chem. Phys.*, 37(2):267–274, 1962.

[139] M. J. Mombourquette and J. A. Weil. Structure Determination of the AlO_4 Hole Centres in α-Quartz by EPR and SCF MO. *J. Magn. Reson.*, 66:105–117, 1986.

[140] R. S. Dickson, J. A. Weil, and P. H. Davis. The paramagnetic germanium-sodium impurity centres $[GeO_4/Na]^0_A$ and $[GeO_4/Na]^0_C$ in α-quartz. *Can. J. Phys.*, 69:761–779, 1991.

[141] Y. Sakai and T. Anno. New set of rules of the Slater type on the screening constants and the effective principal quantum numbers. *J. Chem. Phys.*, 60(2):620–624, 1974.

[142] J. Minge, J. A. Weil, and D. G. McGavin. EPR study of Fe^{3+} in α-quartz: Characterization of a new type of cation-compensated center. *Phys. Rev. B*, 40(10):6490–6498, 1989.

[143] C. M. Scala and D. R. Hutton. Site Assignment of Fe^{3+} in α-Quartz. *Phys. Stat. Sol. (b)*, 73:K115–K117, 1976.

[144] M. J. Mombourquette, W. C. Tennant, and J. A. Weil. EPR study of Fe^{3+} in α-quartz: A reexamination of the so-called *I* center. *J. Chem. Phys.*, 85(1):68–79, 1986.

[145] J. Michoulier and J. M. Gaite. Site Assignment of Fe^{3+} in Low Symmetry Crystals. Application to $NaAlSi_3O_8$. *J. Chem. Phys.*, 56(11):5205–5213, 1972.

[146] W. C. Tennant, C. J. Walsby, R. F. C. Claridge, and D. G. McGavin. Rotation matrix elements and further decomposition functions of two-vector tesseral spherical tensor operators; their uses in electron paramagnetic resonance spectroscopy. *J. Phys.: Condens. Matter*, 12:9481–9495, 2000.